

MANUFACTURING OPTIMAL NANOCRYSTALLINE MICROTRUSS MATERIALS

by

Ante Tony Lausic

A thesis submitted in conformity with the requirements
for the degree of Doctor of Philosophy
Graduate Department of Materials Science and Engineering
University of Toronto

© Copyright 2016 by Ante Tony Lausic

Abstract

Manufacturing Optimal Nanocrystalline Microtruss Materials

Ante Tony Lausic

Doctor of Philosophy

Graduate Department of Materials Science and Engineering

University of Toronto

2016

Fabrication of optimal ultra-lightweight hybrid cellular materials via a two-step synthesis method of rapid prototyping followed by electrodeposition was accomplished in three distinct stages: modelling, fabrication, and validation. For the first stage, a baseline microtruss architecture with multiple geometric and material degrees of freedom was optimized with relation to the expected failure mechanisms. An intrinsic link between material selection and architectural variables was discovered and quantified. For a given electrodeposited polycrystalline Ni/polymer microtruss that has already been optimized for maximum load carrying capacity with minimal mass, substituting a nanocrystalline coating shifts the location of optimal design. It is possible through the redistribution of metal and polymer in this nanocrystalline microtruss to further decrease the total beam mass by a factor of three, showcasing this material-geometry dependency. The second stage hinged on developing a novel processing technique to deposit metal coatings on the as-printed polymer parts. The critical step of adhesion was solved using an 18 M sulphuric acid wash to preferentially smoothen the inherent 0.6 mm roughness on the samples. Finally, the models were validated through the testing of as-printed and coated rods and microtrusses. Nanocrystalline microtrusses showed a 60x increase in peak flexural strength with only a 6x increase in density. Further optimization can more than halve the final density while maintaining the same load carrying capacity by removing the sacrificial polymer core using the same sulphuric acid wash. The experimental values fit very well to those predicted in stage one for varying slenderness ratios, scales, and material systems.

Dedication

To faith, family, and friends:

They say the journey is more important than the destination. That the real learning is in the doing. But none of this is possible without those closest to you. Heavenly Father, thank you for giving me the strength and stubbornness to see this all through. Thank you Mom, Dad, and Sis, for your infinite support and love, and not giving up whenever you heard ‘just a few more months’. To my friends for keeping me sane during this period of my life, be ready for a lot of ‘Doctor’s orders’ in the coming years, and of course, my gratitude for being there for me.

This work is dedicated to all of you.

“When you do things right, people won’t be sure you’ve done anything at all.”

Acknowledgements

Over the six years of summer research, undergraduate thesis work, and this doctoral study, I have been blessed to have Prof. Glenn D. Hibbard's and Prof. Craig A. Steeves' guidance. The work done here is as much a testament of my success as it is their patience, brilliance, and unwavering support, for which I am extremely thankful.

I would like to thank my committee chair Prof. Doug Perovic and committee member Prof. Chandra Veer Singh for their valuable input and discussions on topics relating to this work as well as Prof. Uwe Erb and Prof. Il-Yong Kim for their roles as external advisors. Experimentation and characterization on these materials would not have been possible without the help of Bharat Bhaga, Adam Bird, Sal Boccia, Matthew Daly, Dr. Dan Grozea, Dr. Miroslavna Kovylna, and Adam Yaremko, as well as the support from Dr. Jon McCrea and the rest of Integran Technologies, Inc.

Finally, I extend many thanks to the members of the Hybrid Materials Design Group for their support and friendship; in particular: Khaled Abu Samk, Dr. Eral Bele, Dr. Brandon Bouwhuis, Dr. Megan Hostetter, Dr. Balaji Devatha Venkatesh, and Bosco Yu.

Financial assistance from the following organizations is gratefully acknowledged: Natural Sciences and Engineering Research Council of Canada, Ontario Graduate Scholarship Program, Ontario Research Fund for Research Excellence, Graduate Department of Materials Science and Engineering, and University of Toronto.

Contents

1	Introduction	1
2	Literature Review	5
2.1	Motivation in applications	5
2.2	Types of hybrid materials	7
2.2.1	Cellular materials as a core for sandwich panels	8
2.2.2	Stretch- vs. bending-dominated lattices	9
2.2.3	Optimal architectures	12
2.3	Synthesis routes for stretch-dominated lattices	14
2.3.1	Investment casting	14
2.3.2	Perforation stretching	16
2.3.3	Wire assembly and weaving	19
2.3.4	Summary of current manufacturing techniques for lattices	21
2.4	Rapid prototyping - complete freedom in lattice design	22
2.4.1	A brief history of rapid prototyping	23
2.5	Lattices formed via rapid prototyping: strengthening techniques	29
2.5.1	Electrodeposition of nanocrystalline materials	30
2.6	Summary of key conclusions	35
3	Model derivation: Optimization of hybrid microtruss architecture	37
3.1	Stress in a column loaded in uniaxial compression	37

3.1.1	Stress in a beam during three-point bending	39
3.1.2	Force in the face and core struts of the microtruss	41
3.2	Non-dimensionalization and optimization	45
3.2.1	Columns	46
3.2.2	Microtrusses	50
3.2.3	Optimal trajectories for composite microtrusses	51
3.3	Summary of key conclusions	54
4	Characterization and mechanical performance of rapid prototyped polymer material	56
4.1	Determination of optimal printing conditions for polymer microtruss fabrication	57
4.1.1	Curing conditions in the rapid prototyper	58
4.1.2	Removal of wax supports and finishing process	59
4.2	Post-printing analysis of parts	60
4.2.1	Characterization of part surface and printer resolution	62
4.2.2	Shrinkage measurements and their effect on a polymer density calculation	69
4.3	Material properties extracted from compression, tension, and bending tests . . .	73
4.3.1	Tensile testing of dogbones	73
4.3.2	Strain rate sensitivity in polymer tensile dogbones	78
4.3.3	Tensile vs compressive stiffness comparison	80
4.3.4	Flexural bending of polymer blocks	82
4.4	Summary of key conclusions	85
5	Experimental validation of analytical model	88
5.1	Validation of model for uniaxially compressed polymer tubes	88
5.2	Validation of model for solid, polymer microtrusses in bending	91
5.2.1	Slenderness Effects	95
5.2.2	Scaling Effects	101

5.2.3	Graded micotruss architectures	105
5.3	Weight-specific improvement by moving from blocks to microtrusses	111
5.3.1	Methods to improve on the single material microtruss' weight-specific performance	113
5.4	Summary of key conclusions	121
6	Predictions based on derived models	122
6.1	Electrodeposited nickel material properties	122
6.2	Polycrystalline nickel: columns and microtruss beams	124
6.3	Grain size reduction (increasing \hat{P})	127
6.4	Core removal (decreasing \hat{M})	133
6.5	Other strengthening techniques	139
6.6	Summary of key conclusions	144
7	Metallic microtrusses	145
7.1	Metal/polymer rods in bending	145
7.2	Metal/polymer trusses in bending	153
7.2.1	Comparing hybridization with nanocrystalline Ni to other improvements	161
7.3	Summary of key conclusions	163
8	Hollow Structures and Next Steps	164
8.1	Hollow polymer microtrusses	164
8.1.1	Combinations of structural improvements	169
8.2	Cumulative comparison of polymer and metal/polymer structures	171
8.3	Hollow metallic microtrusses	172
8.3.1	Thermal properties of the wax and finished polymer	173
8.3.2	Polymer dissolution with strong acids and FDM microtrusses	175
9	Conclusion	180

Bibliography	183
A Additional mechanical testing on rapid prototyped polymer parts	200
A.1 Time effect on polymer properties	200
A.2 Tensile tests on full-scale tensile coupons	205
A.3 NiCo stress-strain curve and Voce fit	208
B MATLAB code for the optimization of hybrid microtrusses in bending	210
C Mechanical anisotropy in metal/metal foams	217
D Electrodeposition and metalization recipe	225

List of Tables

4.1	Summarized mechanical properties from tensile dogbones printed in various orientations. Value for the UTS, elongation %, and Young's modulus are accompanied with the standard deviation of the population size for each sample type (ten samples in each case).	76
5.1	Summary of geometries tested in three-point bending as well as predicted and measured peak loads and failure types for each specimen type where P_c , P_{SE} , and P_m represent the predicted critical load, the predicted critical load with size effects accounted for and the experimentally measured peak load, respectively. Values for the requested radius, r_r , and experimentally measured radius, r_e , are included where the measured radius after printing is measured to $\pm 10\mu\text{m}$	93
5.2	Geometries of reduced core polymer microtrusses.	106
6.1	Properties of four different electrodeposited Ni coatings and their fit statistics .	123
6.2	Optimal design dimensions for struts in a 1 m x 0.5 m microtruss supporting 11 kN in three-point bending for the four grain sizes considered and both filled and hollow scenarios	133
6.3	Material properties for the three n-NiFe curves considered	140

7.1 Collective values of radius and coating thickness for each batch of rods produced. Radii of the original rod and after etching performed with micrometer as was coating thickness of deposited Ni. Values for coating thickness of electroless Ni were smaller than accuracy of micrometer and were back calculated from mass. Standard deviation reported for each batch of five samples. 148

7.2 Collective mechanical properties for each batch of rods produced. Peak strength and normalized peak strength are expressed in flexural terms using equation 7.1. Maximum deflection for the as-printed, etched and electroless samples are not provided as samples slipped out before fracture. Standard deviation reported for each batch of five samples. 154

7.3 Measured values for radius and coating thickness of the ten samples tested here along with mechanical properties from three-point bending tests. Radii for the plated samples were not recorded prior to electrodeposition and are quoted as the average of the unplated samples. 157

List of Figures

2.1	A material selection map outlining the strength and density of known materials with a void in the top left corner [11].	6
2.2	Types of hybrid and composites materials that can fill the void in strength-density space [10].	7
2.3	An example of varying pore size in reticulated vitreous carbon (RVC) foam from 10 to 40 to 100 PPI (left to right). While polymer foams can have PPI values up to 100 [18], metals are usually limited to 40 PPI [19].	9
2.4	The first example of a three-dimensional lattice that shows up in published scientific work belongs to Fuller in his 1961 patent (left) [22]. However, structures with triangles resembling lattices go as far back as Roman times. Here is a 113 AD relief from Trajan's column depicting Trajan's bridge in the background (right) [24].	10
2.5	Comparisons between mechanisms active in unit cells in the bending-dominated (top left) and stretch-dominated (top right) structures. Examples of frames that have (a) $M < 0$, (b) $M = 0$, and (c) $M > 0$ [1].	11

2.6	The design of an optimal airplane floor (a) can be broken into a simple three-point bending test (b). Optimization is performed by placing a mesh on the structure, identifying areas of little to no loading and removing those small sections to reinforce areas of higher load. This process repeats through many iterations (c) before it arrives at the optimal shape for the given input parameters (d) [28].	13
2.7	Lattice block structures fabricated by a combination of rapid prototyping and investment casting (left) [53] and a schematic of the modified technique with polymer burnout after the molten metal has been poured into the mold (right) [29].	15
2.8	The jig used to deformation stretch sheets into lattices (left) and the resulting structure formed from a hexagonal punched stainless steel sheet (right) [62]. . .	17
2.9	After perforation stretching, a square punched aluminum sheet becomes a square pyramidal lattice [63].	17
2.10	The process begins with a solid sheet which is first punched to create the hexagonal pattern. Feeding in the extended hexagonal perforated sheet leads to a folded lattice on the other side in the desired tetrahedral pattern [67].	19
2.11	A square weave pattern can be put together using metal wire precursors (left) and then assembled into three-dimensional blocks (right) [69].	20
2.12	The jig that is used to layup metal tubes can be modified to create various lattices, but relies on consistent stacking such that a tetrahedral shape is not possible [29].	21
2.13	By overlapping bent wires in a set pattern, it is possible to create both tetrahedral (left) and Kagome (right) lattices [71].	22

2.14	Hybrid solutions usually incorporate multiple materials to each handle a given function of the design. This means additional care must be taken to engineer a good interaction or interface between these separate materials to ensure failure does not occur prematurely (left) [10]. An example of bond failure at the interface of the face sheet and the core in a sandwich panel (right) [74].	23
2.15	The stereolithography process centers on the use of a photocurable polymer source with a stage just beneath the surface (left). Two dimensional patterns are fabricated using a light source that exposes and cures the polymer only in areas it has focused on. The whole part is then removed when the process is complete [84]. Advances on this technique have removed the vat of liquid photopolymer and instead cure it where it is sprayed with a general UV light source rather than a targeted laser (right) [85].	25
2.16	The FDM process is simply the melting of a wire precursor as it passes through a heating block and is then drawn out onto a stage. It is possible to have multiple channels to print multiple materials or colors at the same time or to print a dissolvable support material to create truly complex architecture [88].	27
2.17	The SLS process uses the same light source, lenses, and mirror technology as the SLA method but the laser is powerful enough to sinter or melt metal powders into a solid shape. Rollers are used to push fresh powder into the build chamber to cover up the previously solidified layer [89].	28
2.18	Brittain <i>et al.</i> 's metal/polymer lattice where the polymer truss was made with photolithography and subsequent deformation folding techniques before being joined by silver paint. Electrodeposition on the entire part creates a metallic coating overtop the polymer preform [93].	29

2.19	Examples of composite lattice structures with recoverable properties. A Ni-polymer lattice fabricated via self-propagated photopolymer waveguide prototyping was crushed and then allowed to recover past its failure point (top) [45]. A ceramic lattice fabricated via two-photon lithography where struts are in the nanometer scale reveal ductile properties after crushing (bottom) [46].	31
2.20	An electrodeposition setup showing the bath, power supply and ammeter displaying the provided current, taken from Ref. [130].	32
2.21	Schematic of a nanocrystalline grain size highlighting the large amount of atoms in the grain boundaries (white) compared to those in the grain itself (black) (top). With decreasing grain size, the percentage of the atoms that are in boundaries and triple junctions increases linearly (bottom) [133, 134].	34
2.22	Electrodeposited tensile stress-strain curves with grain sizes ranging from 10-1000 nm with a 10 μm Ni 200 standard used for comparison (a). Uniform plastic and non-uniform strain distributions for a series of Ni-based electrodeposited coatings ranging from 10-80 nm (b). Maximum uniform plastic strain (c) and hardening capacity (d) plotted against the 0.2% offset yield strength for each tested sample [116].	35
3.1	Setup for uniaxial compression testing of columns	38
3.2	A beam element at mid-span before testing (left) and after some deflection downwards (right)	40
3.3	Setup for three-point bend testing of microtruss architectures	42
3.4	Cross-section at mid-span of square pyramidal microtruss assuming no horizontal face sheet struts	42
4.1	The ProJet 3500 rapid prototyper (model SD shown which is identical to the HD from the exterior) [140]. Capable of storing up to 4 kg each of part and support material and handling low definition parts up to 298 x 185 x 203 mm.	57

4.2	The collection of polymer part materials that can be used in conjunction with the ProJet 3500 HD [140]. Particular focus is paid to the support material S300 and the part material Crystal.	58
4.3	Polymer ASTM D695 coupons tested after 1 week sitting inside a 65° C finisher. Samples were tested in varying time after removal ranging from 4 minutes to 1 week. A trend of increasing stiffness and yield strength is seen with increasing time as the polymer material sets and becomes more brittle.	61
4.4	Optical profilometry results of the rough underside at 5x (a) and 20x (b) magnification. The contrasting upper smooth side is also shown at 5x (c) and 20x (d) magnification. An SEM micrograph is shown of the flat surface at 500x magnification where the polymer microstructure can be observed (e).	63
4.5	SEM micrographs taken of face sheet struts in a microtruss directly adjacent to a node. Small crystal-like features that are presumed to be solidified wax are present on the underside of the structure (top) but not on the top side (bottom).	65
4.6	SEM micrograph of a smooth polymer face and two rough patches on either side due to wax printing below the columns at the bottom of the image (top). SEM micrograph of a microtruss unit cell where the three core struts were built up in horizontal slices (bottom).	67
4.7	(a) SolidWorks inclined view of the 3D CAD model used to create printer resolution tests. (b-d) SEM micrographs of the printer resolution blocks at 1x, 2x and 3x the original size, respectively.	68
4.8	A build plate with three rectangular prisms oriented in the three main directions during printing: vertical, transverse (across the plate), and longitudinal (along the length of the plate). The direction of the plate during printing is shown in the bottom-right.	70

4.9	5x5x50 mm polymer rectangular prisms printed in vertical, transverse, and longitudinal directions measured over the course of one week in length showing tendencies for shrinkage on the order of 1% (top). The desired dimension is shown as the dotted line. The same samples had their mass recorded over the same time frame showing no noticeable change (bottom).	72
4.10	The five different printing orientations used correspond to three transversely oriented dogbones laid flat, on edge and on its side along with a vertical sample and one inclined at 45° to the vertical.	74
4.11	Tensile stress-strain curves for the five printing orientations tested on polymer coupons (top). The side, edge, and flat samples all reached UTS while the vertically aligned coupons fractured prematurely due to debonding of layers. The layering within each orientation is shown for the five configurations against a schematic of the tensile dogbone (bottom).	77
4.12	Tensile stress-strain curves of printed polymer coupons at strains rates of 0.08, 0.8, and 8 mm/mm-min (a). DIC strain maps for the 8 mm/mm-min (b) and 0.08 mm/mm-min (c) testing rates. While the slower rate did result in more ductility and higher strain across the gauge, in both cases the neck appeared in the middle of the gauge and failure occurred well after the UTS was reached.	79
4.13	Plotting the compressive stress-strain curve from a timed polymer coupon with the tensile stress-strain curve of a dogbone. In both cases, the corresponding ASTM standard was followed but gave vastly different elastic moduli.	81
4.14	Flexural stress-strain curves for the polymer blocks tested in the three different printer orientations (top). The conclusion from the tensile dogbones of vertically aligned samples being weaker holds here as well. The three orientations are vertical, flat, and side (bottom).	84

4.15	A flat printed block of Visijet Crystal material reconstructed after failure showing multiple wedges that broke off of at mid-span (a). The origin of the crack likely began on the top side of the sample in the image and spread outwards, creating the wedges. DIC strain maps show the large deflection that the flat sample was able to incur before fracture with strains up to 15% on the underside (b). Reconstruction of a side and vertical block after fracture are shown side-by-side where the larger deflection before failure is also confirmed with the larger crazing zone in the side printed block (c).	86
5.1	Failure mechanism map for a polymer column in uniaxially compression. Zones of elastic buckling (blue), inelastic buckling (yellow), elastic local shell buckling (cyan), inelastic local shell buckling (green) and yield (red) are shown with the optimal trajectory in black overlaid. \hat{M} contours of the designs fabricated are also displayed.	89
5.2	Failure mechanism map overlaid with the experimental data from compression testing polymer columns. The points across all 4 contours lie on the surface and show good correlation to the expected failure mode.	92
5.3	The force-displacement curve for a microtruss beam with slenderness $\lambda = 20$ and scale $s = 8$ loaded in three-point bending which failed by catastrophic fracture at the peak load, indicated by a cross. Inset top left: The microtruss beam oriented in the testing jig. Inset bottom right: Two halves of the microtruss beam reassembled after mid-beam fracture. Failure began on the tensile face (shown at the bottom of the photograph) and progressed through the width of the beam as indicated by the white line terminating on the opposite side.	94
5.4	3-D digital image correlation measurements of strains in the struts for a beam of slenderness $\lambda = 20$ and scale $s = 8$. (a) Strains after 4.2 mm mid-span deflection. (b) Strains after 8.2 mm mid-span deflection; failure by fracture of the lower struts is incipient.	95

5.5	Experimentally measured normalized force as a function of normalized displacement for exemplary beams of each slenderness, all at scale $s = 8$. The mechanisms of failure, either buckling or fracture, are indicated on each trace. Microtrusses with $\lambda=20$ and 25 failed by fracture (figure 5.4) while architectures with $\lambda=33, 43$ and 57 failed by buckling (figure 5.7).	97
5.6	Load index at failure as a function of slenderness. Experimental data are triangles for fracture and circles for buckling. The predictions for a maximum stress criterion and a buckling criterion are solid and dashed lines, respectively.	98
5.7	3-D digital image correlation measurements of strains in the struts for a beam of slenderness $\lambda = 33$ and scale $s = 8$. Buckling of the face struts on the compressive side was simultaneous across all three struts adjacent and perpendicular to the roller.	99
5.8	Principal strains measured by digital image correlation for three-point bending tests on microtrusses with scale $s = 8$ microtrusses with slenderness $\lambda = 20$ in the top row and $\lambda = 33$ at bottom. Three contour plots for each slenderness show the principal strains with maximum magnitude at 6.77 mm, 7.76 mm and 8.63 mm midspan deflection for each microtruss; these displacements are indicated on the graphs by vertical lines. The graphs on the left plot the strains of three points labelled on the structures. Note that these images are cropped and do not show the entire beam.	100
5.9	Experimentally measured normalized load against displacement for microtruss beams with slenderness $\lambda = 20$ and scales $s = 1, 2, 4, 8$. For smaller scale microtrusses, failure is progressive, while for larger scale microtrusses, failure is instantaneous and catastrophic.	102

5.10	(a) Relationship of normalized load to normalized displacement for microtrusses with slenderness $\lambda = 20$ and scale $s = 1$. These microtrusses fail by progressive fracture of the struts in the tensile face. The remnant load-carrying capacity after each fracture is well-predicted by the number of struts remaining; predicted strengths for 4, 3, 2 and one intact struts are indicated by dashed lines. Optical images of the underside of the microtruss beam during testing shown: (b) before first fracture, (c) after one strut had fractured, (d) after two struts have fractured, and (e) after three struts have fractured. Each new fracture is identified by the highlighted circling in the image.	103
5.11	Deterministic energetic size effect in similar polymer microtrusses. The dashed lines are the predictions based on maximum stress, while the solid lines account for a size effect. The predictions and experimental data are for slenderness $\lambda = 20, 25$. The error bars for the experimental data for $s = 8, \lambda = 25$ are obscured by the symbol.	104
5.12	Force-deflection curves for the six reduced core microtruss beams from specimen G1 to G6 by volume thinner core struts. Specimens G1 thru G3 show almost no change.	107
5.13	Close up view of specimen G5 at 5mm deflection from a side view showing a face sheet strut buckling to the right of the central roller.	107
5.14	SE and UVD micrographs of specimen G5 after face sheet buckling failure. Relaxation of the polymer returns it to its starting shape (a) but evidence of buckling is still seen in the central face sheet strut at its midpoint (b).	109
5.15	Nearly constant failure load as the core is thinned from 100% to 50% (top). A shift in failure mechanism results in the dip after 50% as the specimens begin to face sheet buckle (FSB). Normalization by total mass of microtruss shows that the transition point (the boundary between fracture and FSB) is the optimal design (bottom).	110

5.16	Load-deflection curves for the as-printed side block and a SR20 microtruss of the sample scale and total length.	112
5.17	The flexural stress-strain curve for the side block and SR20 microtruss is compared (a). Additionally, a SR20 microtruss with full struts on the outer face as opposed to the repeat unit cell is shown. The SolidWorks schematic of the half strut microtruss is shown (b). When normalized by total mass of the structure, the true benefit in weight performance is seen for microtrusses (c).	114
5.18	Repeat unit cells for microtrusses with 0.5 mm radius fillets (a), 2 mm radius fillets (b), a 50% grading of the core struts (c) and tapering across the strut itself (d) are shown.	116
5.19	Flexural stress-strain curves for the different microtruss improvements are shown (left) next to the normalized ones (right) showing a preference for grading as well as ductility improvements with small increases in fillet radius before the added mass becomes too large (as seen in the 2 mm fillet radius case).	117
5.20	DIC strain maps for unfilleted (a), 0.5 mm fillet radius (b), and 2 mm fillet radius (c) microtrusses in bending. The central unit cell is shown and the scale has been fixed to the 5-15% range to pinpoint failure within the central face strut. The most heavily filleted structure has all the applied load centralized to the middle of the strut whereas and less filleted case spreads it across more of the strut.	119
5.21	DIC raw images of the tapered SR20 microtruss structure during bending. Failure occurs by fracture at mid-point of the strut on the tensile side where it is thinnest (b). Because of the small size of these struts, the absorbed energy is not enough to break through the entire microtruss at once and leads to a strut-by-strut failure similar to the small-scale SR20 microtrusses (c-d).	120
6.1	Experimental true stress-strain curves for four grain sizes of electrodeposited nickel, along with their Voce fits overlaid.	123

6.2	Failure mechanism map for polycrystalline nickel columns and microtrusses showing five active failure zones: elastic and inelastic global buckling, elastic and inelastic local shell buckling and ultimate tensile failure. Note: elastic local shell buckling is along the \bar{r} axis for $\bar{n} < 0.01$. The architectural upper bound for microtrusses with $\bar{r} = 0.1$ (slenderness ratio of 20) is also shown.	125
6.3	Boundaries between global buckling, local shell buckling and ultimate tensile failure for the four considered grain sizes highlighting the movement of the triple point with decreasing grain size. For the 21 nm grain size, the ultimate tensile failure zone falls outside the range of \bar{r} and \bar{n} shown here.	128
6.4	Optimal trajectories for nickel/polymer microtrusses showing a trend of decreasing optimal \bar{n} with decreasing grain size in the inelastic global buckling zone.	129
6.5	Optimal trajectories for nickel/polymer microtrusses as a function of the load index, \hat{P}	131
6.6	Quarter circle cross-sectional view of optimal nickel/polymer microtruss struts for the four different grain sizes indicated based on a load of 11 kN on a 1 m x 0.5 m microtruss beam loaded in three-point bending. With decreasing grain size, the optimal polymer core radius increases and the optimal coating thickness decreases, resulting in an overall beam mass reduction from 32.7 kg for 10 μm nickel to 10.6 kg for 21 nm nickel.	132
6.7	Optimal trajectories for hollow nickel microtruss showing a trend of increasing optimal \bar{n} with decreasing grain size in the inelastic local shell buckling zone. Additionally, all four grain sizes share the same initial optimal trajectory displaying material property independence until local shell buckling activation.	134

6.8	Quarter circle cross-sectional view of optimal hollow nickel microtruss struts for the four different grain sizes indicated based on a load of 11 kN on a 1 m x 0.5 m microtruss beam loaded in three-point bending. With decreasing grain size, the optimal polymer core radius decreases and the optimal coating thickness decreases, resulting in an overall beam mass reduction from 25.4 kg for 10 μm nickel to 5.8 kg for 21 nm nickel.	135
6.9	Optimal design trajectories for nickel/polymer and hollow nickel microtruss beams with 10 μm and 21 nm grain sizes. For a given load index, \hat{P} , a minimal mass index, \hat{M} , is desired, resulting in 21 nm hollow nickel beams being the preferred option over all available \hat{P} design space. At $\hat{P} > 6.6 \times 10^{-6}$, even 21 nm nickel/polymer designs are lighter than 10 μm hollow nickel ones. Arrows indicate the reduction in mass index associated with polymer core removal for a given \hat{P} , such that complete removal leads to the hollow dashed line.	137
6.10	Based on a load of 0.7 kN on a 1 m x 0.5 m microtruss beam in three-point bending, optimal cross-sections for nickel/polymer and hollow nickel struts with the labelled grain sizes are displayed. Starting at the top-left and working clockwise, the mass of the optimal beam decreases from 3.2 kg to 2.0 kg (for both hollow 10 μm nickel and 21 nm nickel/polymer scenarios) to 0.7 kg. . . .	138
6.11	Mapped B and C Voce fitting parameters for 47 n-NiFe curves with varying iron content overlaid with a linear fit.	140
6.12	Experimental stress-strain curves for the three n-NiFe curves considered with their corresponding Voce fits overlaid.	141
6.13	Failure mechanism map for the Ni-3.4%Fe microtruss showing four active zones as well as the optimal trajectory. The load contour of 5×10^{-7} intersects the optimal trajectory at one point the optimal architecture. Additionally, the $\bar{r}=0.1$ limit is shown.	142

6.14	All three optimal trajectories for each of the three curves plotted together showing the same general shape but differing locations for optimal design for the same applied design load. Inset shows a close-up of the three optimal architectures.	143
7.1	Polymer rods were hung five at a time in a modified nickel sulfamate bath and placed between two anodes during electrodeposition (left). The cross-section of a plated polymer rod is shown with a thin blue layer identified as the electroless Ni joining the electrodeposited outer coating to the polymer interior (right).	146
7.2	Force-displacement curves for the as-printed, etched, and electroless Ni coated polymer rods. The predicted peak loads based on the developed analytical models are shown to have good agreement with the experimental data.	147
7.3	Force-deflection (top) and normalized flexural stress-strain (bottom) curves for the Ni/polymer rods ranging from etched polymer (no coating) to the maximum coating of 62 μm	150
7.4	SEM micrographs of sample 57.4/3.7/0.90 at 250x (a) and 45x (b) magnification showing gaps between the polymer core and the Ni coating. Similar results were seen for less thickly coated sample 44.4/2.6/0.91 at 650x (c) and 30x (d) magnification.	151
7.5	Experimental peak flexural load for all Ni/polymer rods grouped into the sets of five that had been plated together. Error bars show the standard deviation in coating thickness and peak flexural load. An etched polymer rod with no coating was also placed for comparison. Peak load predictions are shown for the limiting cases of the polymer rod on its own as well as with the assumption of the composite behaving as if it was a Ni tube without any polymer inside.	152

7.6	Failure mechanism map for 20 nm grain size NiCo plotted in the fully expanded geometric space with the optimal trajectory and four experimental architectures (top). A zoom in on the applicable geometric range for microtrusses (bottom). Colours for failure zones are identical to those from previous chapters with elastic global buckling (blue), inelastic global buckling (yellow), elastic local shell buckling (green), and inelastic local shell buckling (cyan).	156
7.7	SEM micrographs showing the Ni thickness gradient for Ni/Al foams having densities of 0.486 Mg/m ³ (top), 0.690 Mg/m ³ (middle), and 0.959 Mg/m ³ (bottom), taken from Ref. [95].	158
7.8	Force-deflection (left) and normalized flexural stress-strain (right) curves for samples from each of the three sets of coating thickness as well as the uncoated case. The peak load for the uncoated polymer structure was only 15 N, thus the almost flat appearance in the force-deflection figure.	159
7.9	Snapshots of the uncoated microtruss after failure (a) as well as the 47 μm (b), 84 μm (c), and 466 μm (d) thick Ni coated microtrusses. All exhibited face sheet buckling adjacent to the central roller except the most heavily plated sample which failed by nodal collapse at the edges of the sample.	159
7.10	MED35-2 exhibited a noticeable twist along its length (top) while MED635-3 had some struts that were not successfully coated (bottom). These uncoated struts were the origin of failure in the three-point bending test.	161
7.11	Force-deflection (left) and normalized stress-strain (right) curves for a SR20 microtruss with a nominal coating thickness of 140 μm compared to the baseline SR20 polymer microtruss. The hypothetical behaviour of a hollow metallic microtruss is shown by assuming the polymer mass has been removed without compromising the Ni coating.	162
8.1	Schematic of the repeat unit cell used to create the hollow polymer microtruss.	165

8.2	Flexural stress-strain curves for the hollow microtrusses left in the finisher for a day and a week compared to the baseline SR20 microtruss (left). The normalized version shows longer finisher time decreased ductility in the hollow structure (right).	167
8.3	Failure mechanism map for the hollow polymer microtruss. Zones of failure are identical to those presented in previous chapters with the breakdown being elastic global buckling (blue), inelastic global buckling (yellow), ultimate tensile failure (red), elastic local shell buckling (green), and inelastic local shell buckling (cyan).	168
8.4	Normalized flexural stress-strain curves for cases of microtrusses with multiple improvements incorporated into the structure such as being graded and filleted or grading, filleting, and having a hollow interior. The baseline SR20 microtruss is shown along with the deflection increase possible with the addition of 0.5 mm fillets (identified as the shift from the circle to the square on the curve). The combination of grading the core and filleting is seen to have the same deflection increase as does filleting a hollow structure. Schematics show the repeat unit cell for each improvement before filleting.	170
8.5	Peak flexural stress plotted for microtruss and block beams tested in three-point bending against their density calculated based on the bounding box surrounding the microtruss structure. Polymer structures lie in the band of low flexural strength at the bottom with the maximum density of the polymer block sample. Metal/polymer SR20 and SR33 microtrusses are included with their linear fits from the uncoated case up through the experimental data. Two hypothetical hollow structures show the differing benefit of core removal based on starting architecture.	172

8.6	DSC curve for a Visijet Crystal printed polymer that had already been finished for two days at 65°C. Zones of wax melting, crystallization and burning are all identified on the heating portion but the cooling portion has no features implying the sample has been burnt to a crisp.	174
8.7	Percentage of Ni (top) and polymer (bottom) loss as a function of sulfuric acid molarity after being left for 23 hours in a sealed beaker, taken from Ref. [158] .	176
8.8	Example of a fabrication route to making hollow metallic microtrusses for cores in sandwich panels, taken from Ref. [152].	177
8.9	Snapshot taken of the FDM microtruss upon failure with the circled zones representing first failure by core shearing at the nodes and the squared zones being the next row hit by the same failure mechanism (a). DIC raw images of the FDM microtruss as it progressed from unfractured (b) to having two rows sheared within 1 second of each other (c). Much later, the planar failure surfaces are evident (d).	178
8.10	Various types of infill patterns that can be selected from the software used with the Makerbot Replicator FDM machine [159]. Further control is provided on the percentage of infill from 0 (hollow interior) to 100% (fully dense). The microtrusses printed with FDM here used a 75% infill with a hexagonal interior pattern.	179
A.1	Polymer ASTM D695 coupons tested after 3 hours and 1 week sitting inside a 65° C finisher. Each sample was also tested immediately after removal from oven (≈4 minutes) and 1 week later. Lower stiffness and yield strength are seen for samples not cooled adequately.	202
A.2	Polymer ASTM D695 coupons tested after 1 week sitting inside a 65° C finisher. Samples were tested in varying time after removal ranging from 4 minutes to 1 week. A trend of increasing stiffness and yield strength is seen with increasing time as the polymer material sets and becomes more brittle.	203

A.3	Polymer square pyramidal microtrusses tested after 1 week sitting inside a 65° C finisher. Samples were tested in varying time after removal ranging from 4 minutes to 1 week. A trend of increasing stiffness and peak strength is seen with increasing time as the polymer material sets and becomes more brittle.	204
A.4	Tensile stress-strain curves for the as-printed polymer dogbones fabricated in both the HD and UHD modes in flat and vertical directions (a). An increase in UTS with similar Young’s modulus was observed for the UHD samples. DIC images of the UHD flat sample immediately before (b) and after (c) fracture at the shoulder.	205
A.5	Tensile stress-strain curves for the as-printed polymer dogbones fabricated in both the HD and UHD modes in flat and vertical directions (a). Samples have been sanded along the thickness direction in an attempt to remove the steps leading from gauge to shoulder that act as stress concentrations. An increase in UTS and Young’s modulus was observed when comparing sanded to unsanded samples. DIC images of the UHD flat sample immediately before (b) and after (c) fracture at the shoulder. While sanding eliminated most of the steps, some remained and caused the same failure point, but at higher stress.	207
A.6	Experimental tensile stress-strain curve of electrodeposited NiCo dogbone coupon with grain size of 20 nm. Overlain on top of the experimental data is the Voce fit performed using data points up to an including the UTS.	209

Chapter 1

Introduction

The goal of this doctoral thesis is to present a new methodology for the fabrication of ultra-lightweight hybrid nanocrystalline microtrusses with high strength and low density. Additionally, their mechanical performance and the ability to pin-point architectures of optimal design will be predicted through the development of a multi-variable analytical system. Microtrusses can be visualized as small-scale analogues of the triangulated trusses seen in roof framing and bridges, but repeated in two or three dimensions. They represent the most structurally efficient way of transmitting external loads through a lightweight cellular material because they are stretch-dominated [1, 2]. To create this complex internal architecture, a rapid prototyping technique will be utilized that allows for the fabrication of features in the sub-mm range while maintaining the strength and accuracy required to be used in testing. Because of the complex geometry and the small scale of the microtruss features, it is impossible to fabricate microtrusses from most high performance materials [3]; hence, their full capabilities have not yet been exploited. Nanocrystalline electrodeposition is a very promising way to bring this potential forward. Grain size reduction to the nano-scale leads to large strength increases, and electrodeposition allows material to be deposited over virtually any shape [4, 5]. Various studies have already been performed showing high performance in nanocrystalline Ni coatings [6, 7, 8]. By applying these coatings to the polymeric substrate, composite metal/polymer ma-

terials can be created that optimally position the high strength metal farther from the neutral bending axis.

Therefore, the main thesis goal is to create a processing technique to fabricate architecturally complex composite microtrusses with an accompanying failure mechanism modeling to achieve optimal designs in bending. The objectives can be split between the fabrication and modeling pathways with experimental validation used to tie them together. Overall, key steps will be:

- understanding the as-printed polymer properties as relevant to electroplating and metalization
- calculating resolution limits in 3D printing using stereolithography based on current state-of-the-art technology to define the design space
- obtaining reliable material properties for the as-printed and processed polymer material for incorporation into the analytical models
- developing a first failure analytical model for composite microtruss beams in bending
- deriving analytical solutions for optimal trajectories in the available design space
- confirming the predictions for peak load carrying capacity in three point bending in as-printed and composite microtrusses
- validating the locations of optimal architectures
- identifying possible routes for the removal of the polymer core after electrodeposition

In Chapter 2, a review of the relevant literature is presented alongside the current state of the field. First, the history of cellular materials is discussed to understand the available routes for lightweight material design. Through the collective works of Ashby, Deshpande, Wadley and others, lattice structures incorporated into a sandwich panel were identified as significantly

promising. An exhaustive list of fabrication methodologies that have been used to create cellular materials is presented that covers various types of lattices and material systems from wire weaving to casting. Based on this information, rapid prototyping is identified as the leading candidate because of the complete degree of freedom in architecture, vital in the synthesis of large lattice blocks. This is then further refined to a form of stereolithography that was central to this doctoral thesis that outperforms all other additive manufacturing techniques. While work in the field of cellular materials has recently shown the ability to fabricate ultra-lightweight and even ceramic microtrusses, this technique offers larger freedom in design and increased structural stiffness critical for applications in industries like aerospace and transportation.

The first contributions are presented in Chapter 3 in the development of an optimization model for the behaviour of microtrusses in bending applications. The process starts with observed failure mechanisms in columns and tubes before moving to three-point bending scenarios. As the model shifts from pure compression to bending, it is further complicated through the interaction of the metal and polymer components of the microtruss. The final step is the optimization of this hybrid to locate optimal designs using the Kuhn-Tucker condition. Analytical equations for the optimal trajectories of hybrid microtrusses are developed and shown in their full, un-simplified form.

To validate this model's use, a reliable set of material properties for the rapid prototyped polymer is required. Chapter 4 looks at determining values for density, ultimate tensile strength, modulus, and yield strength. Additionally, different printing effects (such as surface roughness, printer orientation, and curing/finishing conditions) are discussed that could potentially affect the failure of a polymeric microtruss. These values are then incorporated into the model to offer predictions on failure strengths for both columns and microtrusses, as discussed in Chapter 5.

The complication of a metal coating is incorporated into the model and failure mechanism maps for the composite material are derived in Chapter 6. Methods to further improve the base architecture, such as grain size reduction and core removal, are also mentioned. The

first metal/polymer microtrusses are shown in Chapter 7 with the recipe for their fabrication introduced. The testing of rods and microtrusses in compression and bending is used to try and validate the model in its most complex form. The final chapter opens the door for future work by presenting methodologies to advance on this hybrid cellular material mainly through the extraction of the polymer core to leave behind a fully hollow metallic structure. Appendices contain additional tensile testing data relevant to sample size, core MATLAB code used to identify optimal architectures, and published work on metal/metal foam anisotropy completed in parallel with rapid prototyped microtruss research presented here.

While the research progresses clearly from initial idea formulation to a realized hollow metallic fabrication technique, the individual chapters will be tied together through the comparison of weight-specific improvement on bending performance of an arbitrary volume of material. The measurement of flexural strength and modulus in Chapter 4 on a solid polymer block is compared to a polymer microtruss of the same exterior volume in Chapter 5. Adding a metal coating should increase the weight-specific mechanical properties, which is predicted and then measured in Chapters 6 and 7, again using the same exterior volume. Finally, a prediction for a hollow metallic microtruss for this same size is included to come full circle on the research goals of this doctoral thesis.

Chapter 2

Literature Review

What follows is a background of the wider foundation of cellular materials with an emphasis on their fabrication using state-of-the-art rapid prototyping techniques, as described in the title of this study. Additionally, discussions on the possibilities of reinforcement to strengthen the core material will be included, based on current advancements in the realm of electroplating. With the subsequent chapter's focus on modeling the behaviour of microtrusses and architectural optimization, the mechanics involved in general cellular materials will also be touched upon in order to facilitate this future discussion.

2.1 Motivation in applications

Typically one discusses the applications of a given material/process after it has been discovered and/or developed. The discovery of a new element, for example, can result in new alloys, composites, or processing techniques that could end up replacing the current use of a similar material. However, the reverse is just as valid: a need is identified and what is available must be used to address the issue. This promises a more likely adoption into real-world systems. In this case, the need centralizes on the design of lightweight, high performance structures. Whether it be the housing for a satellite, the bumper of a car, or the hull of an oil tanker, reducing the mass of a structure while maintaining the required load carrying capacity is a motivation in the

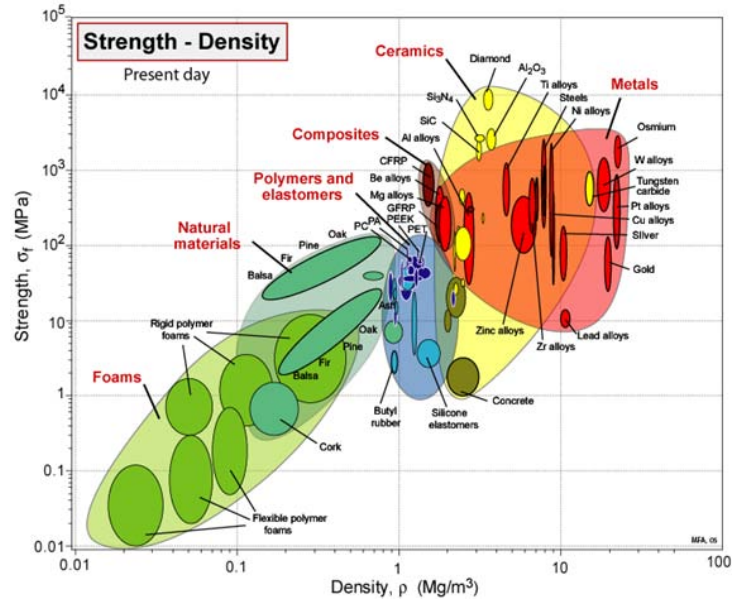


Figure 2.1: A material selection map outlining the strength and density of known materials with a void in the top left corner [11].

ever-larger field of green transportation. Even small savings in weight and fuel can have long term impacts on the costs associated with their continued use.

To design a lightweight structure that can still hold an appreciable amount of load, the trivial solution would be to substitute the current material choice for a stronger one meaning less material is needed. For example, instead of using aluminum as the structure for the housing of an airplane, use titanium. By breaking down the large list of all available materials into their abilities to withstand an applied force, trends can be identified which outline the areas of strength-density required for a given application. This process was popularized by Michael F. Ashby in a series of review articles [1, 9, 10] and, eventually, a popular piece of materials science software known as CES. Within this large space, a void can be identified in the upper left corner of Figure 2.1 where ultra-lightweight, high performance structures would be located. Note: similar maps exist for all ranges of mechanical properties but for the time being, the focus will remain on strength and density.

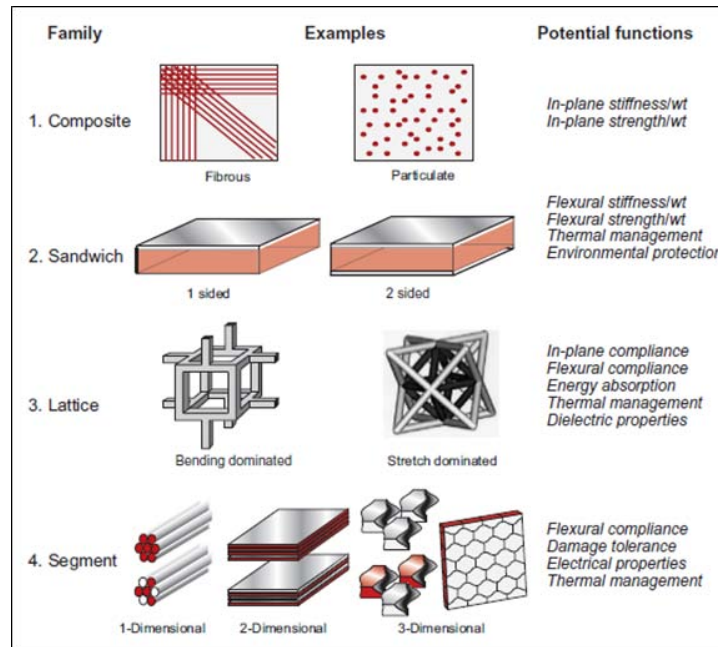


Figure 2.2: Types of hybrid and composites materials that can fill the void in strength-density space [10].

2.2 Types of hybrid materials

Instead of trying to find new materials to place into this void in the material property chart, Ashby identified the possibility of using hybrids (Figure 2.2) that combine the properties of two or more materials to fill these holes in design space [10]. This idea of mixing materials together was by no means a new revelation, but Ashby usefully classified the different hybrid types into groups of: composite, sandwich, lattice, and segmented materials [1]. Referring back to the application-wise approach to designing aerospace grade materials for planes or satellites, composites in the fibrous form are already popular. Carbon fibre sheets are both extremely lightweight and have excellent mechanical properties making them suitable for all types of aerospace applications. Their introduction and use in industry has caused the composites bubble to greatly enlarge towards the stronger and lighter section of Figure 2.1.

Ashby believed that by merging materials into hybrids, one could combine beneficial properties of individual materials into useful new systems. Using this same technique, the next step would be to hybridize the hybrids. Can the combination of composites form a system with

novel new properties not seen before? In particular, the subsection of sandwich composites is intriguing because of the freedom to choose which material will serve as the core in a panel. Traditionally, sandwich panels are composed of stronger face sheets that resist and carry most of the applied load, while lightweight cores are responsible for resisting shear forces [12, 13]. This leads to the common combination of metallic face sheets and foam cores of both polymer and metal varieties [14, 15, 16].

2.2.1 Cellular materials as a core for sandwich panels

The history of foamed materials is especially broad as natural structures like bone contain a porous interior that can be described as a foam. Nature created lightweight yet strong materials like wood, cork and bone, which have been characterized as *cellular materials*. Foams as a man-made entity are further classified as three-dimensional cellular solids compared to two-dimensional versions like honeycombs (while the honeycomb does have a third dimension, it does not vary in this dimension geometrically) [17]. These materials are hybrids of solid material and open-space - a single material put into a complicated shape such that the bounding box around the structure needs to account for the emptiness which is inside. This results in structures with *relative densities* - a mixture of the density of the original material and the air inside.

Foam cores are available in varying degrees of pore sizes defined by their pores per inch (PPI) value, where larger values mean more pores along one inch of cross-section in the foam but also result in smaller single pore sizes. Samples in the 5-100 PPI range (Figure 2.3) are available in both polymer and metallic forms via various suppliers (ex: ERG, Divinycell, Klegecell, etc.). Ashby's definition of hybrids being inclusive of mixtures of solid material and open space means these foam cores should be located somewhere on the hybrids breakdown. Looking back to Figure 2.2, an architected material that has this blend is classified as a lattice-type hybrid. From a structural standpoint, foams are simplified as small geometrically identical shells that carry load through the struts forming the boundaries of the pore (in the case

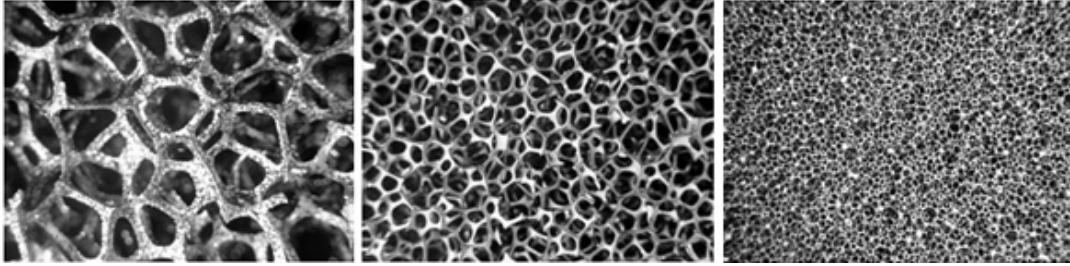


Figure 2.3: An example of varying pore size in reticulated vitreous carbon (RVC) foam from 10 to 40 to 100 PPI (left to right). While polymer foams can have PPI values up to 100 [18], metals are usually limited to 40 PPI [19].

of open cell foams such as these). They resemble the bending-dominated lattices in Figure 2.2.

The development of foams is separated into the polymer and metal subgroups as mentioned before with the latter being more recent. Ashby *et al.* presented a thorough review of the types of metal foams that can be created and the materials which can be used for synthesis [20]. Moreover, they go on to mention applications for these structures such as dampening, thermal management, and, most relevant here, sandwich cores. In particular, they state sandwich panels with a metallic foam core are a good match due to having a ‘low density with good shear and fracture strength’ and that foams with built-in skins on either side such that a sandwich panel can be made in one go hold ‘the greatest promise [for metal foam technology]’ [20]. This notion of an all-in-one technique for fabricating a sandwich panel will serve as a design goal for creating lightweight, high performance microtruss panels. The systems of equations developed to describe the behaviour of these structures in bending will form the basis for the optimization models in this study, covered in Chapter 3.

2.2.2 Stretch- vs. bending-dominated lattices

The goal of combining a hybrid material inside a sandwich panel is justified by the extensive literature on foam-panel systems for both polymer and metallic cores [10, 13, 14, 16, 21]. With bending-dominated lattices being popular as cores in sandwich panels, we look to the right of them in Fig 2.2 and wonder if the stretch-dominated category can also serve as a suitable core

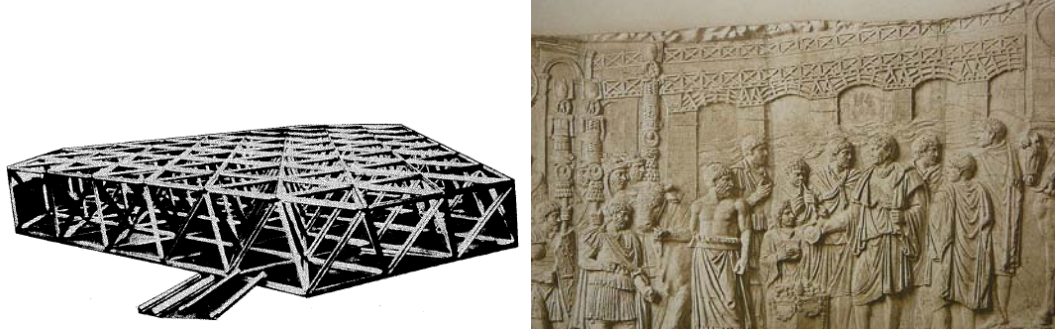


Figure 2.4: The first example of a three-dimensional lattice that shows up in published scientific work belongs to Fuller in his 1961 patent (left) [22]. However, structures with triangles resembling lattices go as far back as Roman times. Here is a 113 AD relief from Trajan's column depicting Trajan's bridge in the background (right) [24].

material. The architect Buckminster Fuller was the first to patent a lattice-like structure under the title 'Synergetic building construction' in a 1956 US Patent (Figure 2.4) [22]. But even before that, evidence exists of truss-like lattices used for bridge supports during Roman times, with Trajan's Bridge of 105AD being a seminal example [23].

Regardless of how long lattices have been in use, their development into the form used today is split between two classifications: bending- and stretch-dominated structures [1]. To distinguish between the two, the unit cell is analyzed against Maxwell's stability criterion in three dimensions (Figure 2.5) [1, 25, 26]:

$$M = b - 3j + 6 \quad (2.1)$$

Here, b represents the number of struts and j the number of frictionless joints. While not comprehensive, it can be determined whether or not the structure is rigid by looking at how the joints are connected in the unit cell of the frame (frame being Maxwell's terminology for a lattice). When an applied load is passed through the structure of the unit cell, a force can be applied on a strut in such a way that it bends rather than being in either pure compression or tension. This is where the labelling of bending-dominated originates; the structure becomes a mechanism due to these degrees of freedom about the joints ($M < 0$). The failure of the overall structure is now dominated by the flexural strength of the struts or the rigidity at the joints

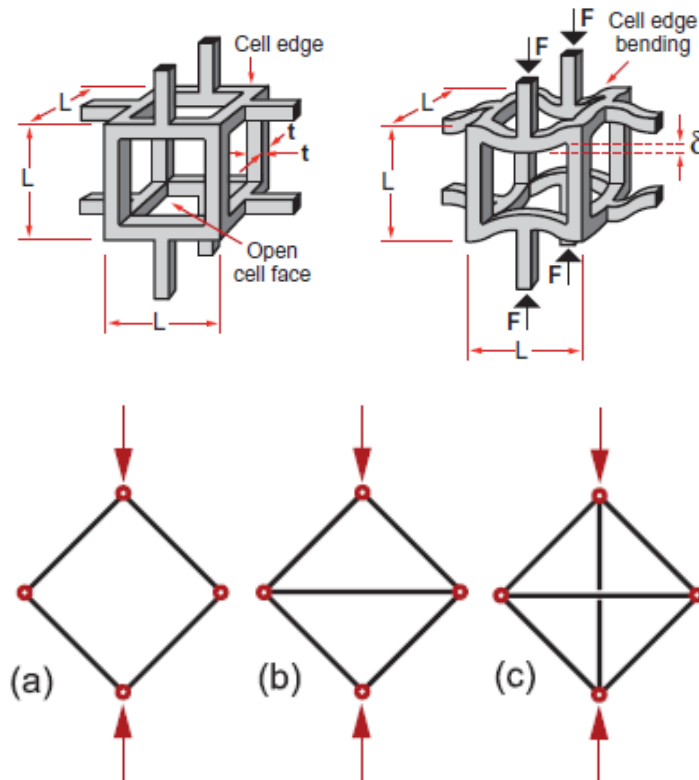


Figure 2.5: Comparisons between mechanisms active in unit cells in the bending-dominated (top left) and stretch-dominated (top right) structures. Examples of frames that have (a) $M < 0$, (b) $M = 0$, and (c) $M > 0$ [1].

(Figure 2.5) [1]. For instance, take a cube lattice resting on its face with an applied load on the opposite face - the structure is only composed of its edges. This structure will eventually fail by the bending in the four vertical edges holding up the structure, which are in states of compression and are effectively isolated from the rest of the structure. The other eight edges have no ability to prevent this and experience no load transmission, creating degrees of freedom and mechanisms. The structure can twist without the face struts changing length.

What is preferred is the transmission of applied load through all members of the unit cell such that no mechanisms are created where $M = 0$ (Figure 2.5b). Now the failure is dominated by the ability for these struts to stretch or squish (undergo tension or compression, respectively) leading to the stretch-dominated label (although squish-dominated would be just as valid, if not less scientific in description). Only certain geometric shapes have this type of

framework with tetrahedrons and octahedrons being part of that exclusive group. In the case of a tetrahedron, an applied load at any node is transmitted down the three adjoining edges with the other three edges working to prevent the nodes from pushing outwards. All struts are either in compression or tension - no mechanisms and no states of self-stress exist. Because of this, lattices that are stretch-dominated have a higher structural efficiency than lattices which are bending-dominated [1, 2]. Unfortunately, no single shape has the ability to fill space and satisfy Maxwell's stability criterion; however, the combination of the tetrahedron and octahedron does both [1]. Deshpande *et al.* termed this repeat unit cell the 'octet' truss [27]. Based on the use of different geometric shapes to optimize structural efficiency, the goal would be to create a larger block of material where a tetrahedral/octahedral unit cell was used as a repeat unit such that the entire structure as a whole would be stretch-dominated.

2.2.3 Optimal architectures

In the example of designing an airplane floor, the solution to having a strong, stiff, and lightweight structure automatically brings to mind structures that have triangles inside of them like most truss bridges. While these are indeed sufficiently strong to hold large loads and incorporate lots of free space to minimize weight, they are not optimal. When topological optimization is performed on a simple three-point bending scenario, the resulting structure on the inside resembles a lattice (Figure 2.6) [28]. This follows from the analysis of lattice structures done by many reviewers showing their favourable load carrying capacities [10, 1, 2, 3, 29]. However, the struts on the inside of this lattice are neither consistent in size nor in shape. A synthesis route is required that will enable the fabrication of the lattice shape and, preferably, a more non-uniform shape, as seen in Figure 2.6d.

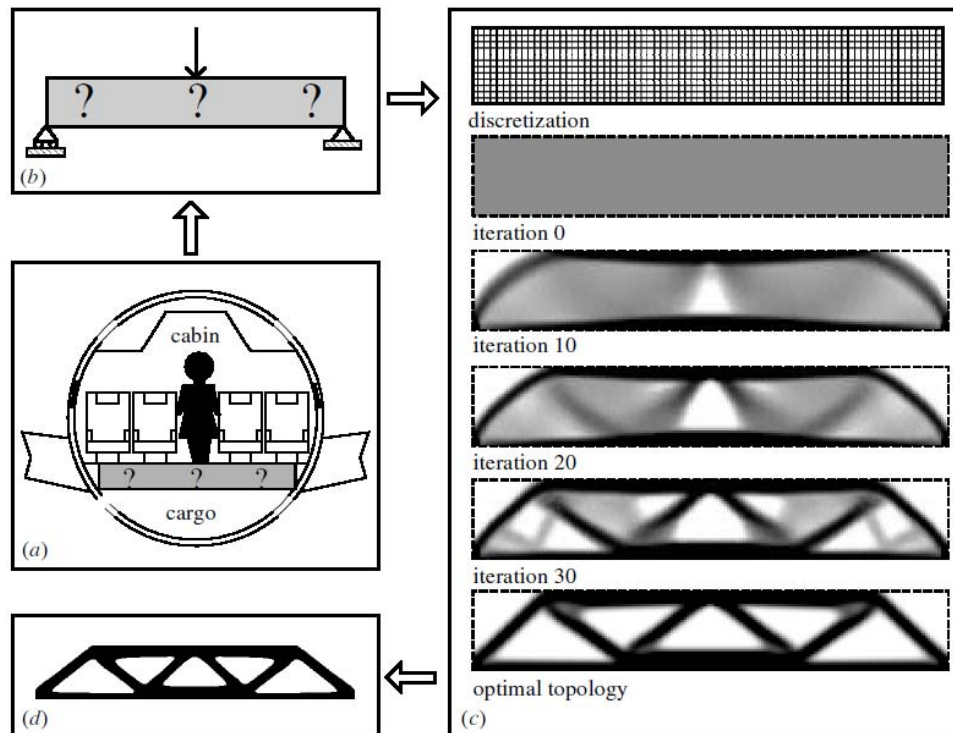


Figure 2.6: The design of an optimal airplane floor (a) can be broken into a simple three-point bending test (b). Optimization is performed by placing a mesh on the structure, identifying areas of little to no loading and removing those small sections to reinforce areas of higher load. This process repeats through many iterations (c) before it arrives at the optimal shape for the given input parameters (d) [28].

2.3 Synthesis routes for stretch-dominated lattices

The benefits of obtaining a stretch-dominated architecture are dependent on the ability to make struts inside the lattice that join at clearly defined nodes such that the applied forces are transmitted axially. To obtain this accuracy, only a few options are available. Note: Foams are not limited to this problem as the unit cell inside these random structures is only simplified to the unit cell design seen in Figure 2.5a, and is actually quite sporadic requiring less precision and uniformity [30].

Attempts have been made to create such structures since the late 20th century with an explosion of literature stemming out in the early 2000s. Some of the techniques that were developed in this period include investment casting [31, 32, 33, 34], perforation stretching [3, 29, 35, 36, 37, 38], wire assembly [39, 40, 41], weaving [42, 43], rapid-prototyping [44, 45, 46] and self-assembly [47]. Selecting a method is dependent on the material one wishes to use, the size of the final structure required, and the cost. Additionally, the inherent flaws that exist in some of these methods can limit their ability to create high-performance parts. The benefits and limitations in these processing routes will be discussed below along with the relevant references to literature for each class. It should be noted that the timeline of these discoveries is intermixed as all were developing simultaneously with some research groups responsible for multiple avenues of synthesis, while others worked to collect and review the available technologies multiple times.

2.3.1 Investment casting

A review of the cellular metal systems available in 1998 by Evans *et al.* identified only a single example of existing routes to making truss structures [48, 49]. This first example of a truss-shaped lattice material that was in the size range of centimeters (instead of meter or more sized trusses seen typically in bridges) was patented in 1996 by Jonathan Priluck [50]. Priluck later started JAMCORP before being taken over by Federal Technology Group where these

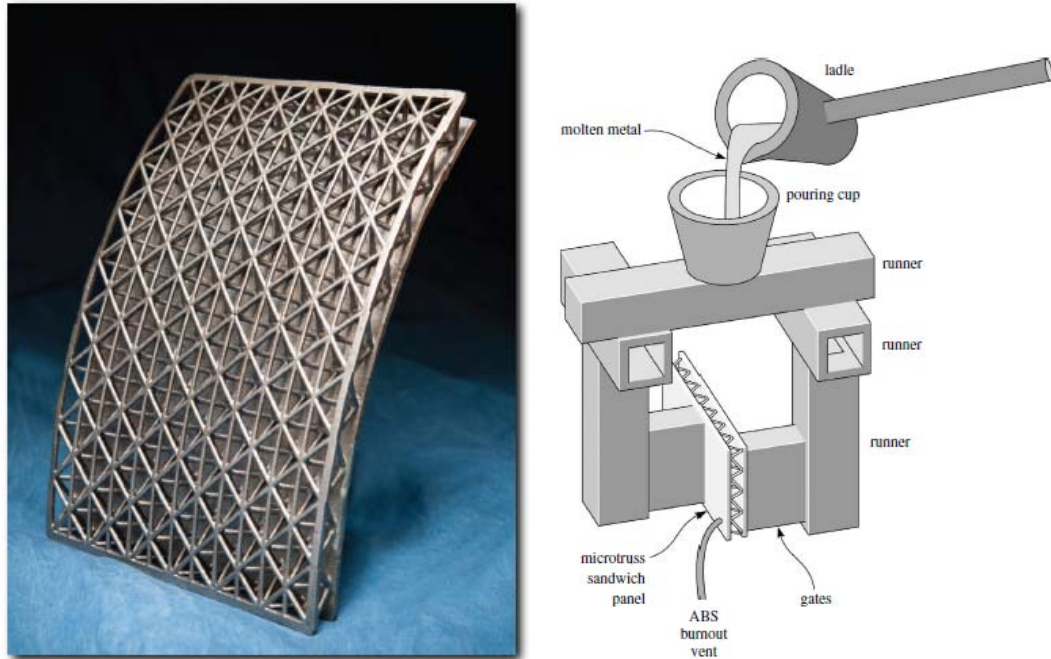


Figure 2.7: Lattice block structures fabricated by a combination of rapid prototyping and investment casting (left) [53] and a schematic of the modified technique with polymer burnout after the molten metal has been poured into the mold (right) [29].

materials are manufactured currently [51]. The only published article on this material by its inventors shows the ability for this technique to be modified for various castable metals such as iron, titanium, aluminum, nickel, and cobalt and observes their properties in compression and bending [52]. Figure 2.7 shows one such structure where the technology has been further advanced allowing for curved shapes with incorporated lattices [53]. The technique centers on the idea of molds. One can make a negative of a desired shape and then make copies of this shape by filling it in with a liquid material that can later be treated to harden. Finally, the mold is removed to leave behind the original shape.

The original lattice block materials were efficient structures, but had not been optimized. It would not be until Wicks *et al.* did the necessary mathematical derivation and optimization that optimal truss plates would be developed with additional input from Wallach *et al* [31, 32, 54, 55]. The molds for these were difficult to fabricate from traditional methods and would require the use of a second emerging technology known as rapid prototyping. In particular, the

use of fused deposition modeling (FDM) allowed for the creation of very complex negatives (made of ABS polymer) where different metals were fed inside and were allowed to harden before burning off the ABS (Figure 2.7 right side) patented first by Daily *et al.* in 2000 [56]. Later publications worked off similar techniques as this to produce their structures [3, 29, 31, 33, 57, 58, 59]. Alternatively, the molds could be produced via injection molding followed by the identical procedure [60]. However, this technique requires expensive dies to be machined making variations on the first design rather expensive [57]. Since then, the field has expanded to include more metals and non-metals that can be cast with variations of these techniques. One example would be making magnesium lattices using a combination of hot-wire cutting and lost foam casting [34].

The optimization work by Wicks *et al.* showed that optimal structures were ones that had lattices composed of very slender struts [54, 55, 61]. This is a problem for casting processes because the tight corners in the center of a larger sheet would be harder to flow material into and would commonly leave casting defects such as porosity and incomplete struts. Additionally, this process is expensive and creates a large amount of waste material, especially with the burning off of polymer to retrieve the final structure [3].

2.3.2 Perforation stretching

Sypeck *et al.* succeeded in achieving metallic lattices that could serve as a core in a sandwich beam through a technique more recently coined as perforation stretching [62]. In this process, the starting material is a sheet of metal that has had a regular pattern of holes perforated into it that would leave behind a 2D lattice of thin struts which join at rounded nodes. It is then placed inside a specially designed jig that pushes down on alternating nodes while holding the position of the remaining nodes, thereby turning this two dimensional sheet into a three dimensional lattice (Figure 2.8).

This initially opens up the design space to almost any metal that can be rolled into a sheet and perforated. Additionally, different unit cells can be fabricated by modifying the perforation

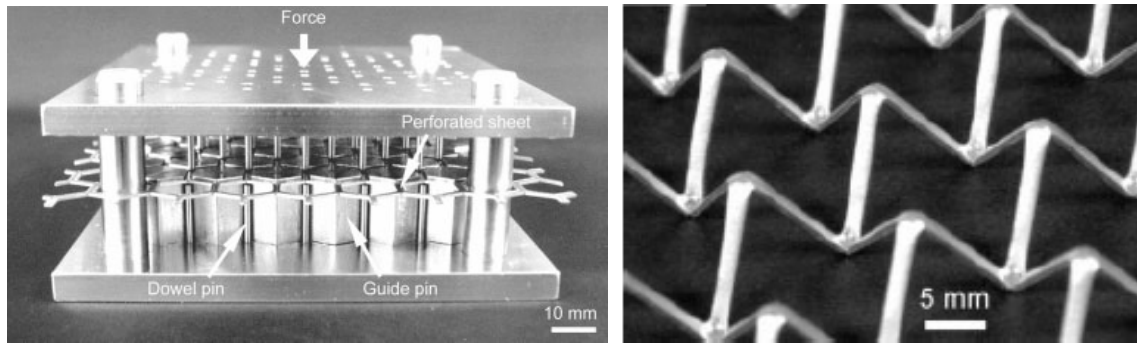


Figure 2.8: The jig used to deformation stretch sheets into lattices (left) and the resulting structure formed from a hexagonal punched stainless steel sheet (right) [62].

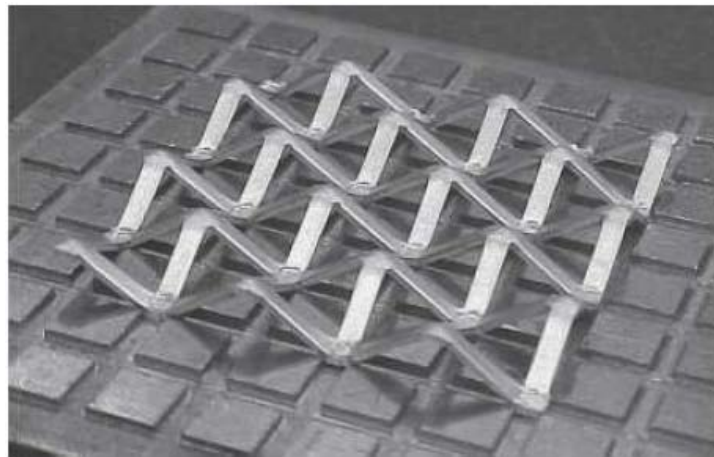


Figure 2.9: After perforation stretching, a square punched aluminum sheet becomes a square pyramidal lattice [63].

pattern. For example, a hexagonal hole pattern, once stretched into three dimensions, becomes a tetrahedral/octahedral unit cell which, as mentioned previously, is both the desired structure that satisfies the Maxwell stability criterion and fills space. Furthermore, one could start with a square hole pattern and by stretching this sheet, create a square pyramidal layout (Figure 2.9). This is the same tetrahedral/octahedral unit cell in three dimensions, but rotated slightly and cut into a single unit cell layer [38, 63, 64].

Taking the top view of a tetrahedron with the peak oriented in the middle, there are three vertices forming the triangular base and one central vertex for the peak. In three dimensions, this central vertex is far from the base as required to form a regular tetrahedron and the desired stretch-dominated architecture. While bending metal is not generally problematic, the stretch-

ing of the metal to reach this height is significant and for most metals would lead to necking or breaking as the metal strain-hardened. To avoid this, the metals which are selected are heat-treatable allowing for an intermittent annealing step that will soften the stretched shape. The sample can then be returned to the jig and stretched further until the desired height is reached. There are physical limits to this process, but angles of $45^\circ+$ are possible [65, 66].

Extracting material properties out of these shapes can also be difficult as uniaxial compression of the lattice will result in the shape being squashed back into a 2D sheet - the tetrahedral shape lacks the necessary struts in the basal plane to lock the vertices of the tetrahedron in place. This creates a structure with $M < 0$ indicating mechanisms and a partially bending-dominated lattice. There are two routes to correct this gap. In one route, in their use as sandwich panel cores, these lattices can have their nodes welded or adhered to planar face sheets that form the outsides of the panel [62]. As long as the joint here is sufficiently strong, failure can still occur in the core before delamination. Alternatively, the mechanical properties can be obtained by using confinement plates - a patterned substrate that the lattice can sit on, locking the nodes in place and mimicking their behaviour in sandwich panels. Figure 2.9 shows a pyramidal lattice sitting on the confinement plate where a similar one would be placed on top of the lattice before uniaxial compression.

Perforation folding

Using the same perforated sheet idea from the deformation forming technique above, a variance on this technique is possible where the sheet is bent along a line by a punch. While this seems like a minor modification, in terms of manufacturing, it is possible to feed in a flat sheet and extract a three dimensional truss much quicker than in the former method. The punch and the die are machined to the exact angles that would allow the flat sheet to achieve the final shape desired (Figure 2.10) [67, 68]. Again, the tetrahedral/octahedral architecture is possible with this method.

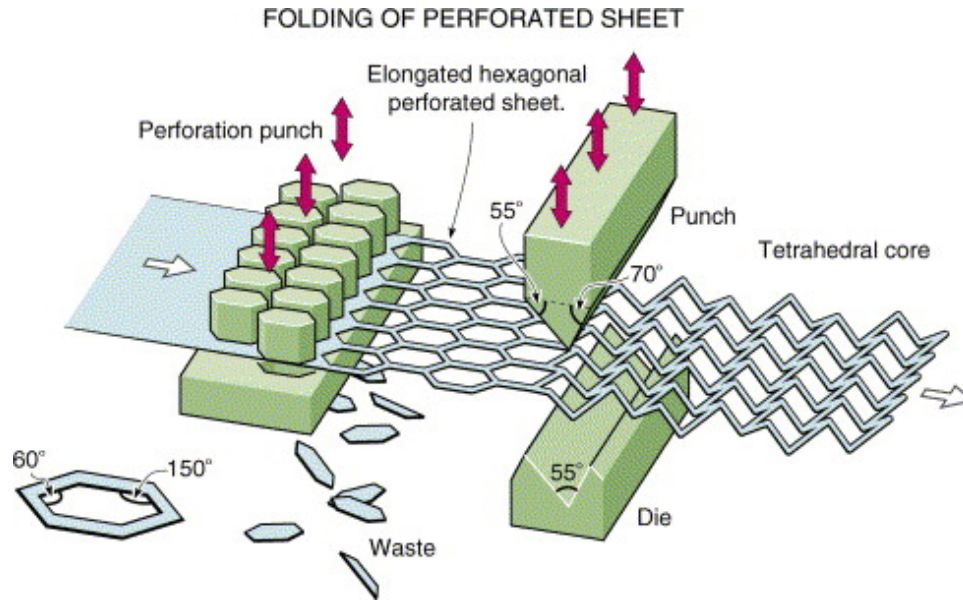


Figure 2.10: The process begins with a solid sheet which is first punched to create the hexagonal pattern. Feeding in the extended hexagonal perforated sheet leads to a folded lattice on the other side in the desired tetrahedral pattern [67].

2.3.3 Wire assembly and weaving

The difficulty in making lattices with very high slenderness ratios (i.e. very long struts with small diameters), which are optimal in most cases [54], can be bypassed if instead of making the whole structure at once, the task is broken down into smaller steps. The fabrication of a single strut may seem like a tedious affair, but techniques have been developed whereby an entire lattice can be created quickly with the careful layering of single wires or tubes. Sypeck *et al.* first published a metal laminate approach based on the weaving of metal wires into bundles (Figure 2.11) with others following suit [69, 70]. Because almost any metal can be drawn into a wire, this technique is very open-ended and is only limited in the ability to join the weaved wires together. Commonly, the wire will be coated in a liquid cement and brazing powder that would allow for joining at points of wire contact as the assembly is heated in a furnace [69].

Instead of using metallic wire, it is similarly possible to use metallic tubes. Tubes are more structurally efficient than solid rods, thus a structure built up with tubes would have an advantage over the textile version. A layup method can be used where tubes are laid into a 2D

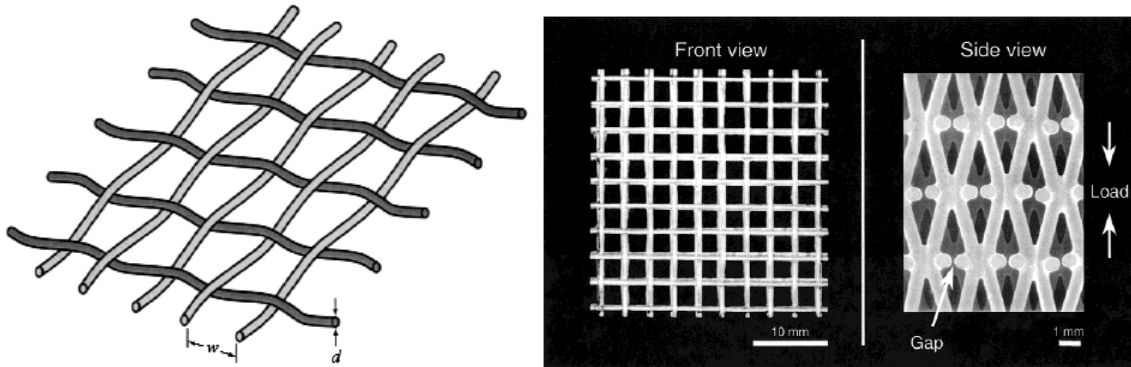


Figure 2.11: A square weave pattern can be put together using metal wire precursors (left) and then assembled into three-dimensional blocks (right) [69].

array inside a fixed jig (Figure 2.12) [29]. Additional layers of tubes are then stacked on top in a different direction, and the process is repeated until the desired height is reached. Any extra pieces that stick out of the overlapping section can be cut off leaving behind the lattice of tubes. The bonding is similar to that of the weaving technique.

Both of these methods, while providing new avenues for material choices, introduce anisotropy in the 3D lattice block - some directions of applied load are stronger than others. Additionally, both methods rely heavily on the ability to braze/weld/join the layers and tubes together. This means that if somewhere in the structure two struts have not been fully joined or the join is of a weaker quality, the structure will have a critical flaw that will greatly reduce the overall mechanical performance. This type of interface engineering is required but ideally would be eliminated in a true single step process.

Another method comes from a combination of the wire approach and the layup of tubes. Lim *et al.* start with a metal wire and bend it into a triangular pattern before overlapping the zig-zag sections to form tetrahedral unit cells (Figure 2.13) [71]. In the final structure, each strut in the unit cell is actually two adjacent wires that have been brazed together. While typical of these design processes, there was evidence of the brazing failing and each individual wire in the strut buckling on its own. This fabrication method was also shown to be modifiable to create unit cells with a Kagome structure (Figure 2.13). A Kagome lattice is similar to the tetrahedral lattice except that the tetrahedron is mirrored at its apex, resembling a letter X from the side

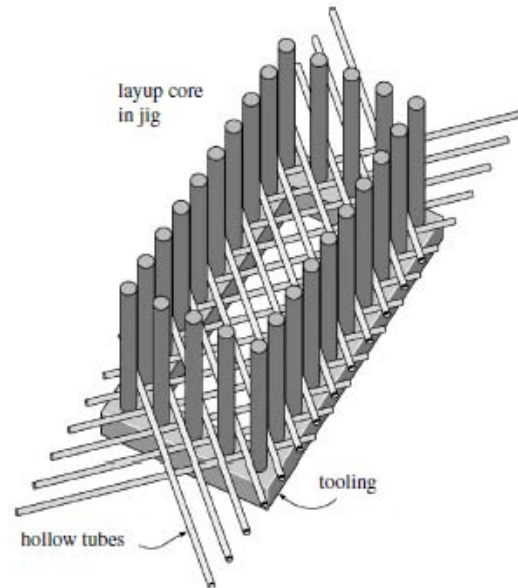


Figure 2.12: The jig that is used to layup metal tubes can be modified to create various lattices, but relies on consistent stacking such that a tetrahedral shape is not possible [29].

view. These shapes have been shown to be just as strong as the optimal tetrahedral/octahedral space filling lattices [57, 71, 72].

Further modifications by Lee *et al.* have highlighted the large freedom in this technique and the ability to use many different materials by creating fully weaved structures where helical wires are twisted into a Kagome lattice [42]. Lee *et al.* even developed a method to weave tubes into a Kagome lattice for the same reason as Wadley above [39]. Since then, wire-woven Kagome lattices have shown great promise for high strength sandwich panel cores and continue to be improved and expanded on today [43, 40, 41, 73].

2.3.4 Summary of current manufacturing techniques for lattices

From the above list of available techniques published in literature, a rich and fast-paced history is evident from the late 1990's to the early 2000's. In the span of five years, the original work by pioneers in the field like Ashby, Deshpande, Wadley, and Kang has exploded into a field that encompasses a wide variety of available materials, processing routes, and lattice architectures. Structures with low density and high strength can be fabricated that approach the gap in the

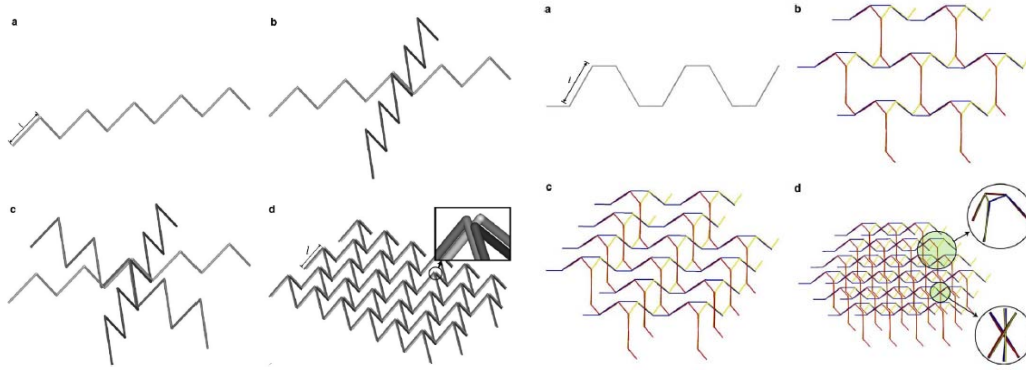


Figure 2.13: By overlapping bent wires in a set pattern, it is possible to create both tetrahedral (left) and Kagome (right) lattices [71].

material design space identified by Ashby in 2005 [10]. Though, some obstacles still remain in manufacturing optimal lattice architectures. In Ashby's discussion of creating hybrids, he mentions that once the required functions are optimized by selecting the correct materials, the choices of configuration and interface engineering remain (Figure 2.14) [10]. The need to plan carefully for how the individual components come together identifies a potential weak spot in the design; welds and adhesives between layers can end up being the weakest points in the structure. The ability for brazed/welded sections to fail before the lattice material has reached its peak capacity highlights a fundamental hindrance to multi-step fabrication routes. Moreover, routes that require a die or mold to be made in order to fabricate a certain architecture are beneficial for instances of mass production, but are costly when the architecture requires modifications.

2.4 Rapid prototyping - complete freedom in lattice design

Of all the presented techniques, few have complete freedom in architectural design. Each process needs a new set of dies, a new press or new perforation methods to modify the architecture, which is especially costly in the initial prototyping stage of engineering design. The exception is investment casting which uses rapid prototyping to make a mold that will eventually be displaced by a molten metal. Even in this case, though, there are limitations in the casting process

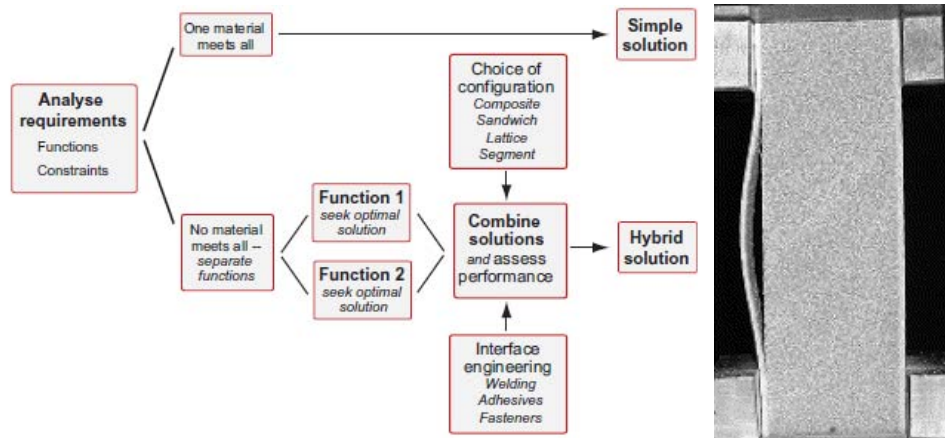


Figure 2.14: Hybrid solutions usually incorporate multiple materials to each handle a given function of the design. This means additional care must be taken to engineer a good interaction or interface between these separate materials to ensure failure does not occur prematurely (left) [10]. An example of bond failure at the interface of the face sheet and the core in a sandwich panel (right) [74].

as a pathway that is too tortuous for the metal to flow through will leave behind porosity and casting defects, as previously mentioned. A truly complex three-dimensional shape seems very difficult, if not impossible, to make with these techniques. If instead of trying to immediately find a way to make a metallic structure, one settles with just the ability to make any complex three-dimensional shapes, the rapid prototyping technology from the investment casting approach suddenly shows great value on its own.

2.4.1 A brief history of rapid prototyping

Literature on the topic of rapid prototyping is strongly biased towards patents. Scientific documentation on the individual techniques is limited to reviews that compare the various techniques and find scenarios when one technique is more beneficial than another in terms of accuracy, speed, or cost [75, 76, 77, 78]. The following section will outline a quick history of the development of this field as well as provide brief explanations of each technique and its benefits and limitations.

The phrase 'rapid prototyping' can be easily defined as fast manufacturing but comes in two forms: subtractive and additive manufacturing. One method starts with a solid block of

material which is removed until the desired shape is left (subtractive) and the other method builds up that same shape from smaller pieces (additive). In the discussion of complex shapes, the simpler and cleaner method seems to be additive manufacturing but history shows that it has been subtractive manufacturing that has had a more visible impact in product design. The simplest example would be taking a piece of wood and whittling away, cut by cut, until you had a cane, knife handle, or miniature figurine left behind. This technique was modernized and automated in computer numerical control (CNC) milling machines where typically a rotating cutter would cut away the unwanted material based on a three dimensional computer aided design (CAD) model. While fast and suitable to many material types, fully complex parts were not possible owing to the cutters and bits needing to get into very small crevices and unable to work out hollow or semi-hollow structures. Moreover, lots of waste material is generated that typically cannot be reused.

Additive manufacturing, usually referred to as 3D printing, works instead by building up layers of material. This requires that the CAD model first be spliced into layers than can be fed into the process such that the machine knows how to join each layer in order to create the final structure. The first example of a prototyper that could make these structures was designed by Chuck Hull of 3D Systems, Inc. in his 1986 patent [79]. The core principles focused on using a UV-curable photopolymer that, when exposed to a concentrated UV light source, cross-links the chains and turns the liquid precursor into a solid form. The fundamentals of this technique date back to the 1960s and is termed stereolithography (SLA) [80]. While similar apparatuses had been made a few years prior by Kodama [81], Hull was able to create a file format that would create those two dimensional slices in the three dimensional shape and feed that information to the prototyper - today's .stl file format. Further work turned this first machine into the global standard for stereolithography machines [82, 83].

Figure 2.15 outlines the general approach of the original stereolithography machine. The stage the product is built upon is submerged just below the surface of a vat of photopolymerizable resin. A UV laser than traces out a two dimensional sketch of the first layer, solidifying

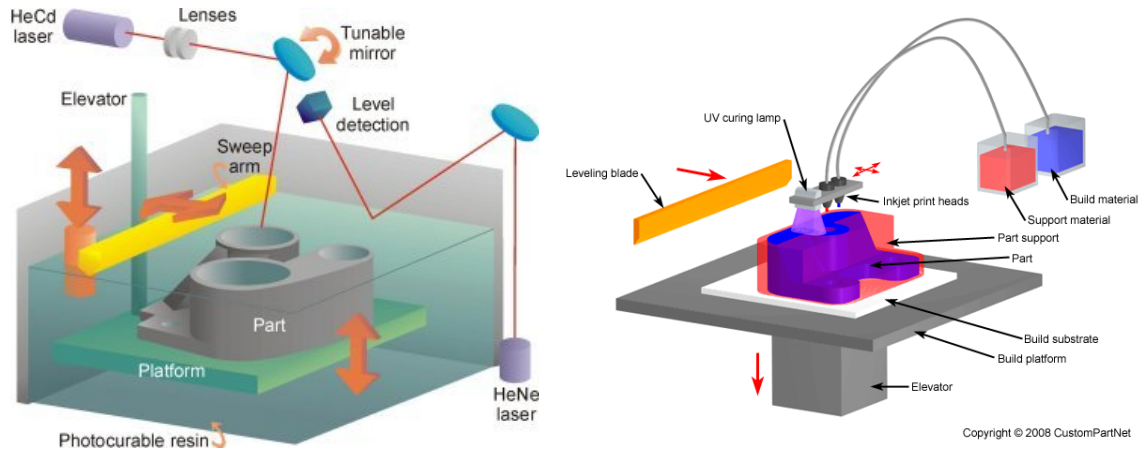


Figure 2.15: The stereolithography process centers on the use of a photocurable polymer source with a stage just beneath the surface (left). Two dimensional patterns are fabricated using a light source that exposes and cures the polymer only in areas it has focused on. The whole part is then removed when the process is complete [84]. Advances on this technique have removed the vat of liquid photopolymer and instead cure it where it is sprayed with a general UV light source rather than a targeted laser (right) [85].

this pattern. The stage is then further submerged to allow fresh liquid photopolymer to cover the previous layer, and the next pattern is then hardened on top of the previous layer. When completed, the part is removed and cleaned. The need for a precision laser to draw the outline was costly and was soon modified to a multi-jet modeling (MJM) system where liquid resin is sprayed onto the stage in precise spots, like an inkjet printer. These spots are then exposed to a general UV lamp that solidifies the structure (Figure 2.15) [82]. Since it is not possible to print a part hanging in free space (or a hollow ball, for example), support material needs to be used in parallel. The prototyper pre-determines locations of structural overhang and prints supports made of a UV-curable wax that can be melted off after printing, thereby creating shapes with true complex architectures [83].

Soon after, other methods of layering material into three dimensional structures were introduced. Fused deposition modeling (FDM), selective laser sintering (SLS), selective laser melting (SLM), laminated object manufacturing (LOM), and powder processes were just some of the many prototypers and techniques introduced [77]. In the last few years, the original patents on FDM and SLA expiring their 20 year hold period, thus the number of small com-

panies that have begun creating their own versions of these machines has risen greatly. Entire websites have been dedicated to listing critics' opinions and reviews on the hundreds of available models that are now rather affordable (<\$1000 CDN). Of all these methods, the two most significant to fabricating complex three-dimensional structures are FDM and SLS.

FDM has been mentioned before in the review of investment casting (section 2.3.1) as some of the complex lattices were made with this technique, which was patented first by Crump in 1992 [86]. He later turned this process into the company Stratasys, which is the largest provider of high quality FDM prototypers. Compared to SLA, all that is needed is a polymer filament passing through a heating block that raises its temperature just past the melting point. Then, it is extruded out of a nozzle and the two dimensional slices are drawn out on a stage (Figure 2.16). The variety of polymers that this can be done for is very large, but the method requires that they be thermoplastics. While some metal/polymer composites have been identified that can be extruded [87], a pure metal extrusion process would be very difficult due to the high melting points of most metals.

A true fully metallic approach relies on the use of metal powders that are then sintered (SLS) or melted (SLM) together such that a metallic block of material can be formed (Figure 2.17). A supply of powder is rolled onto a stage and the laser passes over it creating a two dimensional pattern before the stage is dropped and more powder is added. Upon completion, the remaining unused powder surrounding the part is shaken off and little to no post-processing is needed. The powder bed on which the part is being built upon and around also acts as a support for the top layers. Plastics, ceramics and metals can all be used in this technique. The downside is that the laser required to sinter/melt needs to be very powerful and, therefore, is very expensive. Additionally, sintering leaves a great deal of porosity between particles, significantly reducing the mechanical performance of the structure; whereas, the melting to create a solid block drives up time and cost.

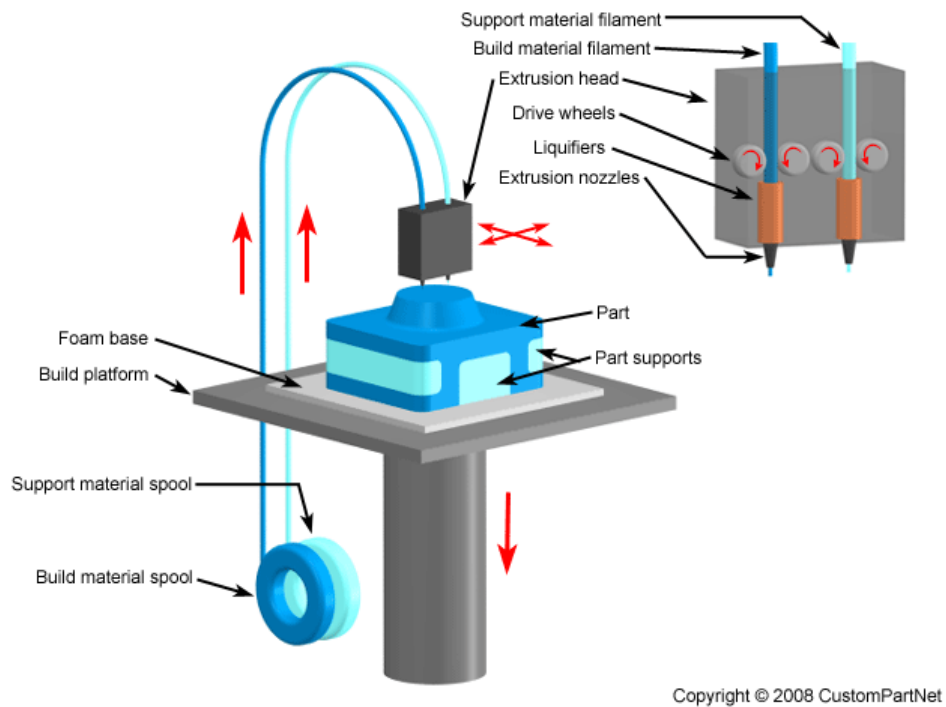


Figure 2.16: The FDM process is simply the melting of a wire precursor as it passes through a heating block and is then drawn out onto a stage. It is possible to have multiple channels to print multiple materials or colors at the same time or to print a dissolvable support material to create truly complex architecture [88].

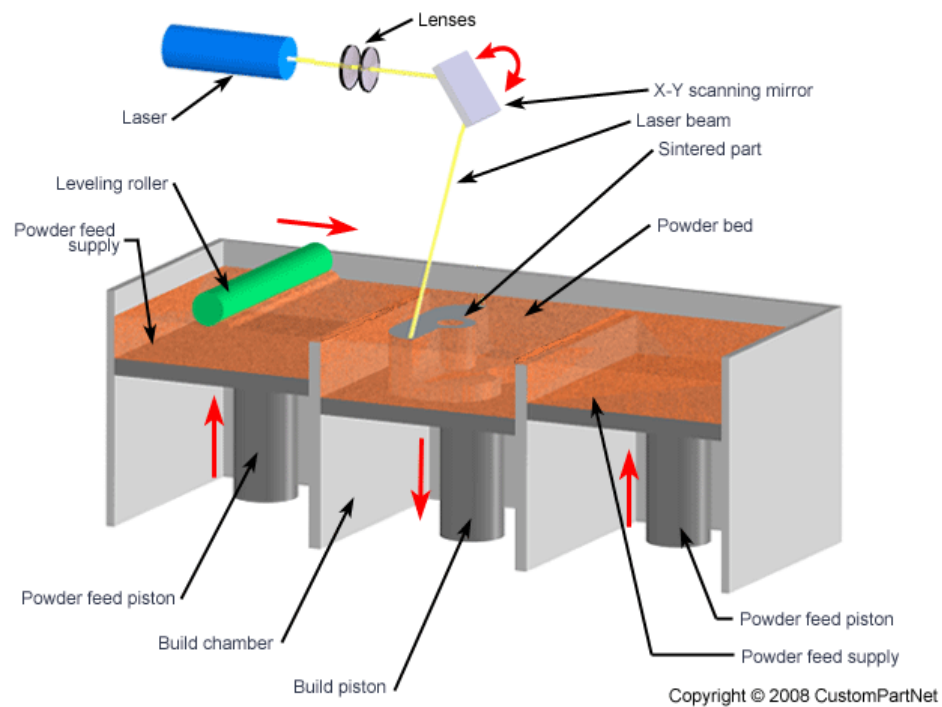


Figure 2.17: The SLS process uses the same light source, lenses, and mirror technology as the SLA method but the laser is powerful enough to sinter or melt metal powders into a solid shape. Rollers are used to push fresh powder into the build chamber to cover up the previously solidified layer [89].

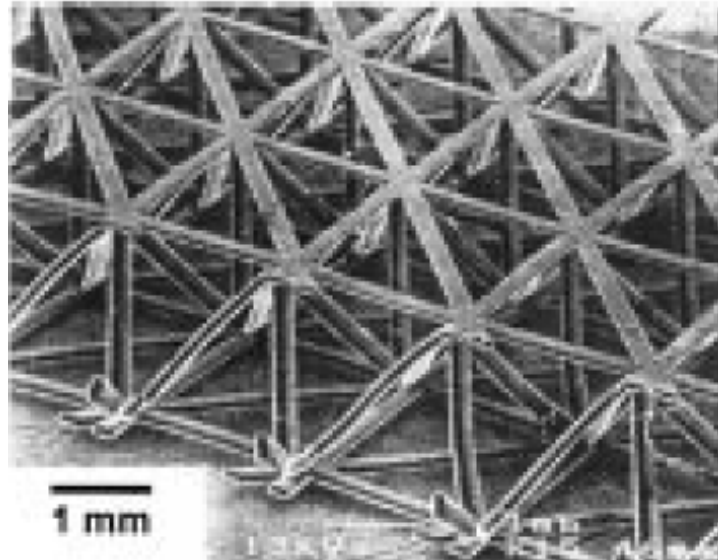


Figure 2.18: Brittain *et al.*'s metal/polymer lattice where the polymer truss was made with photolithography and subsequent deformation folding techniques before being joined by silver paint. Electrodeposition on the entire part creates a metallic coating overtop the polymer preform [93].

2.5 Lattices formed via rapid prototyping: strengthening techniques

For the goal of manufacturing net-shape microtruss materials, the selection of a synthesis technique points in the direction of rapid-prototyping because of the freedom in making very complex designs [77, 90, 91]. Of all the techniques that have been introduced and researched here, one additional one has not been covered in full. Jackman *et al.* showed how to make complex three-dimensional parts using photolithography, which is not the same as the SLA method mentioned above [92]. Instead, the structures are made in two dimensions and assembled together. While this method may not seem as attractive as the other techniques, it led to the first example of a hybrid lattice architecture in the 2001 Science publication by Brittain *et al* [93]. By first making sheets of polymer perforated patterns, then bending them into the desired unit cell architecture, the final lattice could be assembled with some silver paint to hold the edges (Figure 2.18).

What separates this lattice from the rest is the secondary step performed after assembly: a metallic coating was applied to the lattice using electrodeposition. This technique offered a new way of making a single metallic truss entity with the polymer core encapsulated inside. The polymer was now more of a substrate for the metal coating, and allowed the metal to be situated in the optimal position, far away from the neutral bending axis of each strut. Since then, the same process has been applied to foams to create metal/metal cellular materials [94, 95, 96, 97]. There are many ways to treat or coat lattices to create secondary hybrid composites such as work-hardening [66, 98, 99, 100], carburizing [101], anodizing [102], twinning [103], and plating [45, 35, 37, 44, 104]. The polymeric nature of the building material alone necessitates the addition of high-strength metallic coatings to create metal/polymer composites [44]. Overall, the progress in creating lightweight structures to fill the holes in material property space identified by Ashby can be realized through this process and, to date, has resulted in some ground-breaking materials (Figure 2.19) [45, 44].

2.5.1 Electrodeposition of nanocrystalline materials

Of the listed strengthening techniques above, electroplating, or electrodeposition, is the most relevant to the field of cellular materials. Because this technique is not line-of-sight like other deposition methodologies (e.g. chemical vapour deposition), it can be used to uniformly coat foams or lattices as was demonstrated for metal foams and microtrusses [94, 95, 45, 35, 37, 44, 104]. Other benefits include the wide variety of nanostructured coatings that can be applied both in pure form or alloyed with other elements, such as: Au [105], Au-Cu and Au-Cu-Sn [106], Co [107, 108, 109], Co-P [110, 111], Co-Cu [112], Cu [113, 114, 115], Ni [111, 116, 117, 118, 119, 120, 121, 122, 123, 124, 125, 126], Ni-Fe [111, 116, 127, 119, 128, 124], Ni-Mo [111], Ni-SiC [111], and Ni-W [129]. While not an exhaustive list, it provides a sense of the freedom in material selection when using electrodeposition.

The main components of an electrodeposition setup include a power source, a cathode, an anode, and an electrolyte (fig. 2.20). The part that will be coated is setup as the cathode

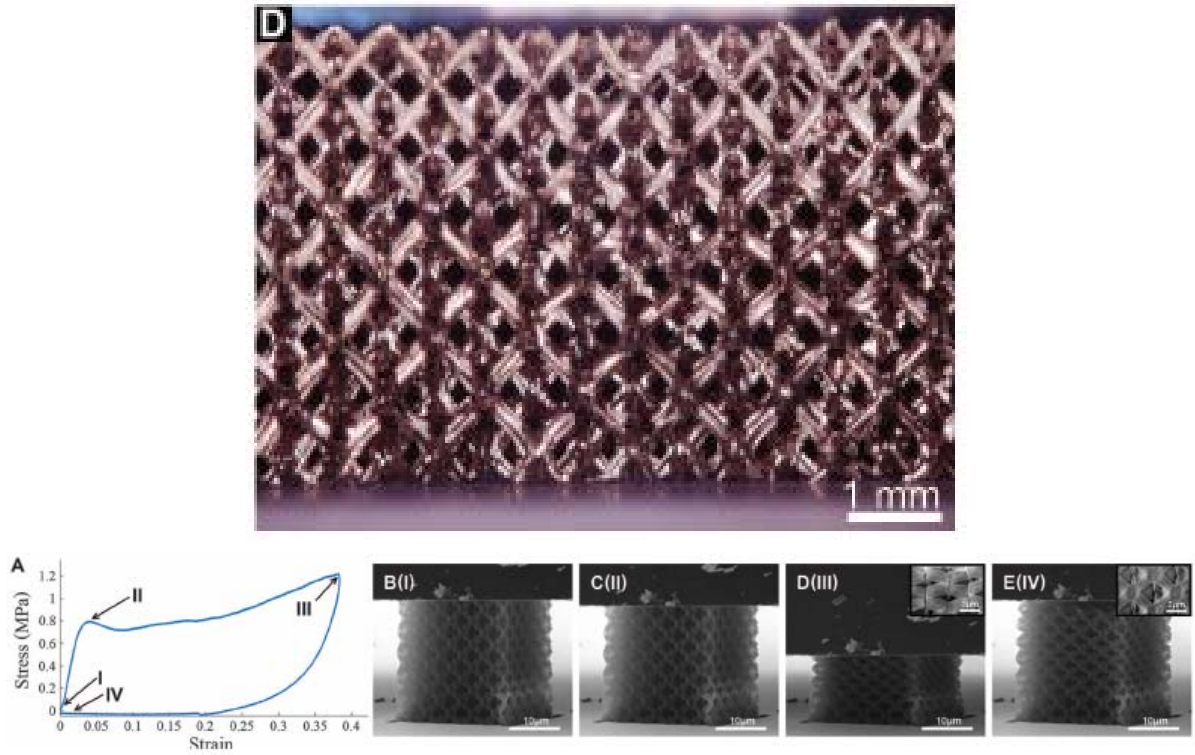


Figure 2.19: Examples of composite lattice structures with recoverable properties. A Ni-polymer lattice fabricated via self-propagated photopolymer waveguide prototyping was crushed and then allowed to recover past its failure point (top) [45]. A ceramic lattice fabricated via two-photon lithography where struts are in the nanometer scale reveal ductile properties after crushing (bottom) [46].

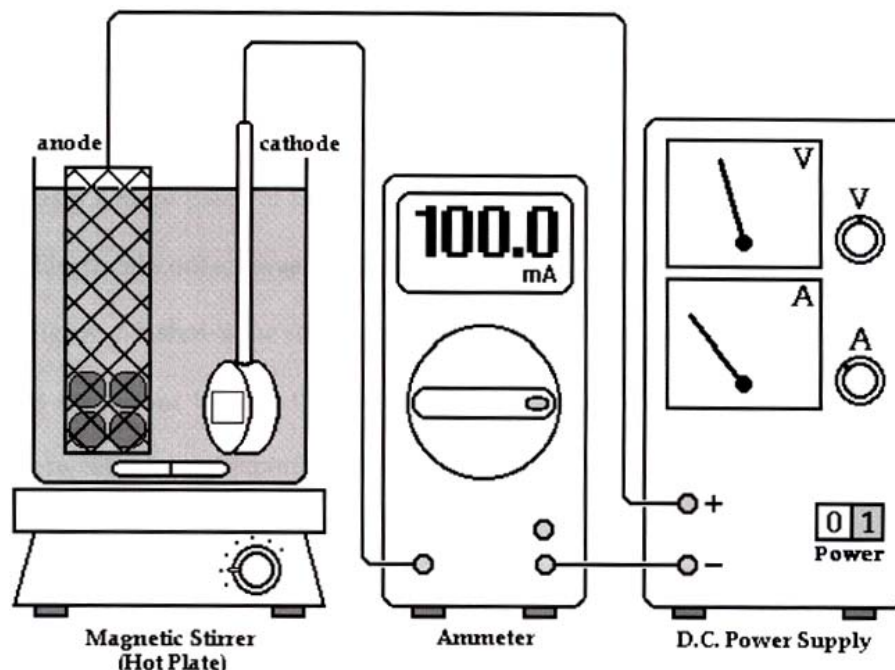


Figure 2.20: An electrodeposition setup showing the bath, power supply and ammeter displaying the provided current, taken from Ref. [130].

in the electrolyte solution where reduction of the metal ions in the solution will occur. A consumable anode is selected that will act as the source for the metal ions in the bath. It is typically a titanium mesh with metal rounds inside such that replenishing the metal is easy. The electrolyte is selected to act as a transporter of the metal ions between anode and cathode. The particular setup for the deposition of Ni coatings, for example, is modeled after a Watts bath with nickel salts (e.g. nickel sulfate and nickel chloride) and hydrogen buffers (e.g. boric acid) forming most of the constituents [130].

The history of depositing metals in a liquid bath starts near the time of Michael Faraday's development of the laws of electrolysis in the 1830s. The first patent was awarded to George and Henry Elkington in 1840 titled "For improvements in coating, covering, or plating certain metals" and given British patent number 8,447. In the hundred and fifty years that followed, the process was modified many times such that different elements and alloys could be plated. The most relevant improvement to this thesis was the development of nanocrystalline grain

size coatings covered in patents by Erb *et al* [4, 5]. By modifying the electrical signal in the bath such that it forms pulses of increased and then decreased current as well as the addition of a grain size inhibitor such as saccharin, the grain size of the metal could be tuned down to the 10 nm range [117, 118]. The saccharin prevents the surface diffusion of adatoms while a pulsed current favours nucleation of new grains over the growth of existing grains on the surface leading to a larger amount of small growth locations and a nanocrystalline structure. The end result is lots of smaller grains growing on the surface and a nanocrystalline structure. The industrial partner for this thesis, Integran Technologies, Inc., used these publications and patents to start the large-scale synthesis of nanocrystalline metal coatings and much of the methodology is proprietary to them.

Multiple review papers discuss the benefit of nanocrystalline materials as well as the multiple processing routes possible to synthesize them [6, 7, 8]. For materials with a grain size less than 100 nm, the term nanocrystalline is typically used while structures with features greater than 1 μm are described as polycrystalline. Terminology for the region between these is inconsistent with sub-micron or ultra-fine grain size typically used [6]. The benefits of this smaller grain size include short grain boundaries, high volume fraction of grain boundaries and triple junctions, and a non-equilibrium state grain boundary with a high density of defects [131]. Overall, these and other features make it so that dislocations find movement through the material more difficult and they pile up boundaries rather than the grains themselves making for a stronger material. This strengthening, termed the Hall-Petch behaviour, does have its limits as grain sizes less than 10 nm demonstrate an inverse to this strength increase [129]. The initiation of new failure modes, most notably grain boundary sliding and grain rotation, cause decreases in material yield strengths [132].

The increases in yield strength and ultimate tensile strength with decreasing grain size have been examined in literature, with fig. 2.22a serving as one example specifically for electrodeposited metals. In contrast to the Hall-Petch behaviour for strength, ductility, in the form of maximum uniform plastic strain, has been reported to be insensitive to grain size in the

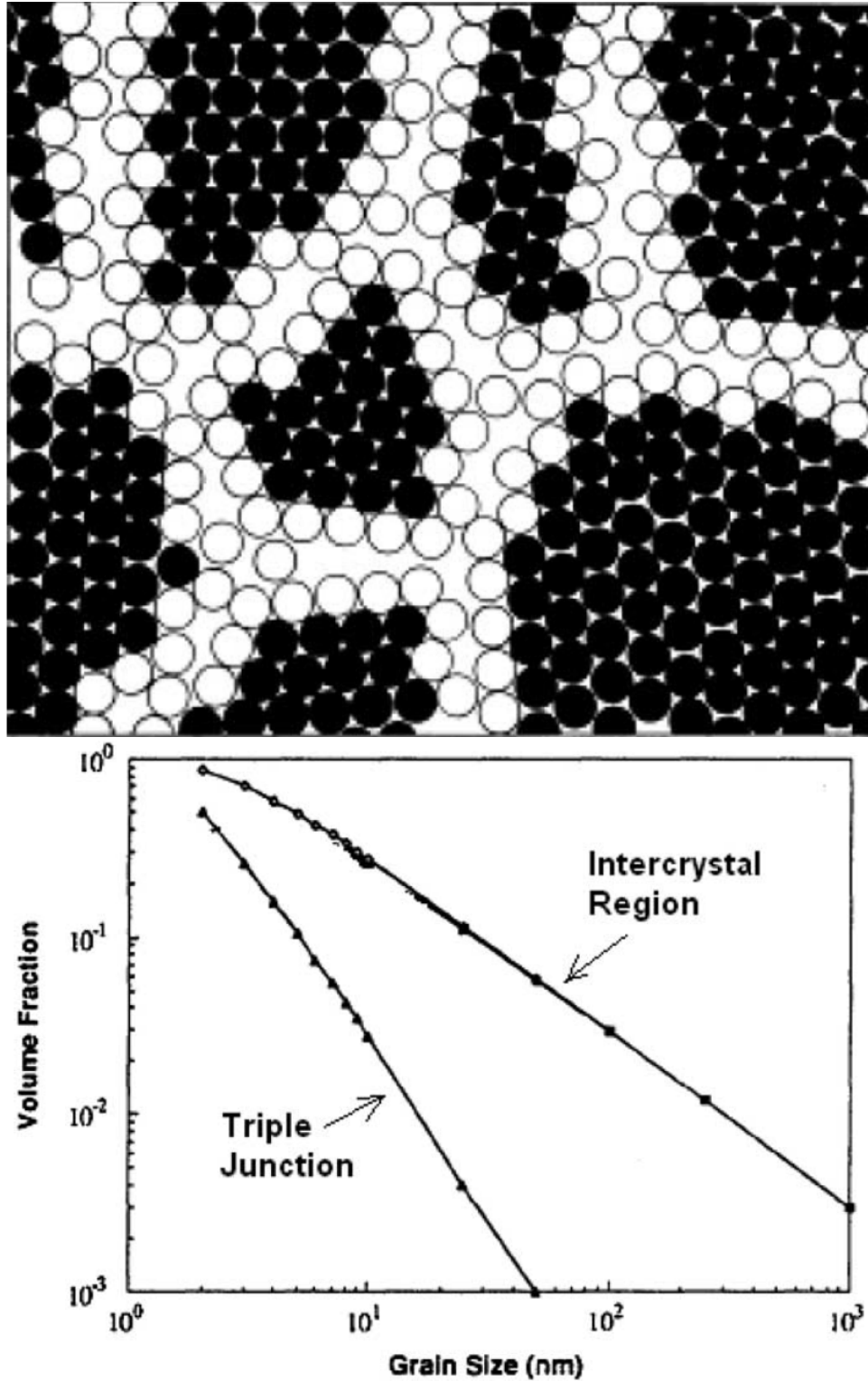


Figure 2.21: Schematic of a nanocrystalline grain size highlighting the large amount of atoms in the grain boundaries (white) compared to those in the grain itself (black) (top). With decreasing grain size, the percentage of the atoms that are in boundaries and triple junctions increases linearly (bottom) [133, 134].

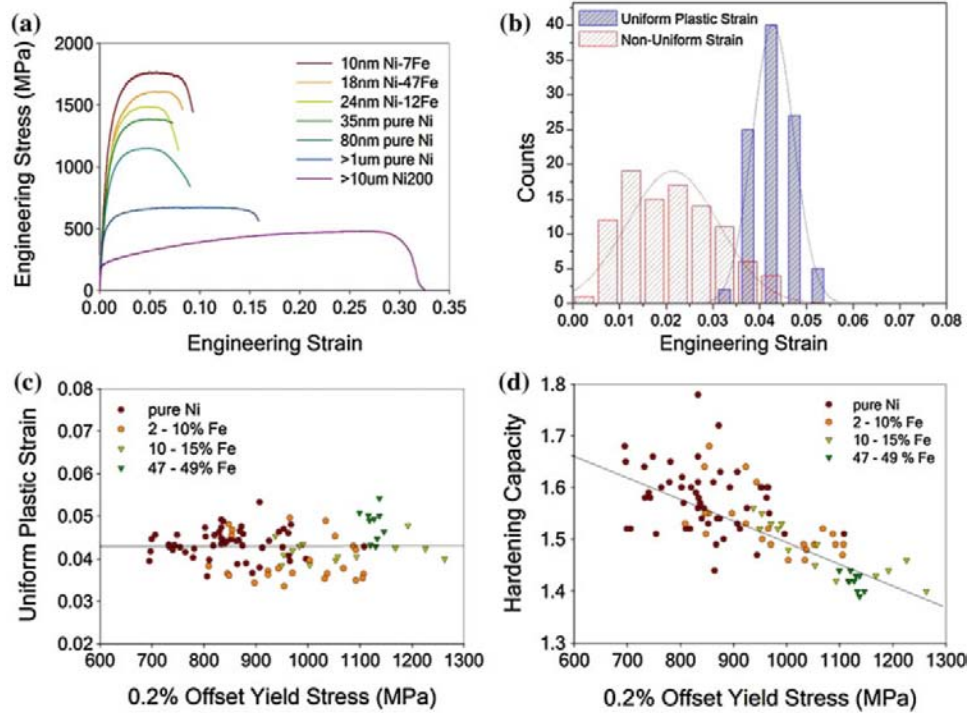


Figure 2.22: Electrodeposited tensile stress-strain curves with grain sizes ranging from 10-1000 nm with a 10 μm Ni 200 standard used for comparison (a). Uniform plastic and non-uniform strain distributions for a series of Ni-based electrodeposited coatings ranging from 10-80 nm (b). Maximum uniform plastic strain (c) and hardening capacity (d) plotted against the 0.2% offset yield strength for each tested sample [116].

nanocrystalline grain size regime (fig. 2.22b-c). Failure is thought to occur through the formation of nanovoids in the grain boundaries such that these materials are better defined by a critical plastic strain [116]. A discussion on the benefit of decreasing grain size from the polycrystalline regime to a nanocrystalline one for microtrusses will be presented in chapter 6.

2.6 Summary of key conclusions

To truly utilize the excellent mechanical properties of electrodeposited nanocrystalline metals in a bending specific application where lattices and sandwich panels are the standard, a template is required. Of the many techniques presented in this chapter in manufacturing these highly complicated templates, rapid prototyping comes out as the clear victor. With an almost 100% freedom in structural design, it can be tailored to specific applications and industries while

being sturdy enough to undergo metalization. Previous metal/polymer lattices fabricated in literature utilized varying prototyping methodologies but lacked complete design freedom due to processing limitations. Instead, the use of 3D printing in the form of stereolithography offers full freedom along with incredible accuracy and precision, down to the sub-100 μm level. This unique process will be discussed in full in subsequent chapters.

Chapter 3

Model derivation: Optimization of hybrid microtruss architecture

What follows is a step-by-step analysis into the derivation of expected failure mechanisms in a variety of microtruss architectures and compositions. It begins with a look at columns since the critical face sheet struts where failure occurs in three-point bending are columns with an applied load on either end from the beam's deflection. Following the coated column derivation, the microtruss structure will be defined, models of the failure mechanisms will be derived, and optimization will be performed to locate optimal architectures for a variety of material selections. In all of this work, the desired improvement on the beam's performance is looked at in terms of improving the peak load carrying capacity. This criterion is sufficient based on the thesis goal defined earlier but could just as well be adapted in the future to cases of maximizing beam stiffness or prolonging lifetime through fatigue analysis.

3.1 Stress in a column loaded in uniaxial compression

For a column loaded uniaxially (Figure 3.1), the applied force is transmitted through the material and can initiate three basic types of failure depending on the column composition: global buckling, local buckling (for hollow or shell columns), or yielding. In general, long columns

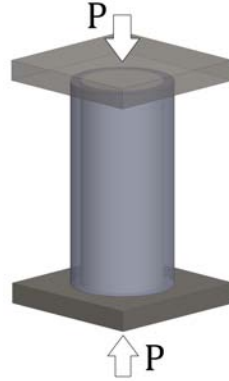


Figure 3.1: Setup for uniaxial compression testing of columns

with very large slenderness ratios are prone to buckling globally and do so in an elastic manner. This means that after unloading, the structure can return to its original shape. As the slenderness ratio is decreased, the column begins to behave inelastically where the critical buckling stress occurs beyond the yield point of the material. Permanent, irreversible deformation has now occurred. Global elastic buckling follows Euler's formula:

$$\sigma_b = \frac{F_b}{A} = \frac{k^2 \pi^2 EI}{u^2 A}, \quad (3.1)$$

where A is the cross-sectional area of the strut, k is the column effective length factor describing the connectivity at the ends of the column, E is the Young's modulus of the material, I is the second moment of area of the cross-section, and u is the length of the column. In the case of inelastic buckling, a reduced modulus, E_T , is used instead.

For a hollow column, a new type of failure mechanism is introduced where buckling can occur locally in small bands at the top or bottom of the column. Cascades of these rings are created as each bulges outwards and collapses in on itself. The derivation of this formula is described by Timoshenko *et al.* with the governing equation [135]:

$$\sigma_{lsb} = \frac{\gamma E n}{r \sqrt{3(1 - \nu^2)}}, \quad (3.2)$$

where n is the wall thickness of the hollow shell, ν is the Poisson's ratio of the material, and γ

is an empirical knockdown factor popularized by Weingarten *et al.* as [136]:

$$\gamma = 1 - 0.901(1 - e^{-\phi}), \quad \phi = \frac{1}{16} \sqrt{\frac{r}{n}}. \quad (3.3)$$

While these modes compete against each other, failure can also be reached through yielding of the material. While this type of failure is harder to observe in a sample during testing, changes in modulus can serve as a useful definition after the fact. Many methods exist in calculating this value, such as the 0.2% offset method; they differ based on tests done in compression or in tension giving yield strengths σ_{YS} and ultimate tensile strengths σ_{UTS} , respectively. Both will be used for the latter case of microtrusses under the symbol σ_{cr} as:

$$\sigma_{cr,1} = \sigma_{YS}, \quad \sigma_{cr,2} = \sigma_{UTS}. \quad (3.4)$$

3.1.1 Stress in a beam during three-point bending

To begin the analysis of a microtruss structure in three-point bending, a quick derivation of the relevant equations will be provided that describes how a general beam in bending will behave. Figure 3.2 shows an element of a beam before testing and after a given deflection which resulted in some bending across the middle of the beam. Before load application, the lines \overline{AB} and \overline{CD} are parallel to each other and perpendicular to the beam length. As the load is applied downwards on the beam at mid-span, the distance between \overline{AC} decreases as the top side undergoes compression. Similarly, the distance between \overline{DB} increases as the bottom side is in tension. However, there does, exist one line segment connecting \overline{AB} to \overline{CD} that will remain the same length regardless of the amount of deflection: the line segment \overline{FE} in Figure 3.2. It is said this line exists on the 'neutral bending axis' which is to say there is a horizontal slice somewhere in this rectangular beam where no elongation or compression occurs (no strain) resulting in no stress. Moving away from this axis, the stress either increases (towards the tensile side) or decreases (towards the compressive side).

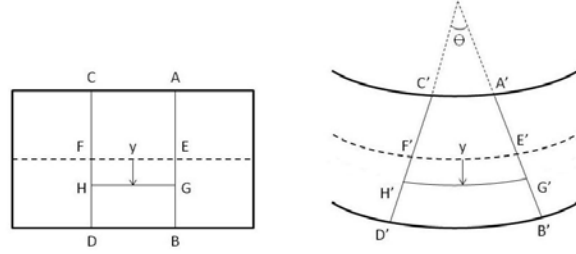


Figure 3.2: A beam element at mid-span before testing (left) and after some deflection downwards (right)

The new line segments $\overline{A'B'}$ and $\overline{C'D'}$ are sections of radii for a large circle where the origin lies above the point of load application and $\overline{F'E'}$ is the arc of that circle bounded by $\overline{A'B'}$ and $\overline{C'D'}$ with angle θ and radius R . To derive the stress in a given horizontal slice of the beam, we define two new points, H and G, that form line segment \overline{HG} at height y below the neutral bending axis (we take this line segment to be below to keep our elongations positive but it can be similarly shown that this is true on the compressive side of the beam as well). The ratios, then, of $\overline{H'G'}$ and $\overline{F'E'}$ can be expressed as:

$$\frac{H'G'}{F'E'} = \frac{(R+y)\theta}{R\theta} = \frac{R+y}{R}. \quad (3.5)$$

The strain along this slice will be the elongation of $\overline{H'G'}$ compared to \overline{HG} where we use the fact that \overline{HG} and \overline{FE} are equal before testing and then substitute the above relationship:

$$\epsilon = \frac{H'G' - HG}{HG} = \frac{H'G' - HG}{EF} = \frac{H'G'}{EF} - \frac{HG}{EF} = \frac{R+y}{R} - 1 = \frac{y}{R}. \quad (3.6)$$

For the case of elastic bending, the strain can be related to the stress using Young's Modulus, E , in the form $\sigma = E\epsilon$. Combining all of this gives:

$$\frac{\sigma}{E} = \frac{y}{R}. \quad (3.7)$$

As y increases, the stress becomes more positive (higher in tension) while values of negative y

represent compressive loads in equation 3.7.

If the beam is under static equilibrium and there is only moment in the beam, the force on each area element across the cross-section of the beam is σA , and the corresponding moment at that point will be $\sigma y A$. The total moment will be a sum of all these area elements into which we sub in equation 3.7:

$$M = \Sigma (y\sigma A) = \Sigma (y (\frac{E y}{R}) A) = \frac{E}{R} \Sigma (y^2 A). \quad (3.8)$$

The last part of the equation is actually the second moment of area, I , for an area element at a given height in the beam. Substituting in I and rearranging, the final equation is arrived at to describe the stress in a beam undergoing bending:

$$M = \frac{EI}{R}, \quad \frac{M}{I} = \frac{E}{R} = \frac{\sigma}{y}, \quad \sigma = \frac{My}{I}. \quad (3.9)$$

3.1.2 Force in the face and core struts of the microtruss

Failure of the struts inside a microtruss beam will be dependent on the applied load and the relative location in the structure. In the case of three-point bending (Figure 3.3), struts in the face sheets will undergo either tension or compression, struts in the core will be resisting shear and struts directly underneath the force application point can be indented due to the large applied load. To convert the applied load into forces in the individual struts, equation 3.9 will be used. Before using this equation directly, the moment and second moment of area need to be derived.

The moment for a beam in three-point bending varies as a function of position along the beam and is given by:

$$M = \frac{Px(L-x)}{L}, \quad (3.10)$$

where L is the distance between the bottom two supports (the effective beam length), P is the applied load at mid-span, and x is the position along the beam such that the first support is at

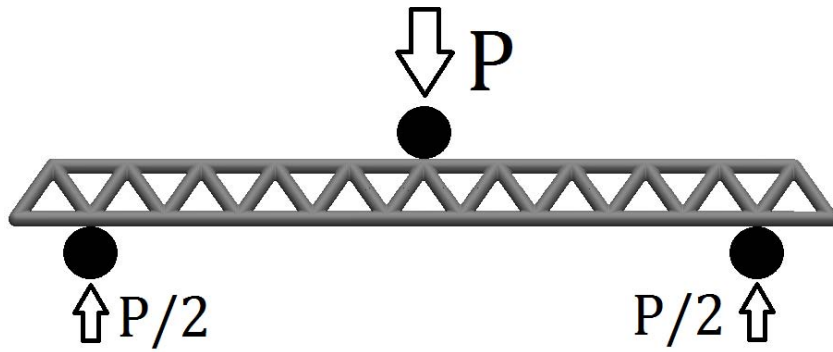


Figure 3.3: Setup for three-point bend testing of microtruss architectures

$x = 0$ and the second at $x = L$. At mid-span, the moment will be largest corresponding to

$$M(x = \frac{L}{2}) = \frac{PL}{4}. \tag{3.11}$$

For the struts in the faces directly adjacent to the central roller applying the load, this is the moment that will be used to derive the force in these struts.

The second moment of area is complicated by the disjointed cross-section of a microtruss. For the following analysis, a square pyramidal microtruss will be assumed, however, the analysis lends itself to any architecture of microtruss. At the midspan (ignoring the face struts that are perpendicular to the beam length and carry no load), there are three face struts in the upper face sheet and four in the lower face sheet that distribute the applied load outwards to the support rollers (for a three unit cell wide beam). For a single circular cross-section with radius r , $I = \frac{\pi}{4}r^4$. However, with seven struts in varying positions, the first step to finding I for the whole microtruss is to locate the centroid.

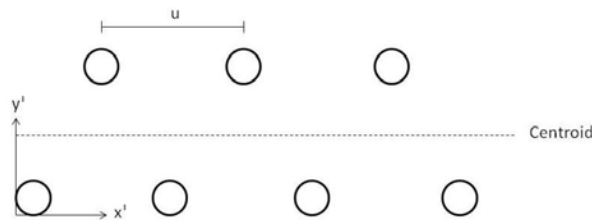


Figure 3.4: Cross-section at mid-span of square pyramidal microtruss assuming no horizontal face sheet struts

Choosing the origin to be the bottom left corner of the structure (Figure 3.4), the centroid can be calculated using a weighted average of each component:

$$x'_{centroid} = \frac{\sum (x'_i A_i)}{\sum A_i}, \quad y'_{centroid} = \frac{\sum (y'_i A_i)}{\sum A_i}, \quad (3.12)$$

where A_i is the cross-sectional area and x'_i and y'_i are the distances from the origin for each shape. For the square pyramidal architecture used here, the x' -centroid is in the middle of the structure as expected due to symmetry while the y' -centroid is slightly closer to the bottom face sheet ($y'_{centroid} = r + \frac{3u}{7\sqrt{2}}$) as is expected with more struts on the bottom side. The last step is to use this centroid location along with the parallel axis theorem to calculate I for the cross-section using:

$$I_{total} = \sum (I_i + A_i \delta d_i), \quad (3.13)$$

where δd_i is the distance for each shape from the y -centroid. The resulting second moment of area for the square pyramidal cross section can be expressed in full form or as an approximation as:

$$I_{total} = \frac{7\pi r^4}{4} + \frac{6\pi r^2 u^2}{7} \approx \frac{6\pi r^2 u^2}{7}. \quad (3.14)$$

Combining equations 3.9, 3.11, and 3.14, the force in each of the top face sheet struts adjacent to the central roller can be expressed as:

$$F_{topstrut} = \sigma_{top} A = \frac{M y_{top} A}{I} = \frac{\sqrt{2} PL}{12u}, \quad (3.15)$$

where $y_{top} = \frac{4u}{7\sqrt{2}}$. Similarly, the force in each of the bottom face sheet struts can be calculated as:

$$F_{bottomstrut} = \sigma_{bottom} A = \frac{M y_{bottom} A}{I} = \frac{\sqrt{2} PL}{16u}. \quad (3.16)$$

Note: Both of these equations used the simplified form of the second moment of area in equation 3.14 but can be modified to include all terms if necessary (for large values of r).

The derivation for forces in the core can be more easily calculated as a function of the forces in the face sheets making this a simple matter of force resolution. The orientation of a core strut relative to a face sheet strut is described by a rotation of 45 degrees (for the case of a square pyramidal structure) about the z-axis (parallel to the load application direction) and then a second rotation of 45 degrees about the y-axis (parallel to the beam width). The forces in the struts can then be derived as:

$$F_{core} = F_{face} \cos(45) \cos(45) = \frac{F_{face}}{2}. \quad (3.17)$$

Because of this, we can be assured that while the architecture of the structure remains such that the face and core struts are the same length, the forces in the face will dominate the forces in the core and the focus can remain solely on the faces. This holds true while the core strut remains inclined at 45 degrees from the face sheet but still follows the general behaviour of sandwich panels in having light cores and strong face sheets [13, 14, 21].

With our focus fully tuned to the face sheets, the last step is to convert these forces into a form that allows the incorporation of the failure stresses for each of the mechanisms analyzed in the simple column case above. To do this, the force in the strut is divided by the cross-sectional area of the strut, A_{cs} , to arrive at the stress in each strut. For each individual failure mechanism, a different critical stress, σ_f , exists for each combination of architectural parameters. The lowest of these will be the first one that is activated and will define the load at which the strut can be expected to fail. This stress should not be confused with the stress calculated using equation 3.9, which gave the stress in a beam undergoing bending at a given height in the beam for a given applied load. Rearranging for the load term, P , the final equations to describe the expected load at failure for the two face sheets are:

$$P_{topstrut} = \frac{12uA_{cs}\sigma_f}{\sqrt{2}L}, \quad (3.18)$$

and

$$P_{bottomstrut} = \frac{16uA_{cs}\sigma_f}{\sqrt{2}L}. \quad (3.19)$$

These simplified forms of the load carrying capacity of face sheet struts in either face sheet have been simplified substantially to make the future optimization analytically solvable. The two biggest simplifications were for the values of y and I in a composite column. Because the assumption is that the polymer will not be carrying substantial load in comparison to a high performance coating, the values for these terms should be modified such that the stress is being calculated at the most extreme point in the microtruss, namely $y_{top} = \frac{4u}{7\sqrt{2}} + r + n$. The extra $r + n$ term is also incorporated in the I calculation. Whereas equation 3.14 was for seven solid struts, if the load is assumed to only be carried by the coating, seven circular shells should instead be used giving:

$$I_{hollow} = \frac{7\pi}{4}((r + n)^4 - r^4) + \frac{6\pi u^2}{7}((r + n)^2 - r^2). \quad (3.20)$$

Plugging these into equation 3.9, the final form of both the force in the top and bottom face struts is arrived at:

$$P_{topstrut} = \frac{4\sigma_f I_{hollow}}{L(\frac{4u}{7\sqrt{2}} + r + n)} \quad (3.21)$$

$$P_{bottomstrut} = \frac{4\sigma_{UTS} I_{hollow}}{L(\frac{3u}{7\sqrt{2}} + r + n)} \quad (3.22)$$

3.2 Non-dimensionalization and optimization

Using the results from the previous sections, the forces in a uniaxially loaded column and a microtruss beam in bending can be determined analytically. Furthermore, the cases for both hollow struts and solid struts can be incorporated to explain single material structures and hybrid, composite structures (with a non-load carrying core). The last step is to use all of this knowledge to predict not only which failure mechanism is active at each geometry, but also to determine optimal designs.

The optimization problem is stated as:

$$\min = \hat{M} = \hat{M}(\bar{n}, \bar{r}, \bar{u}) \quad (3.23)$$

$$s.t. = \hat{P}(\bar{n}, \bar{r}, \bar{u}) - \hat{P}_{cr} = 0. \quad (3.24)$$

This is minimizing a non-dimensional measure of mass, \hat{M} , while maintaining a required non-dimensional strength, \hat{P}_{cr} , by varying the design parameters \bar{n} , \bar{r} , and \bar{u} . This is a standard minimization problem and can be solved by setting $\nabla \hat{M} = \lambda \nabla \hat{P}$, where λ is a Lagrange multiplier; this is the Karush-Kuhn-Tucker (KKT) condition [137]. The problem is made somewhat more difficult because the functional form of $\hat{P}(\bar{n}, \bar{r}, \bar{u})$ varies depending upon the combination of $(\bar{n}, \bar{r}, \bar{u})$. From a physical perspective, the form of the function \hat{P} is determined by the active failure mechanism given a combination of the design parameters. An additional complication arises because optimality can be achieved for designs where two failure mechanisms are simultaneously active without satisfying the KKT condition. However, all of these conditions are analytically tractable and the analysis will follow.

3.2.1 Columns

Taking equations 3.1, 3.2, and 3.4, the load to failure is extracted through a division of cross-sectional area, A_{cs} to give:

$$P_b = \frac{k^2 \pi^2 EI}{u^2}, \quad (3.25)$$

$$P_{lsb} = \frac{\gamma EnA}{r \sqrt{3(1 - \nu^2)}}, \quad (3.26)$$

and

$$P_{cr} = \sigma_{cr} A. \quad (3.27)$$

Single, solid material

In a single material, the cross-sectional area is represented as πr^2 . With that inserted into the above equations, the last step will be to non-dimensionalize the system to prepare for optimization. This step ensures that the scale of the structure is removed from the analysis. For these terms, the non-dimensionalization will take on the form:

$$\hat{P} = \frac{P}{u^2 \sigma_{cr}}. \quad (3.28)$$

This selection should be consistently applied to all terms in order to remove all dimension from the equations. The exact term that is used is not important but is selected to act as a reference load that will make simplification of the variables easier. It will be necessary to define some new terms in this process as the non-dimensional geometric parameters. They are:

$$\bar{r} = \frac{r}{u}, \quad \bar{n} = \frac{n}{r}. \quad (3.29)$$

Here we see the benefit of the choice of $u^2 \sigma_{cr}$ as the non-dimensionalization term. \bar{r} is a representation of the strut slenderness ratio (more accurately an inverse aspect ratio) while \bar{n} represents a ratio of the amount of coating material to the core material.

Combining the load carrying equations with equations 3.28 and 3.29, the final system of equations that describe a single material column in compression are:

$$\hat{P}_b = \frac{k^2 \pi^3 E \bar{r}^4}{\sigma_{cr}}, \quad (3.30)$$

and

$$\hat{P}_{cr} = \pi \bar{r}^2. \quad (3.31)$$

For buckling in particular, the use of E denotes an elastic buckling equation. To include the potential inelastic buckling of the strut, the critical buckling stress is calculated per Shanley

and is substituted instead of E [138].

Locations of optimal design are actually directly given from what is derived here. Because there is only one geometric parameter, \bar{r} , any given design requiring a column to support a load, \hat{P} , will have two values of \bar{r} to choose from and the lower of the two will be the lighter and, therefore, optimal design. While trivial, this process now follows to the more difficult case of a composite column.

Coated, composite structure with parasitic core

Before, with the exclusion of local shell buckling, a simple optimization was possible. Moving to this case complicates matters by having a competition not only of three failure mechanisms but, additionally, a second geometric parameter. The cross-sectional area, A_{cs} , is now a function of the inner core radius and the wall thickness of the shell, be it hollow inside or filled with a parasitic core. In both cases, we take the structure to be defined by its outer shell. Our non-dimensional load equations are now:

$$\hat{P}_b = \frac{k^2 \pi^3 E \bar{r}^4}{4 \sigma_{cr}} (4\bar{n} + 6\bar{n}^2 + 4\bar{n}^3 + \bar{n}^4), \quad (3.32)$$

$$\hat{P}_{cr} = \pi \bar{r}^2 (2\bar{n} + \bar{n}^2), \quad (3.33)$$

and

$$\hat{P}_{lsb} = \frac{\gamma \pi E \bar{n} \bar{r}^2}{\sigma_{cr} \sqrt{3(1-\nu^2)}} (2\bar{n} + \bar{n}^2). \quad (3.34)$$

Just as the buckling equation is split between elastic and inelastic systems, the local shell buckling can do the same giving us 5 total equations describing the failure of composite columns.

To locate optimal designs using the KKT condition, the mass of the column at each architecture is also required. Here we again have two cases that need to be checked: a hollow column (i.e. a tube) or a coated composite column with a parasitic core. In the former, the

mass can be easily calculated and non-dimensionalized using the factor ρu^3 to arrive at:

$$M = \rho V = \rho \pi (2rn + n^2)u, \quad \hat{M} = \frac{M}{\rho u^3} = \pi \bar{r}^2 (2\bar{n} + \bar{n}^2). \quad (3.35)$$

If there is something in the middle, the ratio becomes more complicated as the non-dimensionalization will need to select which value of ρ between the two materials will be used. For the cases of metal/polymer hybrids, the non-dimensionalization will use the density of the polymer.

$$M = \rho_{coating} V_{coating} + \rho_{core} V_{core} = \rho_{coating} \pi (2rn + n^2)u + \rho_{core} \pi r^2 u, \quad (3.36)$$

$$\hat{M} = \frac{M}{\rho_{core} u^3} = \frac{\rho_{coating} \pi \bar{r}^2 (2\bar{n} + \bar{n}^2)}{\rho_{core}} + \pi \bar{r}^2. \quad (3.37)$$

Next the derivatives of \hat{P} and \hat{M} are taken with respect to \bar{r} and \bar{n} . They are then equated in relation to a Lagrangian multiplier such that:

$$\frac{\partial \hat{P}}{\partial \bar{r}} = \lambda \frac{\partial \hat{M}}{\partial \bar{r}} \quad (3.38)$$

and

$$\frac{\partial \hat{P}}{\partial \bar{n}} = \lambda \frac{\partial \hat{M}}{\partial \bar{n}}. \quad (3.39)$$

If a value for λ can be found that satisfies both equations, then an optimal architecture has been temporarily located. The last step is to ensure this optimal architecture is inside an active failure zone of the material. This process is repeated for each failure mechanism. As an example, here is the determination of whether an optimal exists in the critical stress zone for a hollow column:

$$\frac{\partial \hat{P}_{cr}}{\partial \bar{r}} = 2\pi \bar{r} (2\bar{n} + \bar{n}^2), \quad \frac{\partial \hat{P}_{cr}}{\partial \bar{n}} = \pi \bar{r}^2 (2 + 2\bar{n}), \quad (3.40)$$

$$\frac{\partial \hat{M}}{\partial \bar{r}} = 2\pi \bar{r} (2\bar{n} + \bar{n}^2), \quad \frac{\partial \hat{M}}{\partial \bar{n}} = \pi \bar{r}^2 (2 + 2\bar{n}). \quad (3.41)$$

Using equation 3.38 gives $\lambda = 1$ and then using 3.39 with the above derivatives gives:

$$\pi\bar{r}^2(2 + 2\bar{n}) = (1)\pi\bar{r}^2(2 + 2\bar{n}), \quad 1 = 1. \quad (3.42)$$

This result shows that for designs expected to fail by reaching critical stress, they will all be optimal.

3.2.2 Microtrusses

Microtruss optimization begins with using equations 3.18 and 3.19 and non-dimensionalizing by:

$$\hat{P} = \frac{P}{L^2\sigma_{cr}}. \quad (3.43)$$

Note: This is very similar to equation 3.28 except that instead of using the strut length, u , the testing length of the beam, L , is substituted. This is split into two cases once again: microtrusses with single material, solid struts and microtrusses with composite or hollow struts.

For the single material case, local shell buckling is not active and the relevant non-dimensional failure load equations are:

$$\hat{P}_{cr} = \frac{16\pi}{\sqrt{2}}\bar{r}^2\bar{u}^3 \quad (3.44)$$

and

$$\hat{P}_b = \frac{3\pi^3Ek^2}{\sigma_{cr}\sqrt{2}}\bar{r}^4\bar{u}^3 \quad (3.45)$$

with E being substituted according to be elastic and inelastic behaviour. The mass of a beam will be based on the number of unit cells in the structure and can be calculated using the beam width, b , and beam length, L , as:

$$M = N\frac{bL}{u}\rho V_{strut}, \quad (3.46)$$

where N is the number of struts in the unit cell. For a square pyramidal structure, for example,

this number is 8 and after non-dimensionalizing by $bL^2\rho_{ref}$ results:

$$\hat{M} = 8\pi\bar{r}^2\bar{u}. \quad (3.47)$$

For a hybrid material, the three relevant failure mechanisms are:

$$\hat{P}_{cr} = \frac{16\pi}{\sqrt{2}}\bar{r}^2\bar{u}^3(2\bar{n} + \bar{n}^2), \quad (3.48)$$

$$\hat{P}_{lsb} = \frac{12\gamma\pi E\bar{n}\bar{r}^2}{\sigma_{cr}\sqrt{2}\sqrt{3(1-\nu^2)}}(2\bar{n} + \bar{n}^2). \quad (3.49)$$

and

$$\hat{P}_b = \frac{3\pi^3 Ek^2}{\sigma_{cr}\sqrt{2}}\bar{r}^4\bar{u}^3(4\bar{n} + 6\bar{n}^2 + 4\bar{n}^3 + \bar{n}^4), \quad (3.50)$$

with E , again, able to include the elastic and inelastic effects for both global and local shell buckling. The mass is calculated similar to the single material case and with the same distinction as the hybrid column case of being either hollow or having a parasitic core. This gives two \hat{M} equations as:

$$\hat{M}_{hollow} = 8\pi\bar{r}^2\bar{u}(2\bar{n} + \bar{n}^2). \quad (3.51)$$

and

$$\hat{M}_{composite} = 8\pi\rho_{coating}\bar{r}^2\bar{u}(2\bar{n} + \bar{n}^2)/\rho_{core} + 8\pi\bar{r}^2\bar{u}. \quad (3.52)$$

3.2.3 Optimal trajectories for composite microtrusses

Just as for the columns, the KKT condition was used to locate optimal trajectories for each failure zone in the microtruss failure map and then checked to determine if it is active at any point along its trajectory. Because the load equations in the microtruss case are more complicated and contain more architectural parameters, the derivatives with respect to \bar{r} and \bar{n} are more tedious to perform than the example above for a solid strut column. The non-dimensionalized load index of equations 3.21 and 3.22 without the individual failure mechanisms inserted are

longer than the entire set of equations before.

$$\hat{P}_{topstrut} = \frac{\sigma_f \pi \bar{r}^2 \bar{u}^3 ((1 + \bar{n})^2 - 1)(49\bar{r}^2((1 + \bar{n})^2 + 1) + 24)}{\sigma_{cr}(\frac{4}{\sqrt{2}} + 7\bar{r}(1 + n))} \quad (3.53)$$

$$\hat{P}_{bottomstrut} = \frac{\sigma_{UTS} \pi \bar{r}^2 \bar{u}^3 ((1 + \bar{n})^2 - 1)(49\bar{r}^2((1 + \bar{n})^2 + 1) + 24)}{\sigma_{cr}(\frac{3}{\sqrt{2}} + 7\bar{r}(1 + n))} \quad (3.54)$$

After proceeding with the KKT condition, equations for the optimal trajectory are given in terms of \bar{r} . For inelastic global buckling and local shell buckling, the derivation could proceed as it does for the elastic case with the substitution for the tangent modulus at the critical buckling stress for the Young's modulus. However, in the hope of finding an analytical solution, a derivation of the tangent modulus in relation to the stress in the material can be performed if the stress-strain curve behaves according to the Voce strain hardening relation [139]. For this equation,

$$\sigma = B - (B - A)\exp(-C\epsilon), \quad (3.55)$$

its derivative can be written as:

$$E_T = C(B - \sigma). \quad (3.56)$$

For the nickel based alloys predominantly used here, goodness-of-fits of R^2 are readily obtained to three 9s. Using this added step, the trajectories for all five failure mechanisms can be put together and are presented here.

Elastic global buckling is expressed as:

$$\bar{r}_{EGB} = RH \frac{B_L(49\bar{r}^6(6(1 + \bar{n})^5 + 4(1 + \bar{n})^3 + 2(1 + \bar{n})) + 96\bar{r}^4((1 + \bar{n})^3)) - 7\bar{r}T}{B_L(294\bar{r}^5(1 + \bar{n})^4 - 1)((1 + \bar{n})^2 + 1) + 96\bar{r}^3((1 + \bar{n})^4 - 1) - 7T(1 + \bar{n})}, \quad (3.57)$$

where

$$RH = \frac{\bar{\rho}(2\bar{n} + \bar{n}^2) + 1}{\bar{\rho}(1 + \bar{n})^2}, \quad (3.58)$$

$$T = 49\bar{r}^6((1 + \bar{n})^4 - 1)((1 + \bar{n})^2 + 1) + 24\bar{r}^4((1 + \bar{n})^4 - 1), \quad (3.59)$$

and

$$B_L = \frac{4}{\sqrt{2}} + 7\bar{r}(1 + \bar{n}). \quad (3.60)$$

Inelastic global buckling is expressed as:

$$\bar{r}_{IGB} = \frac{RH(B_L B_R (196\bar{r}^4((1 + \bar{n})^3) + 48\bar{r}^2(1 + \bar{n})) - T_{IGB}(7\bar{r}B_R + B_L(\frac{-8(1+\bar{n})}{\bar{r}^2((1+\bar{n})^2+1)})))}{B_L B_R B_{IGB} - T_{IGB}(7(1 + \bar{n})B_R + B_L(\frac{-8}{\bar{r}^3((1+\bar{n})^2+1)})}), \quad (3.61)$$

where

$$Q = (196\bar{r}^2(1 + \bar{n})^2 + 48) - T(1 + \bar{n})(7B_R + \frac{-8B_L(1 + \bar{n})}{\bar{r}^2((1 + \bar{n})^2 + 1)}), \quad (3.62)$$

$$T_{IGB} = 49\bar{r}^4((1 + \bar{n})^4 - 1) + 24((1 + \bar{n})^2 - 1), \quad (3.63)$$

$$B_{IGB} = 196\bar{r}^3((1 + \bar{n})^4 - 1) + 48\bar{r}((1 + \bar{n})^2 - 1), \quad (3.64)$$

and

$$B_R = Ck^2\pi^2 + \frac{4}{\bar{r}^2((1 + \bar{n})^2 + 1)}. \quad (3.65)$$

Elastic local shell buckling is expressed as:

$$\bar{r}_{ELSB} = RH \frac{B_L(T_L + T_R) - 7\bar{r}T_{ELSB}}{B_L(196\bar{r}^3\gamma\bar{n}((1 + \bar{n})^4 - 1) + 48\bar{r}\gamma\bar{n}((1 + \bar{n})^2 - 1)) - 7T_{ELSB}(1 + \bar{n})}, \quad (3.66)$$

where

$$T_{ELSB} = 49\bar{r}^4\gamma\bar{n}((1 + \bar{n})^4 - 1) + 24\bar{r}^2\gamma\bar{n}((1 + \bar{n})^2 - 1), \quad (3.67)$$

$$T_L = 49\bar{r}^4(\gamma_p\bar{n}((1 + \bar{n})^4 - 1) + \gamma((1 + \bar{n})^4 - 1) + 4\gamma\bar{n}((1 + \bar{n})^3)), \quad (3.68)$$

$$T_R = 24\bar{r}^2(\gamma_p\bar{n}((1 + \bar{n})^2 - 1) + \gamma((1 + \bar{n})^2 - 1) + 2\gamma\bar{n}((1 + \bar{n})^2)), \quad (3.69)$$

and

$$\gamma_p = 0.901 \exp\left(\frac{-1}{16\sqrt{\bar{n}}}\right) \left(\frac{1}{32\sqrt{\bar{n}^3}}\right). \quad (3.70)$$

Inelastic local shell buckling is expressed as:

$$\bar{r}_{ELSB} = RH \frac{B_L B_R (T_C) - T_{ILSB} (7\bar{r} B_L + B_R (\gamma_p C - \frac{\sqrt{3(1-\nu^2)}}{\bar{n}^2}))}{B_L B_R (196\bar{r}^3 \gamma (1 + \bar{n})^4 - 1) + 48\bar{r} \gamma ((1 + \bar{n})^2 - 1)) - 7T_{ILSB} B_R (1 + \bar{n})}, \quad (3.71)$$

where

$$T_{ILSB} = 49\bar{r}^4 \gamma ((1 + \bar{n})^4 - 1) + 24\bar{r}^2 \gamma ((1 + \bar{n})^2 - 1), \quad (3.72)$$

$$T_C = \gamma_p (49\bar{r}^4 ((1 + \bar{n})^4 - 1) + 24\bar{r}^2 ((1 + \bar{n})^2 - 1)) + \gamma (196\bar{r}^3 ((1 + \bar{n})^3) + 48\bar{r}^2 (1 + \bar{n})), \quad (3.73)$$

and

$$B_R = C\gamma + \frac{\sqrt{3(1-\nu^2)}}{\bar{n}}. \quad (3.74)$$

The presence of \bar{r} on the right side of each equation necessitates a numerical step to solve this system (similar to the solutions to transcendental equations), which was performed in the computation of these failure maps in MATLAB. While not completely analytical anymore, the system can still be described and analyzed using this, the most complicated of equations. Considering this incorporates the inelastic behaviour of the stress-strain curve, it is a contribution to the future experimental validation while greatly reducing computation time.

3.3 Summary of key conclusions

This chapter has shown the necessary background and mathematical analysis required to predict the failure load of a microtruss beam in three-point bending. In order to arrive at the desired equations which express locations of optimal architecture, some assumptions had to be made. In the case of the hybrid coated structure, the metal and polymer are assumed to have no bonding strength in this derivation. Furthermore, due to the large difference in yield strains between the two material classes, the polymer core's contribution to carrying any load is negated in this study and serves only as a mass component. These assumptions will be checked during the experimental validation of these models in subsequent chapters. In terms of testing

conditions, the central point load is assumed to be applied directly on top of a set of nodes thus negating indentation failure. Additionally, the rollers in this system are assumed to be frictionless. Based on these simplifications, the arrived at system of equations governing the failure of these microtruss beams is formed.

Chapter 4

Characterization and mechanical performance of rapid prototyped polymer material

The analytical models describing failure of composite microtrusses (from Chapter 3) are reliant on the input of material parameters. This means the model is only as accurate as the determination of these properties. For the metallic compounds that will form the coatings, values for strength and stiffness can be obtained from material property databases and publications in the scientific community. However, rapid prototyped polymer is not represented in literature with respect to material properties beyond those quoted by individual suppliers. While companies will post some basic details, they lack full stress-strain curves, especially critical for analysis and prediction of buckling modes. The following chapter, along with Appendix A, discusses the testing and analysis performed in this doctoral study to obtain an initial understanding of the rapid prototyping process and extract material properties.



Figure 4.1: The ProJet 3500 rapid prototyper (model SD shown which is identical to the HD from the exterior) [140]. Capable of storing up to 4 kg each of part and support material and handling low definition parts up to 298 x 185 x 203 mm.

4.1 Determination of optimal printing conditions for polymer microtruss fabrication

Section 2.4 on page 22 discussed the development of rapid prototyping techniques with an emphasis on stereolithography and an updated version called multi-jet modeling (Fig. 2.15). During the progression of this thesis, a 3D Systems, Inc. ProJet 3500 HD MJM rapid prototyper was purchased and installed (Fig. 4.1). This system has the capabilities to print single layers as thin as 29 μm in an ultra-high definition mode over a build volume of 127 x 178 x 152 mm and quotes a typical accuracy of 25 μm per inch of part dimension in this mode [140].

In addition to the multiple modes, there are a collection of materials that can be selected from, depending on the needs of the final part. Some of the materials are biocompatible, some focus on casting, while others specialize in dental applications. The standard material is VisiJet

Properties	Condition	VisiJet M3-X	VisiJet M3 Black	VisiJet M3 Crystal	VisiJet M3 Propplast	VisiJet M3 Navy	VisiJet M3 Techplast	VisiJet M3 Procast	VisiJet® S300
Composition		UV Curable Plastic							Wax Support Material
Color		White	Black	Natural	Natural	Blue	Gray	Dark Blue	White
Bottle Quantity		2 kg	2 kg	2 kg	2 kg	2 kg	2 kg	2 kg	2 kg
Density @ 80 °C (liquid)	ASTM D4164	1.04 g/cm ³	1.02 g/cm ³	1.02 g/cm ³	1.02 g/cm ³	1.02 g/cm ³	1.02 g/cm ³	1.02 g/cm ³	N/A
Tensile Strength	ASTM D638	49 MPa	35.2 MPa	42.4 MPa	26.2 MPa	20.5 MPa	22.1 MPa	32 MPa	N/A
Tensile Modulus	ASTM D638	2168 MPa	1594 MPa	1463 MPa	1108 MPa	735 MPa	866 MPa	1724 MPa	N/A
Elongation at Break	ASTM D638	8.3 %	19.7 %	6.83 %	8.97 %	8 %	6.1 %	12.3 %	N/A
Flexural Strength	ASTM D790	65 MPa	44.5 MPa	49 MPa	26.6 MPa	28.1 MPa	28.1 MPa	45 MPa	N/A
Heat Distortion Temperature @ 0.45MPa	ASTM D648	88 °C	57 °C	56 °C	46 °C	46 °C	46 °C	N/A	N/A
Ash Content		N/A	N/A	N/A	0.01 %	0.01 %	0.01 %	0.01 %	N/A
Melting Point		N/A	N/A	N/A	N/A	N/A	N/A	N/A	60 °C
Softening Point		N/A	N/A	N/A	N/A	N/A	N/A	N/A	40 °C
USP Class VI Certified*		No	No	Yes	No	No	No	No	N/A
ProJet Compatibility		SD, HD	SD, HD	SD, HD	SD, HD	SD, HD	SD, HD	HD	SD, HD
Description		ABS-like Plastic	High strength & flexibility plastic	Tough Plastic, Translucent	Plastic, Natural	Plastic, Blue	Plastic, Gray	Castable Plastic	Non-toxic wax material for hands-free melt-away supports

Figure 4.2: The collection of polymer part materials that can be used in conjunction with the ProJet 3500 HD [140]. Particular focus is paid to the support material S300 and the part material Crystal.

Crystal and is the one the majority of the work in this thesis is based on. The full list and their material properties is shown in Fig. 4.2 [140].

4.1.1 Curing conditions in the rapid prototyper

With the use of a 3D rapid prototyper, there are a wide variety of parameters that can be configured to change the properties of the finished product. These include the length of UV curing during each printed layer, the length of post-processing UV curing, the resolution setting of the printer, and the finishing techniques applied to the as-printed product. The critical three parameters to the polymer's finished mechanical state have been optimized by 3D Systems, Inc. resulting in the following default settings:

- cure time per layer from 0.1 to 30 seconds - default is 2 seconds
- frequency of curing cycle from every layer to every fifth layer - default is every other layer
- number of passes of UV curing upon completion of part to harden whole structure from 0 to 25 - default is 10 passes

If one were to modify these variables and try to decide which setting is optimal, some sort of metric would need to be used to distinguish good prints from bad ones. It could be the ultimate tensile strength of an as-printed dogbone coupon tested in uniaxial tension, the 0.2% offset yield strength of a cylindrical compression coupon, or the bending behaviour of a solid beam to obtain flexural material properties. There are still other metrics that further specify the polymer structure's fracture toughness or heat tolerance. However, the goal of creating a hollow, metallic microtruss means the polymer behaviour of most relevance and interest to the fabrication process would be its ability to be reliably coated with a high-strength metal. Discussions with 3D Systems, Inc. and their technicians revealed that they had had success plating onto as-printed structures with minimal extra treatment and, therefore, the defaults set on the printer were left mostly as is.

Variations on these settings were attempted by printing samples on either end of extremes of curing and comparing to the default. Rectangular blocks 10x10x1 mm were printed in a minimally cured condition (0.1 s curing every fifth layer with no post-printing curing) and a fully hardened one (30 s curing every layer with 25 post-printing curing passes). The minimally cured structures did print and maintained their rectangular shape but had a tacky texture and would easily deform with small applied forces. In contrast, the fully hardened sample exited the process in a robust block form but the extensive time taken to cure each cycle meant a print that took 2.5 hrs with the default settings now took 14 hrs. It also created substantially more waste material due the prototyper head needing to purge itself more frequently. In the end, the choice was made to maintain the curing conditions as those set in the default settings to allow for direct comparisons between measured material properties and those quoted in Fig. 4.2.

4.1.2 Removal of wax supports and finishing process

The layer-by-layer process in rapid prototyping makes it necessary to build supports underneath structures that have an overhang. For example, if a capital letter T was to be printed, the central vertical ascent would be easy enough to fabricate but the first layer that contains the horizontal

cross-piece would not be possible. The extruder, regardless of manufacturing technique, would extrude material where it thinks material should be but with nothing below to hold it at this level, it would fall to the bottom. Realistically, one would simply rotate the part such that it was upside down to avoid this problem. However, in complicated structures like microtrusses, no orientation exists where parts would not need support during fabrication.

In MJM, the software calculates all such overhangs and pre-prints a second material underneath these areas such that the actual part can be printed onto this support. A good choice for this second material would be something that could easily be removed after printing. It could be loosely bound to the desired structure such that it can be broken off, as typically seen in FDM, or a material that can be dissolved away. Both methodologies have their pros and cons but in the fabrication of small-scale features, breaking off a support may damage the final part and so dissolution is preferred. In the ProJet 3500 HD rapid prototyper, a wax support material called VisiJet S300 (fig.4.2) is melted off in a low-temperature oven to retrieve the part.

This introduced a new processing step into the fabrication sequence and it was noticed that the length of time in the finisher and length of time before testing had an impact on the material properties of the polymer. When samples were still warm (minutes after being removed from the finisher), they had greatly reduced mechanical properties (Fig. A.2). The time left inside the finisher did not measurably affect the parts as long as all the wax had been removed. These conclusions were consistent for both compression coupons according to ASTM D695 and microtruss beams in bending. A full discussion on experimental design and results can be found in Appendix A.1.

4.2 Post-printing analysis of parts

The methodology developed to get from the printed part to the final specimen was decided upon based on machine preferences, default supplier configuration, and mechanical performance in control tests. Limitations in feature sizes were expected but no reliable number had been pro-

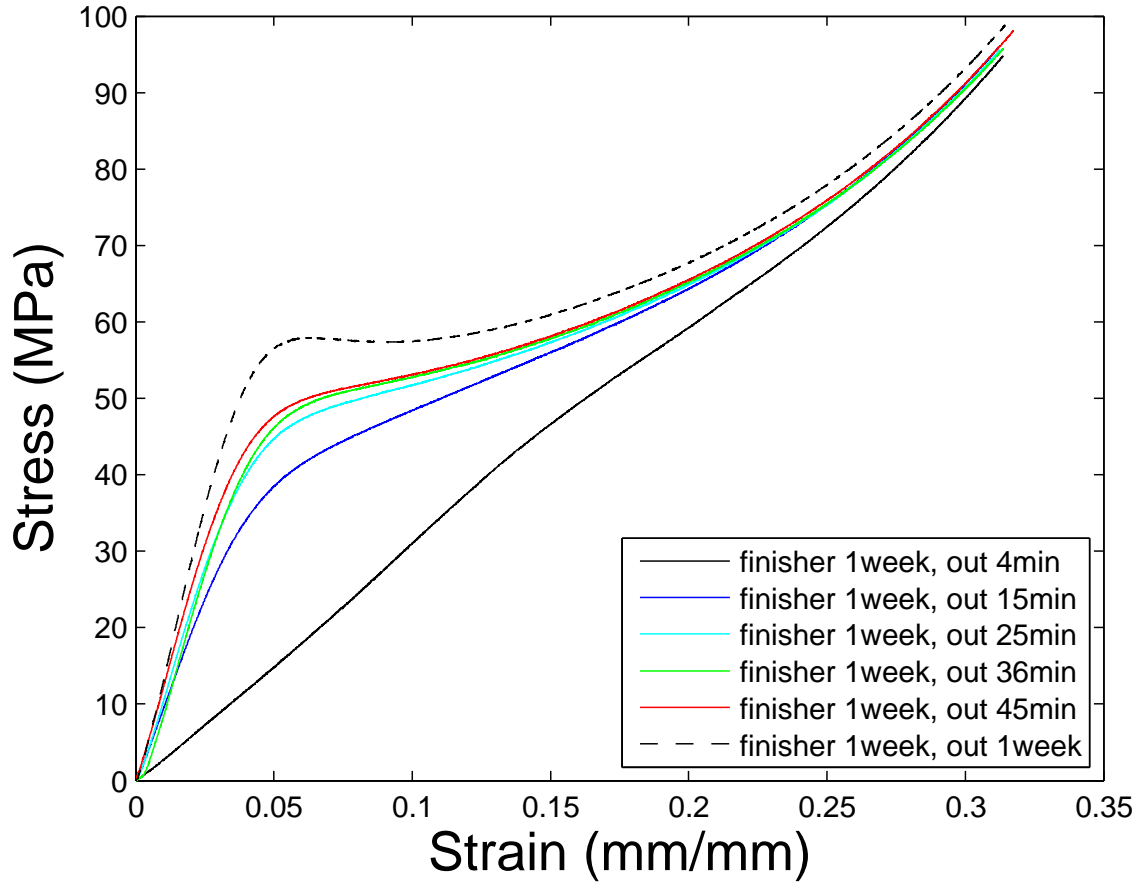


Figure 4.3: Polymer ASTM D695 coupons tested after 1 week sitting inside a 65° C finisher. Samples were tested in varying time after removal ranging from 4 minutes to 1 week. A trend of increasing stiffness and yield strength is seen with increasing time as the polymer material sets and becomes more brittle.

vided which required the fabrication of small-featured structures that would then be analyzed with electron microscopy. Additionally, the surface morphology was observed to differ based on printer orientation and was analyzed using optical profilometry.

4.2.1 Characterization of part surface and printer resolution

After finishing, it was observed that the polymer surface was rougher on some areas of samples than others. Some spots felt extremely smooth, as would be expected from a very high accuracy printer, but others felt coarse, like a grinding pad. This roughness occurred only in areas where wax precursor was placed adjacent to polymer, whether below or to the side. To test this, a 10x10 mm square box with height 5 mm was printed such that the 10x10 mm side was connected to the build plate via the wax support. During the printing process, the base wax layer would be placed first before the polymer was layered on top. This ensured that the top of the box and its sides never came into contact with wax. The wax was removed and their roughnesses were calculated using optical profilometry.

Figures 4.4a and 4.4c show the rough and smooth sides of the box at 5.0x magnification. The roughness was determined using the arithmetic average of absolute means (R_a) and was 2.7 μm for the rough side compared to 1.9 μm for the smooth side. This difference is too small to be noticeable by feel alone. Instead, the roughness that is felt on the sample is more likely the large ridges spaced apart by approximately 0.6 mm. Their maximum height protrudes $\approx 50 \mu\text{m}$ from the flat areas of the sample. These ridges are parallel to the build plate travelling direction and are concluded to be area where spraying liquid polymer overlaps between two ejection jets on the printer head.

Looking closely at Fig. 4.4c, there is residual evidence of the ridges travelling in the same direction as on the rough side but their total height is now within the error of the software itself as its colour blends with that around it. The disappearance of the ridges is due to the sharp flattening knife that travels across the sample after each curing step to leave a flat base for the next layer. After 5 mm of height being deposited (approximately 150 layers), the

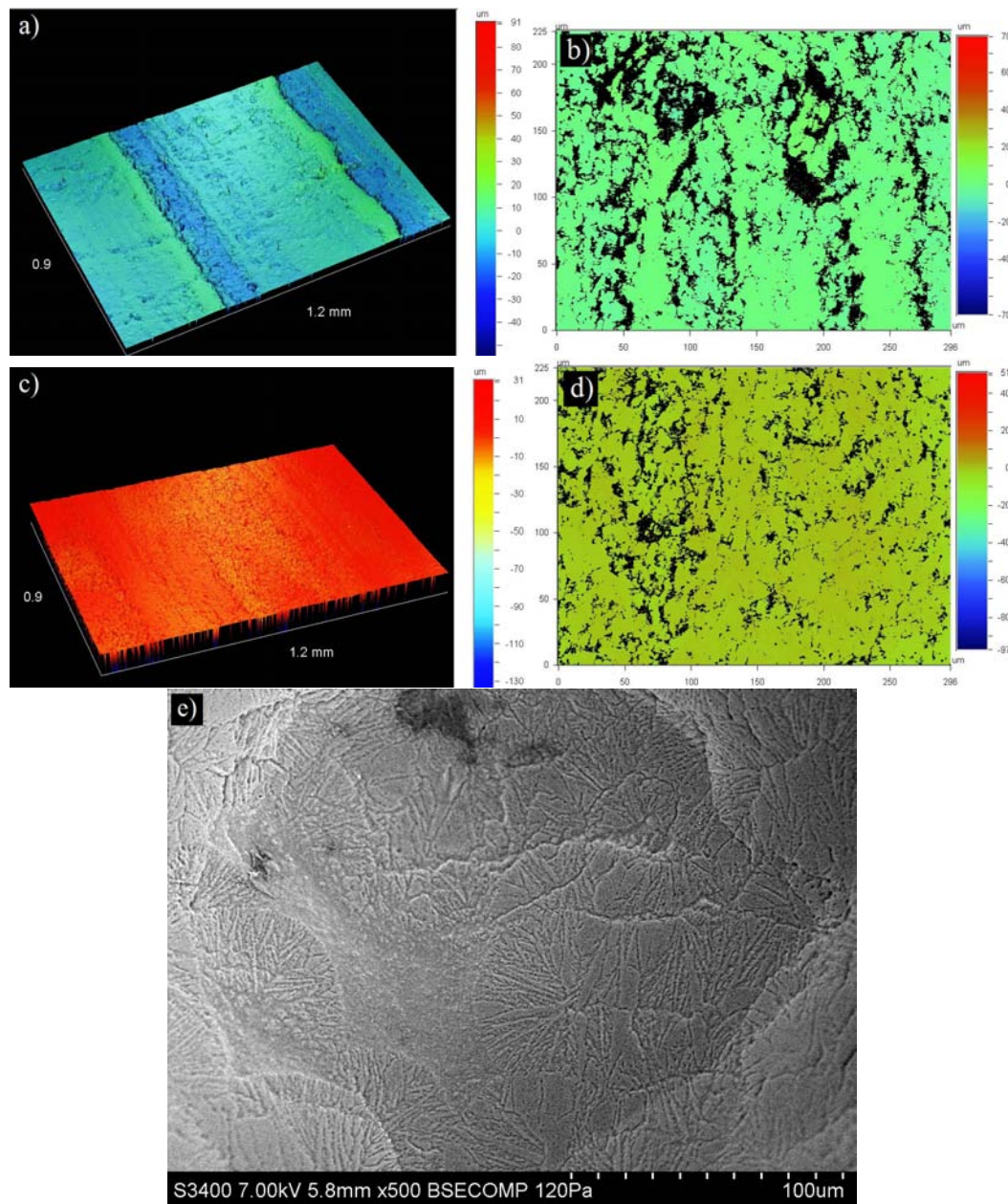


Figure 4.4: Optical profilometry results of the rough underside at 5x (a) and 20x (b) magnification. The contrasting upper smooth side is also shown at 5x (c) and 20x (d) magnification. An SEM micrograph is shown of the flat surface at 500x magnification where the polymer microstructure can be observed (e).

knife has effectively removed the ridge and filled in the plateau areas between the ridges. It is hypothesized that with many more layers, the ridges would all but disappear. On the first pass, however, the wax base beneath the first deposited polymer layer can deflect and the knife is not as effective at creating a uniform surface.

Second scans were completed at a higher magnification (21x) in order to look between the ridges and get a sense of roughness of the flat areas. Again the values were close with the rough side having R_a around $1.2\ \mu\text{m}$ while the smooth side was $0.9\ \mu\text{m}$ (Fig. 4.4b, d). Overall, a slightly porous wax substructure still allows some liquid polymer to settle into the grooves and leaves a rougher surface than seen on the top side after much flattening and layering. An SEM micrograph of this surface was obtained in Fig. 4.4e showing grooves and microstructure across the entirety of the sample. The multiple waves and ridges are the result of crystallization as the liquid polymer cures when exposed to the UV light source and have the same pattern of ditches and grooves as those shown in Fig. 4.4b and d.

To complement the optical profilometry data, SEM micrographs were taken of a microtruss from two directions: on the underside of the structure where the wax/polymer interface is present and on the topside where the polymer was layered freely (Fig. 4.5). In Fig. 4.5, the lowest point of the face sheet strut is mostly flat and this first polymer layer deposited on the hardened wax support has minimal feature roughness. As the structure is built up (moving outwards from the strut), liquid wax is being deposited at the same time as polymer and leaves behind the embedded crystals seen in the micrograph. In contrast, Fig. 4.5 shows a face sheet strut from the opposite side such that no wax was ever in contact with the polymer. The absence of the protrusions supports this conclusion.

The wax/polymer interface can also impact the sides of the box. A rectangular block was printed with circular columns protruding from the top of the box resembling cantilevers. As these cantilevers are hovering above open space, the printer places wax underneath them. This means that polymer and wax are placed adjacent to each other near the cantilever as it builds the two up. Using an SEM, micrographs can magnify this side to observe differences in surface

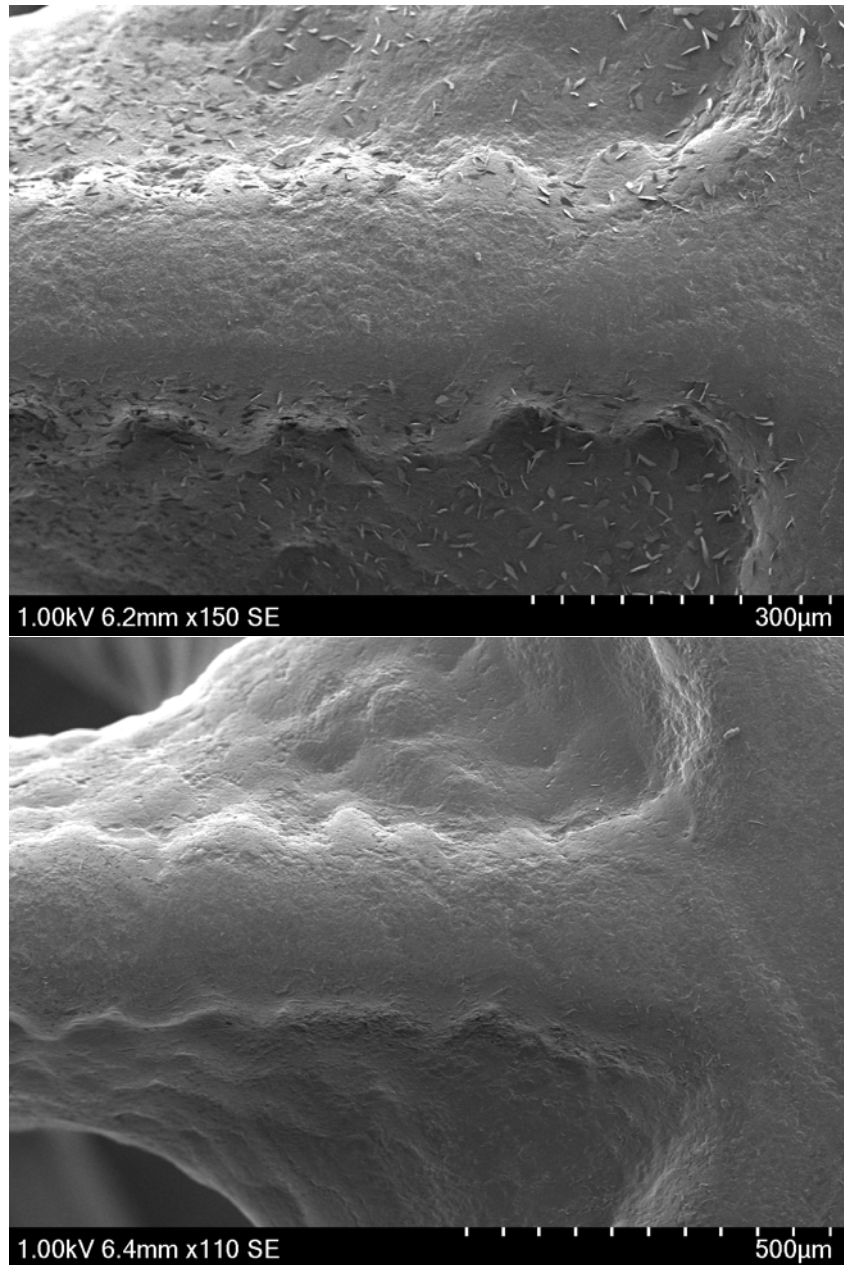


Figure 4.5: SEM micrographs taken of face sheet struts in a microtruss directly adjacent to a node. Small crystal-like features that are presumed to be solidified wax are present on the underside of the structure (top) but not on the top side (bottom).

roughness (Fig. 4.6). When liquid wax and polymer are deposited in a layer, as is the case under the cantilever, they diffuse into each other. After finishing, the polymer is not as stable in these blended regions and melts away with the wax due to a poor bond to the solid polymer layer next to it.

In between the cantilevers, no wax is used but some roughness was still observed. The deposition of a liquid layer on top of a solid one leads to build up along the edges due to surface tension such that upon curing, these edges can bleed outwards and vary from layer to layer. Therefore, even in the most pristine zones, some roughness still exists but is minimal compared to the wax/polymer interfaces. A better view of this layering is seen in the fabrication of microtrusses where the core struts are built up of horizontal circles layered on top of each other plus a small shift to achieve the tilt required (Fig. 4.6).

Ridges along the bottom of a sample, polymer/wax interaction between subsequent layers, and polymer/wax blending within a layer all create varying degrees of roughness. Therefore, a series of surface features are evident during printing that could have large impacts on both the testing of polymer material properties and in the latter electrodeposition stages of hybrid microtruss fabrication. This also has a large effect on the accuracy of printing small features. Having slightly larger or smaller edges can make printing sub-mm parts problematic.

While the accuracy of the printer is quoted as $34\ \mu\text{m}$ [140], the minimal feature size in these directions is not quoted (only the layer thickness of $29\ \mu\text{m}$ is known). Small, hollow columns with varying inner radius and wall thickness were printed on a substrate to allow for comparison across multiple length scales at once (Figure 4.7a). The substrate contained 11 columns, starting with the top right and moving clockwise, labelled as 1 through 11 (Figure 4.7b). The wall thicknesses for the first seven were kept constant at $200\ \mu\text{m}$ while the inner radius increased in $12.5\ \mu\text{m}$ increments from 25 to $100\ \mu\text{m}$. After this, the inner radius was kept constant at $100\ \mu\text{m}$ while the wall thickness decreased by $25\ \mu\text{m}$ from 200 to $100\ \mu\text{m}$.

Pores smaller than $100\ \mu\text{m}$ in radius were not visible across the first seven columns (Figure 4.7b). However, the last two columns, while still having an inner radius of $100\ \mu\text{m}$, sud-

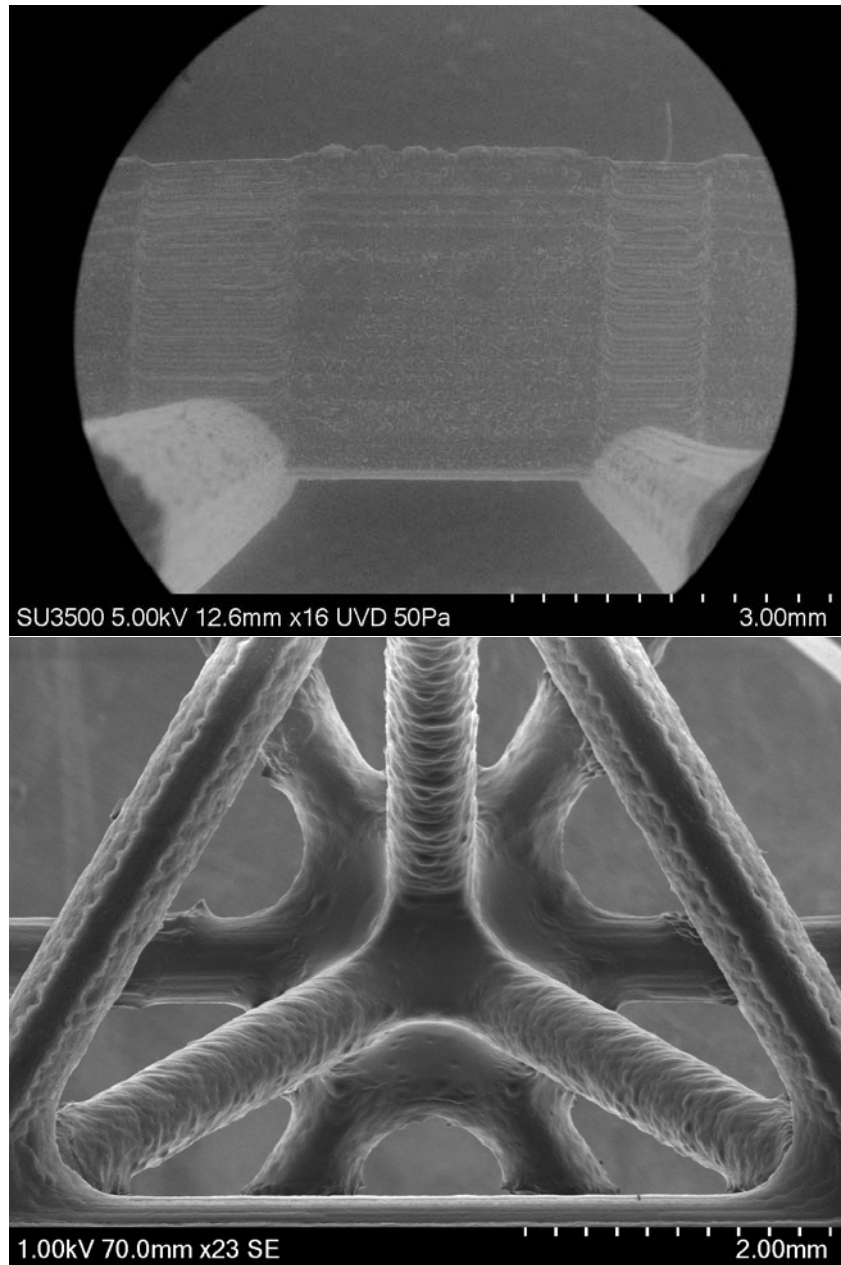


Figure 4.6: SEM micrograph of a smooth polymer face and two rough patches on either side due to wax printing below the columns at the bottom of the image (top). SEM micrograph of a microtruss unit cell where the three core struts were built up in horizontal slices (bottom).

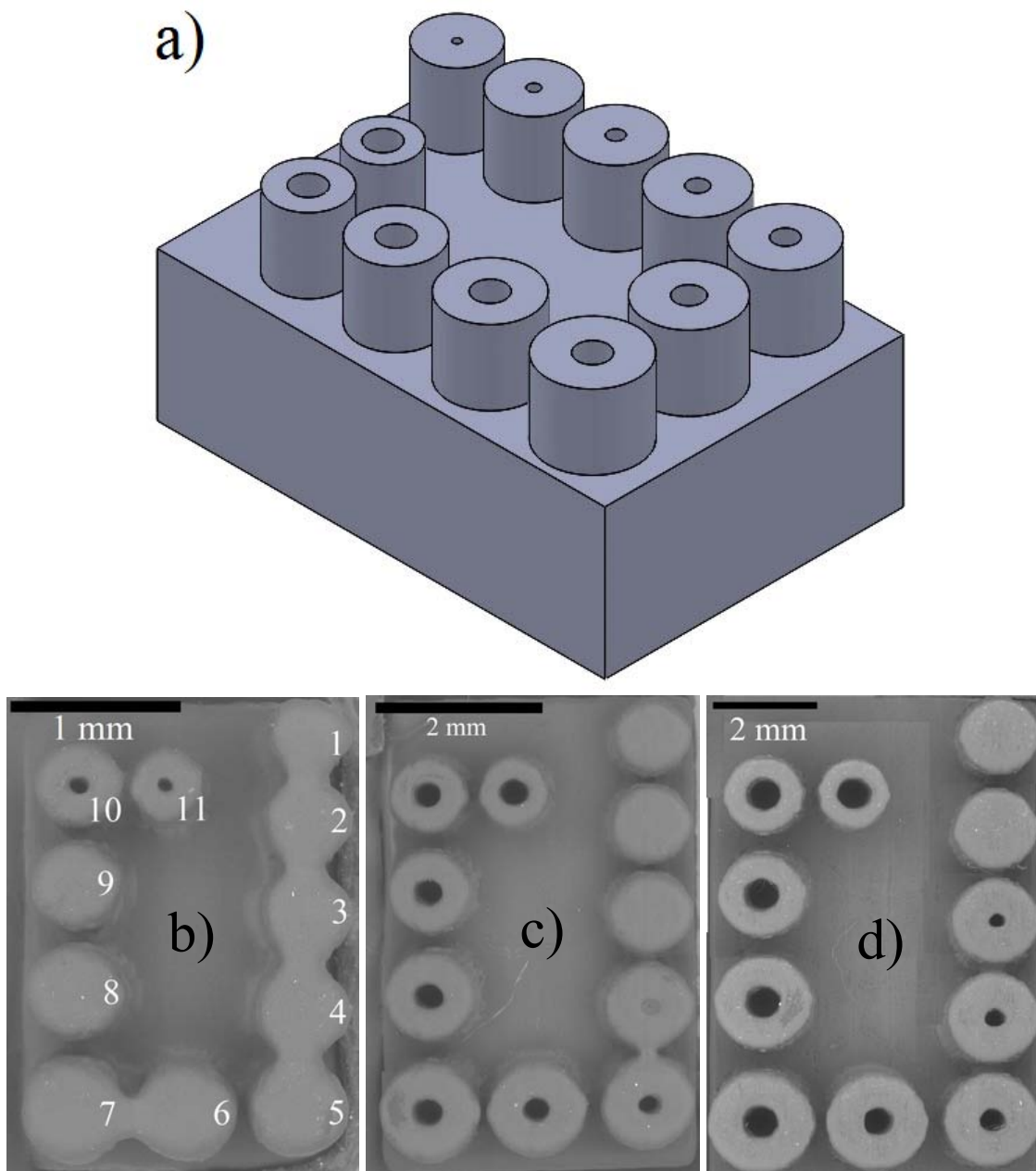


Figure 4.7: (a) SolidWorks inclined view of the 3D CAD model used to create printer resolution tests. (b-d) SEM micrographs of the printer resolution blocks at 1x, 2x and 3x the original size, respectively.

denly had a pore when the wall thickness was 125 and 100 μm . This implies that quantized step sizes are used where, by making something slightly larger, a second drop of polymer is needed causing the hole to fill itself in. Based on the first size, this stepping seems to be $\approx 150 \mu\text{m}$. To confirm this, the block was scaled up two times to create Figure 4.7c. We now see the creation of a ‘mostly’ pore in the 4th position when the wall thickness was to be 400 μm and the pore size was 125 μm . While the printer attempted to leave the space empty, the liquid closed up parts of the pore and left only the remnants of an interior pore. Finally, when we scale to three times (Figure 4.7d) the 112.5 μm hole is not printed while the 150 μm hole is printed. It can be concluded that the minimum feature size (the size of one droplet of polymer when cured) is between 125 and 150 μm . Conservatively, all structures should have pores larger than the latter to ensure they are created. Additional tests where the blocks were scaled even smaller showed that the minimum single feature that could be printed was $\approx 70\mu\text{m}$.

4.2.2 Shrinkage measurements and their effect on a polymer density calculation

For the hybrid system of a polymer microtruss with a metallic coating, the analytical models rely on the material properties of both materials in order to predict locations of optimal design. While the density of the polymer is quoted from the supplier as 1.02 g/cm^3 (Fig. 4.2), rough calculations of mass and volume from SolidWorks and finished rods and trusses implied noticeable deviation from this value. Rectangular prisms with length 50 mm and width and depth of 5 mm were printed in the three main printer orientations - vertical, longitudinal, and transverse - and used to determine the density of the polymer and shape changes during the finishing process. Vertical printing means 5x5 mm squares are printed on top of each other until the 50 mm length dimension is achieved. Transverse and longitudinal printing directions both have 5 mm heights during printing, but transverse prisms are positioned perpendicular to the build tray movement axis and longitudinal are parallel to it (see Fig. 4.8).

A digital caliper with a reading error of ± 0.005 mm was used to record the measurements

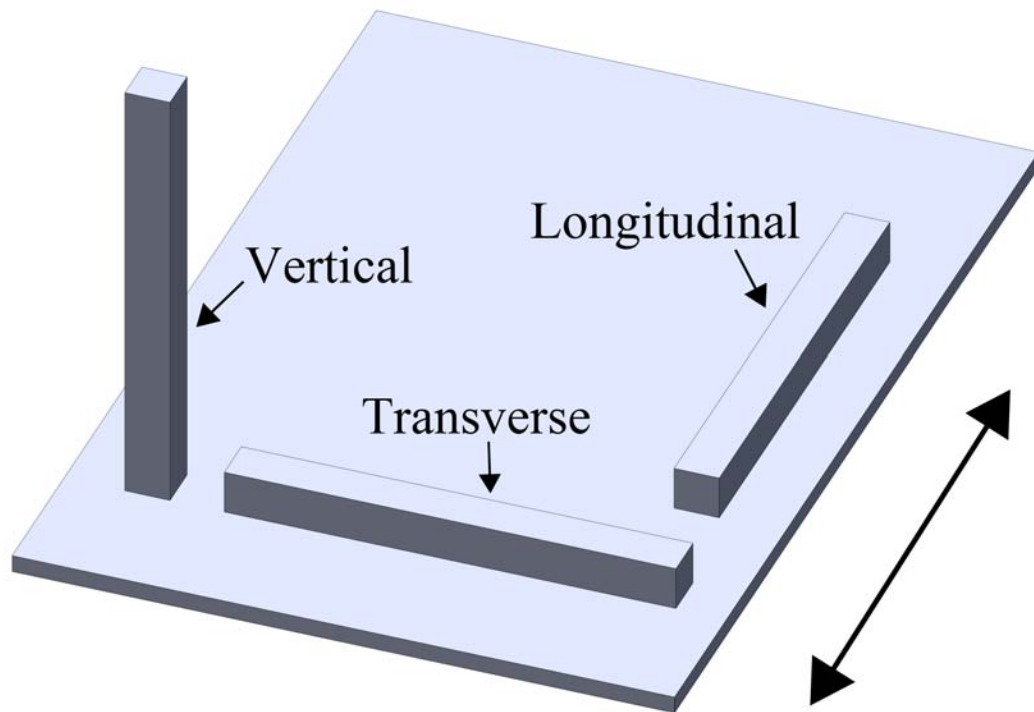


Figure 4.8: A build plate with three rectangular prisms oriented in the three main directions during printing: vertical, transverse (across the plate), and longitudinal (along the length of the plate). The direction of the plate during printing is shown in the bottom-right.

of the rectangular prisms at varying time intervals after they were removed from the finisher. Each of the five samples in each subset of printer orientations was measured three times at each time step to arrive at the recorded value. Depth was always maintained to be the measurement from the surface attached to the build plate up to the highest surface. For the length of the prisms, a 1% reduction in size was observed between removal from the finisher and one week of sitting outside at room temperature (Fig. 4.9). At first a large reduction in size is seen as the samples cooled to room temperature. But after an hour, a slight decrease was still seen that continued up to the week, as seen in the power fit overlaid on each data set. During that time span, the mass of the structure remained constant confirming an increase in density and not a loss of material (Fig. 4.9).

The length showed a significant drop during the first few measurements and its plateau reading was 100 – 400 μm less than requested (Fig. 4.9), which corresponded to a 1% discrepancy at most. Additionally, the trend for prism length showed a distinct difference between vertical samples and the longitudinal or transverse ones. No difference should be expected in the laying down of polymer in the MJM printing process and in all sample types, wax was not needed at any point. The vertical direction only differed in the distance the printer head inside the printer needed to travel as it built up the prism. As the head travels on a set of threaded screws, it is theorized that the requirement to always raise the head by the layer height of 32 μm leads to a compounding of error layer-by-layer as the vertical distance increases. This explains why the samples printed flat showed little-to-no difference in their measurements between orientations.

Using the measured dimensions after one week of resting, the densities of each prism were determined. For the vertical, transverse, and longitudinal orientations, the densities were calculated to be $1.189 \pm 0.004 \text{ g/cm}^3$, $1.187 \pm 0.004 \text{ g/cm}^3$, and $1.189 \pm 0.004 \text{ g/cm}^3$, respectively. All orientations are within calculated error of each other. Therefore, even though a difference may exist in the length of the vertical prism, its larger dimension was the result of additional mass and was, therefore, the same density.

Two points are concluded from this analysis. Firstly, the samples laid flat had wax across

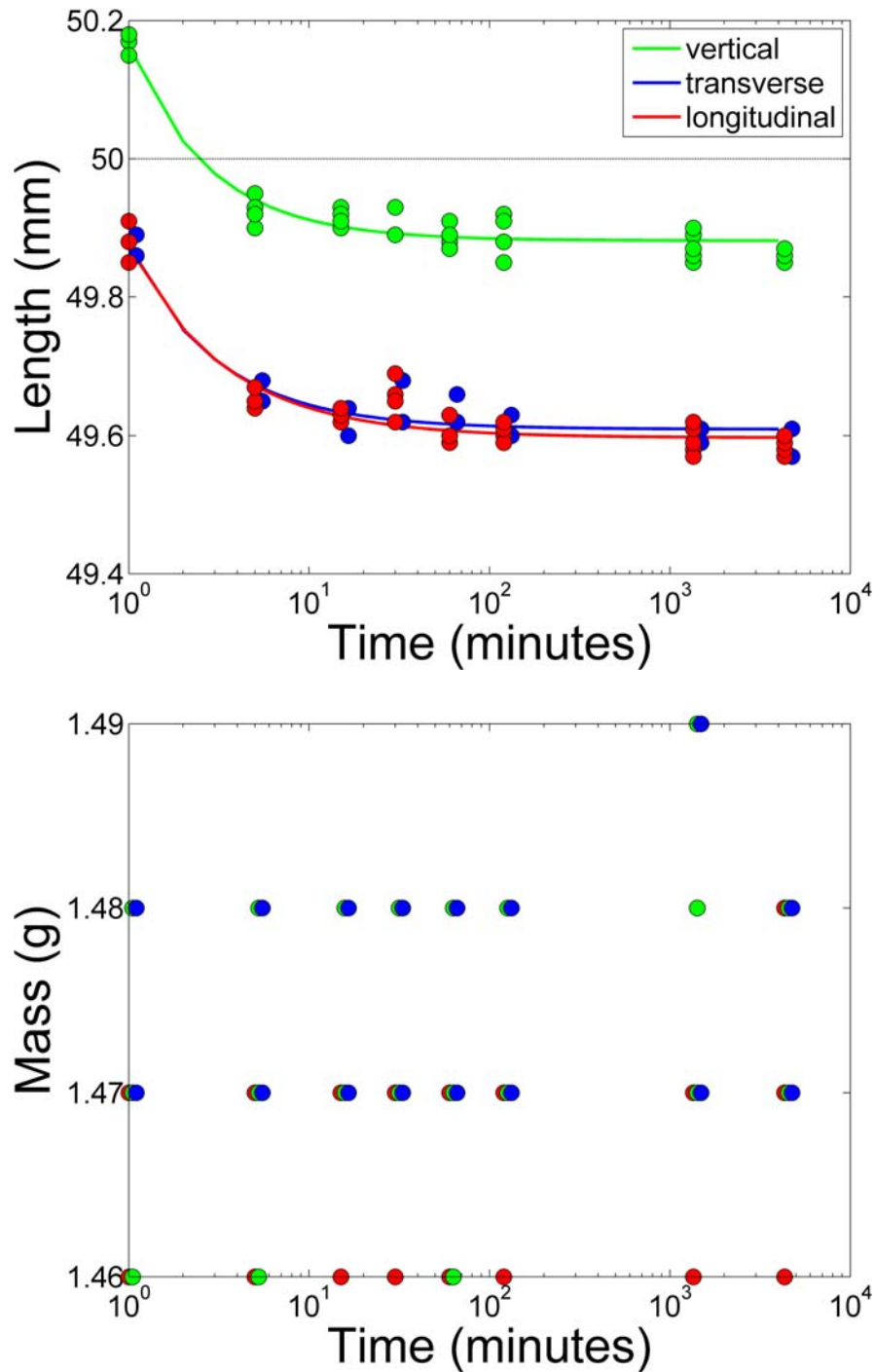


Figure 4.9: 5x5x50 mm polymer rectangular prisms printed in vertical, transverse, and longitudinal directions measured over the course of one week in length showing tendencies for shrinkage on the order of 1% (top). The desired dimension is shown as the dotted line. The same samples had their mass recorded over the same time frame showing no noticeable change (bottom).

the entirety of one of the large faces. While this interface leads to the roughness mentioned previously, the consistent densities imply this roughness is smaller than can be determined with the calipers and should be on the order of 5 – 10 μm . Secondly, the density is 17% larger than that published by the supplier. As the finishing process is identical in both cases based on the videos provided with the installation of the ProJet printer, the difference is due to settings on the printer itself. An option that exists is to calibrate sizes by sending the printer the part at slightly larger or smaller scales to adjust for these discrepancies. Whether or not the printer also makes an adjustment process when this is done is unknown. Regardless, the settings were kept constant throughout this thesis and the measured density of $1.189 \pm 0.004 \text{ g/cm}^3$ was used.

4.3 Material properties extracted from compression, tension, and bending tests

The analytical models describing microtruss beams in bending require Young's modulus, UTS, and yield strength to accurately pinpoint locations of optimal design in the failure mechanism maps. From the information gathered to date, the material properties of the polymer precursor can be significantly altered by the finishing process. Additionally, surface roughness could result in new failure mechanisms. Testing was done in both tension and compression to extract the key material properties for microtruss optimization. Bending tests were performed with polymer blocks to act as a comparative tool for microtruss designs in bending.

4.3.1 Tensile testing of dogbones

An ultimate tensile strength (UTS) and Young's modulus were extracted from dogbone samples made and tested according to ASTM D638, "Standard Test Method for Tensile Properties of Plastic" [141]. ASTM D638 dogbones were scaled down to 25% of the original size as this smaller size is more realistic of the sizes of struts in the microtruss. It is also easier to grip inside the testing apparatus as a smaller and more precise 5 kN load cell Shimadzu universal

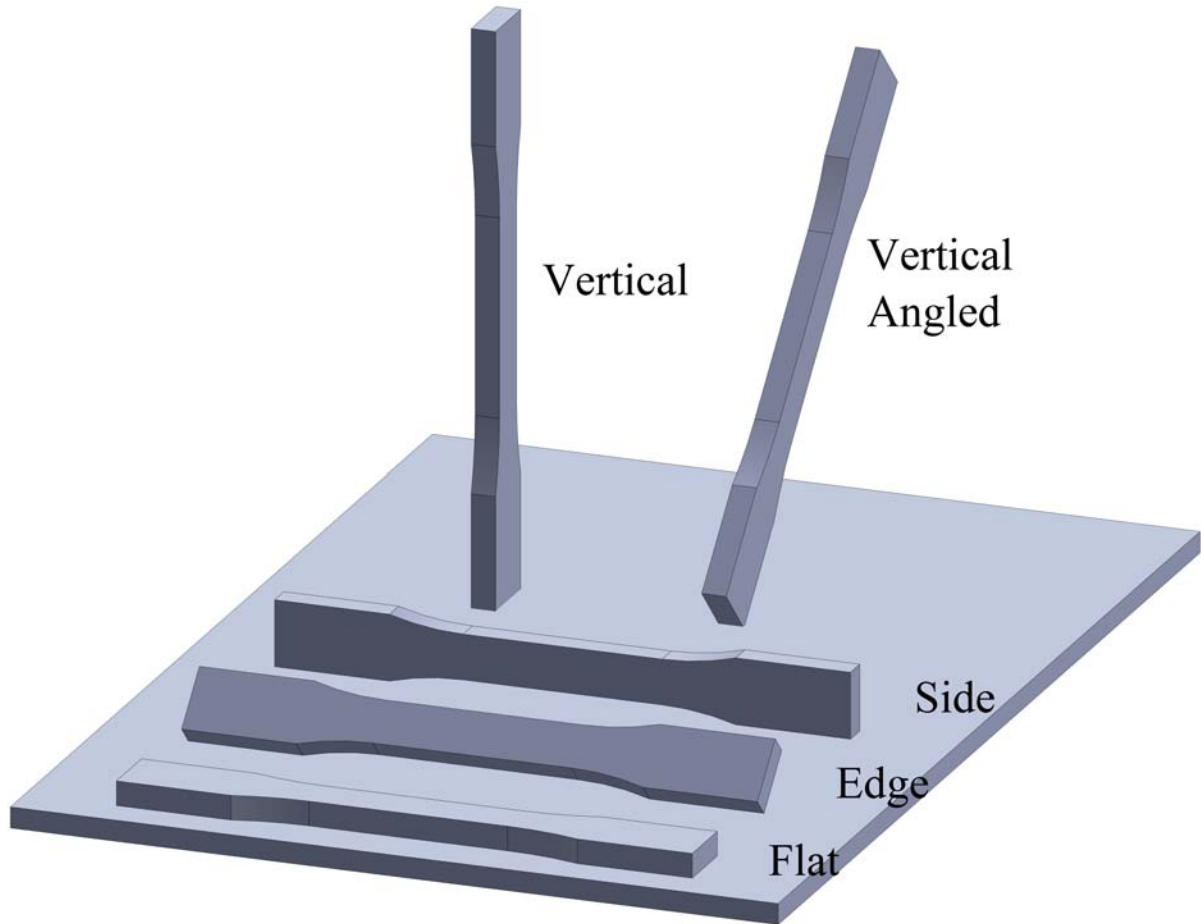


Figure 4.10: The five different printing orientations used correspond to three transversely oriented dogbones laid flat, on edge and on its side along with a vertical sample and one inclined at 45° to the vertical.

testing machine could be used that minimizes slipping during testing.

Because of the layer-up build methodology, it was expected that different orientations in the printer would lead to samples with a range of material properties. Thus, samples were printed in vertical and transverse directions to see the impact of layering in the gauge region (Fig. 4.10). Dogbones were also printed in angled orientations with a vertical specimen being rotated 45° while flat samples were rotated by 45° on their edge and a full 90° onto their side. These changes control where the wax support structure will lay - the edge sample had wax on one face and one edge while the side sample had wax along the thickness direction. It was expected, having observed that the wax/printer interface creates more roughness on the sample

(Fig. 4.6), that wax along the sides would create more areas of stress concentration.

Previous tests on tensile dogbones did show a tendency for fracture to occur before the UTS due to stress concentrations at the meeting point of the gauge and the shoulder in the coupon. As such, samples were sanded on the side to remove this step feature but not in the center as the effect of roughness was also being tested. Appendix A.2 covers the original testing on sanded and unsanded dogbones showing a large increase in measured strength and modulus with this surface preparation.

Samples were additionally prepared for digital image correlation (DIC) analysis. This entailed the application of a matte white base coat on the larger face of the gauge length from shoulder to shoulder. Next, a black speckle pattern was deposited overtop the white. After calibration, two 3D cameras on a tripod photograph the sample during testing at one second intervals. Post-processing of the images create a 3D model of the surface by matching fingerprints of the black speckle pattern across the entire face and tracking them as the sample stretches or compresses in every direction. Upon completion, a collection of stills or a movie is provided that reveals the strain at each point and can identify areas of increased stress to determine the root cause of failure.

The results of the tensile tests are recorded in table 4.1. Here the division between vertically printed samples and those printed flat becomes very distinct. The vertical samples fail in the linking between layers within the sample. Because the degree of cross-linking between layers is not a controllable parameter, some layers are more tightly linked than others, which also causes the spread in peak stress values. The term UTS does not apply for these samples as they have not approached plasticity or necking and instead fracture while their stress is still increasing, characteristic of a brittle material. The elongation at failure was also significantly lower than for the flat dogbones.

Looking at the three variations of dogbones printed flat, the UTS is now higher than the 42.4 MPa expected based on this material (Fig. 4.2). The spread is within 1 MPa on the UTS values showing confidence in a UTS of ≈ 45 MPa. To understand the spread in elongation

<i>Print Orientation</i>	<i>UTS (MPa)</i>	<i>Elongation (%)</i>	<i>Young's Modulus (MPa)</i>
Vertical	36.8 ± 3.7	0.10 ± 0.02	620 ± 20
Vertical Angled	39.3 ± 3.0	0.09 ± 0.01	670 ± 10
Flat	45.0 ± 0.3	0.18 ± 0.07	700 ± 20
Edge	45.0 ± 0.2	0.31 ± 0.01	760 ± 10
Side	46.3 ± 0.5	0.26 ± 0.04	760 ± 30

Table 4.1: Summarized mechanical properties from tensile dogbones printed in various orientations. Value for the UTS, elongation %, and Young's modulus are accompanied with the standard deviation of the population size for each sample type (ten samples in each case).

values, the stress-strain curves for a characteristic sample from each printer orientation set are shown in Fig. 4.11. While both vertical orientations had fracture before necking, the other three all reach their UTS. But the edge and side dogbones were then observed to neck - this was visible as a change in opacity and colour in the dogbone from a half-transparent yellow appearance to opaque and white. This type of necking is identified in polymer literature as crazing - the movement of the polymer chains inside a bulk material such that they line up parallel to the axis of elongation [142]. At the UTS, the cross-linked chains in the polymer begin to move and their freedom between locked sites causes a decrease in stress down to a valley stress once all the chains are as parallel as possible. Increases in stress begin after this low point until the chains themselves rupture, which can occur at levels even above the original UTS. For the sake of consistency, the first peak is what is recorded in table 4.1 as the secondary peak at failure is described as a tensile strength at break in ASTM standards [141, 143].

The increased performance of the side dogbone deserves further discussion. As all three were printed in the transverse direction, on the same plate, and finished the same way, the only difference is the number of layers that make up the gauge volume (visualized in Fig. 4.11). While the flat dogbone only requires 55 layers to form the complete height, the side dogbone needs 407. This large increase means more curing and potentially an increase in strength due to more cross-linking between layers. While the edge sample has the most layers at 444, the layers are at an angle to the gauge volume and could lead to torsional or shear components during uniaxial tensile testing parallel to the layers. Also, some of the layers are extremely

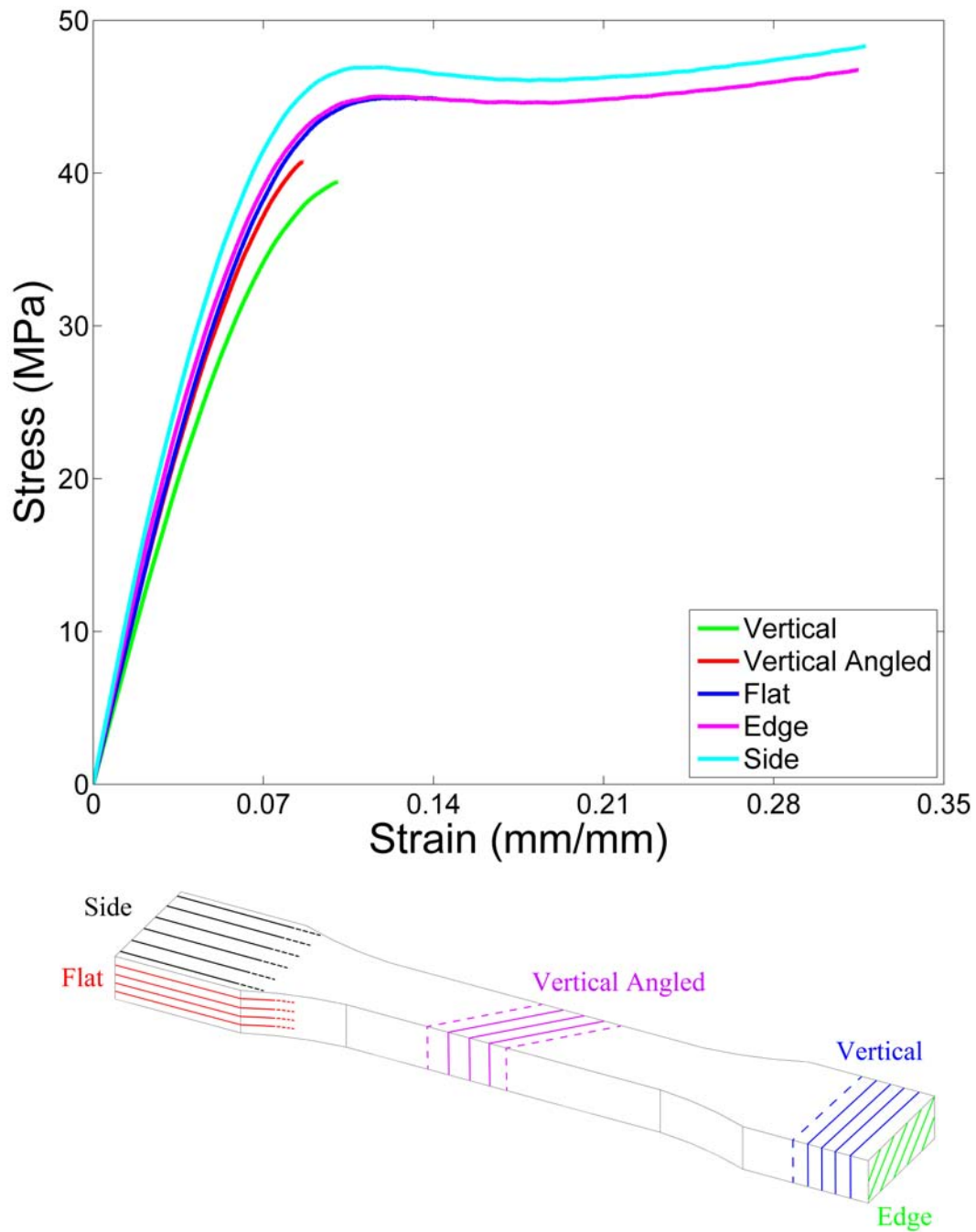


Figure 4.11: Tensile stress-strain curves for the five printing orientations tested on polymer coupons (top). The side, edge, and flat samples all reached UTS while the vertically aligned coupons fractured prematurely due to debonding of layers. The layering within each orientation is shown for the five configurations against a schematic of the tensile dogbone (bottom).

narrow and exist only at the edge (see Fig. 4.11 edge graphic) which would be easy to break and could initiate failure throughout the cross-section.

In terms of the other important material properties, the stiffness of the dogbones should be fairly consistent, at least in the elastic Young's modulus regime but a spread of 140 MPa between the five orientations was observed. The consistency between samples in a set was good as the initial slope is unaffected by premature failure when plastic behaviour begins in the dogbone. When testing in the vertical direction, the pulling apart of layers that led to premature failure means the stiffness in the material is not a characteristic of the polymer chains but on their ability to crosslink. This means measurements for the vertical direction were lower because the polymer itself was not being tested. For the flat samples, the larger values corroborated this idea. Referring back to the Visijet Crystal data sheet [ref], the recorded stiffness is only half of the 1436 MPa being cited by 3D Systems, Inc. However, when measuring Young's modulus, uniaxial compression of a column is preferred, not tensile testing of a dogbone. Therefore, section 4.3.3 will analyze those types of samples to arrive at a more accurate Young's modulus value. The 0.2% offset yield strength is also a value that should be obtained from columns and not dogbones but for the sake of comparison was found to range from $22 - 27 \pm 2$ MPa with the lower end coming from vertically printed samples and the high end from flat dogbones.

4.3.2 Strain rate sensitivity in polymer tensile dogbones

Maintaining the same testing speed in dogbones is trivial as the control of the crosshead displacement rate means the strain rate will be identical. For the compression and bending of microtruss beams, though, these values can differ. The effect of strain rate on material properties is not understood for this polymer. To get a sense of the degree of performance change at varying strain rates, tensile dogbones were used just as in the UTS calculation in section 4.3.1. Strain rates were selected that spanned three orders of magnitude: 0.08, 0.8, and 8 mm/mm-min. These can also be expressed as 1.3×10^{-3} , 1.3×10^{-2} , and $1.3 \times 10^{-1} \text{ s}^{-1}$, respectively.

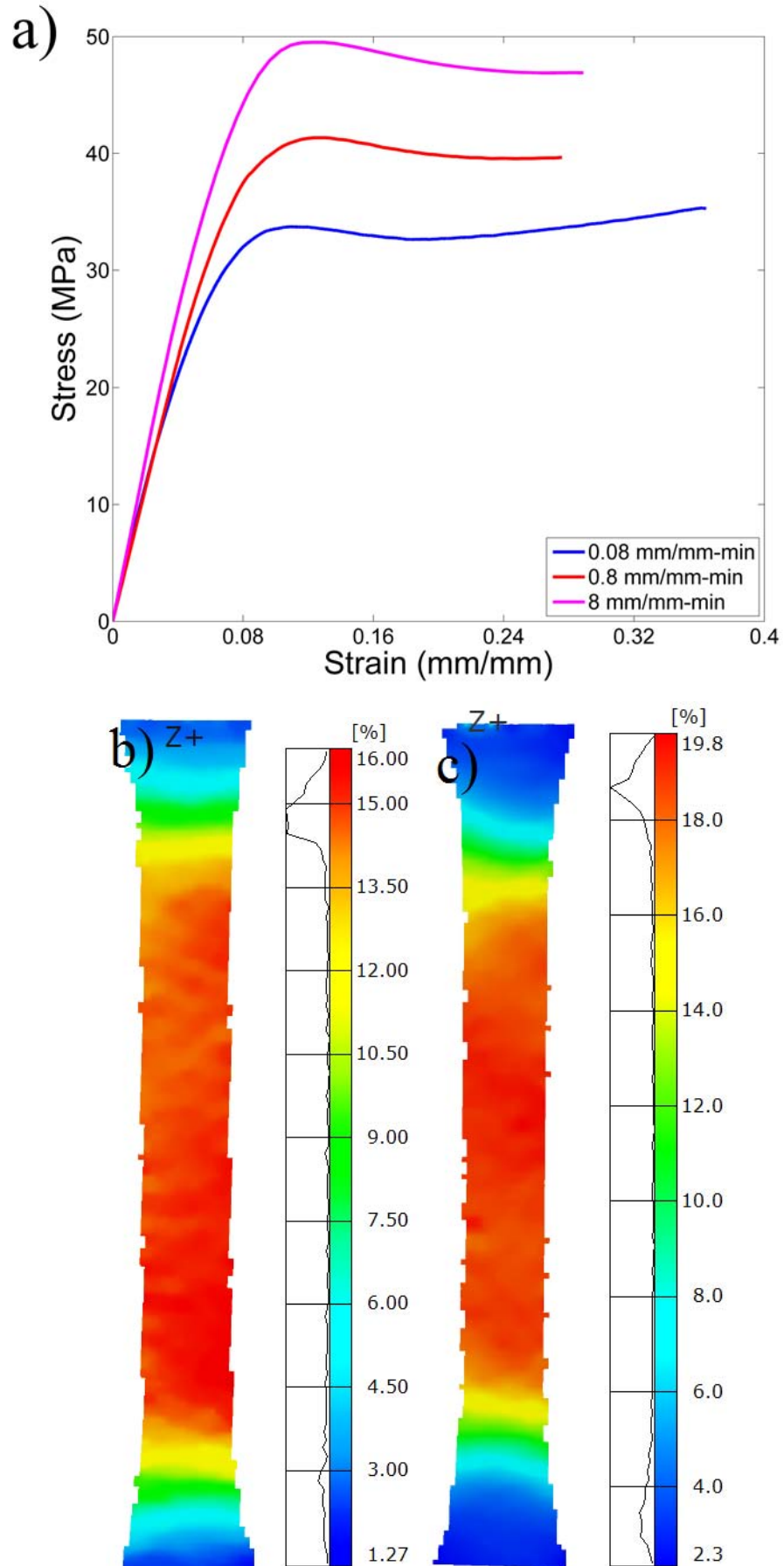


Figure 4.12: Tensile stress-strain curves of printed polymer coupons at strains rates of 0.08, 0.8, and 8 mm/mm-min (a). DIC strain maps for the 8 mm/mm-min (b) and 0.08 mm/mm-min

While the initial modulus was common between the three strain rates, the UTS values ranged increased from 31.8 ± 0.8 MPa to 41 ± 1 MPa to 49 ± 1 MPa as the strain rate increased (Fig. 4.12a). While having a dependence on strain rate is not novel, the performance increase should begin to plateau. Instead, the gap between successive orders of magnitude seems to be constant. Testing at slower speeds would be possible but going faster is not feasible on the universal testing machines available as a speed of 80 mm/mm-min corresponds to a 1 m/min crosshead displacement and could easily result in missing the failure point and causing machine damage. Between the samples, failure is consistent as observed by the DIC analysis on the 0.08 mm/mm-min and 8 mm/mm-min (fig.4.12b-c) and breaks in the middle of the gauge each time. Unless otherwise stated in this study, a strain rate of 0.08 mm/mm-min was kept constant for all geometries and architectures.

4.3.3 Tensile vs compressive stiffness comparison

In the analytical models for a microtruss beam in bending, the struts in the face sheet control most of the tension and compression stresses, especially at mid-span. Failure mechanisms were derived that predicted the applied load required to initiate failure after the UTS has been reached on the tensile side and when buckling would occur on the compressive side. By inputting a stress-strain curve of the polymer or its material properties alone, it is assumed that the tensile strength and compressive strength are relatively similar. However, the timed data on the compression columns shows a very different response than the dogbone samples, even in the initial elastic zone (Appendix A.1).

The calculated Young's modulus in tension from table 4.1 was ≈ 700 MPa while the compression coupons that had been left to stabilize for a week showed an average Young's modulus of 2000 ± 100 MPa. This large difference is further unclear based on a value of 1436 MPa from the supplier (fig.4.2), which lies in the middle of these two. A 0.2% offset yield strength was also calculated to be 42 ± 2 MPa. This value matched that for columns printed in different orientations within 1 MPa, a tighter bound than that seen in tensile dogbones but much higher.

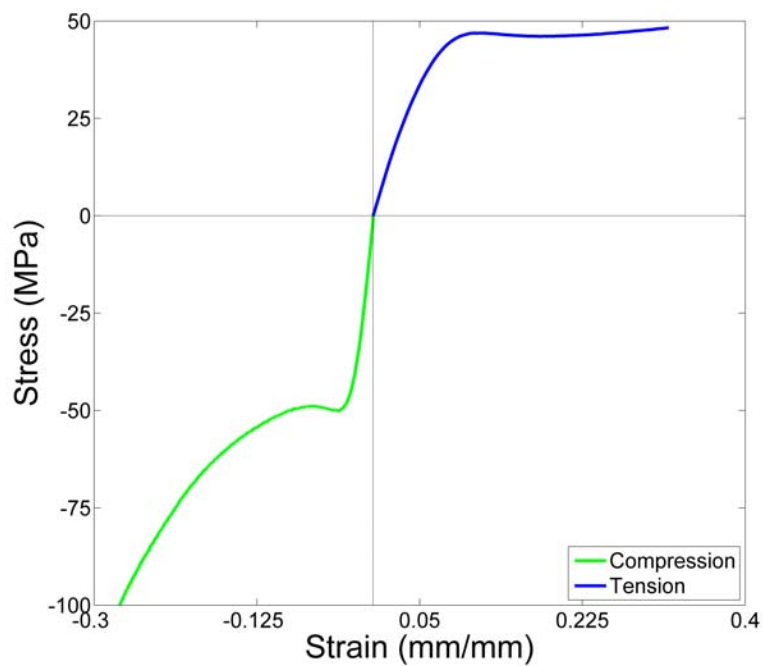


Figure 4.13: Plotting the compressive stress-strain curve from a timed polymer coupon with the tensile stress-strain curve of a dogbone. In both cases, the corresponding ASTM standard was followed but gave vastly different elastic moduli.

Oddly enough, this value is also very close to the UTS for the dogbones. Because compression coupons are preferred for yield strength and modulus calculations, these values will be incorporated into the microtruss model (i.e. one stress-strain curve for the compressive underside of the microtruss beams and one stress-strain curve for the tensile side).

4.3.4 Flexural bending of polymer blocks

For the final key material property, a different type of testing setup is required. Because microtrusses will be tested in three-point bending in subsequent chapters, it was necessary to obtain the flexural strength, flexural modulus, and overall bending behaviour of the polymer on its own to serve as a baseline. The source material for Visijet Crystal quoted a flexural strength of 49 MPa (fig.4.2) based on ASTM D790 titled “Standard Test Methods for Flexural Properties of Unreinforced and Reinforced Plastics and Electrical Insulating Materials” [143]. Without a definite recommended sample size, the conditions of overhang length, maximum width, and maximum depth were followed. Therefore, rectangular blocks were fabricated with dimensions 136.6 x 37.3 x 9.1 mm and were tested in three-point bending with a support span length of 100 mm. While these seem at first glance to be arbitrary values, they were selected to bound the size of a square pyramidal microtruss and act as a comparative tool for weight-specific performance.

In order to obtain the flexural properties of the polymer, the load-deflection curve obtained during testing has to be converted to a flexural stress-strain curve. The calculation of flexural stress, strain, and modulus in a beam undergoing three-point bending can be derived in a similar manner as those presented in section 3.1.2 where the force in a face strut was determined. The flexural stress is:

$$\sigma_f = \frac{My}{I} = \frac{FL}{4} \frac{d}{2} \frac{12}{bd^3} = \frac{3FL}{2bd^2}. \quad (4.1)$$

The flexural strain requires the use of the deflection formula,

$$D = \frac{FL^3}{48EI} \quad (4.2)$$

which rearranges to

$$EI = \frac{FL^3}{48D}. \quad (4.3)$$

This can then be substituted and the flexural strain arrived at using:

$$\epsilon_f = \frac{y}{r} = \frac{yM}{EI} = \frac{d}{2} \frac{FL}{4} \frac{48D}{FL^3} = \frac{6Dd}{L^2}. \quad (4.4)$$

Finally, the flexural modulus is a ratio of the flexural stress and strain giving:

$$E_f = \frac{\sigma_f}{\epsilon_f} = \frac{3FL}{2bd^2} \frac{L^2}{6Dd} = \frac{L^3m}{4bd^3}. \quad (4.5)$$

In these equations, the key terms are F , the load at each point, L , the span length, b , the beam width, d , the beam depth or thickness, D , the deflection at each point, and m , the initial slope in the load-deflection curve. In the flexural modulus derivation, the calculation of m is done in the elastic region such that the ratio of F and D gives m . The stress that is being calculated here is the maximum tensile and compressive stress on either side of the mid-span of the beam where the stress is the largest. In all three derivations, the second moment of area for a rectangular cross-section is used.

As with the tensile dogbones, the rectangular blocks were printed in different orientations to probe the effect of the printer on mechanical properties. Five samples were printed vertically, on their side, and flat. For all three scenarios, the block was oriented transversely in the long direction (see Fig. 4.14). Figure 4.14 shows the flexural stress-strain curves for all three blocks and reinforces the conclusions reached from the tensile dogbone analysis, namely that vertical samples failed prematurely while side-printed samples were slightly stronger and more ductile than flat samples due to a longer cure time in the printer. The flexural strength is defined as

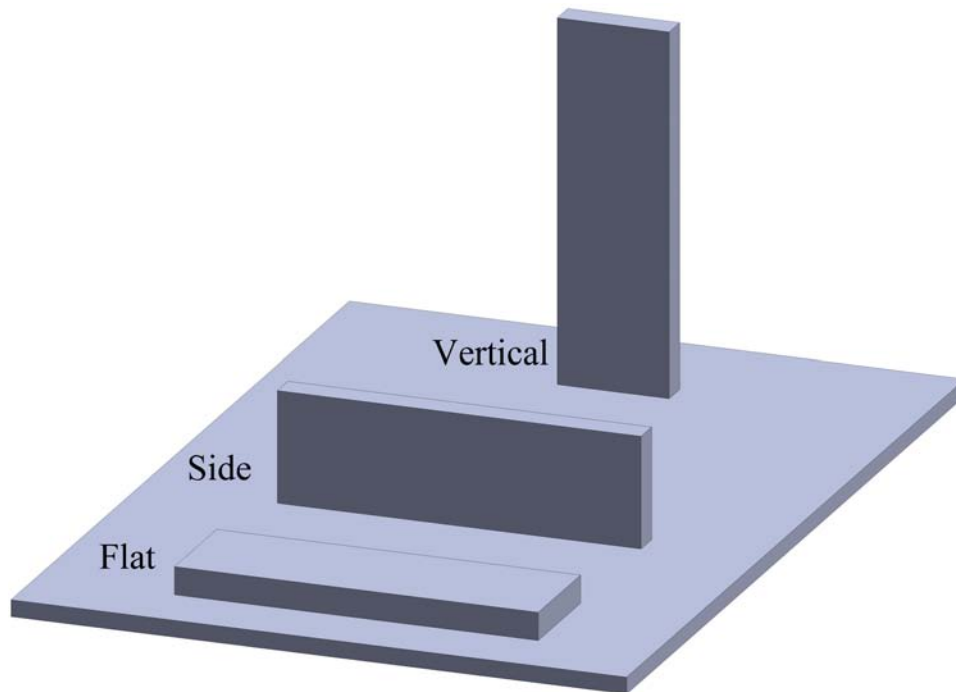
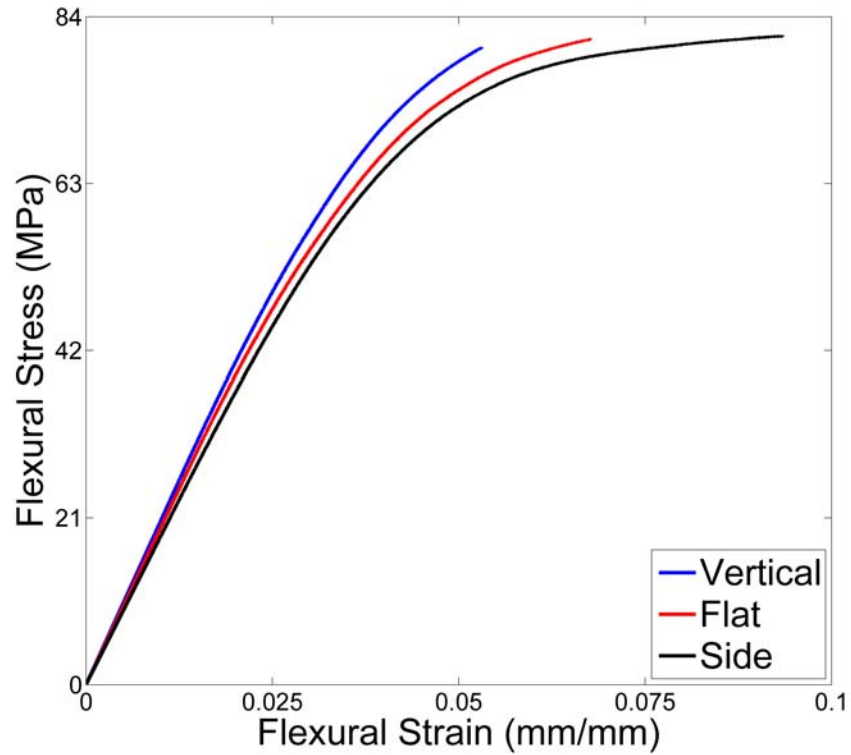


Figure 4.14: Flexural stress-strain curves for the polymer blocks tested in the three different printer orientations (top). The conclusion from the tensile dogbones of vertically aligned samples being weaker holds here as well. The three orientations are vertical, flat, and side (bottom).

the maximum flexural stress during a bending test [143] and increases from 80.1 MPa in the vertical sample to 81.2 and 81.6 MPa in the flat and side blocks. While the trend is expected, the values are much higher than that reported by 3D Systems, Inc. With the conversion to stress and strain removing geometric effects and the ASTM standard followed, one possibility is the reporting of an offset flexural strength [143] by 3D Systems which would compare well to the curves shown here.

In the case of the vertical sample, it broke cleanly into two pieces before reaching a peak value of stress. For the flat and side blocks, the printing layers were parallel to the bending supports meaning failure had to occur through the layers. Upon fracture, the single point of failure deviated outwards and left two larger pieces on the sides as well as multiple wedge pieces that made up the failure region (Fig. 4.15a). The wedge shape of the smaller central pieces resembled the tensile dogbone wedges that came off after fracture. Looking at the DIC analysis for the side-printed block (Fig. 4.15b), a typical tensile stress is seen at the bottom at mid-span of the beam while the top had a compressive stress. Along the middle runs the neutral bending axis where little to no stress is recorded. Figure 4.15c shows the depth of the blocks printed on their side and vertically after they have been reassembled following fracture. A highlighted zone of crazing is seen on the tensile side (bottom) of both blocks with that for the side block being larger, relating to the higher strain achieved before fracture.

4.4 Summary of key conclusions

The as-printed Visijet Crystal material was extensively analyzed and characterized in this chapter. Roughness on different sides of polymer blocks was revealed to be a by-product of the jetting process based on 0.6 mm ridges seen in optical profilometry results. Electron microscopy identified wax/polymer interface effects that added further roughness onto the parts as seen in crystals on the finished part. A minimum feature size of 125 μm was reported with accuracy down to 10 μm . The cooling of the part after finishing was also observed to shrink the sample

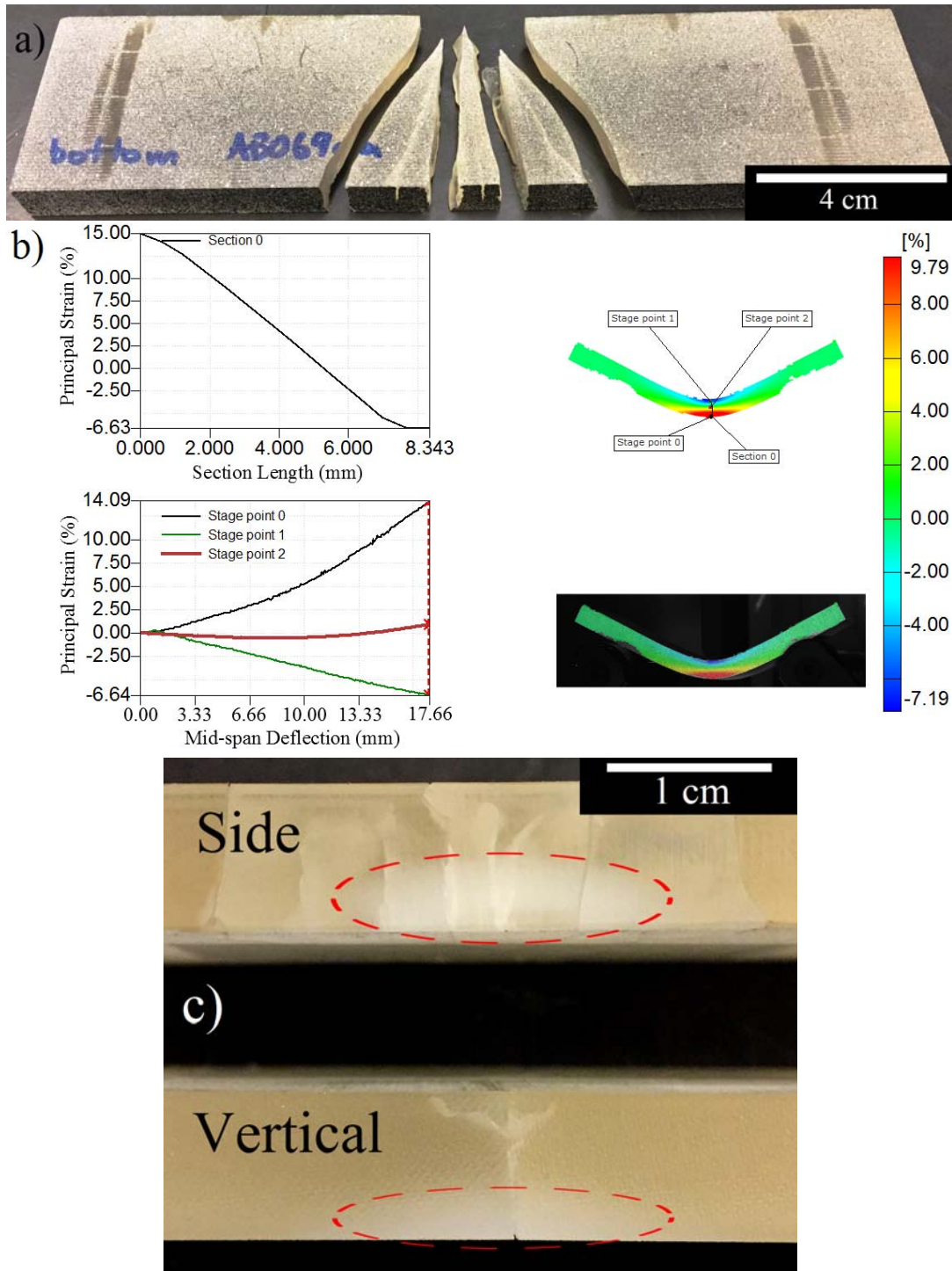


Figure 4.15: A flat printed block of Visijet Crystal material reconstructed after failure showing multiple wedges that broke off of at mid-span (a). The origin of the crack likely began on the top side of the sample in the image and spread outwards, creating the wedges. DIC strain maps show the large deflection that the flat sample was able to incur before fracture with strains up to 15% on the underside (b). Reconstruction of a side and vertical block after fracture are shown side-by-side where the larger deflection before failure is also confirmed with the larger crazing zone in the side printed block (c).

by as much as 1%.

Material properties vital to the predictions made in subsequent chapters were measured and compared to quoted supplier values. The orientation of the print as well as the mode the printer was set at had the largest impact with samples being laid flat and printed in UHD mode having the best performance. For example, the UTS for a vertically printed sample was 37 MPa compared to 45 MPa for one printed flat. Other important properties were a density of $1.189 \pm 0.004 \text{ g/cm}^3$, a 0.2% offset yield strength of $42 \pm 2 \text{ MPa}$, a flexural strength of $51 \pm 2 \text{ MPa}$, and a flexural modulus of $1700 \pm 100 \text{ MPa}$. Crazeing was seen in dogbones during the onset of necking and brittle fracture of this material was identified by wedge-shaped pieces that broke off upon failure in tension and bending. Finally, a Young's modulus of 700 MPa was calculated in tension but in compression jumped to 2000 MPa.

Chapter 5

Experimental validation of analytical model

Chapter 3 presented the development of an analytical model for the behaviour of microtruss beams in three-point bending based on uniaxial compression of simply supported columns. Using the material properties of rapid prototyped polymer, shown in Chapter 4, predictions for the failure strength of as-printed polymer microtrusses can be carried out. The failure mechanism maps will be demonstrated and compared against the experimental testing of these structures.

5.1 Validation of model for uniaxially compressed polymer tubes

Before moving to the more complicated hybrid system, some initial steps were taken to validate the model. The original derivation of failure in a column was compared to uniaxial compression tests of hollow polymer tubes before moving to microtrusses. Because the model assumes nothing of the material, any constitutive relationship (i.e. a polymer) can be used in its place. This would find locations of optimal design based on the material properties extracted from the

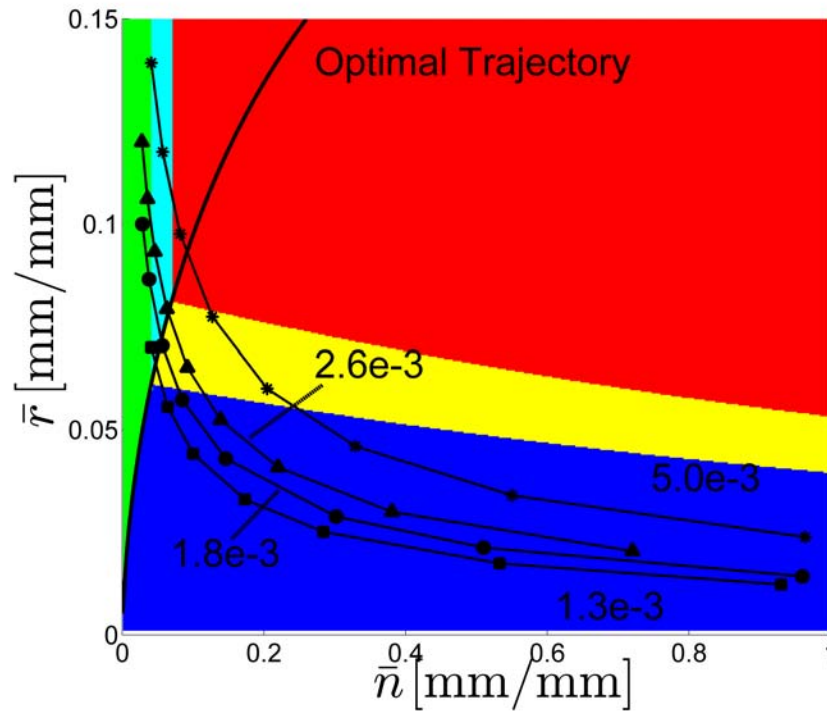


Figure 5.1: Failure mechanism map for a polymer column in uniaxially compression. Zones of elastic buckling (blue), inelastic buckling (yellow), elastic local shell buckling (cyan), inelastic local shell buckling (green) and yield (red) are shown with the optimal trajectory in black overlaid. \hat{M} contours of the designs fabricated are also displayed.

polymer curve. The only modification is purely cosmetic as the wall thickness of the tube is treated now as the coating thickness in the model with the inner radius being equivalent to the original strut radius variable.

Substituting the compressive properties of the polymer, the predicted behaviour across all of (\bar{n}, \bar{r}) space is shown in figure 5.1. The tensile polymer data is ignored because the entirety of the tube before bifurcation will be in a state of compression. The optimal trajectory, shown in black, travels along the boundary between global buckling and local shell buckling before terminating at the start of the critical stress zone. Once inside the critical zone, all designs have equal ratios of mass to strength.

Figure 5.1 has been flattened into just the x-y plane to allow for visualization of the optimal trajectory and desired architectures being built; however, it also continues into the z-direction

where at each point, the predicted failure load is calculated. Four contours of constant mass (constant \hat{M}) were selected that would cross large parts of the surface and fall on both sides of the optimal. Then, comparing the peak loads along one contour, the one holding the most load before failure would be considered optimal and can be compared to the predictions. The design space here is non-dimensional so a value for the length of the column needs to be set such that for the four mass contours, no features are too small to print, after section 4.2.1. The end result is the choice of a 70 mm tall column ensuring wall thicknesses remain greater than 150 μm .

After printing and finishing all the columns, compressing them, and measuring their peak loads, the results are plotted in Fig. 5.2. The experimental data points for each \hat{M} contour follow the general trend of approaching a maximum value at the optimal trajectory before decreasing in load carrying capacity at higher \bar{n} . The predicted \hat{P} for each point is also shown as the lines on the figure. While good agreement is seen in locating the optimal design and predicting the local shell buckling critical load, the entirety of the inelastic global buckling zone underpredicts the peak load. An underprediction implies our material is stronger than the compressive stress-strain curve input into the model. This is because of the geometry of the sample itself.

The tubes designed here have thin walls that, while UV curing, can be exposed from both the inside and outside leading to more cross-linking and increased strength. Moreover, these 70 mm tall columns were printed vertically; printing times for the samples exceeded 24 hours. The continuous UV exposure through the entire sample volume further impacts this hardening factor. The stocky compression coupon, in comparison, is expected to have significantly less cross-linking in the middle of the sample as it is shielded by each subsequent layer of polymer. Since the analytical model used a compressive stress-strain curve, it is not surprisingly to see this difference. It is hypothesized that the exterior face of this ASTM compression coupon would be more heavily cross-linked than the core but this was not tested during this thesis due to the quick shift to microtruss fabrication.

Moreover, the local shell buckling prediction for the two lightest contours is also slightly underpredicted but here the wall thicknesses requested were on the order of 150-200 μm . A small over print, which is expected at this scale after the analysis of minimum pore size previously, will have a large impact on its peak load. This over print could also impact the tubes in the inelastic global buckling zone and compound the extra curing effect to push the tube strength even higher than that predicted.

Interestingly, the points in the critical stress zone, which should all be optimal for a given mass contour, do not all hold the same load ($\hat{M} = 5.0e^{-3}$) and instead a small peak is observed. Instead, the extrapolation of the global buckling/local shell buckling boundary through this zone serves as the true optimal. This can be attributed to how the critical stress zone is defined - as a intercept in the buckling equation within 95% of the critical stress. While it works as a first approximation, the structure after yielding will still be able to buckle either locally or globally as the true peak compressive strength is not reached.

While not a perfect model for the hollow polymer tubes, the ability to locate and predict the optimal design for each \hat{M} contour is promising for the next steps where more complicated microtruss architectures will be analyzed. Additionally, good agreement for local shell buckling will be especially important in the hybrid microtrusses in future chapters where the metal coating is expected to carry all the load and fail first.

5.2 Validation of model for solid, polymer microtrusses in bending

A variety of microtrusses were printed with slenderness ratios and scales as is seen in table 5.1. As an exemplary case, the microtruss with scale $s = 8$ and slenderness $\lambda = 20$, which is the stockiest microtruss at the largest scale, is described in detail. During three-point bending, the force-displacement relation was linear until a mid-span deflection of ≈ 5 mm, or 4.4% of the beam length between the supports (see figure 5.3 for a typical result). Subsequent deflection

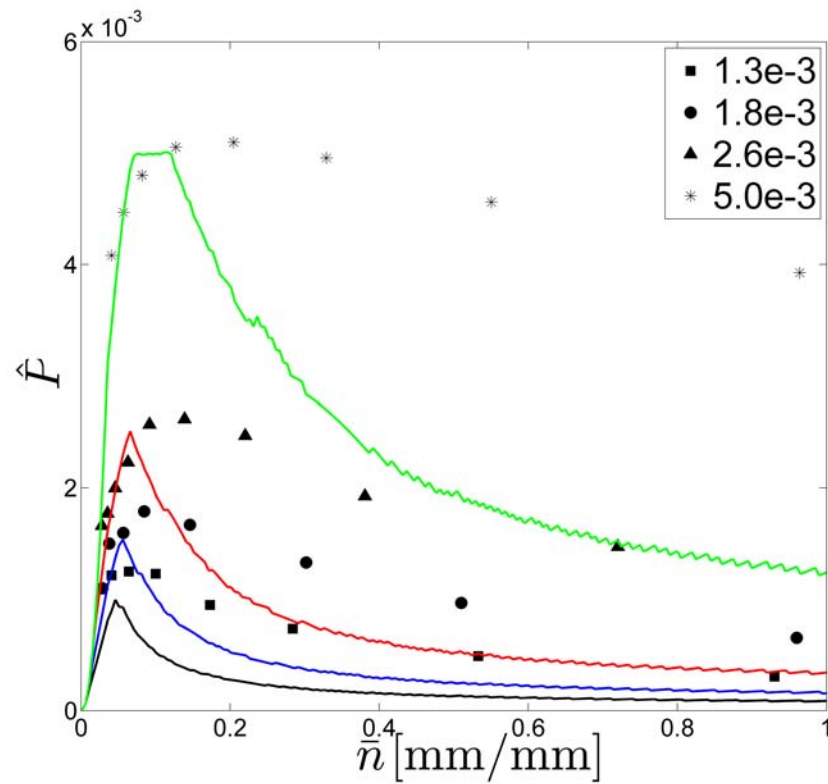


Figure 5.2: Failure mechanism map overlaid with the experimental data from compression testing polymer columns. The points across all 4 contours lie on the surface and show good correlation to the expected failure mode.

λ	s	L (mm)	u (mm)	r_r (μm)	r_e (μm)	Mechanism Predicted	P_c (N)	P_{SE} (N)	Mechanism Observed	P_m (N)
20	1	14.1	1.56	156	160	Maximum Stress	4.37	4.14	Node-by-Node	4.3 ± 0.2
	2	28.1	3.12	312	320		17.6	15.3	Fracture	15.9 ± 0.3
	4	56.2	6.25	625	630		70.3	54.1	Complete	55.5 ± 0.7
	8	112.5	12.50	1250	1250		281.4	180.0	Fracture	211.3 ± 4.0
25	1	14.1	1.56	125	120	Maximum Stress	2.81	2.65	Node-by-Node	2.2 ± 0.2
	2	28.1	3.12	250	240		11.3	9.81	Fracture	9.6 ± 0.5
	4	56.2	6.25	500	500		45.0	34.6	Complete	36.0 ± 0.8
	8	112.5	12.50	1000	1000		180.1	115.1	Fracture	116.5 ± 0.5
33	1	14.1	1.56	94	90	Maximum Stress	1.58	-	Face Sheet Buckling	1.0 ± 0.1
	2	28.1	3.12	188	190		6.33			5.5 ± 0.3
	4	56.2	6.25	375	370		25.3			17.3 ± 1.6
	8	112.5	12.50	750	760		101.3			60.3 ± 0.4
43	2	28.1	3.12	144	140	Buckling	2.42	-	Face Sheet Buckling	2.5 ± 0.1
	4	56.2	6.25	288	280		9.71			8.2 ± 0.4
	8	112.5	12.50	575	570		38.9			33.7 ± 0.5
57	4	56.2	6.25	219	210	Buckling	3.25	-	Face Sheet Buckling	2.2 ± 0.1
	8	112.5	12.50	438	440		13.0			7.5 ± 0.2

Table 5.1: Summary of geometries tested in three-point bending as well as predicted and measured peak loads and failure types for each specimen type where P_c , P_{SE} , and P_m represent the predicted critical load, the predicted critical load with size effects accounted for and the experimentally measured peak load, respectively. Values for the requested radius, r_r , and experimentally measured radius, r_e , are included where the measured radius after printing is measured to $\pm 10\mu\text{m}$.

was non-linear, due to material and geometric effects. Failure occurred at a mid-span deflection of ≈ 8 mm (7.1% of the supported length) at a peak force of 209.9 ± 3.8 N, averaged amongst five identical specimens. Failure occurred by fracture along the central width of the beam near the loading roller. The fracture path was disjointed but ran through the nodes (see figure 5.3 inset).

The evolution of the strain state of the microtruss was visualized using 3-D digital image correlation; the processed images are shown in figure 5.4. Figure 5.4(a) shows the beam after 4.2 mm mid-span deflection. As expected, the maximum compressive and tensile strains, shown, respectively, by dark blue and dark red, occur at the mid-span, under the loading roller. Figure 5.4(a) clearly shows the concentration of tensile strain at the ends of the lower face strut beneath the roller. The ends of the struts are subject to stress concentrations due to the junction

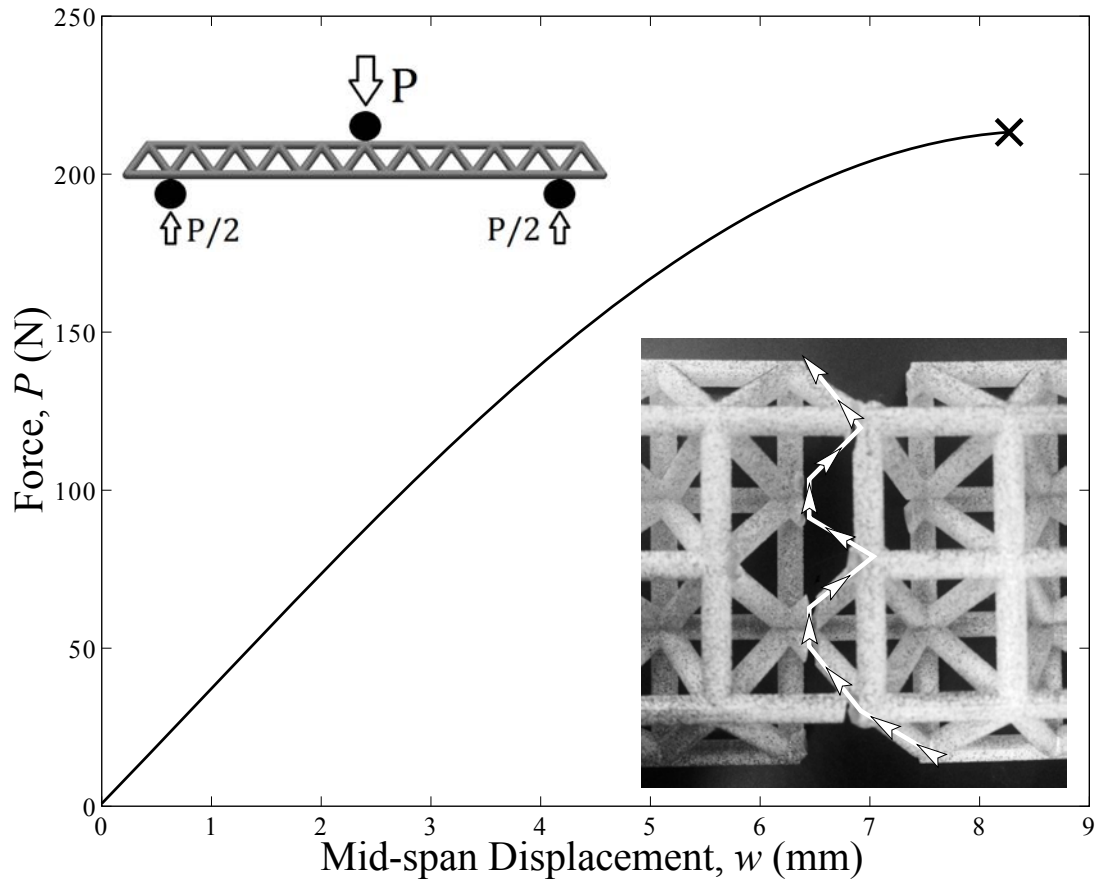


Figure 5.3: The force-displacement curve for a microtruss beam with slenderness $\lambda = 20$ and scale $s = 8$ loaded in three-point bending which failed by catastrophic fracture at the peak load, indicated by a cross. Inset top left: The microtruss beam oriented in the testing jig. Inset bottom right: Two halves of the microtruss beam reassembled after mid-beam fracture. Failure began on the tensile face (shown at the bottom of the photograph) and progressed through the width of the beam as indicated by the white line terminating on the opposite side.

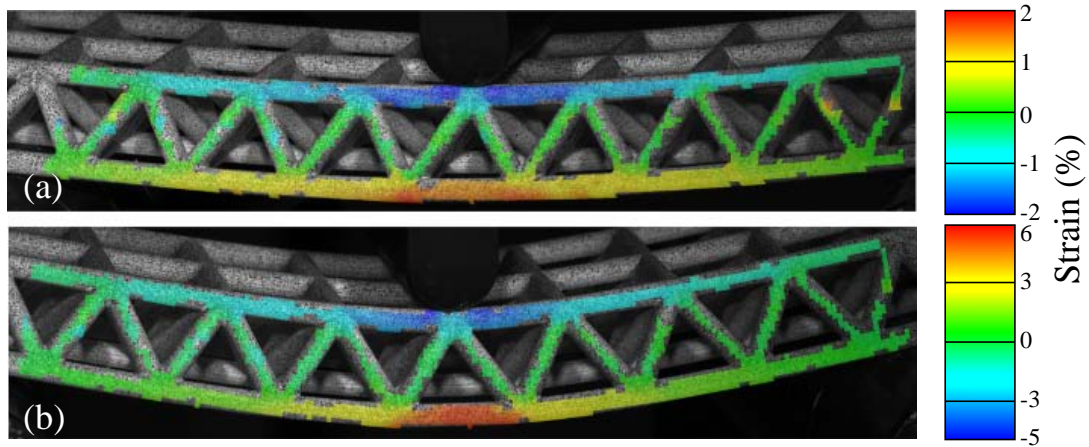


Figure 5.4: 3-D digital image correlation measurements of strains in the struts for a beam of slenderness $\lambda = 20$ and scale $s = 8$. (a) Strains after 4.2 mm mid-span deflection. (b) Strains after 8.2 mm mid-span deflection; failure by fracture of the lower struts is incipient.

between the face struts and the core struts; the maximum tensile strain at these concentrations is approximately 2%. With fracture incipient, after mid-span deflection of 8.2 mm, figure 5.4(b) shows large deformation and high tensile strain throughout the lower face sheet struts. At this stage of the loading, the maximum tensile strain, exhibited throughout the struts of the bottom face, is approximately 6%. The strain concentrations are still present but masked by the large overall strains. It is believed that fracture initiates at the junction between the core and face on the bottom face sheet and then cascades rapidly throughout the nearby struts due to the energy release accompanying local stress relaxation, consistent with previous work on graded polymer microtrusses in bending [144].

5.2.1 Slenderness Effects

Increasing the slenderness λ of the microtrusses leads to a propensity for Euler buckling of struts loaded in compression. Microtrusses with slenderness $\lambda = 20, 25, 33, 44, 57$ were tested at several scales. For comparison with the exemplary beam ($s = 8; \lambda = 20$), the microtrusses with scale $s = 8$ will be discussed. Employing classical analysis [30], all of the beams should

obey the normalized force - displacement relation:

$$\frac{w}{L} = \frac{PL^2}{48EI} \quad (5.1)$$

where w is the mid-span deflection, E the Young's modulus of the material and I the second moment of area of the beam. Figure 5.5 shows the normalized load and beam mid-span deflection for beams of scale $s = 8$ and all slenderness ratios. All of the experimental data should fall on the same line (with slope 48). Deviations from this line are a result of manufacturing or testing imperfections and, later in the test, inelastic behaviour. For beams where failure is governed by a maximum stress criterion that drives fracture, the maximum normalized loads and deflections should also be equal. In these experiments, the beams with slenderness $\lambda = 20, 25$ failed by material fracture.

A comparison of the non-dimensional load index at failure with predicted load indices is shown in figure 5.6 for restraint parameter $k = 2$. For slenderness greater than 35, the predicted failure load for buckling is less than the predicted load for a maximum stress criterion and such microtrusses should fail due to Euler buckling of compressive struts. This is generally consistent with the observed results and the measured loads at failure for most specimens. For specimens with slenderness $\lambda = 33$, the specimens failed consistently by buckling. We hypothesise that, for microtrusses with large slenderness, the constraint against rotation at the nodes is reduced. The results here are consistent with a value $k \approx 1.7$, but note that k varies with slenderness and hence cannot be considered a constant.

The other three beams, with slenderness $\lambda = 33, 43, 57$ failed through Euler buckling of the struts in the top face near the loading roller, where the moment in the beam is greatest. Figure 5.7 is an image of a strut near the loading roller buckling in compression overlaid with strain measurements. Note that the other struts in the same row also buckled. The buckling event is accompanied by a sharp drop in the load-carrying capacity of the microtruss, but not instantaneous catastrophic failure; see figure 5.5. Once buckling has occurred, the beams tend

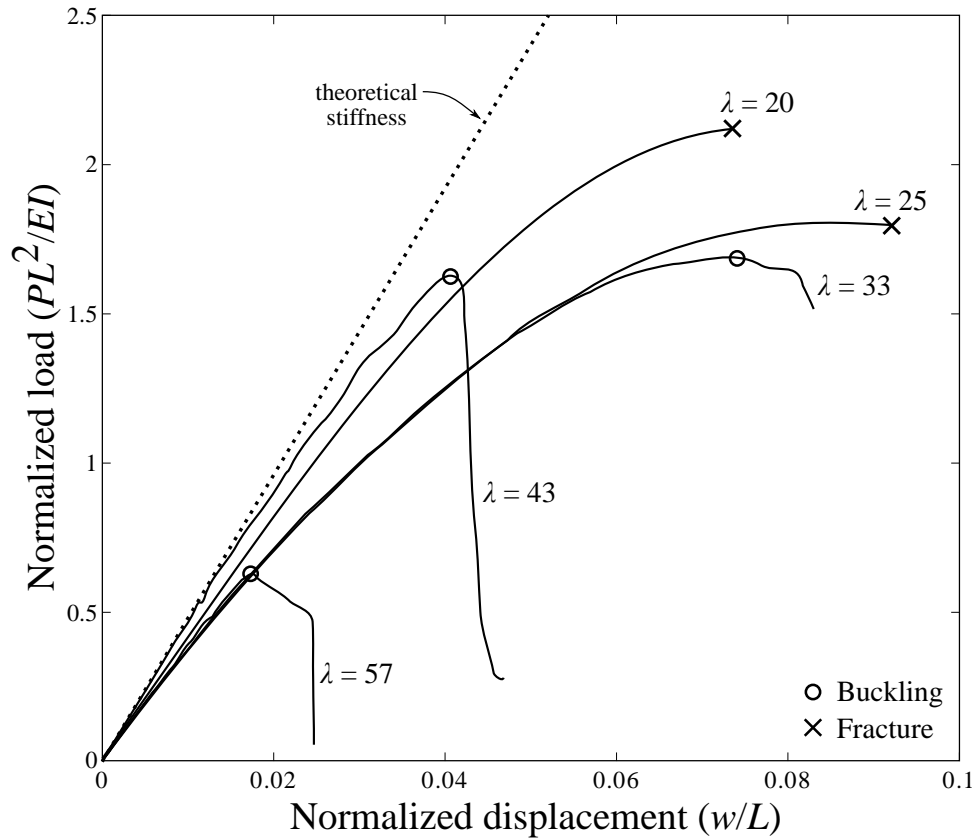


Figure 5.5: Experimentally measured normalized force as a function of normalized displacement for exemplary beams of each slenderness, all at scale $s = 8$. The mechanisms of failure, either buckling or fracture, are indicated on each trace. Microtrusses with $\lambda=20$ and 25 failed by fracture (figure 5.4) while architectures with $\lambda=33, 43$ and 57 failed by buckling (figure 5.7).

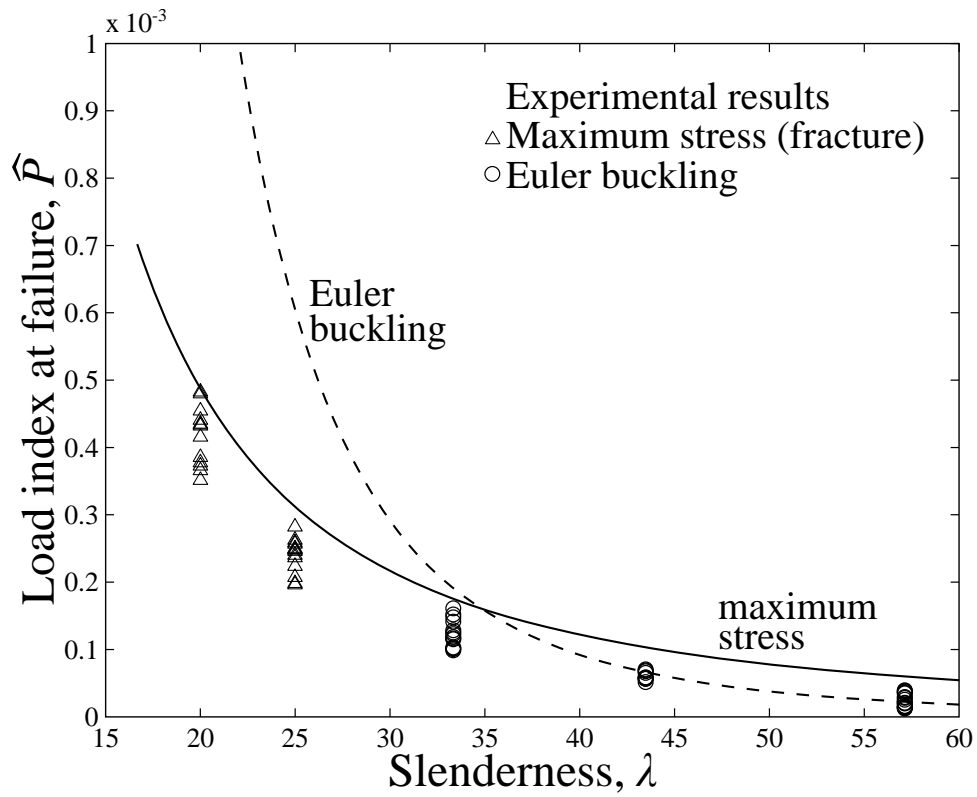


Figure 5.6: Load index at failure as a function of slenderness. Experimental data are triangles for fracture and circles for buckling. The predictions for a maximum stress criterion and a buckling criterion are solid and dashed lines, respectively.

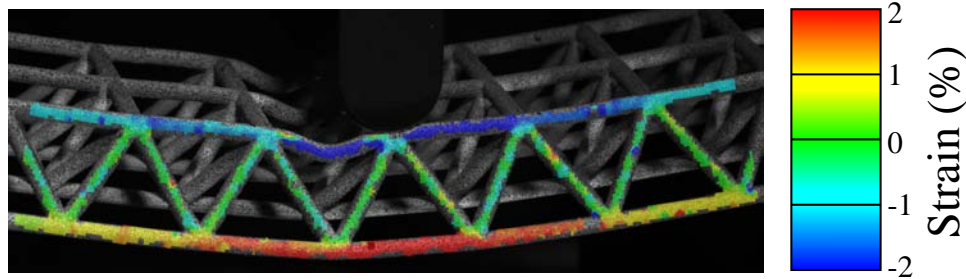


Figure 5.7: 3-D digital image correlation measurements of strains in the struts for a beam of slenderness $\lambda = 33$ and scale $s = 8$. Buckling of the face struts on the compressive side was simultaneous across all three struts adjacent and perpendicular to the roller.

to fracture shortly thereafter. Unlike beams failing by fracture, the maximum normalized load for beams failing due to buckling is a function of slenderness.

Using digital image correlation images on beams with slenderness $\lambda = 20, 33$, the evolution of the principal strains was followed through a three-point bending test. The results are shown in figure 5.8, where the contour plots show the magnitude of the principal strain with the largest absolute value. In general the principal directions are aligned with the axial and transverse directions of the struts. In both cases, the top row of face struts is strongly in compression for the majority of the test, while the bottom row of face struts is in tension. Three particular points were selected, and the strains at these locations were followed throughout the test.

For the microtruss with slenderness $\lambda = 20$ the strains remain nearly linear until failure, which occurred by fracture of the tensile struts in the bottom face of the beam at displacement ≈ 8.8 mm. In contrast, the strains at the three locations followed for the microtruss of slenderness $\lambda = 33$ are not monotonic; this is characteristic of a buckling event. The buckling is evident in the contour plots corresponding to this microtruss: the strut immediately to the left of the beam centre has buckled by mid-span displacement of 7.76 mm. This has already exceeded the peak load that this beam can sustain. Throughout the tests, the core struts remain relatively lightly strained. This is consistent with the predictions of classical sandwich theory.

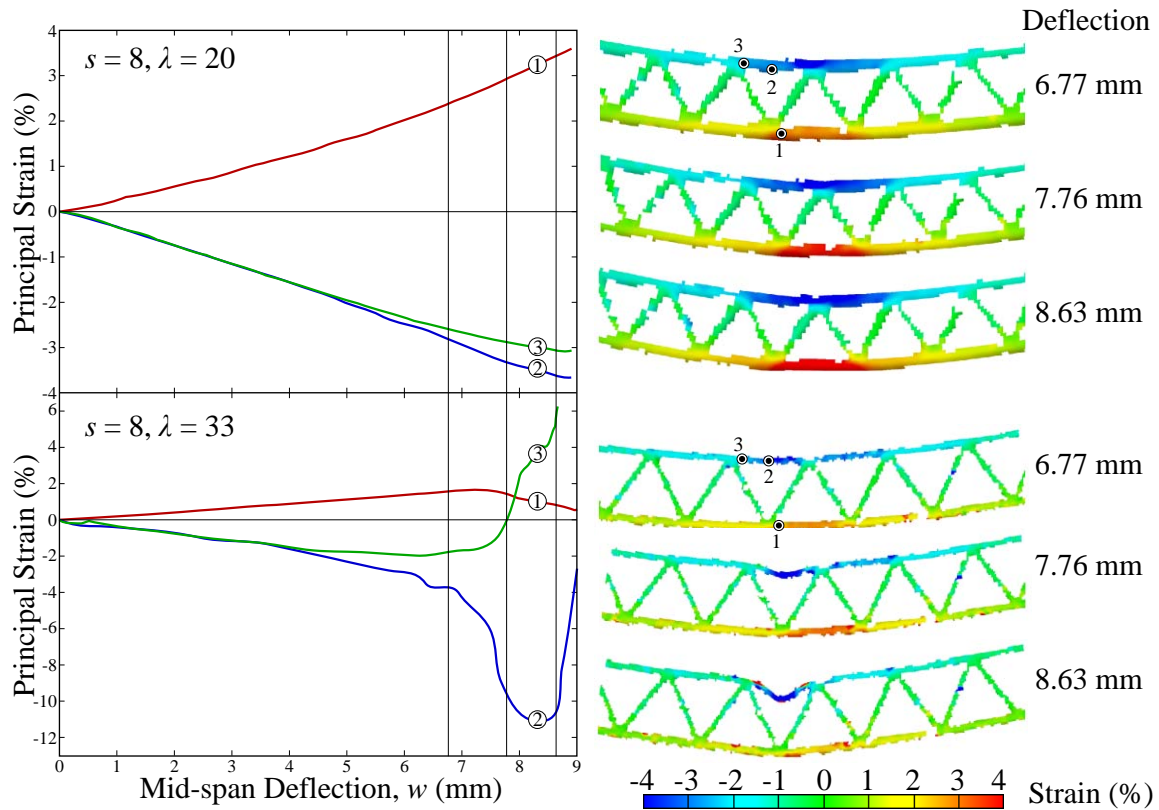


Figure 5.8: Principal strains measured by digital image correlation for three-point bending tests on microtrusses with scale $s = 8$ microtrusses with slenderness $\lambda = 20$ in the top row and $\lambda = 33$ at bottom. Three contour plots for each slenderness show the principal strains with maximum magnitude at 6.77 mm, 7.76 mm and 8.63 mm midspan deflection for each microtruss; these displacements are indicated on the graphs by vertical lines. The graphs on the left plot the strains of three points labelled on the structures. Note that these images are cropped and do not show the entire beam.

5.2.2 Scaling Effects

Classical analysis suggests that increasing the slenderness of the beam struts will induce buckling rather than fracture, while scaling the structure up or down should result in no such changes in failure behaviour for macro-scale microtruss beams [145, 146, 13]. However, change of scale induces two significant effects, both related to the release of strain energy when fracture initiates. As the scale of the microtruss increases, the strain energy released during a fracture event increases with the square of the scale. Thus, larger microtrusses release larger amounts of strain energy during post-fracture relaxation for an equivalently scaled crack extension.

The first consequence is that smaller-scale microtrusses do not exhibit instantaneous catastrophic fracture initiated by the first fracture event. Instead, the struts fracture progressively, with each fracture accompanied by a decrease in the load carried by the microtruss. The normalized load - displacement results for microtrusses of slenderness $\lambda = 20$ are shown in figure 5.9. As the scale decreases from 8 to 1, from largest to smallest, the fracture events become marked by partial load drops. At scale $s = 4, 8$, there is complete failure after the first fracture event, while for scales $s = 1, 2$ the fracture is progressive and leads to a staircase-like load - displacement relation. For four specimens with slenderness $\lambda = 20$ and scale $s = 1$ (that is, the smallest scale), the load capacity of the beam after fracture of one or more struts in tension was approximately predicted by the number of struts remaining (see figure 5.10). That is, the undamaged microtrusses had four intact struts in tension. After one strut fractured, the remnant strength was approximately three-fourths of the initial strength.

The second consequence is that polymer microtrusses with equal slenderness but different scales - that is, microtrusses that are geometrically similar - exhibit a pronounced size effect when failure is due to fracture. The average tensile stress in the longitudinal struts that compose the face of the microtruss is:

$$\sigma_T = \frac{PL}{16dA} \quad (5.2)$$

where d is the distance between the centroids of the face sheets and A is the cross-sectional

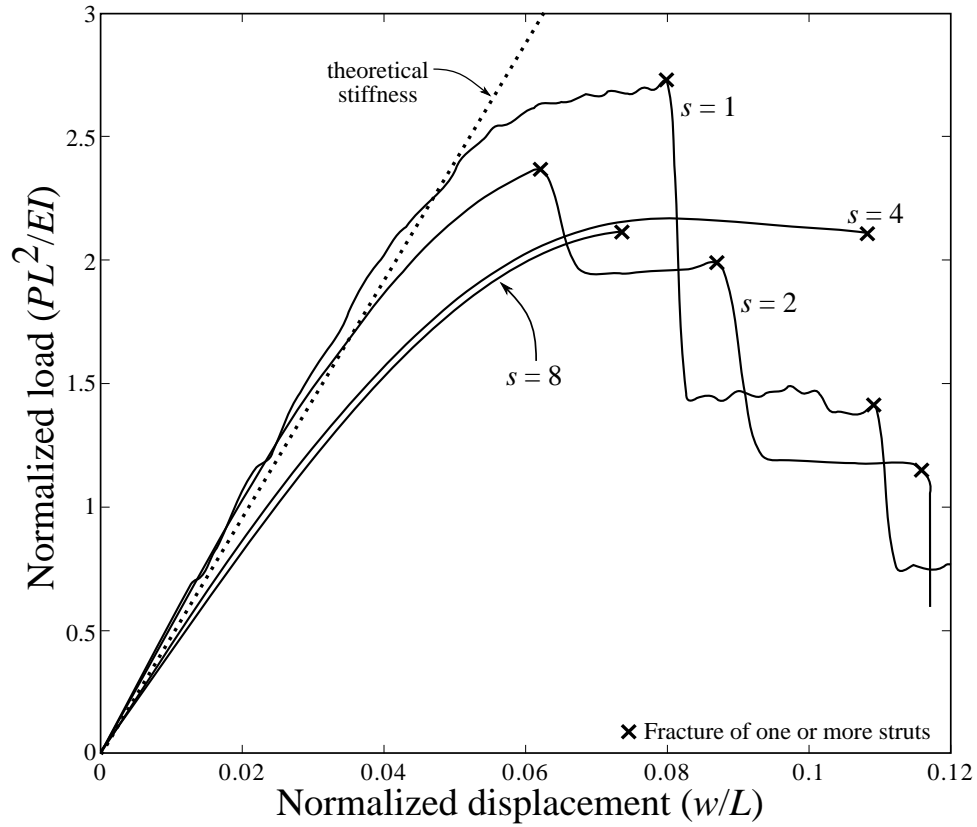


Figure 5.9: Experimentally measured normalized load against displacement for microtruss beams with slenderness $\lambda = 20$ and scales $s = 1, 2, 4, 8$. For smaller scale microtrusses, failure is progressive, while for larger scale microtrusses, failure is instantaneous and catastrophic.

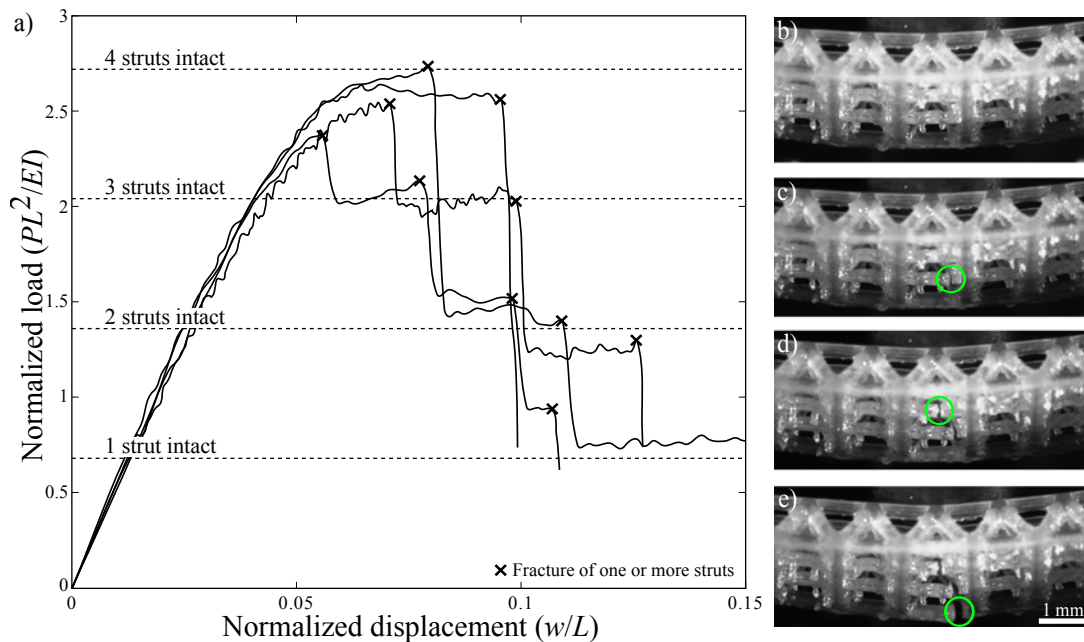


Figure 5.10: (a) Relationship of normalized load to normalized displacement for microtrusses with slenderness $\lambda = 20$ and scale $s = 1$. These microtrusses fail by progressive fracture of the struts in the tensile face. The remnant load-carrying capacity after each fracture is well-predicted by the number of struts remaining; predicted strengths for 4, 3, 2 and one intact struts are indicated by dashed lines. Optical images of the underside of the microtruss beam during testing shown: (b) before first fracture, (c) after one strut had fractured, (d) after two struts have fractured, and (e) after three struts have fractured. Each new fracture is identified by the highlighted circling in the image.

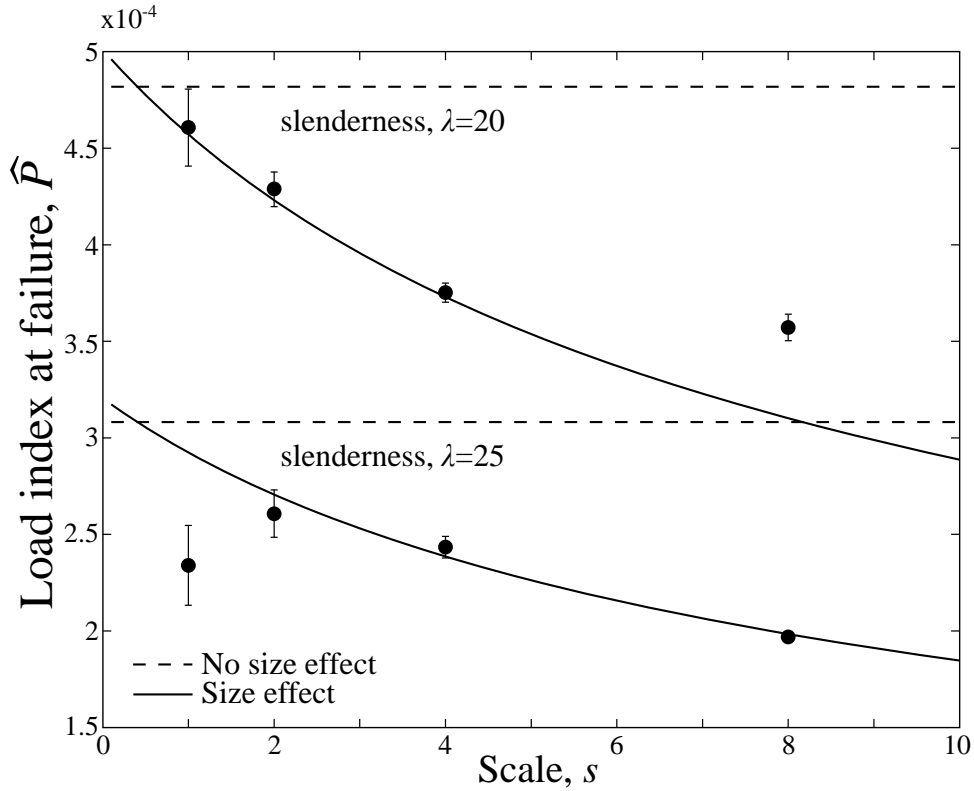


Figure 5.11: Deterministic energetic size effect in similar polymer microtrusses. The dashed lines are the predictions based on maximum stress, while the solid lines account for a size effect. The predictions and experimental data are for slenderness $\lambda = 20, 25$. The error bars for the experimental data for $s = 8, \lambda = 25$ are obscured by the symbol.

area of the struts. Given that the strength of the polymer, σ_{cr} , is 42.4 MPa, if the maximum stress were to govern the failure load, then:

$$P_C = \frac{16\sigma_{cr}dA}{L}. \quad (5.3)$$

The dashed lines in figure 5.11 show this relationship; for larger scales, this relation overpredicts the strength measured through experiment.

Because the polymer material behaves in a quasi-brittle manner, these structures should be subject to a deterministic energetic size effect [147, 148]. The load at failure would then be:

$$P_{SE} = \frac{16\pi d_1 r_1^2 \sigma_{cr}}{L_1} \frac{Bs^2}{\sqrt{1 + C_s}}, \quad (5.4)$$

where s is the scale of the structure, B and C are constants, and the subscript 1 refers to the dimensions of the microtruss with scale 1. B and C are calculated from best fits to the experimental data. One value of B and one value of C are calculated using all data at all scales and slenderness, rather than individual B and C for each value of slenderness. For the experimental data collected here, $B = 1.0399$ and $C = 0.2012$. The solid lines in figure 5.11 show the predicted load, P_{SE} , if a size effect of this sort is present. This size effect arises because, as the scale of the structure increases, the energy required to extend a crack is linearly proportional to the scale, while the energy released by stress relaxation varies quadratically. This leads to a reduction in the stress at which fracture will occur as the scale of the structure increases. The most significant discrepancy between prediction and experiment is for the smallest (scale $s = 1$) microtrusses of slenderness $\lambda = 25$. For these microtrusses, the strut radius is $125 \mu\text{m}$, or $4.3x$ the minimum layer thickness of the 3D printer used in this study. In general, as sample size is decreased, the probability of a critical flaw decreases leading to a positive material size effect [149, 11], trends not seen in the macro-scale range of lattice core sandwich panels [62, 60, 150, 33]. The decrease seen for this smallest structure suggests otherwise. It is hypothesized that the inherent flaw length associated with the stereolithographic process is sufficiently large compared to the strut radius that these structures are affected by a stochastic size effect, reducing their measured strength. In contrast, structures at the same scale ($s = 1$) but with an increased strut radius ($r=156 \mu\text{m}$, $\lambda = 20$), i.e. $5.4x$ the minimum layer thickness, did not exhibit this discrepancy.

5.2.3 Graded micotruss architectures

In direct compression, the loads in the oblique core struts of microtrusses are large relative to the loads in the face struts and govern failure. By contrast, in a microtruss beam in three-point bending, the oblique core struts are loaded relatively lightly compared to the face struts; see the difference in strains between the face struts and core struts shown in Fig. 5.4. In bending, the oblique core struts are not critical points of failure and their mass is partly parasitic. The total

<i>Name</i>	<i>CoreStrutRadius</i> (mm)	<i>SlendernessRatio</i>	V_r (%)	<i>Mass</i> (g)
NG	0.62	20	100	2.02
G1	0.56	22	80	1.82
G2	0.52	24	70	1.77
G3	0.48	26	60	1.67
G4	0.44	28	50	1.57
G5	0.42	30	45	1.49
G6	0.40	32	40	1.44

Table 5.2: Geometries of reduced core polymer microtrusses.

mass of the structure can therefore be reduced by decreasing the size of the core struts while leaving the face struts unchanged. The limits of this are tested experimentally in the following section.

Microtruss beams were created with face sheet struts having a radius of 0.625mm (identical to the SR20 microtruss scaled 4x from the previous section) and core struts having radii ranging from 0.5mm to 0.25mm. Table 5.2 provides the sample geometries and masses for each structure. All beams were of the same length and width (\pm one strut diameter) and the same total thickness. These thinner core struts had slenderness ratios ranging from 22 to 32 resulting in reductions of volume over the standard face sheet strut size (V_r) of 80 to 40%.

For small reductions in the radius of the core struts (specimens G1-G3), the maximum bending load is constant and equal to the maximum bending load for the baseline beam, approximately 55 N. The maximum bending load for all specimens is shown in Fig. 5.12. The failure event was similar to the baseline beam failure: sudden and catastrophic. It is believed that failure in all cases is attributable to the stresses in the tensile face exceeding a critical level, leading to brittle failure in a single strut that rapidly propagated through the width of the structure and fracturing the beam into two pieces. With further reductions in the radii of the core struts (specimens G5-G6), the behaviour at failure of the microtruss beams changed markedly. Rather than catastrophic failure, failure was marked by buckling of the struts in the compressive face (see Fig. 5.13) and the peak measured load was lower than for the baseline beam. (Specimen G4 was intermediate between specimens G3 and G5.)

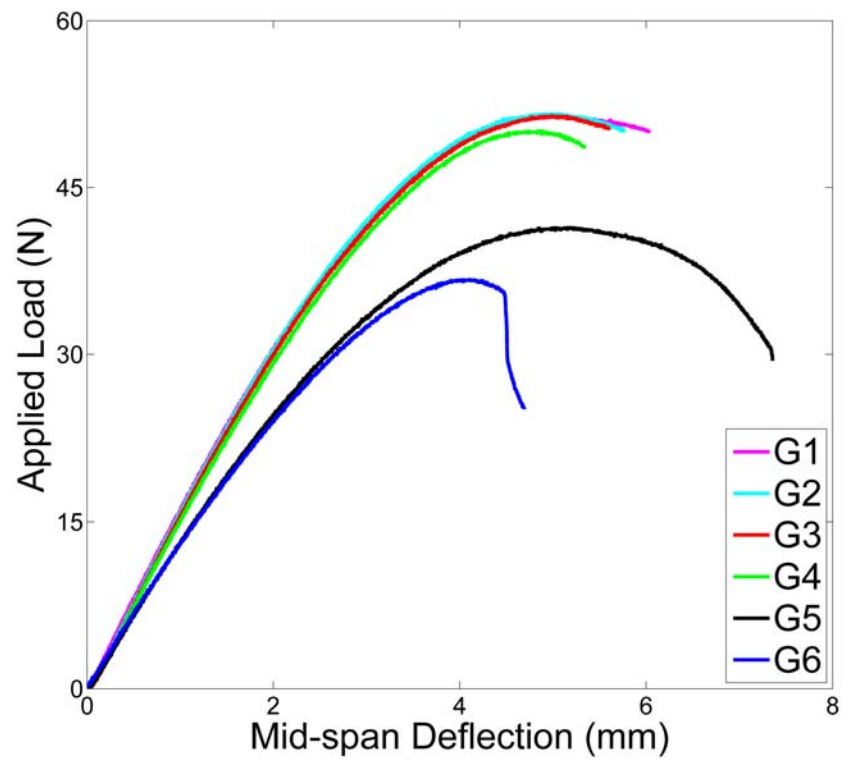


Figure 5.12: Force-deflection curves for the six reduced core microtruss beams from specimen G1 to G6 by volume thinner core struts. Specimens G1 thru G3 show almost no change.

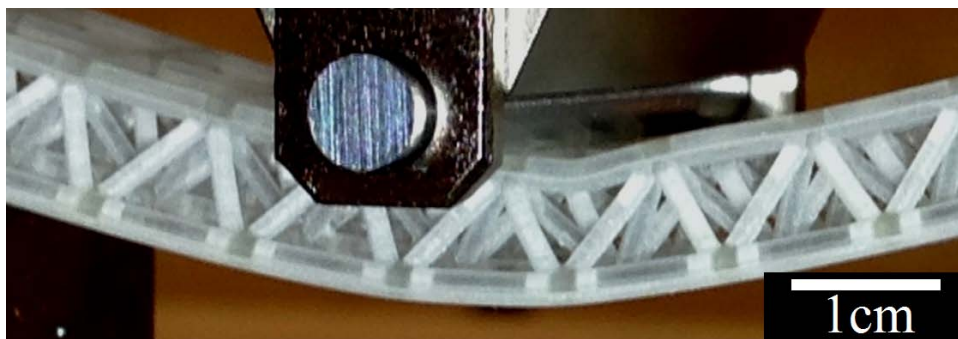


Figure 5.13: Close up view of specimen G5 at 5mm deflection from a side view showing a face sheet strut buckling to the right of the central roller.

When SEM imaging was to be done on the specimens, the truss was observed to have returned to its original state without any evidence of the face sheet buckling seen in Fig. 5.13. This relaxation and return to the original shape is evidence of the elastic nature of the polymer material. In the electron microscope, bright white sections appeared on the struts due to charging on the surface of the specimen. Since a large depth of field was required for images on this small magnification, the secondary electron (SE) mode was utilized with the downside of higher accelerating voltage and vacuum leading to the charging (Fig. 5.14a). For higher magnification images, Ultra Variable-Pressure Detector (UVD) mode was utilized as depth of field was no longer essential. This removed the charging effect seen in SE mode and showed detail on the strut level such as some increase in cross-sectional area at the midpoint of the strut and bulging/deformation along the sides of the strut (Fig. 5.14b).

These results indicate that face failure of the microtruss sandwich beam in bending is subject to multiple competing mechanisms. It is believed that the reduction in the size of the core struts reduced the rotational constraint on the face struts, increasing their propensity to buckle. For robust core struts, the constraint that the core supplies against face strut buckling is large and the face struts fail by yielding or brittle fracture. As the core struts become more slender, this constraint is relaxed and eventually the face struts are subject to buckling failure. As the core strut radii are reduced further, the load carrying capacity of the beam is also reduced. In Fig. 5.15, these competing mechanisms are represented by zones of fracture and face sheet buckling (FSB); at a given core geometry, the mechanism capable of withstanding the least load is active. Eventually, as the core struts are further reduced in size, buckling of the core struts themselves should become the active failure mechanism.

In Fig. 5.15, the failure load for each level of core thinning percentage is normalized by the mass of the microtruss. As the core is thinned to the transition point between face sheet buckling and fracture, the decrease in mass without a decrease in failure load leads to an improvement in structural efficiency. Earlier claim that the core is over-engineered are substantiated here with this peak existing at the boundary between two failure mechanisms. Furthermore,

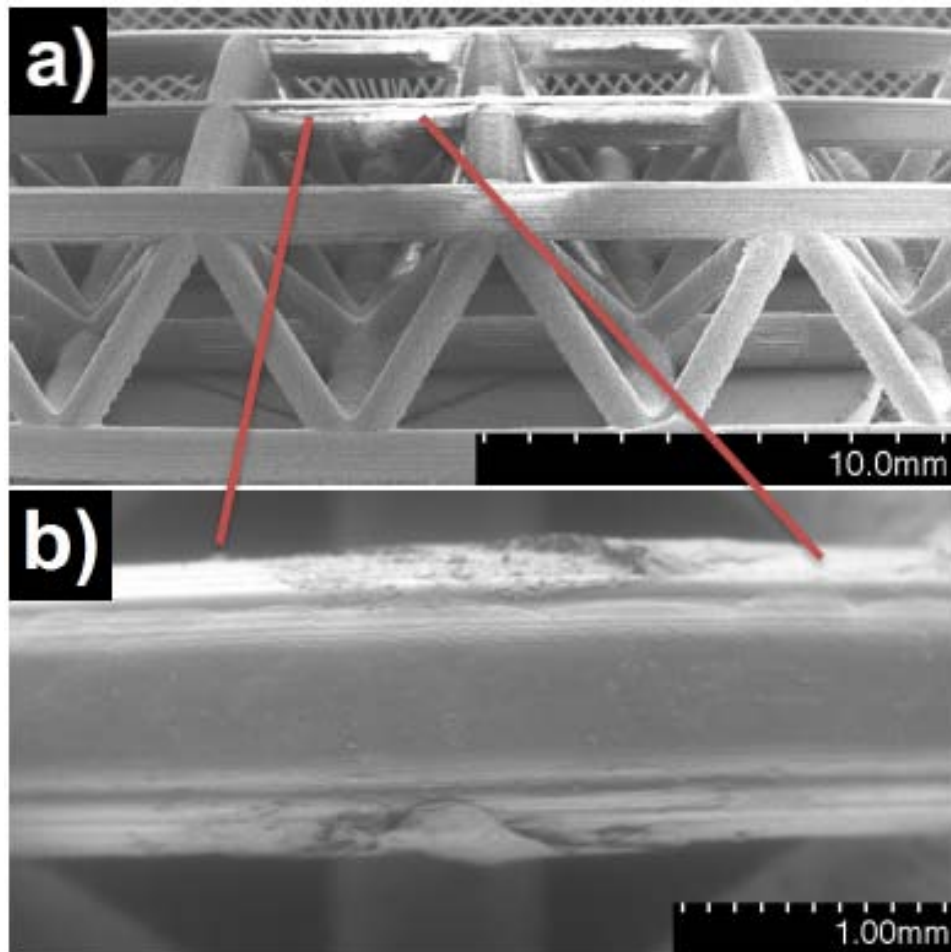


Figure 5.14: SE and UVD micrographs of specimen G5 after face sheet buckling failure. Relaxation of the polymer returns it to its starting shape (a) but evidence of buckling is still seen in the central face sheet strut at its midpoint (b).

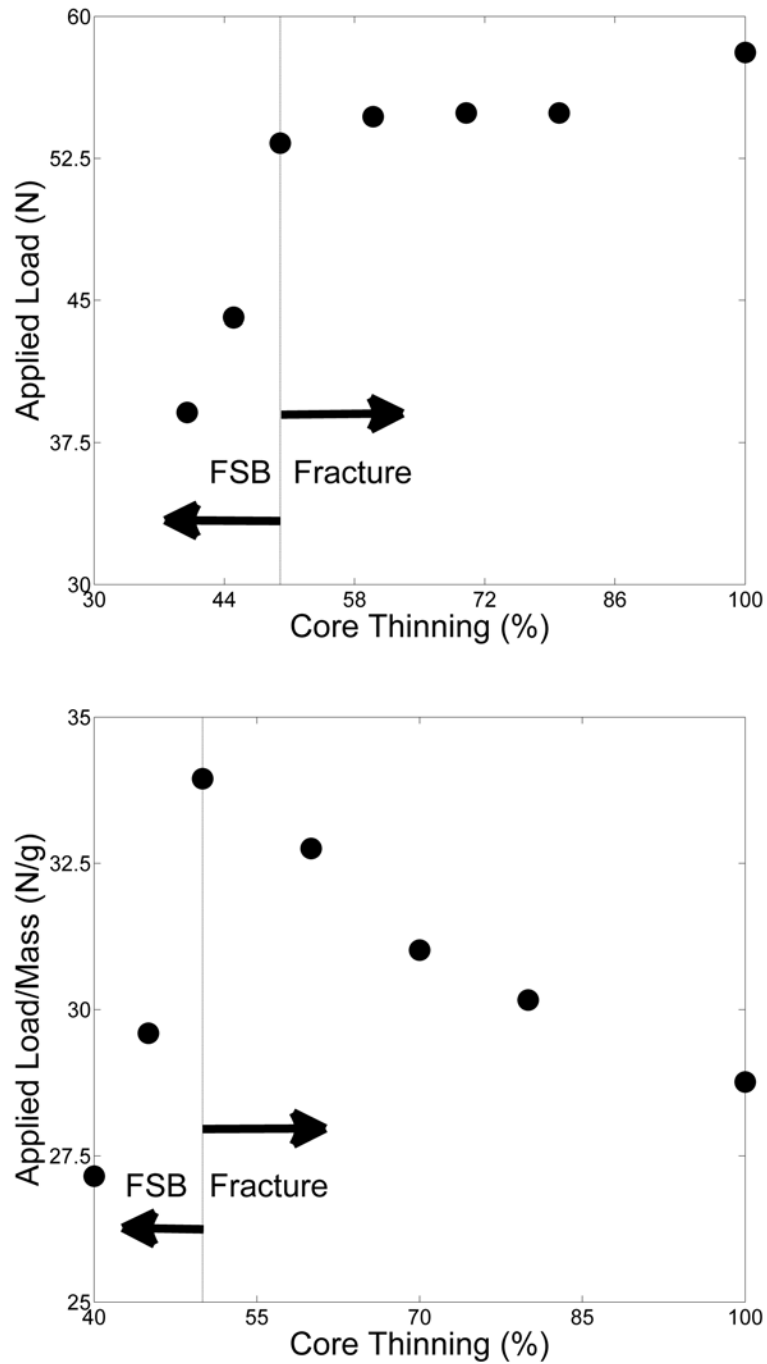


Figure 5.15: Nearly constant failure load as the core is thinned from 100% to 50% (top). A shift in failure mechanism results in the dip after 50% as the specimens begin to face sheet buckle (FSB). Normalization by total mass of microtruss shows that the transition point (the boundary between fracture and FSB) is the optimal design (bottom).

the location of this optimal at that exact boundary will come back in the discussion of composite microtruss beams in future chapters. Finally, a 50% thinning of the core is not expected to be a constant for all slenderness ratios and scales, as those effects compound differently as seen above. As long as a transition does exist from fracture to buckling in a single material microtruss, a point like this can be found.

5.3 Weight-specific improvement by moving from blocks to microtrusses

In section 4.3.4, the mechanical performance of a solid polymer block was tested in various printing orientations. These blocks showed a large flexural strength but at the expense of large amounts of material. With the discussion in this chapter centering on the behaviour of polymer microtrusses, a fair comparison would be to select a microtruss of the same exterior dimensions as the polymer blocks in section 4.3.4. Indeed, this is why the dimensions of the block were selected to be non-integer values as the fairest comparison is to a microtruss with an integer number of unit cells in all three dimensions. Now, both the block and microtruss encompass the same volume.

Just as the base case for the scaling and slenderness ratio effect studies was a SR20 microtruss, the same was selected here. To fill the polymer block volume, the strut length was selected such that an 11 by 3 unit cell square pyramidal sheet could fit inside. The corresponding strut length was 12.5 mm with a strut radius of 1.25 mm to keep the slenderness ratio at 20. Three-point bend tests were performed and looking at the force-deflection results in Fig. 5.16, the block withstood more force and absorbed more energy than the microtruss. This was to be expected due to the four times larger mass difference.

Two steps were done to normalize both systems for their overall size. First, the curves were converted to flexural stress and strain. While the equations presented in section 4.3.4 work for the block, the location of the neutral bending axis and second moment of area are different for

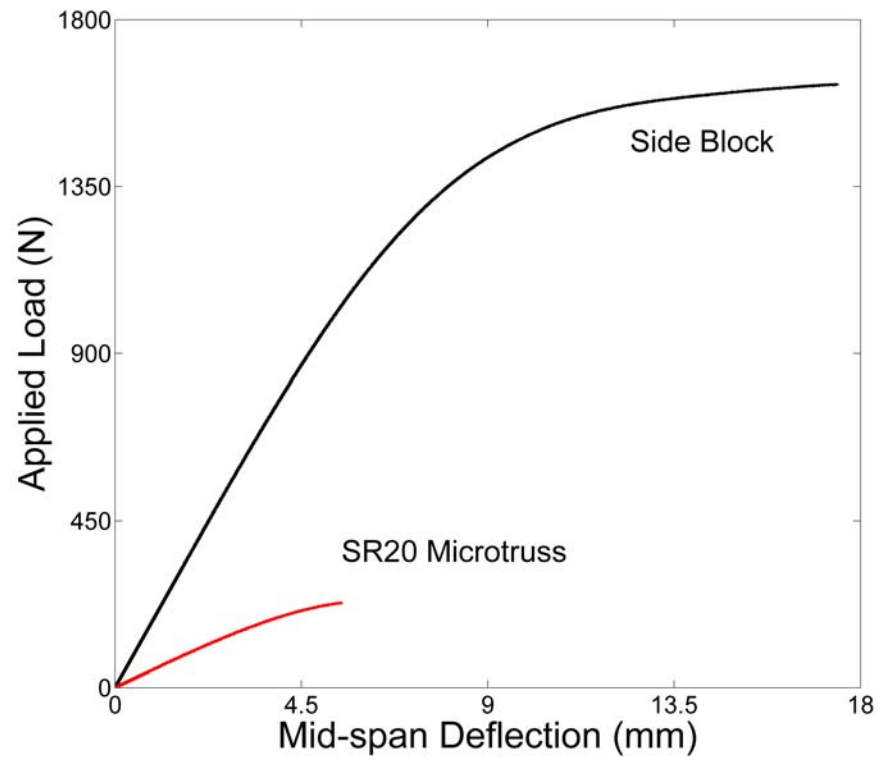


Figure 5.16: Load-deflection curves for the as-printed side block and a SR20 microtruss of the sample scale and total length.

a truss. Following a similar derivation, the arrived at flexural strength, strain, and modulus are

$$\sigma_f = \frac{My}{I} = PL\left(r + \frac{3u}{7\sqrt{2}}\right) \frac{1}{7\pi r^4 + 4\pi r^2\left(\frac{6u^2}{7}\right)}, \quad (5.5)$$

$$\epsilon_f = \frac{12D}{L^2}\left(r + \frac{3u}{7\sqrt{2}}\right), \quad (5.6)$$

and

$$E_f = \frac{mL^3}{12} \frac{1}{7\pi r^4 + 4\pi r^2\left(\frac{6u^2}{7}\right)}, \quad (5.7)$$

respectively. In terms of stress and strain, the block still outperformed the microtruss because the mass of the structure had not been incorporated (Fig. 5.17a). However, before moving to the next step, it was noticed that the flexural modulus of the block and microtruss were different. This was because to create a repeat unit cell in SolidWorks, the outer face of the sides of the microtruss were composed of half struts (Fig. 5.17b). With failure already known to occur on the tensile side, weakening this key load supporting strut severely disabled the microtruss' performance. To remedy this, these half struts were turned into fully circular struts like the rest of the microtruss. Repeating this test resulted in a large increase in flexural strength and a match in modulus between the block and the full strut microtruss.

The second step was to normalize the flexural stress by the mass. With a mass of 54.6 g for the block compared to 15.7 and 16.5 g for the half and full strut microtrusses, the microtrusses surpassed the block's strength (Fig. 5.17c). A fair comparison, therefore, that incorporated the geometry and the mass resulted in a microtruss that had improved weight-specific mechanical properties over a block made of the same material.

5.3.1 Methods to improve on the single material microtruss' weight-specific performance

As can be gleaned from section 5.2.3, a microtruss with identical struts in the face and core can maintain its load carrying capacity and still trim some mass by thinning the core struts.

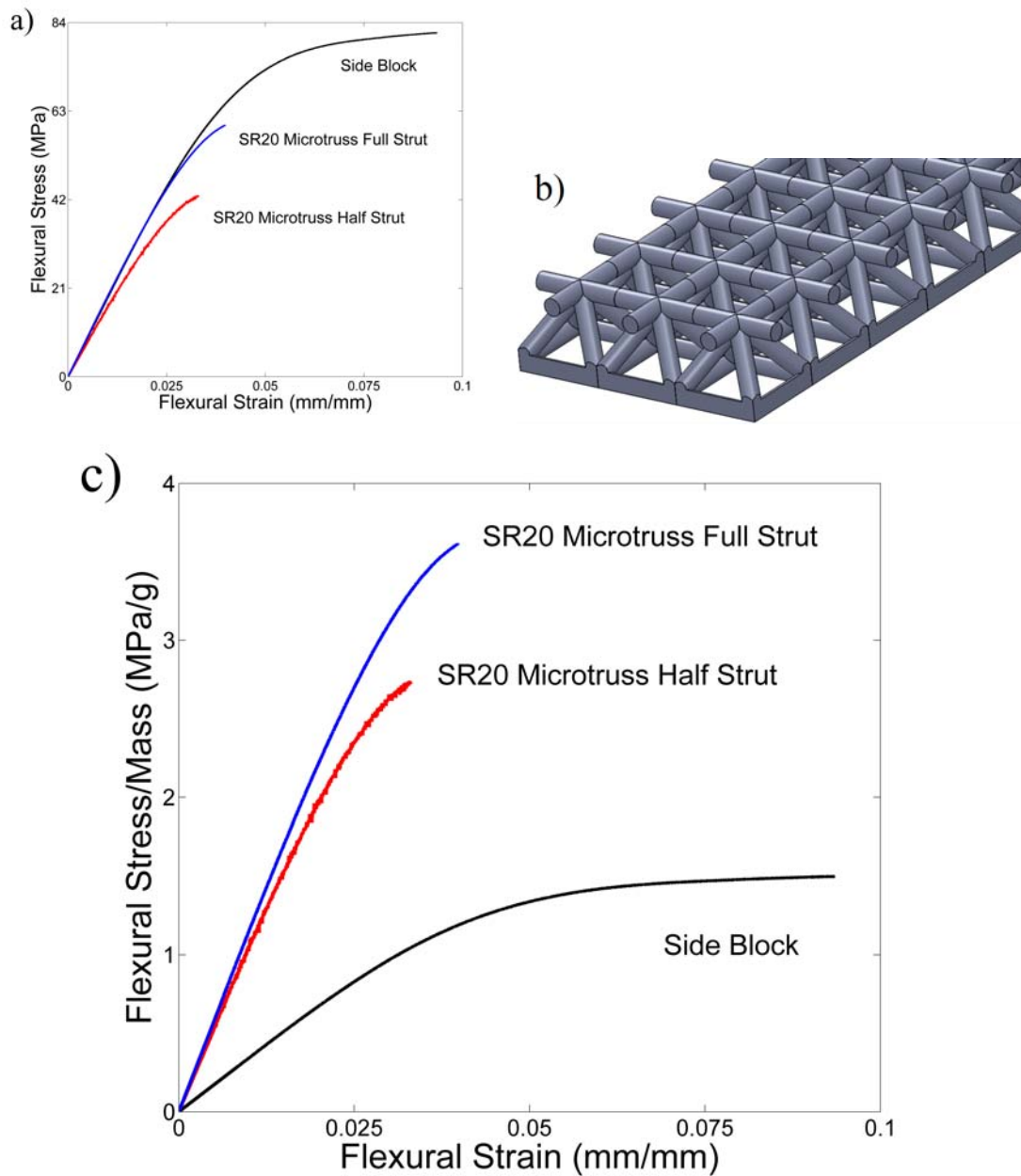


Figure 5.17: The flexural stress-strain curve for the side block and SR20 microtruss is compared (a). Additionally, a SR20 microtruss with full struts on the outer face as opposed to the repeat unit cell is shown. The SolidWorks schematic of the half strut microtruss is shown (b). When normalized by total mass of the structure, the true benefit in weight performance is seen for microtrusses (c).

In a strictly bending scenario, the loads in these struts are small enough that repositioning the mass to the face struts creates a more efficient structure. Following on that idea and on the comparison between a truss and a block, microtrusses with other modifications were designed to try and create lighter structures with similar load carrying capacity.

The inspiration for these designs was from topological optimization studies on beams in bending performed by Sigmund [28] (see the airplane floor example in Fig. 2.6 in the literature review). In these two-dimensional loading examples, the tendency early in the optimization was for the fabrication of a truss-like shape and while a microtruss seems to be the final design, there is significant non-uniformity in its shape. In places of sharp transitions in material, like core-face strut joins, a stress concentration exists that can be compensated for with fillets. The struts in the face are also thicker than in the core and a gradient in strut size exists with thicker ones near the middle of the beam where the moment forces are the largest and decrease as you move to the supports. The addition of these shape changes through fillets and non-uniform strut sizes came about as a result of the topological optimization software and can similar be labeled as shape optimization on this 2D block.

Using these ideas, some experimental designs were printed to test the possibility for further microtruss refinement. Once again, a SR20 microtruss was used as a baseline with a scale of 8 times. To this architecture, the first modification was the use of fillets in all corners and recesses in the microtruss. A small fillet of 0.5 mm in size and a much larger one of 2 mm was added into the structure. Next, a graded core structure with volume reduction in the core of 50% was tested. Additionally, a tapered strut design was built where the struts would be thinner towards the center. Because failure in fracture at midspan for the SR20 microtrusses was on either end of the face strut joining two nodes, removing some mass from the middle might shift failure inwards while decreasing mass. This one modification most greatly exemplifies the freedom in this manufacturing technique and shows how complicated geometries that typically come about from topological and shape optimization can be realized. All microtrusses were printed such that the face struts in the long direction were longitudinal and on their side, as the highest

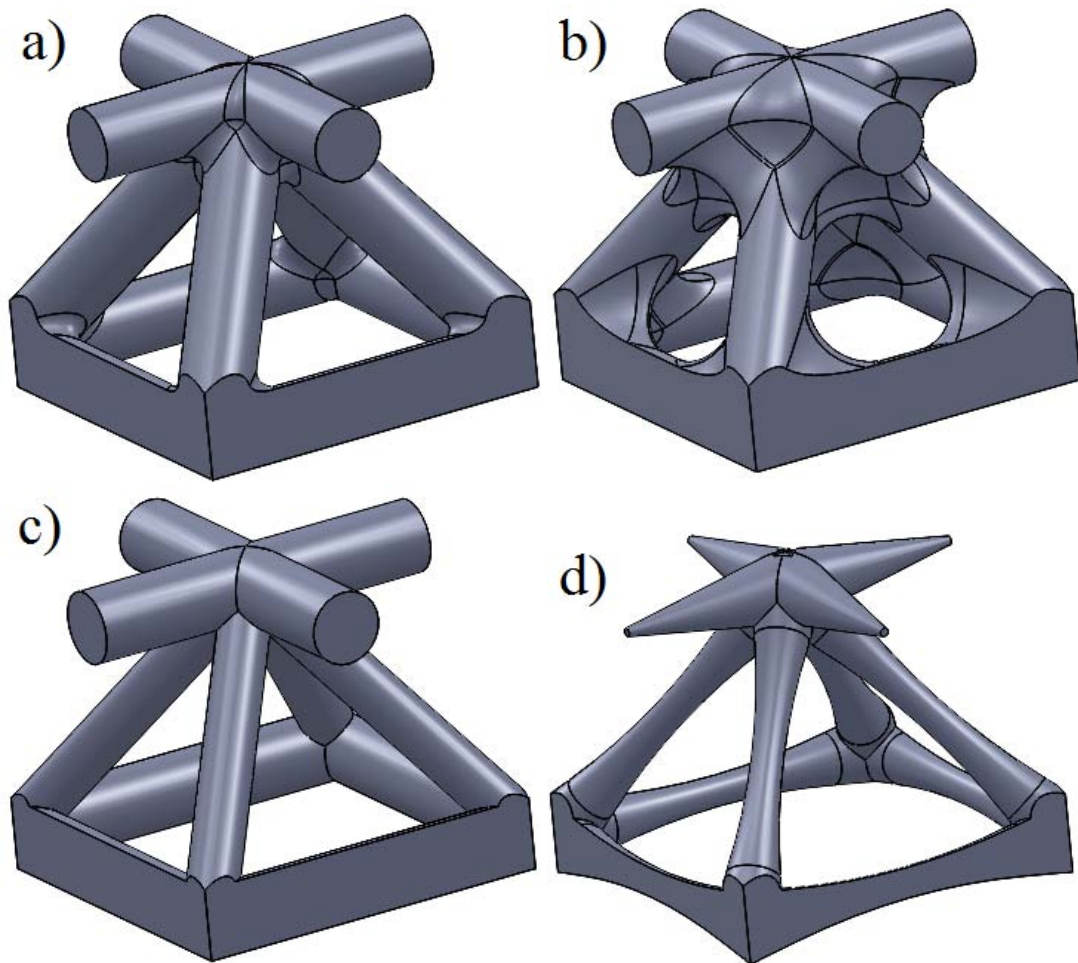


Figure 5.18: Repeat unit cells for microtrusses with 0.5 mm radius fillets (a), 2 mm radius fillets (b), a 50% grading of the core struts (c) and tapering across the strut itself (d) are shown.

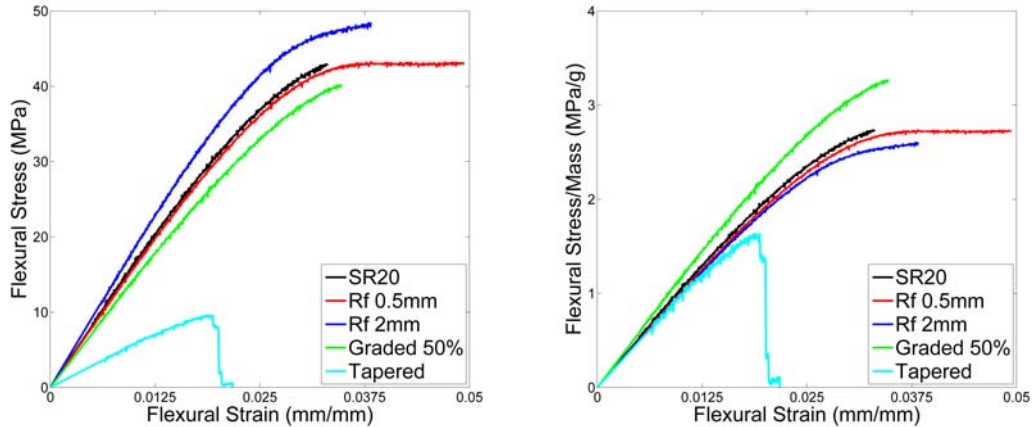


Figure 5.19: Flexural stress-strain curves for the different microtruss improvements are shown (left) next to the normalized ones (right) showing a preference for grading as well as ductility improvements with small increases in fillet radius before the added mass becomes too large (as seen in the 2 mm fillet radius case).

performing block was. Figure 5.18 shows the designs as created in SolidWorks. Of the four designs, the non-uniformity that exists in the tapered design (Fig. 5.18d) is a testament to the unparalleled power of MJM 3D printing.

Figure 5.19 presents the results of three-point bending tests on these architectures. Small fillets on the order of 0.5 mm did not improve the overall load carrying capacity in relation to the SR20 unfilleted microtruss but did increase the ductility. The lack of a stress concentrator in the corners resulted in an increased load being required to start a crack and fracture the microtruss. When it did fail, it was sudden and complete as seen in all SR20 microtrusses. Increasing the fillet radius even further to 2 mm led to a noticeable increase in peak flexural stress with a less profound increase in ductility. Failure was still dominated by fracture. While going to even larger fillet radii should continue to increase the peak flexural stress, looking at Fig. 5.19 shows it has already gone too far. Because a bigger fillet adds mass to the microtruss, the normalized curves place the 2 mm fillet radius microtruss (mass of 18.6 g) below the SR20 and 0.5 mm fillet microtrusses (masses of 15.7 and 15.8 g, respectively).

The filleted microtrusses were also analyzed using DIC to understand their impact on failure (Fig. 5.20). The scale for the principal strain percentage was modified to the tight range of

5-15% for the cases of unfilleted, slightly filleted (0.5 mm), and large fillets (2 mm). This strain overlay was placed on top of the actual image of the microtruss. All three images are of the last frame recorded before fracture. As the fillet radius increases, deformed volume of the strut decreases; areas under the fillet are not nearly as stressed as when no fillet is there. The large fillet goes as far as centralizing all the deformation to the exact middle of the strut. The closer the fillets come to creating circular pores, the less the face strut behaves as a strut and more like the polymer block. Failure moves from the edges of the strut inwards. Because of this movement, material under the fillets is considered less essential and results in the weaker normalized performance seen in the largely filleted microtruss. Having just a small fillet removes the presence of the sharp corner but keeps the entire length of the strut stressed and utilizes the material more efficiently.

The 50% graded microtruss has the opposite pattern where the pre-normalized flexural strength is lower than the baseline while after normalizing, it is the highest performing of the group as it has a greatly reduced mass of 12.3 g. Tapered microtrusses offer the greatest mass reduction down to a mere 5.9 g but this tapering was too severe for the face struts in tension at mid-span. Four distinctive drops are seen near the end of the flexural stress-strain curve that correspond to individual strut-by-strut failure along the four bottom tensile face struts, very similar to the case of SR20 microtrusses at their smallest scale failing node-by-node (fig.5.21). While there may exist some small degree of tapering that would be beneficial in tensile struts, it was not observed here. For face sheet buckling architectures, it would be even more detrimental as the thinner middle would induce global buckling of the strut even sooner.

Overall, a combination of a graded microtruss having a thinner core in addition to small fillets would approach the limit in normalized load carrying capacity for a square pyramidal microtruss. Additional steps that could improve the microtruss' bending performance would be the thinning of struts in the faces near the supports and turning the struts into tubes instead of solid cylinders. This will be discussed in Chapter 8.

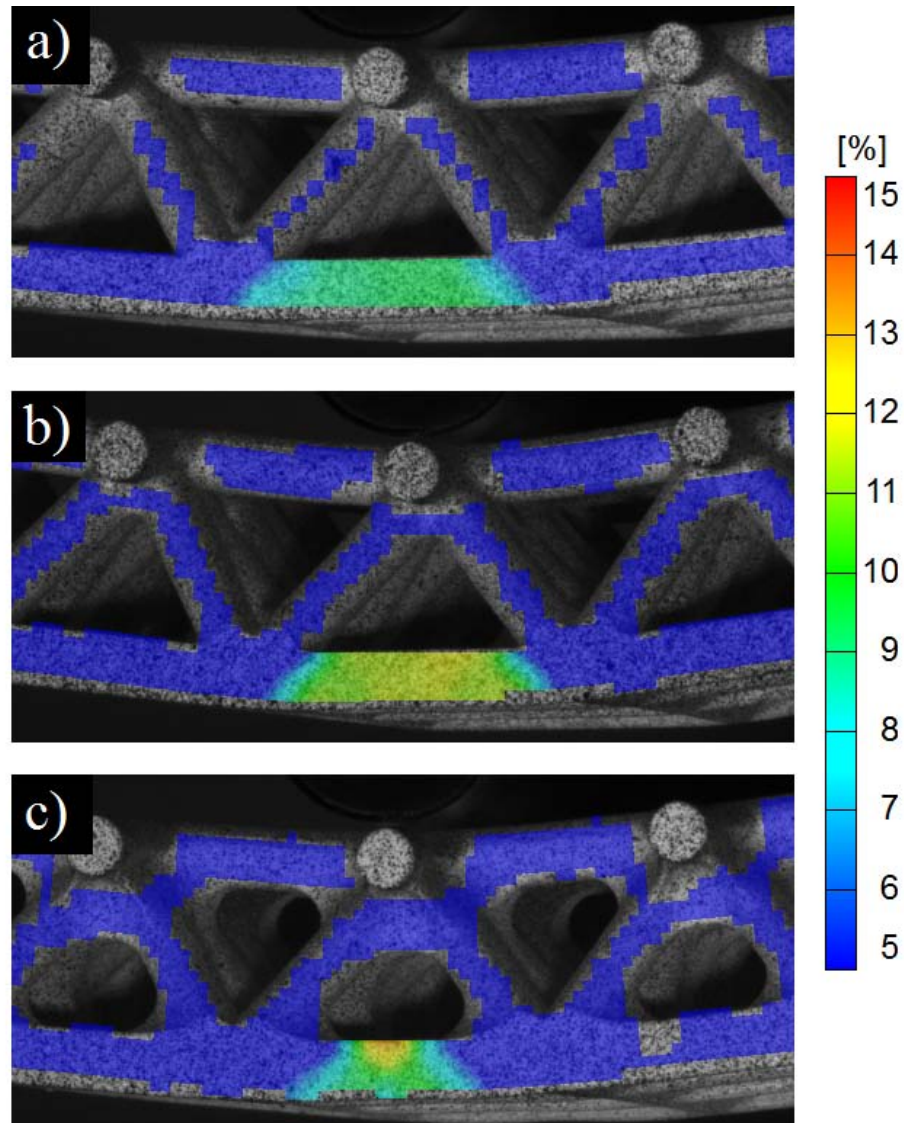


Figure 5.20: DIC strain maps for unfilleted (a), 0.5 mm fillet radius (b), and 2 mm fillet radius (c) microtrusses in bending. The central unit cell is shown and the scale has been fixed to the 5-15% range to pinpoint failure within the central face strut. The most heavily filleted structure has all the applied load centralized to the middle of the strut whereas less filleted case spreads it across more of the strut.

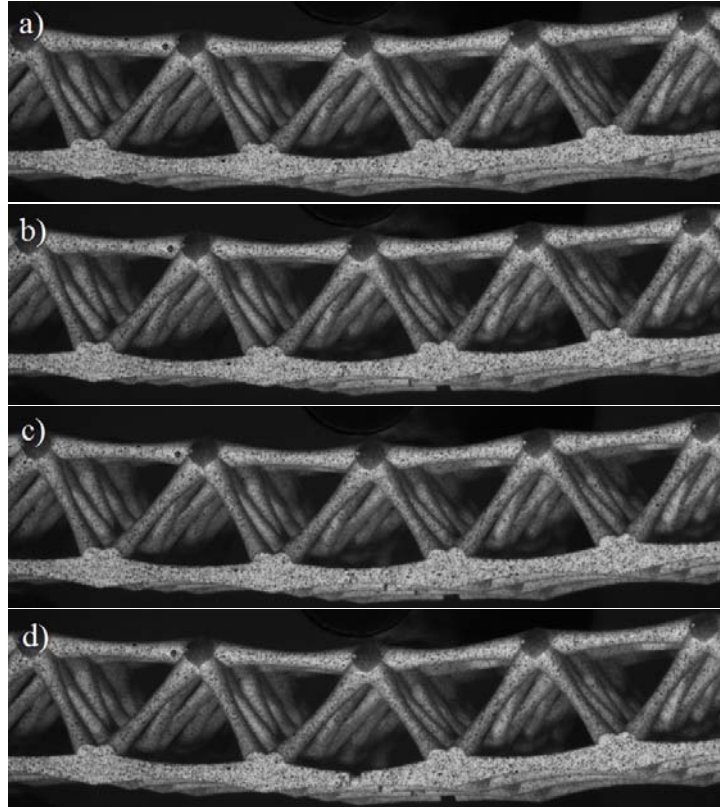


Figure 5.21: DIC raw images of the tapered SR20 microtruss structure during bending. Failure occurs by fracture at mid-point of the strut on the tensile side where it is thinnest (b). Because of the small size of these struts, the absorbed energy is not enough to break through the entire microtruss at once and leads to a strut-by-strut failure similar to the small-scale SR20 microtrusses (c-d).

5.4 Summary of key conclusions

The ability for the analytical model to predict the behaviour of microtrusses in bending was first tested on as-printed polymer microtrusses in this chapter. Across a variety of slenderness ratios and scales, good agreement was found. Only at the smallest scale did the printer begin to impact the load carrying capacity and the addition of a size effect term was required, which fit the data very well. Almost all predictions broke down at the extreme level of features less than 5x the layer height of the printer. The locations of optimal designs were predicted well for hollow columns, although deviations did exist in the inelastic global buckling regime due to curing effects on hollow structures. Improvements on the SR20 microtruss were attempted with the thinning of the lightly loaded core members offering significant weight performance benefit. Furthermore, the addition of fillets at the nodes increased ductility without compromising load carrying capacity as long as the fillets were not exceptionally large.

Chapter 6

Predictions based on derived models

Using the derived models for microtruss beams and individual columns in different loading scenarios, predictions can be made on the performance of these materials and locating optimal configurations. While this was performed in conjunction for purely polymer systems in Chapters 4 and 5, a truly versatile implementation of the analytical models will allow for various materials to be input to observe their effect on this optimal architecture such that even material selection can be optimized. This chapter looks at the input of metallic stress-strain curves and predicts the behaviour of metallic trusses in the following chapter. The majority of this work has been transferred into code in MATLAB and can be found in Appendix B.

6.1 Electrodeposited nickel material properties

Experimental tensile stress-strain curves for electrodeposited nickel having grain sizes of 10 μm , 71 nm, 38 nm and 21 nm are shown in Fig. 6.1. They were produced via pulsed electrodeposition on a Ti cathode in a modified Watts bath, after Erb *et al.* [4, 5], mechanically stripped from the Ti substrate and cut into coupons according to ASTM E8M-01 (see [116]). The coefficients, A , B and C , to fit these relations to the Voce constitutive relationship [139],

$$\sigma = B - (B - A)e^{-C\epsilon}, \quad (6.1)$$

The stocky compression coupon is expected to have significantly less cross-linking.

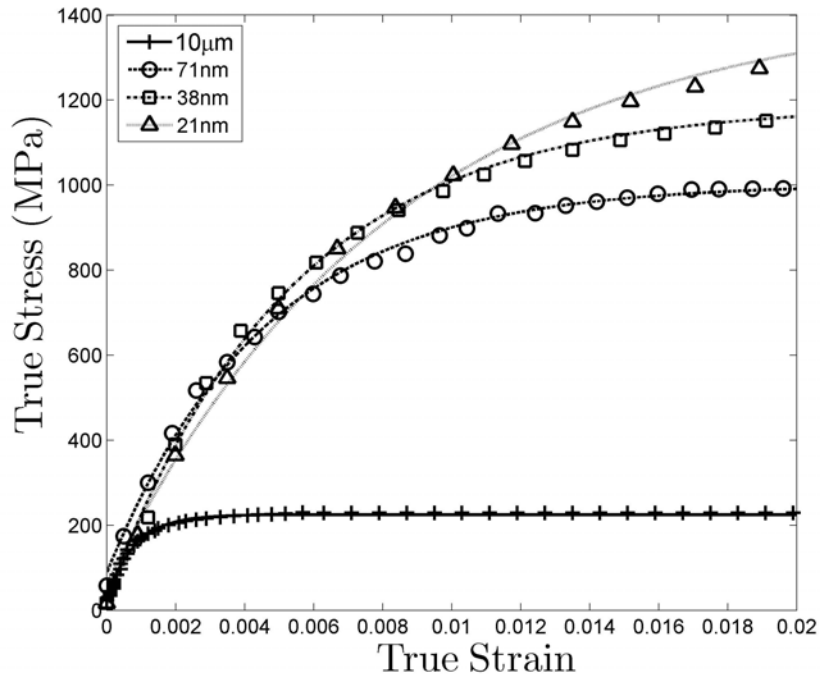


Figure 6.1: Experimental true stress-strain curves for four grain sizes of electrodeposited nickel, along with their Voce fits overlaid.

with strain ϵ and stress σ , are given in table 6.1.

The most conservative modeling approach assumes that the polymer preform ($\tilde{\rho} = 1.189 \pm 0.004 \text{ g/cm}^3$) contributes nothing but its mass to the beam (a reasonable assumption given the large differences in strength and elastic modulus). Ideally, the polymer preform is removed after electrodeposition, resulting in an all-metal lattice of hollow tubes. This configuration is inspired by INCOFOAM nickel foams, which are produced by electrodepositing conventional

Grain size (nm)	Young's modulus (GPa)	Yield strength (MPa)	Voce A parameter (MPa)	Voce B parameter (MPa)	Voce C parameter	R ² value for Voce fit
10,000	200	217	25	225	1240	0.992
71	199	726	87	1003	219	0.998
38	198	817	26	1189	187	0.998
21	162	905	61	1435	120	0.998

Table 6.1: Properties of four different electrodeposited Ni coatings and their fit statistics

polycrystalline nickel onto a polyurethane foam core before annealing at high temperature to vaporize the polymer [151]. This approach may be possible for the case of conventional polycrystalline nickel electrodeposition onto a polymer microtruss preform. In general, however, it would not be possible to apply a high temperature thermal decomposition treatment to the nanocrystalline nickel microtrusses given the comparatively low thermal stability exhibited in nanocrystalline metals [125]. For heat sensitive coatings, chemical dissolution methods may be developed to remove the polymer preform, as was recently outlined for ultralight-weight architectures [152, 45]. Both the hollow tube and polymer-filled configuration are considered here in order to bound the possible behaviour of the nanocrystalline microtrusses.

6.2 Polycrystalline nickel: columns and microtruss beams

Two design variables, \bar{r} and \bar{n} , determine the slenderness and coating thickness of the column, and must be optimised to find the minimum mass for a required design load [153]. Failure mechanism maps [30] are used here as graphical illustrations of the relationship between the modes of failure and the optimal trajectory in design space. Figure 6.2 shows the failure mechanism map for a polycrystalline (10 μm grain size) nickel column. The mechanism maps assume that there is no interaction between failure mechanisms; that is, impending failure in one mechanism does not cause premature failure by another mechanism. At the boundaries between regions, failure occurs by two or more mechanisms simultaneously. Small \bar{n} promotes local shell buckling while small \bar{r} encourages global buckling. Each buckling zone is further divided into elastic and inelastic zones - elastic global buckling at small \bar{n} and elastic local shell buckling at very small \bar{r} . As the column becomes stockier and the coating thicker, inelastic buckling prevails. In addition, a region corresponding to ultimate failure for a tensile specimen and governed by σ_u is included on the assumption that at this stress level the column is fully yielded and cannot carry larger loads. Note that for the case of very low coating thicknesses ($\bar{n} < 0.01$) (see [154]), complex buckling modes may begin to dominate the mechanical

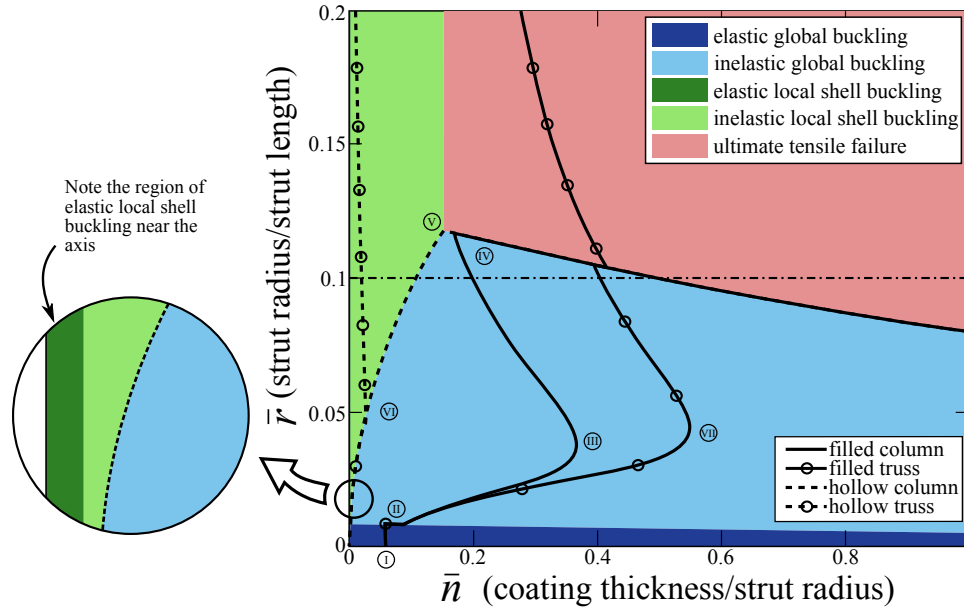


Figure 6.2: Failure mechanism map for polycrystalline nickel columns and microtrusses showing five active failure zones: elastic and inelastic global buckling, elastic and inelastic local shell buckling and ultimate tensile failure. Note: elastic local shell buckling is along the \bar{r} axis for $\bar{n} < 0.01$. The architectural upper bound for microtrusses with $\bar{r} = 0.1$ (slenderness ratio of 20) is also shown.

behaviour. Further analysis would be required to optimize the architecture for such low density materials.

Because the polymer preform is treated as a parasitic mass that does not influence the strength of the column, the mechanism maps are identical for the hollow and filled cases. However, the optimal trajectories for minimum mass designs are very different. The optimal trajectory for filled columns begins in the elastic global buckling region, at $\bar{r} = 0$ (Fig. 6.2, I), while \bar{n} is a function only of $\tilde{\rho}$. As \hat{F} increases, the trajectory crosses the elastic global buckling region at nearly constant \bar{n} and passes into the inelastic global buckling region (Fig. 6.2, II), whereas \bar{r} increases \bar{n} increases to a maximum, and then diminishes, creating a nose-like feature on the trajectory (Fig. 6.2, III). The optimal trajectory subsequently follows the boundary between inelastic global buckling and ultimate strength (Fig. 6.2, IV). In contrast, for a hollow column, the optimal trajectory begins at the origin and with increasing \hat{F} follows the boundary between global buckling and local shell buckling, both in the elastic and inelastic

regions, to the point where inelastic global buckling, inelastic local shell buckling and ultimate failure occur simultaneously (Fig. 6.2, V). For greater \hat{F} , all optimal designs governed by ultimate strength have equal mass. In all cases, the optimal filled columns have substantially smaller radii and thicker coatings than the hollow columns.

For microtrusses, \bar{r} and \bar{n} are supplemented by the design variable \bar{u} , which determines the scale of the unit cell relative to the extent of the beam. However, the value of \bar{u} does not affect the operative failure mechanism: the boundaries between the failure regions are all parallel to the \bar{u} axis as each governing failure equation is a function of \bar{u}^2 . The optimal design of a truss-core beam maximizes \bar{u} , subject to manufacturing constraints. Microtruss mechanism maps will therefore be restricted to the (\bar{n}, \bar{r}) design space with an assumed value of $\bar{u} = 0.05$, equivalent to twenty unit cells along the length of the beam. A key consequence of the insensitivity to \bar{u} is that the failure mechanism map for a microtruss in the (\bar{n}, \bar{r}) design space is identical to that of a column of the same material; Fig. 6.2 is therefore also the failure mechanism map for a polycrystalline nickel microtruss.

The optimal trajectories for filled and hollow polycrystalline nickel microtrusses were computed and are also plotted on Fig. 6.2. For polymer-filled structures, the column and microtruss trajectories both originate from the elastic global buckling zone at a fixed \bar{n} of 0.06 (a function of the density ratio of the nickel and polymer), pass through the inelastic global buckling zone but follow different paths at the ultimate tensile failure boundary. For hollow structures, both columns and microtrusses initially follow the local shell buckling/global buckling boundary. While hollow columns reach ultimate tensile failure and progress down the tensile failure/inelastic global buckling boundary, hollow microtrusses remain optimal at low \bar{n} and the optimal trajectory enters the inelastic local shell buckling zone (Fig. 6.2, VI). Manufacturing considerations typically militate a maximum \bar{r} for microtrusses, so that the struts are sufficiently slender to enable the assembly of the unit cells. In this case an upper bound of $\bar{r} \leq 0.1$, equivalent to a slenderness ratio of 20, is plotted on Fig. 6.2, as well as the continuations of the optimal trajectories were this restriction not in place.

6.3 Grain size reduction (increasing \hat{P})

For the four electrodeposited material systems studied herein, reducing the grain size greatly increases the yield strength and moderately decreases the elastic modulus (see table 6.1). For both columns and microtrusses, grain size reduction decreases the region of design space associated with ultimate tensile failure, replacing it with inelastic global buckling and inelastic local shell buckling. That is, some designs governed by ultimate tensile strength when the coating is polycrystalline nickel experience failure by buckling at greater \hat{P} when the coating is nanocrystalline. As the strength of the nanocrystalline coating increases, larger regions of design space switch from ultimate failure to buckling failure. Fig. 6.3 shows the evolution with decreasing grain size of the triple point where inelastic global buckling, inelastic local shell buckling and ultimate tensile failure occur simultaneously. Note that the boundary between global buckling and local shell buckling is a function only of Poisson's ratio, which is equal for the nickel variants, and hence this boundary is constant for all cases here.

Increasing the nickel yield strength by grain size reduction increases the structural strength for all microtrusses subject to ultimate tensile failure. A direct substitution of nanocrystalline nickel for polycrystalline nickel produces a gain in strength of up to a factor of 6 if the strengths of both designs are governed by ultimate tensile failure. On the other hand, in the small regions of elastic global buckling ($\bar{r} < 0.01$) and elastic local shell buckling ($\bar{n} < 0.01$) that are relevant for extremely low loads, the performance of the structure is determined by the Young's modulus of the nickel. Since the three nanocrystalline nickels considered here have slightly lower Young's modulus than the 10 μm polycrystalline nickel (most likely from crystallographic texture effects [124]), the polycrystalline nickel is preferred. In the inelastic buckling regions, the strength of the microtruss depends upon the shape of the nickel stress-strain curve and the rate of tangent modulus reduction before ultimate strength. Grain size dependent strain hardening characteristics are therefore a key consideration of the overall microtruss design.

However, even though decreasing the grain size in an optimally designed polycrystalline

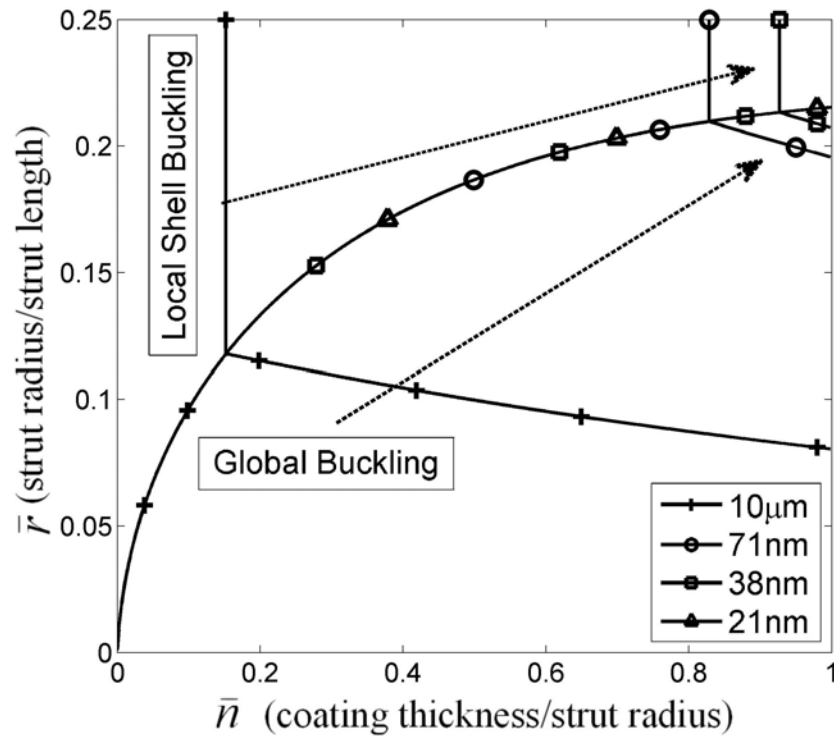


Figure 6.3: Boundaries between global buckling, local shell buckling and ultimate tensile failure for the four considered grain sizes highlighting the movement of the triple point with decreasing grain size. For the 21 nm grain size, the ultimate tensile failure zone falls outside the range of \bar{r} and \bar{n} shown here.

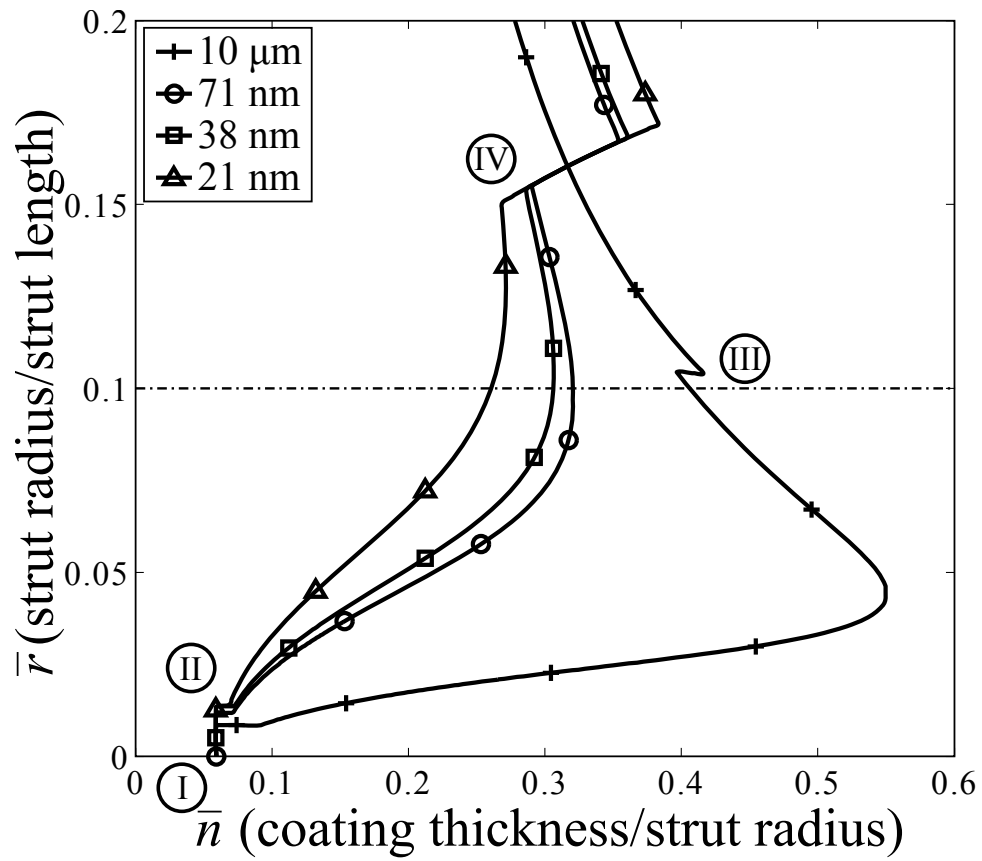


Figure 6.4: Optimal trajectories for nickel/polymer microtrusses showing a trend of decreasing optimal \bar{n} with decreasing grain size in the inelastic global buckling zone.

nickel microtruss can significantly increase the load carrying capacity, the new nanocrystalline nickel microtruss would no longer be optimal. This is because the failure mechanism map and optimal trajectory are functions of the grain size through the changing material properties. The trajectories, shown in Fig. 6.4, all begin at $\bar{r} = 0, \bar{n} = (1 - \bar{\rho})^{-1/2} - 1$ (Fig. 6.4, I), determined by the nickel and polymer densities. At low \hat{P} , elastic global buckling dominates and the trajectories are similar until inelastic global buckling is activated (Fig. 6.4, II). Thereafter, as \hat{P} increases, the coating thickness, \bar{n} , increases more rapidly for nickel variants with lower ultimate tensile strengths. At high \hat{P} , the polycrystalline nickel microtruss is subject to ultimate tensile failure (Fig. 6.4, III). The strength of optimally designed 21 nm grain size nickel microtrusses are never governed by ultimate tensile failure; instead, the optimal trajectories pass along the boundary between global buckling and local shell buckling, and finally into the inelastic local shell buckling region (subject to the maximum \bar{r} restriction noted above) (Fig. 6.4, IV).

The extent to which the strut design must also be changed when the grain size is decreased can be seen in Fig. 6.5 where optimal \bar{n} is plotted as a function of \hat{P} for 10 μm grain size and 21 nm grain size variants. The difference between optimal \bar{n} is smallest in the low \hat{P} regime (where failure is controlled by elastic global buckling) (Fig. 6.5, I), becomes increasingly divergent at moderate ratios of \hat{P} (where failure in both materials is controlled by inelastic global buckling) (Fig. 6.5, II) and decreases again once the polycrystalline microtruss reaches its ultimate tensile strength (Fig. 6.5, III). The effect of grain size on the optimal design is best illustrated by taking a specific example. Here, 1 m long by 0.5 m wide microtruss beams supporting an 11 kN applied load are considered. Substituting these values into equation (3.43) gives a load index of $\hat{P} \approx 1 \times 10^{-4}$ which, for the polycrystalline nickel/polymer microtruss, gives an optimal design near the maximum \bar{n} on the optimal trajectory (Fig. 6.2, VII). This selection will exemplify the maximum effect of grain size on the optimal architecture in the microtruss. Choosing $\bar{u} = 0.05$ results in 58 mm long struts with 20 unit cells along the length of the beam. The resulting optimal strut designs are shown in Fig. 6.6 and summarized in

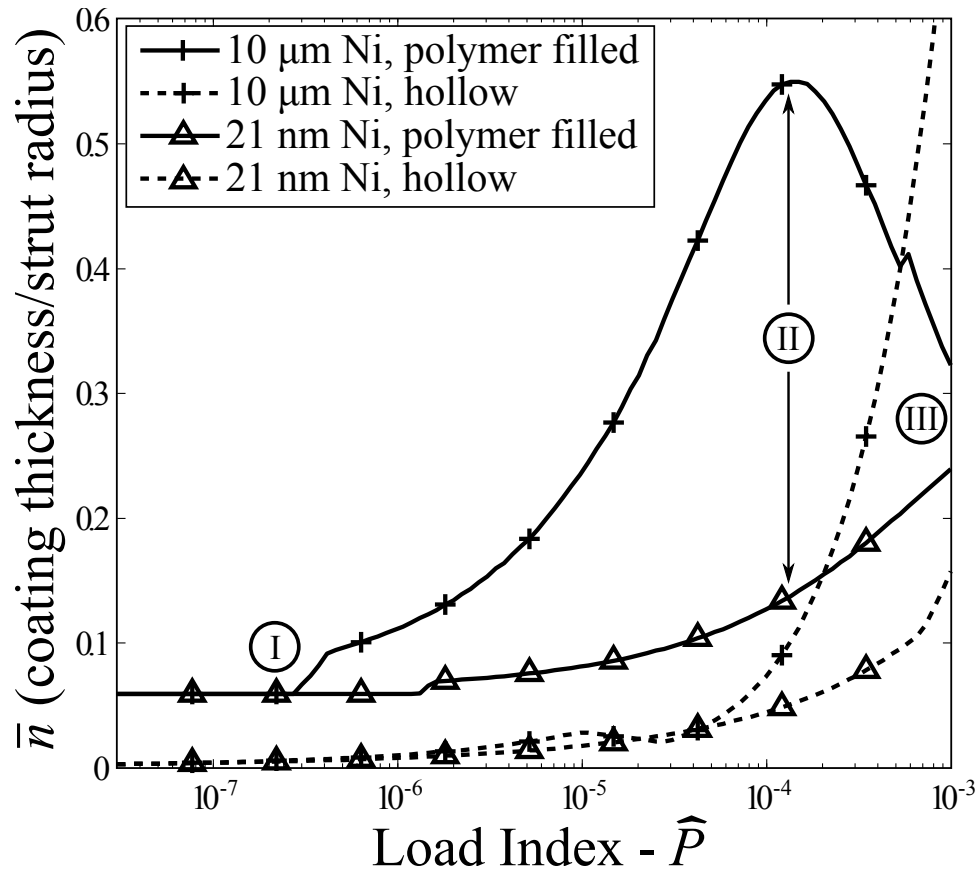


Figure 6.5: Optimal trajectories for nickel/polymer microtrusses as a function of the load index, \hat{P} .

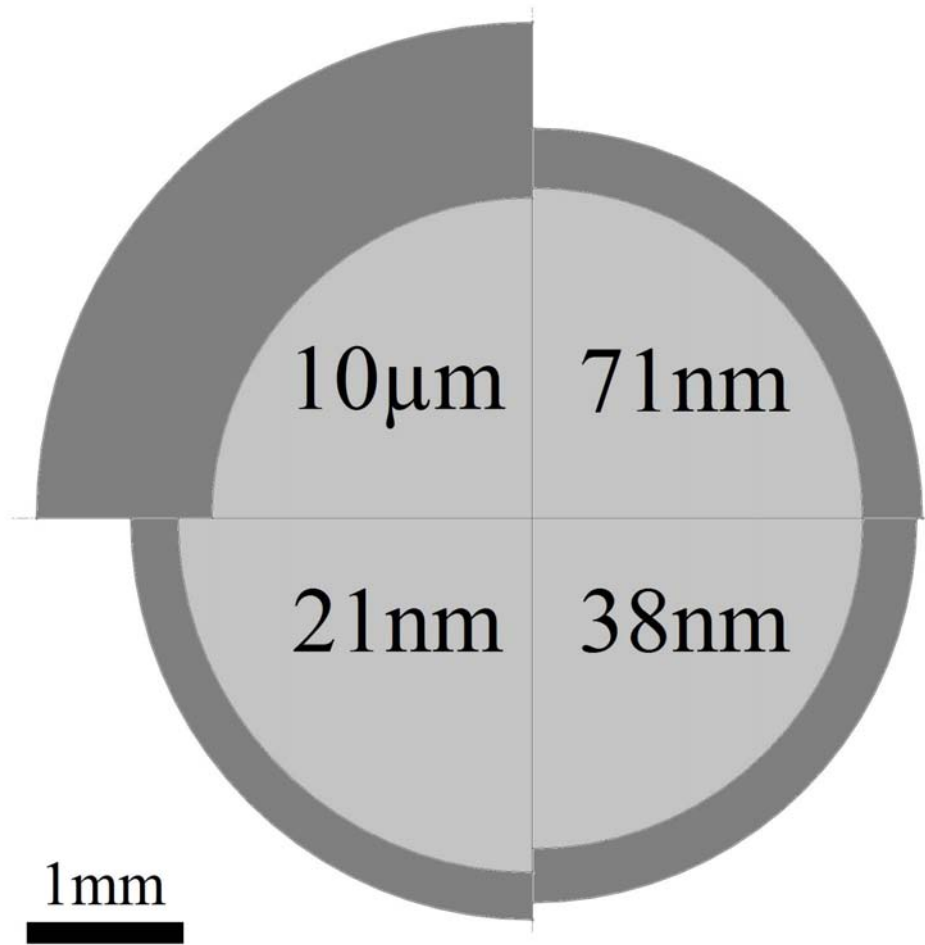


Figure 6.6: Quarter circle cross-sectional view of optimal nickel/polymer microtruss struts for the four different grain sizes indicated based on a load of 11 kN on a 1 m x 0.5 m microtruss beam loaded in three-point bending. With decreasing grain size, the optimal polymer core radius increases and the optimal coating thickness decreases, resulting in an overall beam mass reduction from 32.7 kg for 10 μm nickel to 10.6 kg for 21 nm nickel.

table 6.2. There is a general trend of increasing polymer core radius and decreasing coating thickness as the grain size is reduced (the slight decrease in core radius between the 71 nm and 38 nm grain size struts is due to subtle differences in the elastic to plastic transition of these two materials). The struts fail by plastic global buckling in all four cases, but the overall mass of the microtruss decreases from 32.7 kg to 10.6 kg as the grain size is reduced from 10 μm to 21 nm.

Grain size (nm)	Filled			Hollow		
	Optimal r (mm)	Optimal n (mm)	Mass (kg)	Optimal r (mm)	Optimal n (mm)	Mass (kg)
10,000	2.07	1.14	32.7	5.00	0.48	25.4
71	2.13	0.39	11.7	3.54	0.19	7.1
38	2.13	0.35	10.8	3.42	0.18	6.2
21	2.29	0.31	10.6	3.35	0.17	5.8

Table 6.2: Optimal design dimensions for struts in a 1 m x 0.5 m microtruss supporting 11 kN in three-point bending for the four grain sizes considered and both filled and hollow scenarios

6.4 Core removal (decreasing \hat{M})

An alternative route for maximizing the efficiency of electrodeposited microtrusses is removal of the polymer preform after coating. Given the conservative assumption that the polymer preform does not contribute to the load carrying capacity, the failure mechanism map does not change with preform removal. However, the optimal trajectories differ significantly because of their strong dependence upon $\bar{\rho}$, which becomes zero once the core is removed. The trajectories of optimal design for hollow microtrusses, shown on Fig. 6.7, begin at the origin and follow the boundary between local shell buckling and global buckling until deviating into the inelastic local shell buckling region (Fig. 6.7, I), with the deviation occurring at a higher load level for stronger materials (Fig. 6.7, II). At relatively low load levels, hollow microtrusses are subject to the restriction on maximum \bar{r} . Optimally designed hollow microtrusses have larger internal diameters and smaller coating thicknesses than optimal filled microtrusses, favouring local shell buckling failure. Figure 6.8 illustrates (and table 6.2 summarizes) the optimal strut design for the example previously given (58 mm long struts, 20 unit cells along the beam length and $P=11$ kN). That the removal of the polymer preform material entails significant geometric changes to maintain optimality is illustrative of the key point of this paper: material changes, such as core removal (which is in effect a change in the material properties of the core) or a direct material substitution, may bring direct benefits, but *to exploit fully the advantages of the material change requires large geometric changes to the design.*

Because of the thermal instability of nanocrystalline nickel, it may not be possible to re-

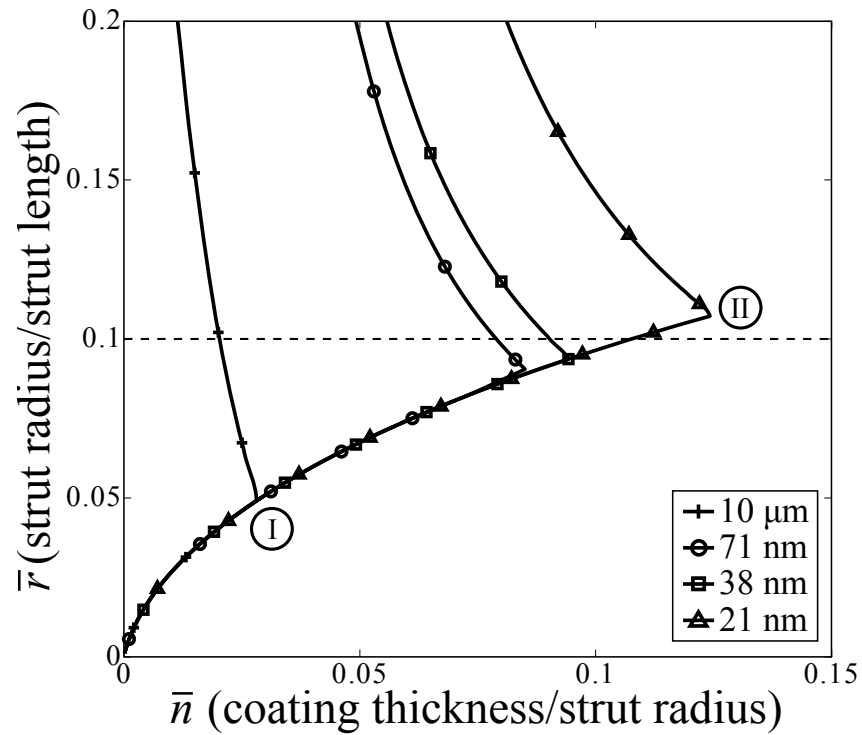


Figure 6.7: Optimal trajectories for hollow nickel microtruss showing a trend of increasing optimal \bar{n} with decreasing grain size in the inelastic local shell buckling zone. Additionally, all four grain sizes share the same initial optimal trajectory displaying material property independence until local shell buckling activation.

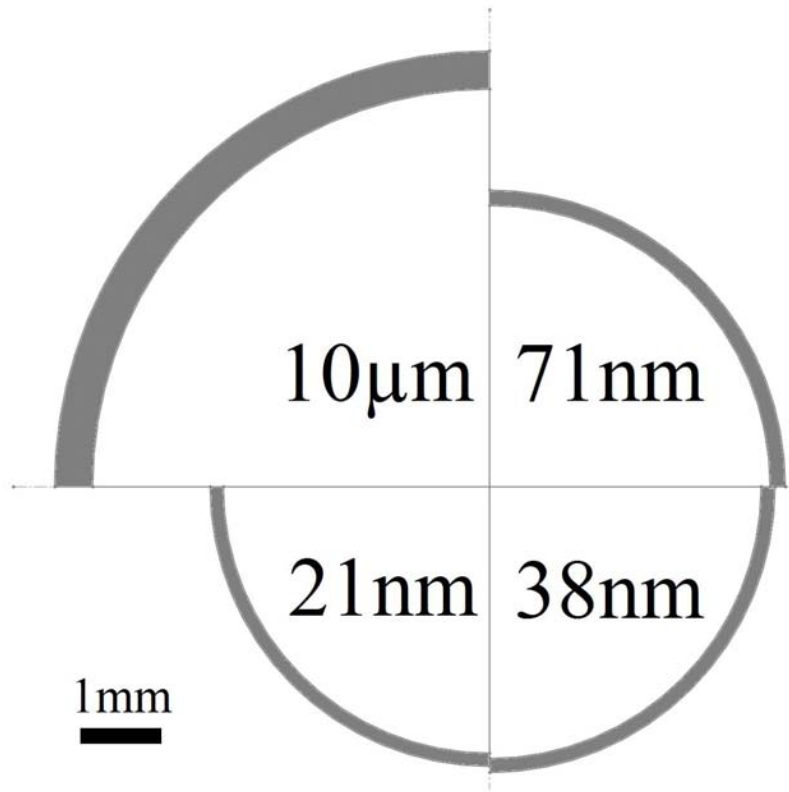


Figure 6.8: Quarter circle cross-sectional view of optimal hollow nickel microtruss struts for the four different grain sizes indicated based on a load of 11 kN on a 1 m x 0.5 m microtruss beam loaded in three-point bending. With decreasing grain size, the optimal polymer core radius decreases and the optimal coating thickness decreases, resulting in an overall beam mass reduction from 25.4 kg for 10 μm nickel to 5.8 kg for 21 nm nickel.

move the polymer preform without degrading the nickel properties. A key question is whether it is preferable to concentrate on removing the polymer preform from a polycrystalline microtruss, or use a nanocrystalline coating despite being forced to retain the parasitic core. Figure 6.9 displays the minimum mass index as a function of desired load index for filled and hollow microtruss beams composed of 10 μm and 21 nm grain size nickel. At a load index near zero, the filled microtrusses exhibit non-zero mass: this is because of the mass of the parasitic polymer core. Hollow structures, by contrast, approach zero mass for zero load index. At small load indices, the effect of removing the polymer core is greater than the effect of decreasing the grain size because the strains at failure are in the elastic or near-elastic regime; the hollow polycrystalline nickel structures are lighter than the nanocrystalline nickel structures with polymer cores (Fig. 6.9, I). As the load index increases, the mass of optimal polycrystalline microtrusses increases more rapidly than the mass of optimal nanocrystalline microtrusses because the specific strength of the polycrystalline nickel is much lower. Consequently, there is a transition \hat{P} above which the *filled* nanocrystalline nickel microtruss is more mass efficient than the *hollow* polycrystalline nickel microtruss; the transition occurs at $\hat{P} \approx 6.6 \times 10^{-6}$ (Fig. 6.9, II). Thereafter, and for the remainder of the potential design space, nanocrystalline nickel coatings with parasitic polymer cores are more mass-efficient than hollow polycrystalline nickel microtrusses. Using the example of a 1 m by 0.5 m microtruss, this transition point corresponds to a load of 0.7 kN. Figure 6.10 illustrates the optimal strut design at this applied load. The 10 μm nickel/polymer microtruss has a mass of 3.2 kg and relative density of 1.4%. The 10 μm grain size hollow core and the filled 21 nm grain size optimal configuration yield in a 38% mass reduction to 2.0 kg (0.9% relative density). A hypothetical 21 nm grain size hollow microtruss would perform best with a total mass of only 0.7 kg (0.3% relative density). For loads greater than the transition point of 0.7 kN, the 21 nm grain size microtruss with the polymer core has a lower mass than the hollow polycrystalline configuration. Thus, for most design cases, *an optimal filled nanocrystalline microtruss is lighter than an optimal hollow polycrystalline microtruss.*

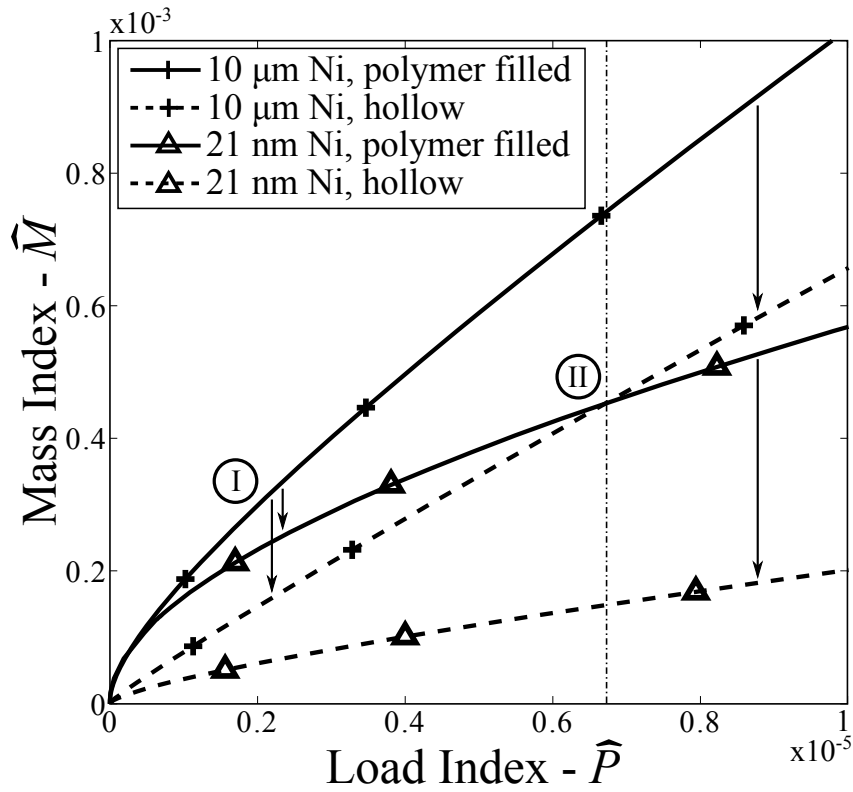


Figure 6.9: Optimal design trajectories for nickel/polymer and hollow nickel microtruss beams with 10 μm and 21 nm grain sizes. For a given load index, \hat{P} , a minimal mass index, \hat{M} , is desired, resulting in 21 nm hollow nickel beams being the preferred option over all available \hat{P} design space. At $\hat{P} > 6.6 \times 10^{-6}$, even 21 nm nickel/polymer designs are lighter than 10 μm hollow nickel ones. Arrows indicate the reduction in mass index associated with polymer core removal for a given \hat{P} , such that complete removal leads to the hollow dashed line.

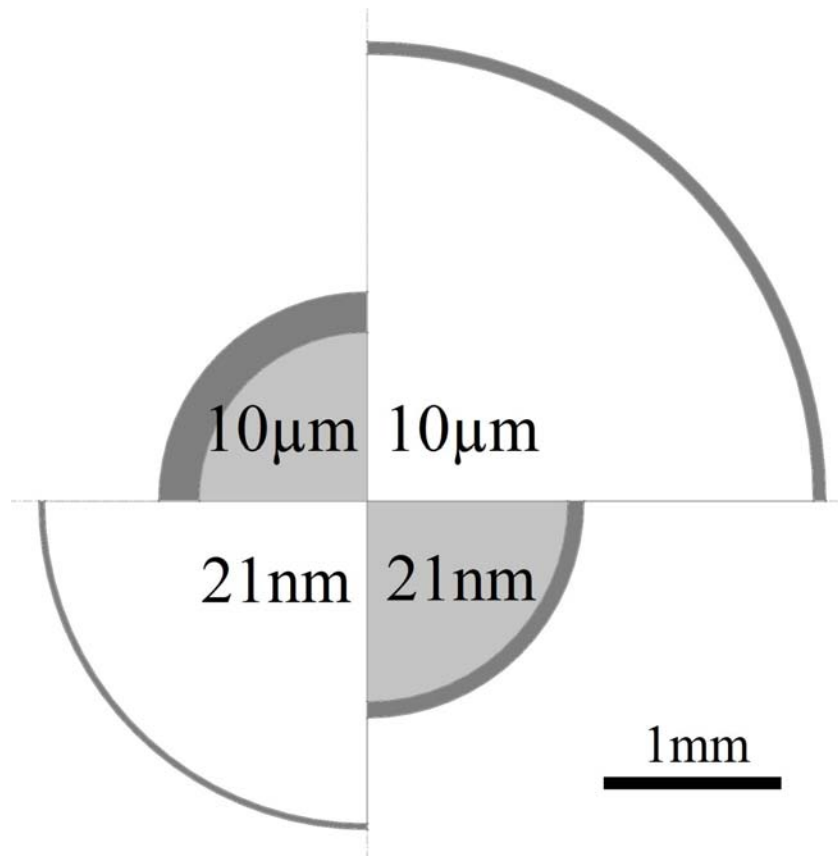


Figure 6.10: Based on a load of 0.7 kN on a 1 m x 0.5 m microtruss beam in three-point bending, optimal cross-sections for nickel/polymer and hollow nickel struts with the labelled grain sizes are displayed. Starting at the top-left and working clockwise, the mass of the optimal beam decreases from 3.2 kg to 2.0 kg (for both hollow 10 μm nickel and 21 nm nickel/polymer scenarios) to 0.7 kg.

6.5 Other strengthening techniques

By decreasing the crystalline grain size to the nm-scale, nanocrystalline materials have been shown to offer a large improvement in mechanical strength over their conventional polycrystalline counterparts. However, this is not the only route to improving the quality of the electrodeposited coating. This section looks at the additional effect of alloy chemistry in nanocrystalline Ni-Fe alloy (n-NiFe) microtrusses having a pyramidal internal architecture. In order to evaluate the effects that grain size and alloy chemistry would have on the architectural optimization of n-NiFe microtrusses, a database of 47 n-NiFe tensile curves (grain sizes ranging from 11 nm to 20 nm and alloy concentrations ranging from 3 to 14wt.% Fe) was provided by the industrial partner, Integran Technologies, Inc. [155]. The electrodeposited n-NiFe had been plated on Ti cathodes, after Ref. [erb patent], to thicknesses in the range of 0.5 to 2 mm, after which the deposits were mechanically stripped from the cathode and tensile coupons were cut using electrical discharge machining to dimensions based on ASTM E8M [156]. These tensile curves were then fit to a Voce fit, described in equation 6.1, and the main fitting parameters were extracted.

A map of the B and C Voce parameters for the analyzed tensile curves is plotted in Fig. 6.11. The 47 values are clustered along a relatively narrow band of fitting parameter space, extending from $B = 1367$, $C = 114$ (generally larger grain size) to $B = 1874$, $C = 97$ (generally smaller grain size). Figure 6.11 therefore illustrates that those n-NiFe electrodeposits exhibiting a higher tensile strength (i.e. having larger values of B) tend to have a more gradual (less sharp) knee in the stress-strain curve leading to a lower value of the C fitting parameter. This change in the elastic to plastic transition of the stress-strain curve represents an important consideration for the design of n-NiFe reinforced microtrusses, since the failure strength (and by extension the optimal architecture) depends on local values of the tangent modulus of the stress strain curve. To see the impact of this behaviour on the optimal architecture of n-NiFe microtrusses, three representative curves (falling at the upper, lower, and middle of the cluster of values shown in Fig. 6.11) were selected as the basis for further consideration and are shown below

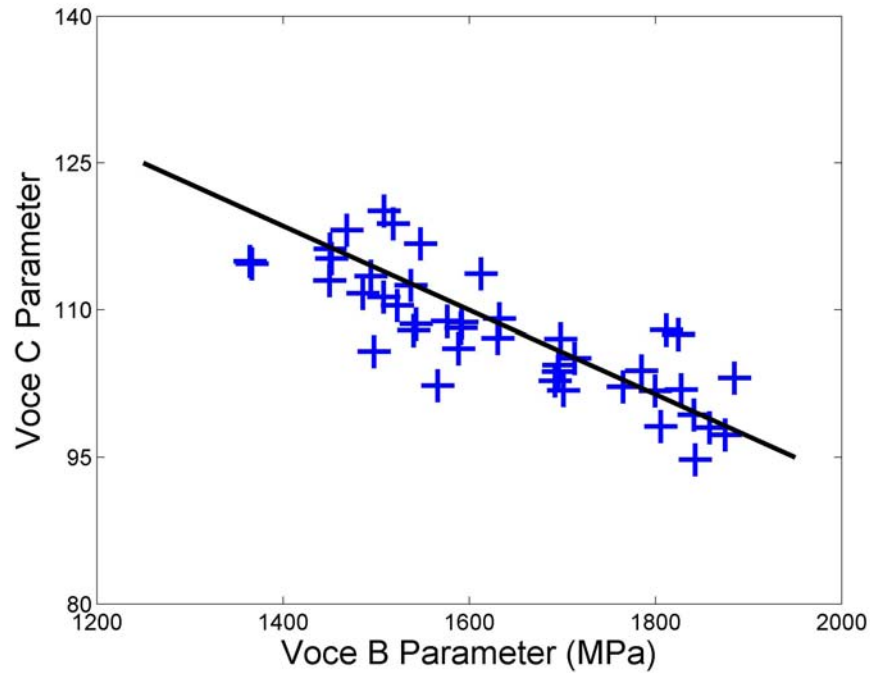


Figure 6.11: Mapped B and C Voce fitting parameters for 47 n-NiFe curves with varying iron content overlaid with a linear fit.

	Grain size (nm)	Young's modulus (GPa)	Yield strength (MPa)	Voce B parameter (MPa)	Voce C parameter	R ² value for Voce fit
Ni-3.4% Fe	19	139	858	1367	114	0.999
Ni-8.5% Fe	16	148	998	1592	109	0.998
Ni-11.7% Fe	15	150	1164	1874	97	0.999

Table 6.3: Material properties for the three n-NiFe curves considered

(Fig. 6.12), with their relevant material properties outlined in table 6.3.

Using the derived failure mechanism equations, Fig. 6.13 shows a failure map of the 19 nm grain size Ni-3.4%Fe sample that plots the available design space in terms of \bar{r} and \bar{n} . The optimal is plotted on the failure mechanism map for the Ni-3.4%Fe curve (Fig. 6.13). The trajectory begins at the x-axis in the elastic global buckling zone. It travels upwards until reaching the inelastic global buckling region where it follows a curved path up until the boundary with the inelastic local shell buckling zone. After a short distance along this boundary, it continues upward through the inelastic local shell buckling region. Although all points along this curve

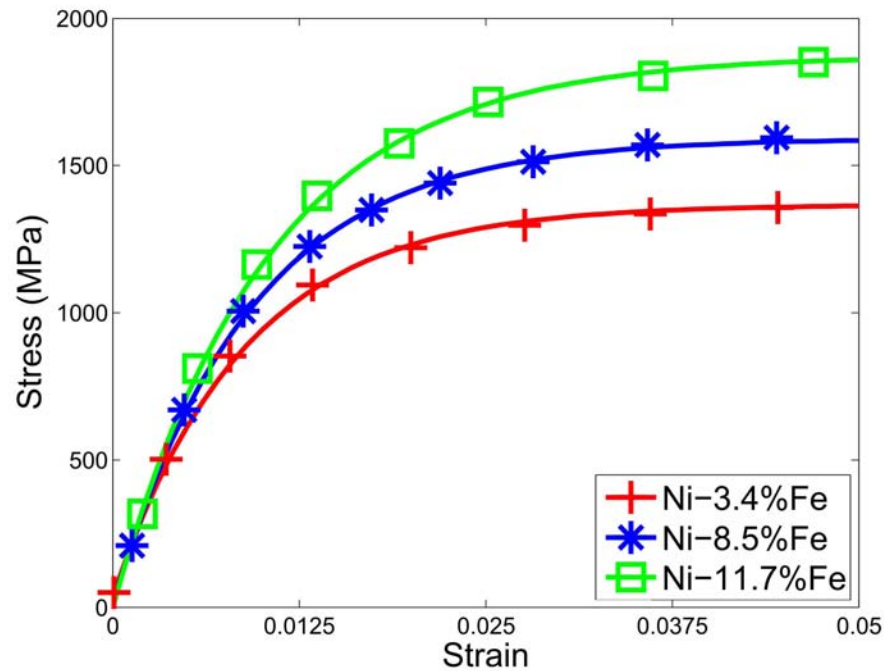


Figure 6.12: Experimental stress-strain curves for the three n-NiFe curves considered with their corresponding Voce fits overlaid.

are optimal, a cut-off was set at $\bar{r}=0.1$ as structures with higher \bar{r} values have struts too stocky to form into a square pyramidal unit cell without the introduction of a significant nodal region in which the model would underpredict the microtruss strength severely.

The map can now be used as a design guide for a given loading scenario as done for the effect of grain size on nickel coatings. For a beam of microtruss material with length 1 m, width 0.5 m and holding a load of 5 kN at mid-span in three-point bending, the non-dimensionalized load index is 5×10^7 . All points in the failure map with this load index can be shown as a load contour (Fig. 6.13). This contour will intersect the optimal trajectory at one point and that is where the optimal architecture lies for this design example.

By repeating this analysis for the other two NiFe curves, the three optimal trajectories are extracted and are plotted below (Fig. 6.14); a similar shape and trend is seen in all three cases. However, if the optimal architecture from the Ni-3.4%Fe were used for the two stronger coatings, the structures would be sub-optimal. With increasing iron content in the coating, the

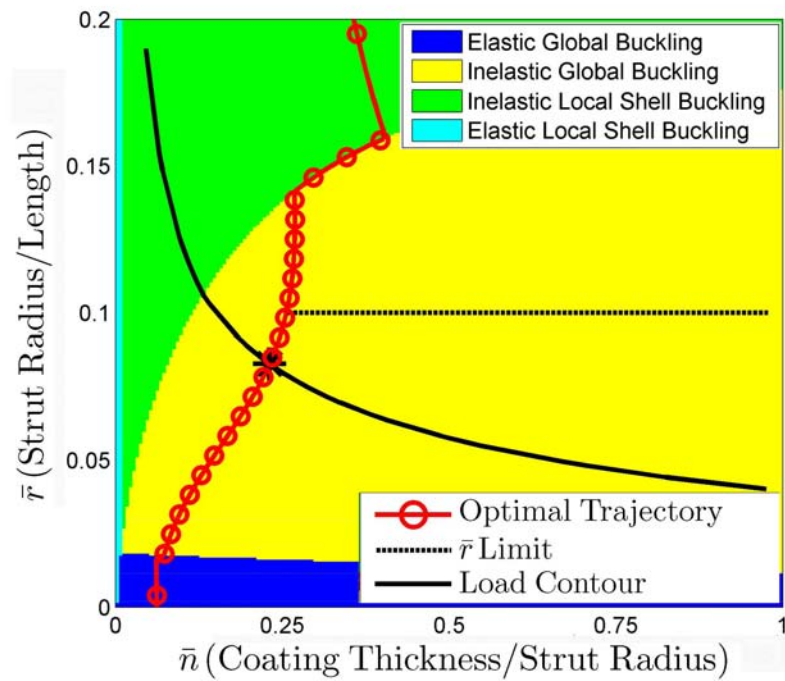


Figure 6.13: Failure mechanism map for the Ni-3.4%Fe microtruss showing four active zones as well as the optimal trajectory. The load contour of 5×10^{-7} intersects the optimal trajectory at one point the optimal architecture. Additionally, the $\bar{r}=0.1$ limit is shown.

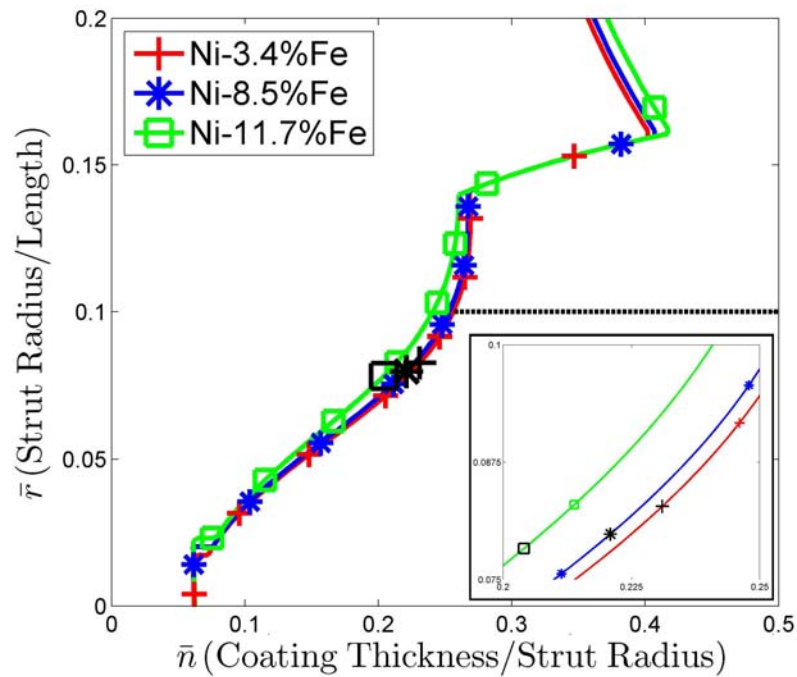


Figure 6.14: All three optimal trajectories for each of the three curves plotted together showing the same general shape but differing locations for optimal design for the same applied design load. Inset shows a close-up of the three optimal architectures.

optimal architecture shifts to smaller \bar{r} and \bar{n} values for the same applied load. A higher iron content (smaller grain sized material) requires a thinner coating and smaller strut radius making the overall mass of the microtruss lower: from 2.4kg to 1.9kg as the grain size is reduced from 19nm to 15nm and the Fe concentration increased from 3.4% to 11.7% illustrating the significant effect that subtle microstructural changes can have on the mechanical performance of nanocrystalline microtruss materials. Just as in the case of decreasing grain size in nanocrystalline Ni coatings, the use of a stronger coating material offers improvements in mechanical performance but results in a non-optimal design. Modifications to the architecture can utilize this improved coating more efficiently to create new optimal composites. Overall, the specific properties of the nanocrystalline alloy will determine the ideal architecture and design.

6.6 Summary of key conclusions

The direct impact of material selection and geometry on the optimal design of a microtruss was looked at in this chapter. Designing a microtruss with a given material choice in mind results in the prediction of an optimal architecture. Substituting this material for a stronger one (e.g. decreasing grain size in the coating, alloying the coating, new material altogether, etc.) will improve performance but there exists an architecture with this new material choice that would perform even better. Furthermore, the removal of the polymer core would also improve the beam performance but again, if this was intended from the start, a better architecture can be located that will outperform this hollow system. This chapter serves to show that the model developed here is extremely applicable and useful in that you need only select the load you wish to apply and optimal structures will be identified for you.

Chapter 7

Metallic microtrusses

The quality of these coatings was characterized in the bending of Ni-coated polymer rods and the bending of Ni-coated polymer trusses. For the case of microtruss beams in bending, the results here will be compared to the predictions in chapter 6 to further validate the derived optimization model in this thesis. The exact recipe that was developed to create a conductive coating on the polymer material as well as the steps involved in electrodeposition are presented in appendix D. They were used on both the rods and microtrusses presented here.

7.1 Metal/polymer rods in bending

With a methodology present that works on this specific stereolithographic polymer, small rods were plated with increasingly thicker coatings of Ni to probe the quality of the electrodeposited material. Figure 7.1 provides a schematic of the setup for electroplating with five rods racked up at once during one plating cycle. Anodes are kept on either side to improve coating uniformity; the outer of the five will still coat slightly thicker due to the anode geometry. A cross-section is also shown of the polymer interior with a thin electroless layer and the final Ni top layer. The intermediate tin monolayer and thin palladium layer are neglected.

To distinguish between the different rods with different levels of treatment on them, a labelling system was introduced. This was necessary not just for identification but also because

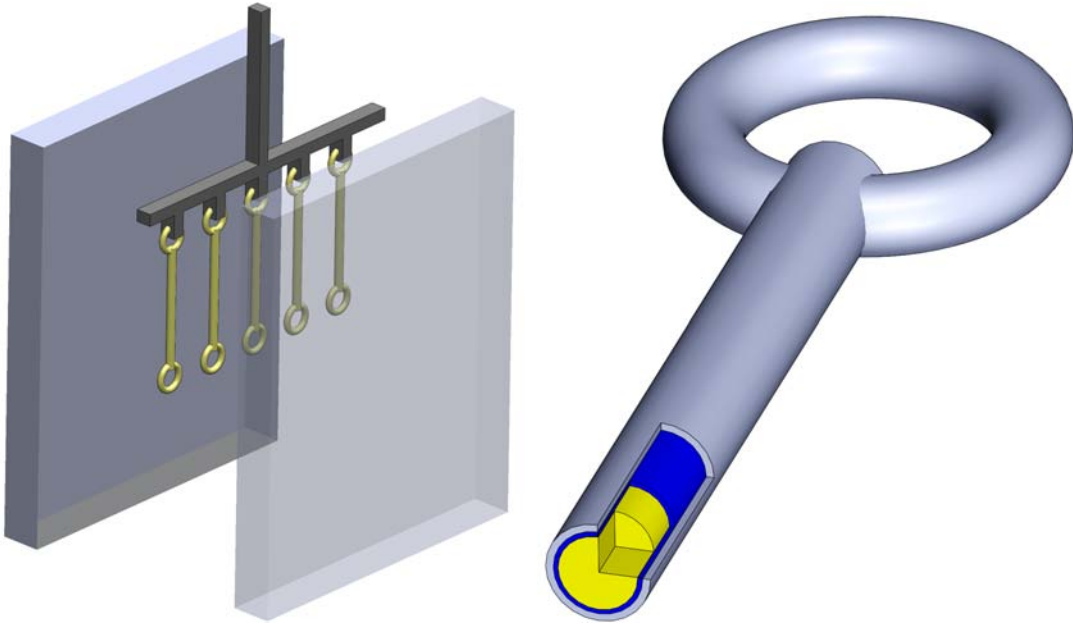


Figure 7.1: Polymer rods were hung five at a time in a modified nickel sulfamate bath and placed between two anodes during electrodeposition (left). The cross-section of a plated polymer rod is shown with a thin blue layer identified as the electroless Ni joining the electrodeposited outer coating to the polymer interior (right).

the level of etching from batch to batch differed slightly. A three number system was used where the first value corresponds to the thickness of Ni in μm electrodeposited followed by the thickness in μm of Ni deposited during the electroless deposition step. Finally, the radius of the polymer rod in the as-finished structure is listed in *mm* as the third number. For example, an as-printed rod with radius 0.9 mm would be labelled 0/0/0.9, while a 10 μm thick Ni coating on a 3 μm electroless Ni layer with a polymer rod of radius 0.95 mm would be labelled 10/3/0.95.

The use of an etching step was necessary to metalize the sample, but it also changed the mechanical performance of the polymer rod. Samples were removed from different stages of the plating process to see how etching and applying the thin electroless Ni coating affected its bending behaviour (Fig. 7.2). The average peak force fell from 8.2 ± 0.2 N to 6.1 ± 0.1 N but the maximum deflection did increase slightly from 5.8 ± 0.4 mm to 6.0 ± 0.1 mm. The decrease in force was attributed to the 10% decrease in radius after etching (table 7.1), while the newly smoothed surface was devoid of obvious surface roughness that can act as stress concentrators and potentially lead to earlier fracture. The addition of a 3.6 ± 0.1 μm electroless

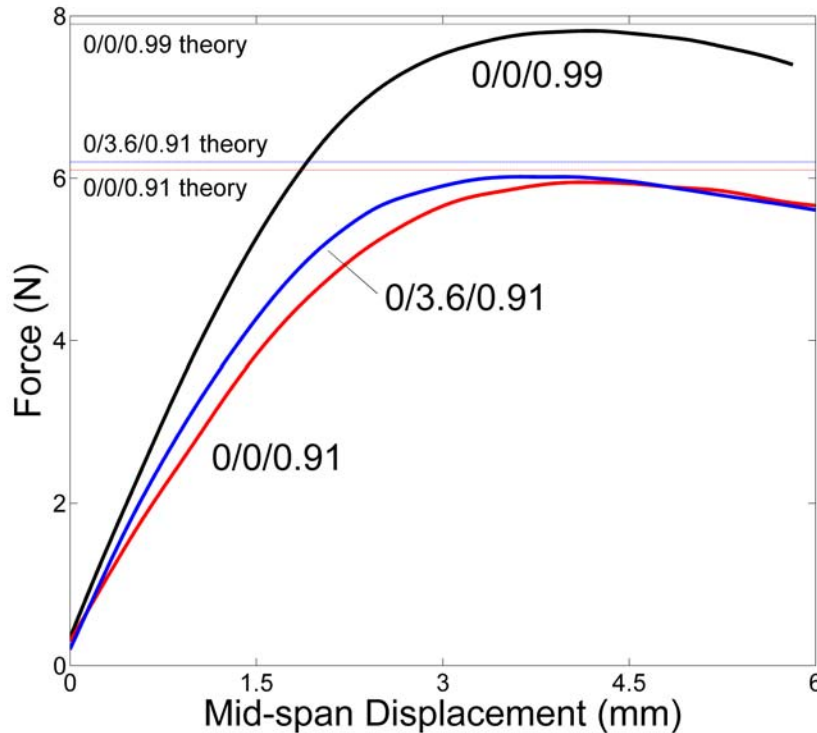


Figure 7.2: Force-displacement curves for the as-printed, etched, and electroless Ni coated polymer rods. The predicted peak loads based on the developed analytical models are shown to have good agreement with the experimental data.

Ni strike layer (determined from the increase in mass after plating) had almost no effect on the performance of the rod with the peak force practically identical at 6.2 ± 0.1 N.

The peak flexural strength for the polymer rods can be predicted using the bending theory developed in section 4.3.4. The theory overpredicts the strength by a small amount (Fig. 7.2). Issues with surface roughness, as discussed previously, as well as exact measurements for span length and radius can cause this overprediction. The theory is meant to match the peak strength; fall-off after the peak is the result of crazing and permanent deformation on the tensile side of the rod. This is similar to the necking seen in a polymer tensile coupon. None of the polymer rods, etched or as-is, had fracture and continued to bend until they slipped out of the testing apparatus.

Moving from the rods pulled out at different points of the process, Figure 7.3 plots the

<i>Condition</i>	r_i (mm)	r_e (mm)	n_{less} (μm)	n_{dep} (μm)	<i>Label</i>
as-printed	0.992 0.004	- -	- -	- -	0/0/0.99
etched	0.994 0.005	0.908 0.002	- -	- -	0/0/0.91
electroless	0.990 0.003	0.913 0.001	3.6 0.1	- -	0/3.6/0.91
10 μm	0.992 0.006	0.912 0.007	3.1 0.3	9.7 1.8	9.7/3.1/0.99
20 μm	1.001 0.008	0.914 0.002	2.7 0.2	19.4 1.5	19.4/2.7/0.91
30 μm	0.989 0.003	0.907 0.002	3.1 0.1	29.4 3.5	29.4/3.1/0.91
40 μm	0.992 0.002	0.908 0.002	2.6 0.1	44.4 5.7	44.4/2.6/0.91
50 μm	0.991 0.005	0.899 0.003	3.3 0.1	51.5 6.2	51.5/3.3/0.90
60 μm	0.994 0.005	0.902 0.002	3.7 0.1	57.4 5.3	57.4/3.7/0.90

Table 7.1: Collective values of radius and coating thickness for each batch of rods produced. Radii of the original rod and after etching performed with micrometer as was coating thickness of deposited Ni. Values for coating thickness of electroless Ni were smaller than accuracy of micrometer and were back calculated from mass. Standard deviation reported for each batch of five samples.

force-deflection curves for samples with electrodeposited Ni coatings ranging from 10 μm to the maximum of 60 μm of Ni deposited. Each rod was measured to obtain a coating thickness accurate to $\pm 5 \mu\text{m}$ using a micrometer. For small coating thicknesses, the thin Ni sleeve fractures on the tensile side of the rod and the crack continues to grow until it meets at the top side of the rod. When the thin Ni coating fractures, the energy absorbed in the coating is released and the polymer core takes up this force. Because its mid-span deflection at fracture is six times larger than the fracture point for the Ni coating, it continues to carry load until it fractures.

Comparing the rods' performance is better performed with the normalization techniques used for the blocks and microtrusses throughout this thesis. In this case, a circular cross-section is being tested and so the equations for flexural strength and strain need to be modified as:

$$\sigma_f = \frac{FL}{\pi(r+n)^3} \quad (7.1)$$

and

$$\epsilon_f = \frac{12D(r+n)}{L^2}. \quad (7.2)$$

The variables here are identical to those presented in sections 4.3.4 and 5.3. With this conversion and a second normalization of mass, Fig. 7.3 (bottom) is created. The addition of a very thin layer of Ni was not as beneficial, especially after the fracture of the coating early in the curve. The post fracture point for the 9 μm coated rod is lower than the uncoated curve because the added mass of the Ni on the rod is now not carrying any load but continues to add weight on the rod. The rate of increase in the peak flexural strength normalized by mass accelerates with increasing coating thickness up to 31 μm where it then begins to plateau, seen in the small difference between 44 μm and 62 μm . The 62 μm is still the most structurally efficient based on this comparison method but further coating thicknesses are expected to stay near this peak value and eventually decrease.

Predicting the performance of the hybrid metal/polymer rods required extra steps compared

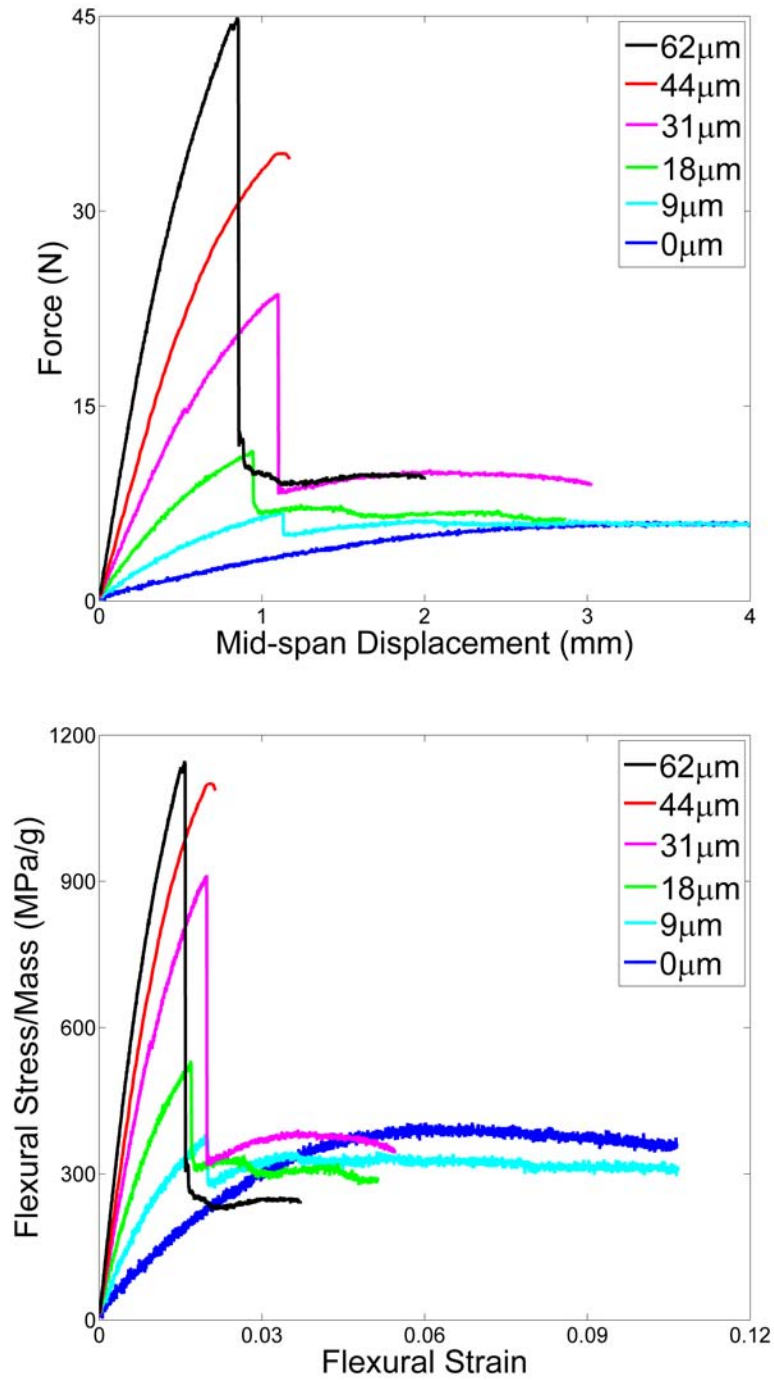


Figure 7.3: Force-deflection (top) and normalized flexural stress-strain (bottom) curves for the Ni/polymer rods ranging from etched polymer (no coating) to the maximum coating of 62 μm .

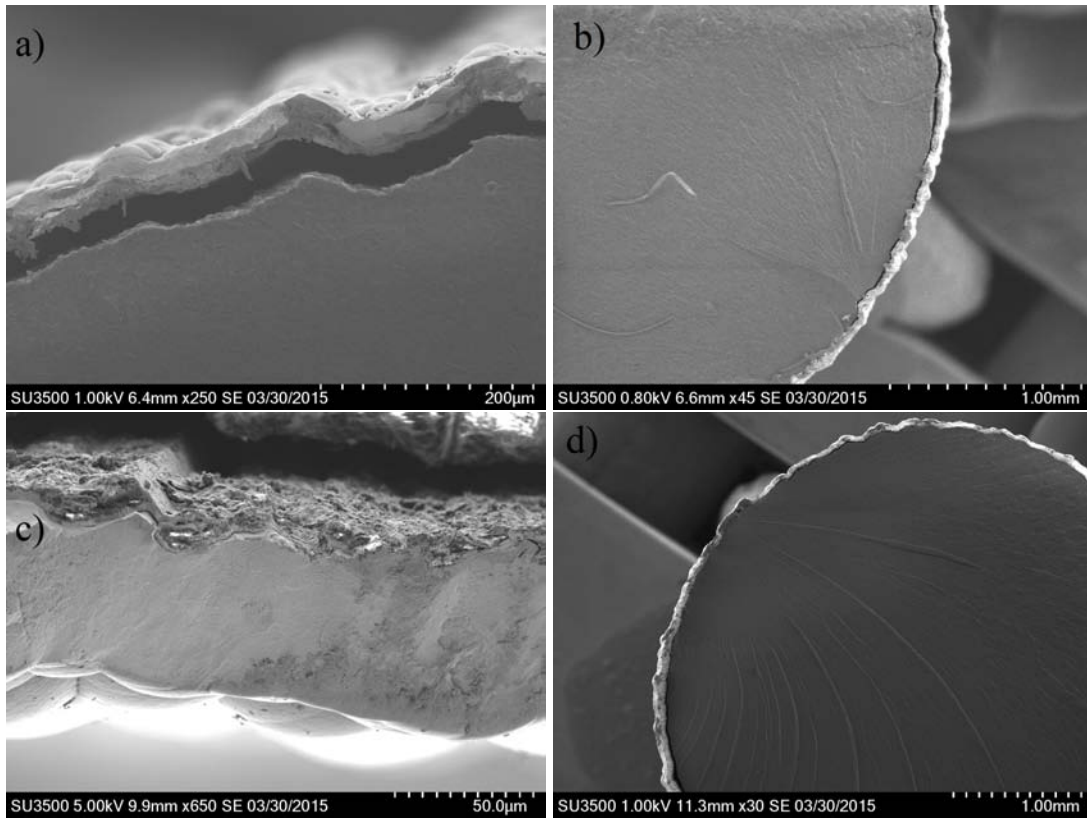


Figure 7.4: SEM micrographs of sample 57.4/3.7/0.90 at 250x (a) and 45x (b) magnification showing gaps between the polymer core and the Ni coating. Similar results were seen for less thickly coated sample 44.4/2.6/0.91 at 650x (c) and 30x (d) magnification.

to the polymer rod theory in Fig. 7.2. Through the thickness of a beam in bending, the stress increases until it reaches a maximum at the outer face. This stress is a result of the deflection occurring at mid-span which eventually causes the rod to rupture/deform on the tensile side when the material exceeds its fracture or tensile strength locally. If the composite is treated as a single material, the calculation of peak strength at the outer face involves the use of the entire cross-section in the second moment of area. This resulted in a poor fit to theory. Instead, SEM images of the failed struts identified a gap between the polymer core and Ni coating (fig.7.4a).

This gap implied a poor level of adhesion between the two materials and a reworking of the theory into two parts: failure in the core and failure in the coating. Instead of using the entire cross-section of the rod in the strength calculations, the failure force for the Ni coating assumed the polymer core was not there, similar to the hollow Ni predictions in the previous chapter.

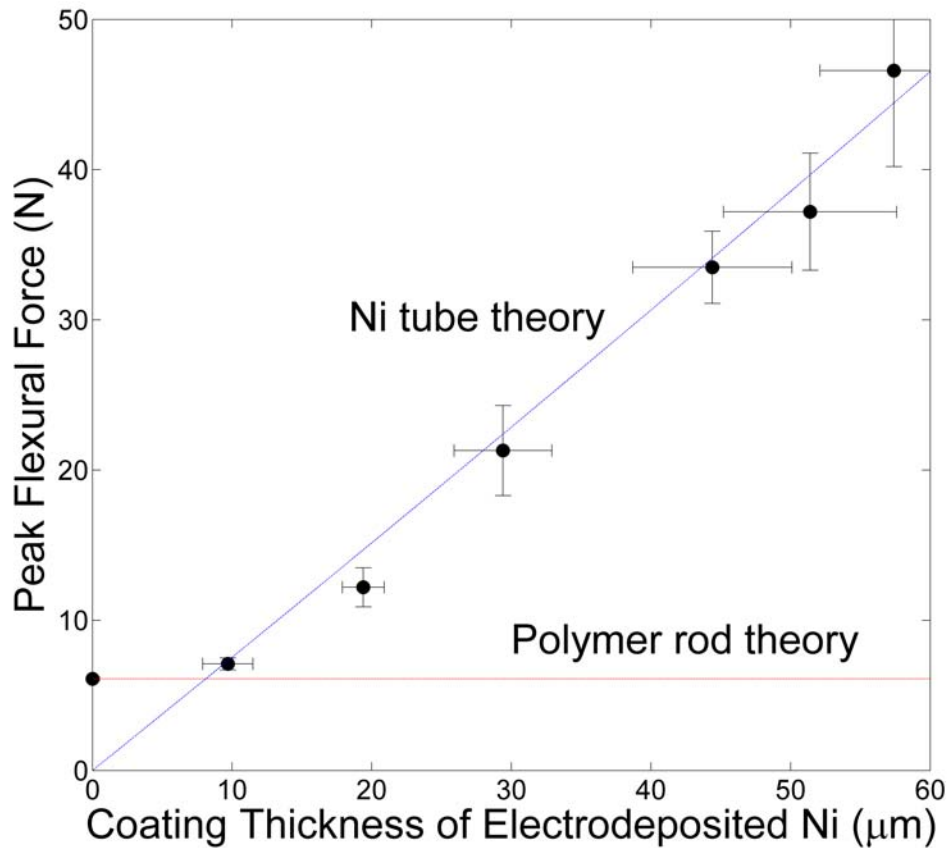


Figure 7.5: Experimental peak flexural load for all Ni/polymer rods grouped into the sets of five that had been plated together. Error bars show the standard deviation in coating thickness and peak flexural load. An etched polymer rod with no coating was also placed for comparison. Peak load predictions are shown for the limiting cases of the polymer rod on its own as well as with the assumption of the composite behaving as if it was a Ni tube without any polymer inside.

This prediction is plotted in Fig. 7.5 and matches the coated samples very well. However, tracing the trend back to zero coating thickness suggests no flexural strength. In the case of thin coatings, a second check is performed where the stress at the outer surface of the polymer, regardless of Ni presence, is calculated to see if it has surpassed the polymer tensile strength. This appears as the horizontal polymer rod theory line as the load for the polymer to break is unaffected by the addition of Ni on the exterior.

One would potentially add the two force levels to arrive at a total applied force required to break the composite. However, the stress at each point in the rod during bending is not

additive; the use of the total cross-sectional area of both metal and polymer skew the predictions upwards. Instead, the applied force creates deflection that induces stress in the material. Because the polymer deflects much farther than the composites (table 7.2), the rod inside is not near failure when the coating breaks. In the regime between no coating and 10 μm of Ni, a transition should occur but the bounding lines of pure polymer and Ni tube serve as a good match to this data.

The normalized values for peak flexural strength express most of the conclusions that are drawn from this sample set. The etching removes much of the stress concentrators on the polymer rod and for a smaller mass and radius is able to achieve the same peak stress. The addition of a thin electroless Ni layer adds to structural benefit and the added mass causes its normalized strength to decrease. This is further compounded in the 10 μm of electrodeposited Ni samples. It is only with greater coating thicknesses that the stress at the outer face climbs faster than the addition of the mass from more Ni on the sample.

7.2 Metal/polymer trusses in bending

Before the development of the metalization technique, the industrial partner for this thesis (Integran Technologies, Inc. [155]) proceeded to plate their high-quality nanocrystalline metal coatings on some large-scale microtrusses. This capacity is not one that is available in the laboratory size baths that had been used for the polymer rod bending data. A 20 nm grain size NiCo alloy was used based on availability and similarity to the 21 nm nanocrystalline Ni material used in chapter 6. One strut from the most heavily plated sample was removed from the overhang region and mounted for hardness testing. Using a 100 gf load with a dwell time of 10 s, an average Vickers hardness of 564 ± 4 HV was obtained after taking ten measurements around the circumference of the coating in cross-section. A NiCo tensile stress-strain curve was fit to the Voce equation and gave values of $A=17$, $B=1785$, and $C=110$ with a goodness of fit of $R^2=0.9997$ (see Appendix A.3). Using these fitting parameters, the model was run for

<i>Condition</i>	<i>PeakForce</i> (N)	<i>PeakStrength</i> (MPa)	<i>NormalizedPeak</i> <i>Strength</i> (MPa/g)	<i>Maximum</i> <i>Deflection</i> (mm)	<i>Label</i>
as-printed	8.2	68.0	385	-	0/0/0.99
	0.2	1.5	9	-	
etched	6.1	65.2	446	-	0/0/0.91
	0.1	1.1	11	-	
electroless	6.2	63.6	403	-	0/3.6/0.91
	0.1	1.0	6	-	
10 μm	7.1	73.4	392	4.86	9.7/3.1/0.99
	0.4	5.7	24	1.21	
20 μm	12.3	124.9	576	2.84	19.4/2.7/0.91
	1.3	13.3	52	0.83	
30 μm	21.3	221.0	894	2.18	29.4/3.1/0.91
	3.0	34.4	106	0.98	
40 μm	33.5	345.3	1184	1.10	44.4/2.6/0.91
	2.4	31.0	60	0.08	
50 μm	37.2	375.2	1204	1.47	51.5/3.3/0.90
	3.9	35.0	142	1.00	
60 μm	46.6	477.4	1434	2.10	57.4/3.7/0.90
	6.4	40.8	84	0.81	

Table 7.2: Collective mechanical properties for each batch of rods produced. Peak strength and normalized peak strength are expressed in flexural terms using equation 7.1. Maximum deflection for the as-printed, etched and electroless samples are not provided as samples slipped out before fracture. Standard deviation reported for each batch of five samples.

this NiCo alloy and gave the failure map seen in Fig. 7.6.

The optimal trajectory on this map resembles the trajectories seen for the Ni curves seen in chapter 6. The characteristic bulge towards larger \bar{n} before returning and increasing in \bar{r} is still seen. Optimal structures can be found in both inelastic and elastic global buckling zones as well as in the inelastic local shell buckling zones. One difference here is that the bulge extends to much larger values of \bar{n} . While difficult to visualize, the fabrication of microtrusses with strut radii as small as 100 μm in chapter 5 combined with the potential for coating thicknesses to be in the millimeter range could result in \bar{n} values in double digits (a coating thickness of 1 mm would give $\bar{n}=10$). Regardless, the failure map has been reduced to a size that applied to much of this work where \bar{r} is limited to 0.1 and \bar{n} reaches up to 1 (fig 7.6).

With a prediction ready, microtrusses were printed with architectures having a slenderness ratio of 33. With a thinner polymer strut radius, a thinner coating was required to reach the optimal as shown in section 6.3, which was preferable from a time and coating thickness uniformity perspective. Based on these dimensions, the resulting \bar{r} of 0.033 has an optimal at \bar{n} of approximately 0.12. To calculate the nominal thickness of the coating received, the mass of deposited NiCo was converted to a volume which was then assumed to uniformly coat the entire surface area of the structure. This gave a value of 47 μm , for example, for the thinnest coating. A complete list of architectural values and experimental results is shown in table 7.3. Also, the four architectures calculated from the nominal thickness are plotted on Fig. 7.6b to visually compare to the optimal trajectory.

Thickness anisotropy in electrodeposited coatings due to shielding was observed by contrasting coating thickness on outer face struts versus interior core struts. This was well documented in a mechanical anisotropy study done on metal/metal foams performed parallel to this thesis' work on microtrusses (see Appendix C). There, Al open cell foams were electroplated with nanocrystalline Ni of varying desired thickness and cell size in the foam. Because of the large through-thickness, cells in the interior of the foam were shielded by the cells on the outer edges and did not receive as much coating. The longer the plating cycle, the worse

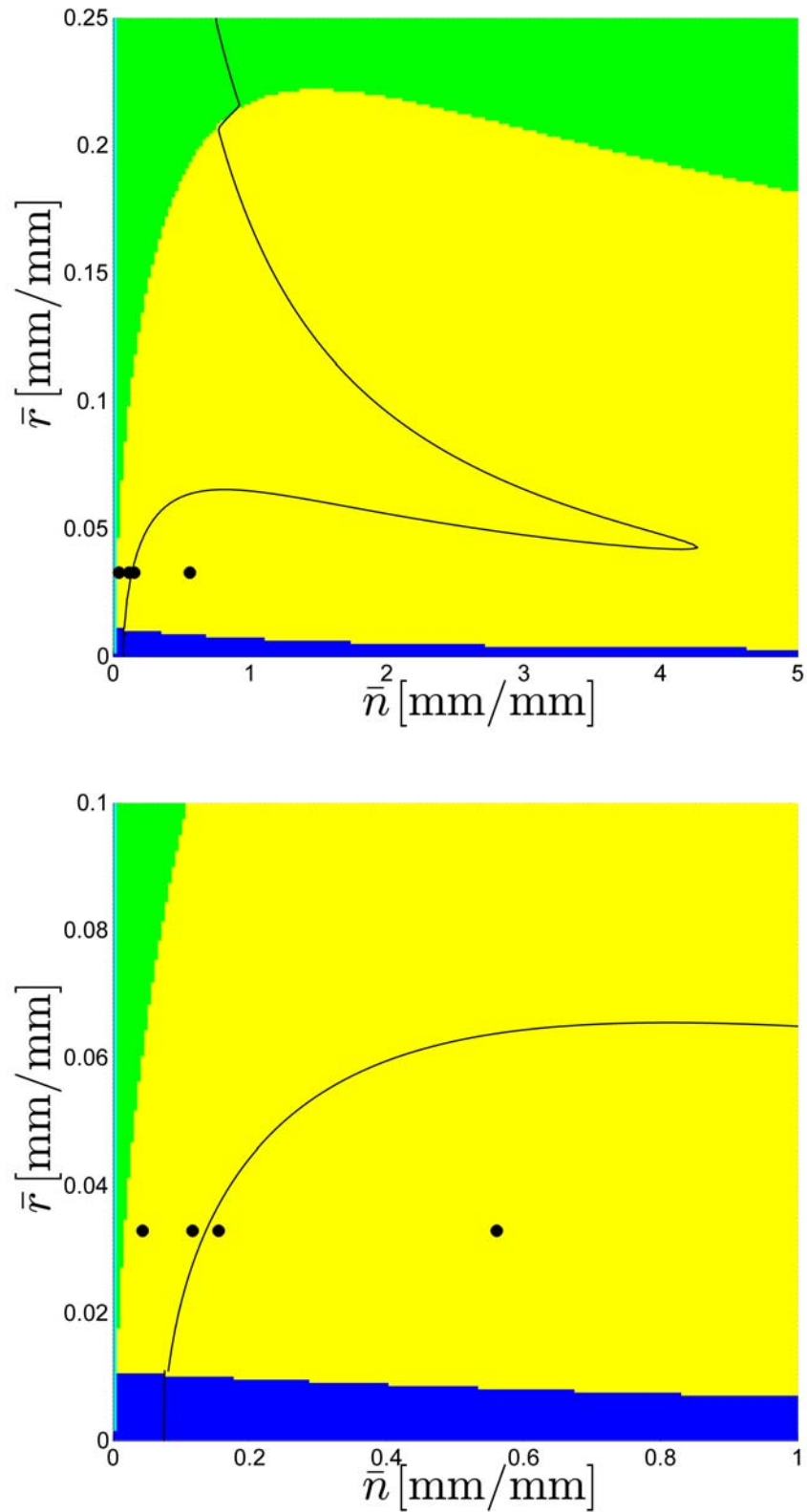


Figure 7.6: Failure mechanism map for 20 nm grain size NiCo plotted in the fully expanded geometric space with the optimal trajectory and four experimental architectures (top). A zoom in on the applicable geometric range for microtrusses (bottom). Colours for failure zones are identical to those from previous chapters with elastic global buckling (blue), inelastic global buckling (yellow), elastic local shell buckling (green), and inelastic local shell buckling (cyan).

<i>Sample</i>	<i>Mass</i> (g)	<i>r</i> (mm)	<i>n_{nom}</i> (μm)	<i>n_{max}</i> (μm)	<i>F_{peak}^{exp}</i> (N)	<i>F_{nom}^{the}</i> (N)	<i>F_{max}^{the}</i> (N)	σ_{peak} (MPa)	<i>E_f</i> (MPa)
MED0-1	15.9	0.831	-	-	15	18	-	6	676
MED0-2	15.9	0.821	-	-	19	18	-	8	912
MED0-3	16.0	0.813	-	-	19	20	-	8	932
MED35-1	32.1	0.822	52	116	275	170	400	89	10,304
MED35-2	30.5	0.822	47	95	197	150	320	66	9,629
MED35-3	27.4	0.822	38	48	145	120	160	54	7,400
MED95-1	46.6	0.822	101	182	516	350	690	146	18,423
MED95-3	42.6	0.822	88	128	399	300	460	126	16,383
MED95-4	41.8	0.822	85	126	389	180	450	131	16,459
MED625-3	159.0	0.822	471	456	2024	2400	2340	640	51,485

Table 7.3: Measured values for radius and coating thickness of the ten samples tested here along with mechanical properties from three-point bending tests. Radii for the plated samples were not recorded prior to electrodeposition and are quoted as the average of the unplated samples.

the anisotropy became. Figure 7.7 shows a series of metal foams with increasing plating time where the most heavily plated samples showed a tenfold difference in Ni coating thickness between outer and inner cells. While the microtrusses here do not suffer from as severe an anisotropy as this, anode position and plating conditions can result in some visible thickness variations.

Testing these beams at a displacement rate of 4 mm/min with a support span of 225 mm (equivalent to nine unit cells along the length), the force-deflection curve is shown in Fig. 7.8. The uncoated version of the metal/polymer microtrusses peaked at 15 N with failure occurring simultaneously in all three face struts to one side of the central roller via face sheet buckling (Fig. 7.9a). The addition of a thin layer of the nanocrystalline NiCo in this case greatly increased the flexural modulus and strength.

Using the largest measured coating thickness for the three face struts adjacent to the central node, the force-deflection curve was converted to a flexural stress-strain curve and normalized by mass. This largest thickness will have material furthest from the neutral bending axis, which should be at the highest induced stress state and, all things being equal between face struts, will fail first. Even with this normalization for the added metallic coating, the 47 μm

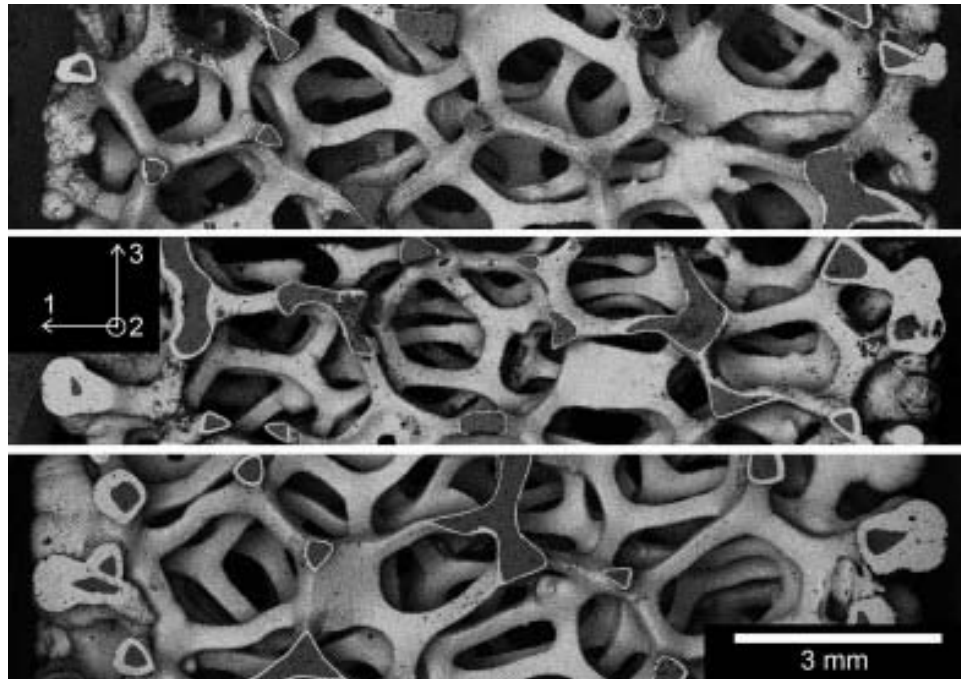


Figure 7.7: SEM micrographs showing the Ni thickness gradient for Ni/Al foams having densities of 0.486 Mg/m^3 (top), 0.690 Mg/m^3 (middle), and 0.959 Mg/m^3 (bottom), taken from Ref. [95].

thick coating greatly outperformed the baseline polymer structure (Fig. 7.8 (right)). Failure was still centralized to the three face sheet struts with the coating rupturing as the strut buckled inwards (Fig. 7.9b), exactly as predicted by the failure map in section 6.3. Similar failure and improved performance were observed with a larger coating of $84 \text{ }\mu\text{m}$ except one of the face struts fractured near a node instead of buckling (Fig. 7.9c).

For the largest deposited coating, the measured thickness in the face struts came to $466 \text{ }\mu\text{m}$ while some struts further on the outside had as much as $800 \text{ }\mu\text{m}$. The resultant \bar{n} of 0.555 was still used to observe how a structure far from the optimal trajectory would behave. When tested and normalized for its much larger mass, the curve and peak flexural strength do outperform all the previous structures (Fig. 7.8b). Failure was also short-circuited in this sample by the collapse of struts that were not coated on the sides of the microtruss (Fig. 7.10b). Figure 7.9d shows that instead of face sheet buckling at the middle of the beam, failure occurred on the extremities of the structure. Had these areas been coated, an even higher peak flexural strength

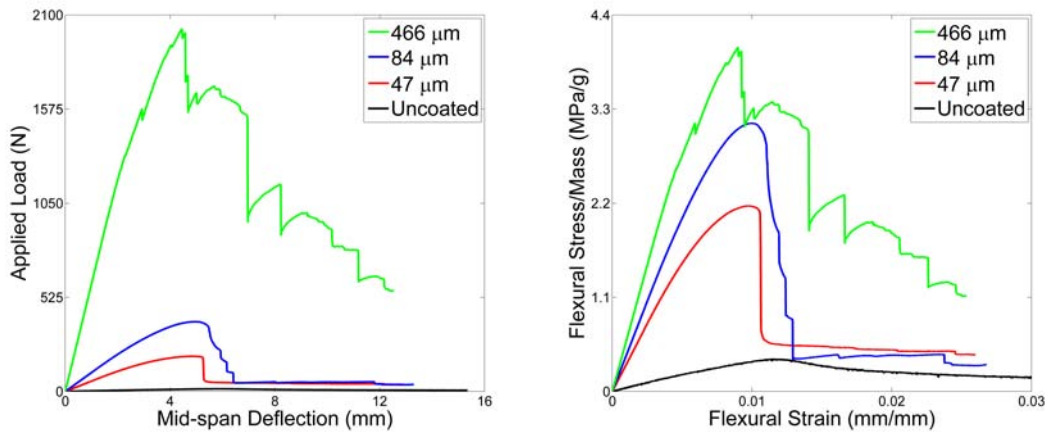


Figure 7.8: Force-deflection (left) and normalized flexural stress-strain (right) curves for samples from each of the three sets of coating thickness as well as the uncoated case. The peak load for the uncoated polymer structure was only 15 N, thus the almost flat appearance in the force-deflection figure.

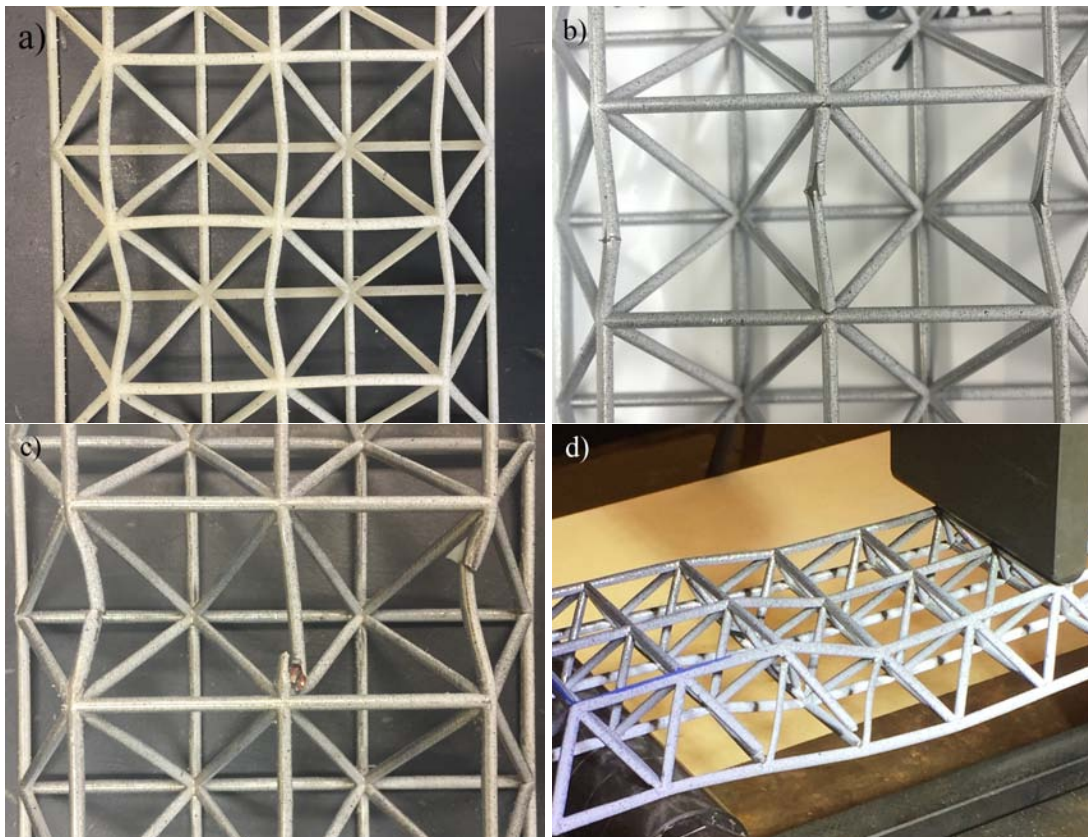


Figure 7.9: Snapshots of the uncoated microtruss after failure (a) as well as the 47 μm (b), 84 μm (c), and 466 μm (d) thick Ni coated microtrusses. All exhibited face sheet buckling adjacent to the central roller except the most heavily plated sample which failed by nodal collapse at the edges of the sample.

is expected, owing to the pre-peak load drops from these core struts collapsing and comprising the whole beam (Fig. 7.8).

The purpose of testing these architectures in particular was to serve as a check on the analytical model developed here. Table 7.3 shows the experimental peak load, F_{peak}^{exp} , for each of the beams. Next to this value is the predicted peak load based on either the nominal thickness calculation giving F_{nom}^{the} or based on the maximum thickness measured on the face struts giving F_{max}^{the} . While the range is large in some cases, the placement of the experimental peak in between these bounds shows that the microtruss has been accurately modeled. Even in cases where the nominal and maximum coating thicknesses were close, such as in MED35-3, the experimental peak force of 145 N was between the bounds of 160 N and 120 N.

Outstanding processing issues include sample twisting and incomplete electrodeposition. The combination of a low heat deformation temperature of the polymer, a high bath temperature for nanocrystalline Ni plating, and strong bath currents to flow the solution around the microtruss led to some microtrusses twisting (Fig. 7.10). This twist is unavoidable because of the polymer selection but in a three-point bending test should have minimal impact. A larger toe will be observed in a force-deflection curve as the beam is flattened into a straight sheet between the rollers, which can be removed and adjusted, according to ASTM standards [141, 157, 143].

Additionally, these large trusses were made without the use of fillets resulting in sharp recesses on the undersides of nodes that were not plated completely due to shielding from the outer face sheet (Fig. 7.10). This already sensitive spot due to stress concentrations is made even weaker as the coating is suspect here. This explains the overprediction of strength for the thickest Ni/polymer sample, MED625-3. While the models based on nominal and maximum coating thickness gives bounds of 2300 and 2400 N, the actual peak load was 2000 N. The deviation from the expected strength is most likely to come from these defects but future hybrids will be created with fillets that match the 0.5 mm fillet size seen in the analysis of graded and filleted structures in chapter 5. This will allow the recesses to be better plated and should bring

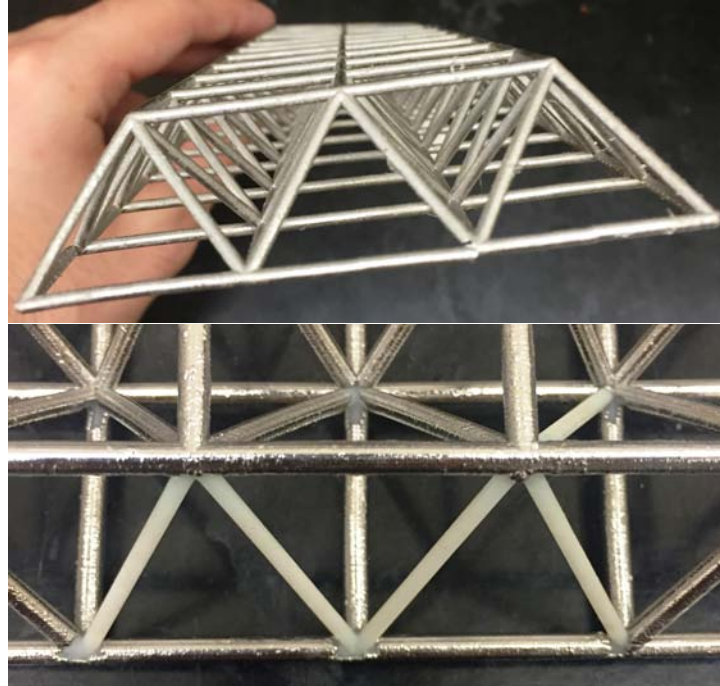


Figure 7.10: MED35-2 exhibited a noticeable twist along its length (top) while MED635-3 had some struts that were not successfully coated (bottom). These uncoated struts were the origin of failure in the three-point bending test.

this structure's strength into line with the model, as was the case for all other samples.

Overall, the large-scale NiCo microtrusses achieved two main goals. Firstly, they showed that the idea of fabricating complex architectures with a nanocrystalline metal exterior are realized. Secondly, the ability to predict the load carrying capacity of the microtruss beams to within a range considering the distribution in coating thickness was successful and, with the data from the rest of the validation studies, shows the strength of this model. Remaining issues are ones of process optimization, not model development, which can be corrected for with small modifications in the electrodeposition process.

7.2.1 Comparing hybridization with nanocrystalline Ni to other improvements

In the previous chapters, much was made on the ability to improve weight-specific mechanical performance. After the discussion in this chapter on the properties of metal reinforced poly-

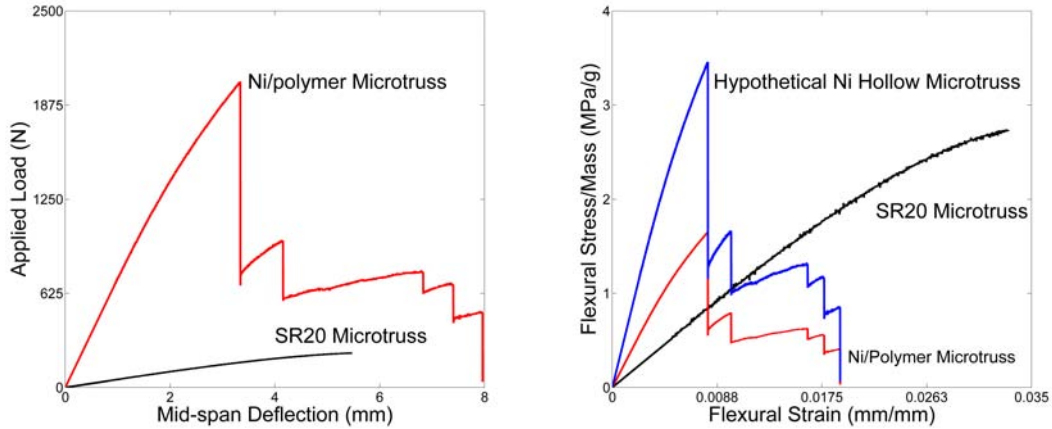


Figure 7.11: Force-deflection (left) and normalized stress-strain (right) curves for a SR20 microtruss with a nominal coating thickness of $140\ \mu\text{m}$ compared to the baseline SR20 polymer microtruss. The hypothetical behaviour of a hollow metallic microtruss is shown by assuming the polymer mass has been removed without compromising the Ni coating.

mers, a Ni plated polymer microtruss was created that would compare to the baseline SR20 polymer microtruss used throughout this thesis. This sample was plated by the industrial partner Integran Technologies, Inc. [155]. For their large-scale plating baths, the SR20 microtruss was doubled in size. Measurements of coating thickness upon delivery of the part showed central core struts had coatings as thin as $100\ \mu\text{m}$, while outer face struts were as thick as $400\ \mu\text{m}$, similar to the anisotropy discussed previously.

Three-point bending tests of the beam are shown in Fig. 7.11. Failure of the composite beam was observed to follow a similar trend as seen in the small-scale SR20 microtrusses in section 5.2. One of the face struts on the tensile side of the beam (outer-most) fractures but does not release enough energy to break through all the other tensile face struts. With further deflection and a now missing connection on one side of the beam, the microtruss begins to bend outwards towards this failed strut. The next load drop occurs when the node directly above the failed strut splits followed by failure in the next tensile face strut inwards. This process of face strut followed by node on compressive side continues as the microtruss bends further outwards. This strut-node-strut failure is very similar to Fig. 5.10.

The required force before failure was an order of magnitude larger but the effect of mak-

ing the microtruss twice as large has not been normalized for. A flexural stress-strain curve balances out these differences and is shown in Fig. 7.11 (right). With the normalization of mass, the composite microtruss is underperforming the baseline SR20 microtruss. However, the hybrid still has the polymer core within the structure, which is carrying minimal load when the first strut fractures. Instead of normalizing by the large mass of the composite (245 g), the mass of the deposited Ni (117 g) can be used to approximate how a hollow metallic microtruss would perform. This large improvement over the composite and the baseline motivates the subsequent chapter on the fabrication of hollow metallic microtrusses.

7.3 Summary of key conclusions

A methodology was developed that successfully plated Ni coatings onto a stereolithographic UV cured polymer. The key step was the etching in sulfuric acid to leave a uniformly smooth surface regardless of printer orientation. Ni/polymer rods were fabricated and showed good agreement to bending models under the assumption of no polymer core. Failure in three-point bending was fracture on the tensile face for all studied coating thicknesses. In the limit of extremely thin coatings, the behaviour is expected to follow the uncoated polymer rod prediction. For NiCo/polymer microtrusses fabricated at Integran Technologies, Inc., the model was also able to predict the peak load in three-point bending based on the lower bound of a nominal coating thickness and an upper bound of the largest measured coating thickness. Larger coating thicknesses deviated from the model do to processing errors in the electrodeposition that resulted in unplated sections of the microtruss, which can be corrected for in the future.

Chapter 8

Hollow Structures and Next Steps

After seeing the strength benefits in hybrid structures in the previous chapter, the next section looks back at the conclusions of chapter 6. The fully optimized analytical models pointed towards the fabrication of hollow metallic microtrusses as being the most structurally efficient architectures available. Work to date on the fabrication of hollow polymer microtrusses will be presented culminating in the comparison of all the material and architectural effects analyzed here. Limitations in the ability to remove a parasitic polymer core from within an outer metallic framework are also discussed. With all of the research presented to date, best practices for continuing towards the goal of ultra-lightweight structures with true geometric freedom in all directions are introduced.

8.1 Hollow polymer microtrusses

Section 5.3 showed that by normalizing the force-deflection response in terms of flexural stress-strain and the mass of the structure, a microtruss outperformed a solid polymer block in bending. Section 5.3.1 introduced various architecture modifications that could improve this weight-specific mechanical performance further. Additionally, chapter 6 showed that hollow structures, albeit made of metal, could be significantly lighter when optimized than hybrid coated trusses. Before attempting to fabricate these types of structures, an attempt was made

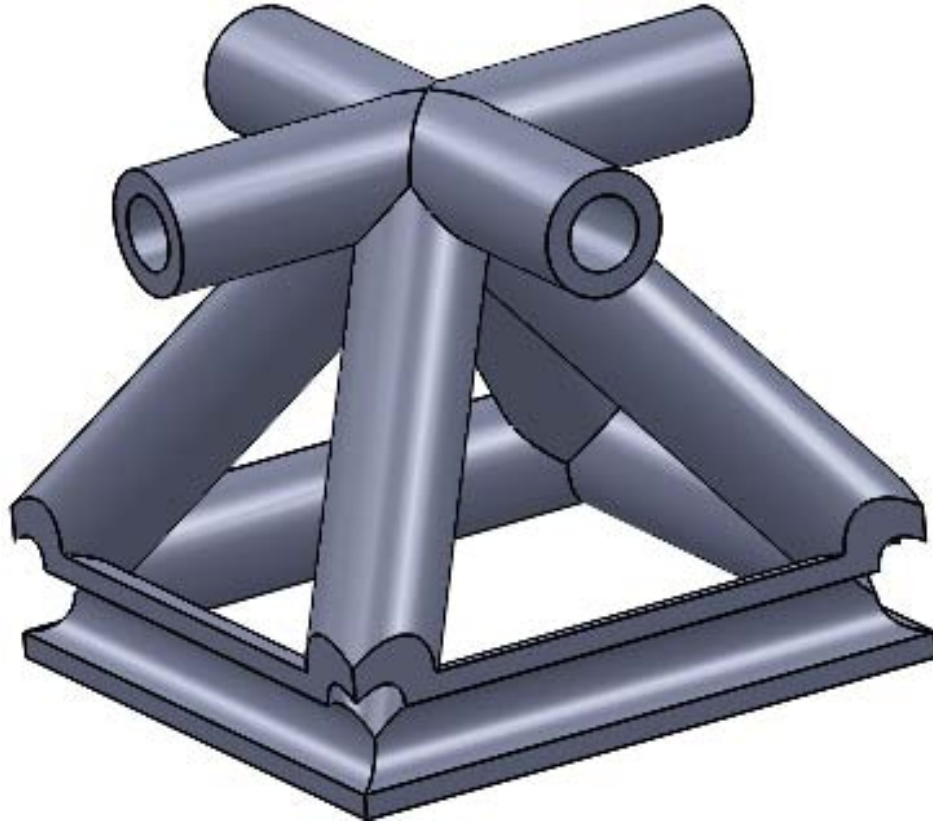


Figure 8.1: Schematic of the repeat unit cell used to create the hollow polymer microtruss.

at using the high degree of complexity available with MJM to print some hollow polymer microtrusses.

Making the 3D CAD file for the part and having it printed were trivial complications compared to finding a suitable method to remove the wax support structure that had been deposited within the hollow framework of the microtruss. Placing the part in the finisher and letting the wax melt was made more difficult because the liquid wax has a high surface tension and preferred to stay inside the microtruss. Vigorous shaking and prolonged periods in the finisher were required to finally extract most of the wax. Even then, some internal nodes showed signs of residual wax based on the opacity in those regions. Regardless, the leftover wax provides zero structural support to the microtruss as it crumbles under any small applied load (i.e. pressing with a finger) when hardened. Leaving it inside only negatively affects the weighed mass of the microtruss.

To be consistent with all the improvements and comparisons done in previous chapters, an SR20 microtruss will be used as the baseline yet again. For the hollow metal polymer designs in chapter 7, the radius was considered the internal radius of the hollow section with the coating thickness counting outwards from this. For this example, the wall thickness will still be kept as one variable but instead of measuring the radius from the center of a strut outwards to the polymer, the outer radius of the entire strut will be used. This treats the structure as an identical SR20 microtruss that has had part of its central material in each strut removed. Figure 8.1 shows this design with the outer strut radius being the same 1.25 mm, the wall thickness being 0.5 mm, and the resultant internal pore radius then being 0.75 mm.

As seen in the case of blocks compared to trusses and the various attempted improvements on weight-specific properties, the removal of any mass usually constituted a decrease in load carrying capacity but an increase in normalized bending performance. The hollow microtruss beams follow this conclusion (Fig. 8.2). A difference in ductility and peak flexural strength was also seen depending on how long the part remained inside the finisher, as was discussed in section 4.1.2. Two hollow SR20 microtrusses were printed and placed in the finisher at the same time with the first being extracted the next day when most the wax had been removed. The second was removed a full week later and was almost completely devoid of wax inside the pores. This excess wax constituted an $\approx 10\%$ increase in mass as the first microtruss weighed in at 10.4 g compared to 9.7 g for the sample left in the finisher for a week.

The original hypothesis that both microtrusses should perform identically due to the inability for the wax to support meaningful loads ignored the finisher time effect on the polymer. After sitting inside at elevated temperatures for a week, the polymer further cured and became more brittle than one left inside for six fewer days. When normalized for mass, the extra removal of wax did equate the performance of both microtrusses but the decreased ductility resulted in poorer maximum deflection. In both cases, failure occurs suddenly, similar to the solid strut beams, before any plateau in flexural stress can be reached.

Trying to use the model for microtrusses in bending requires the full modification to hollow

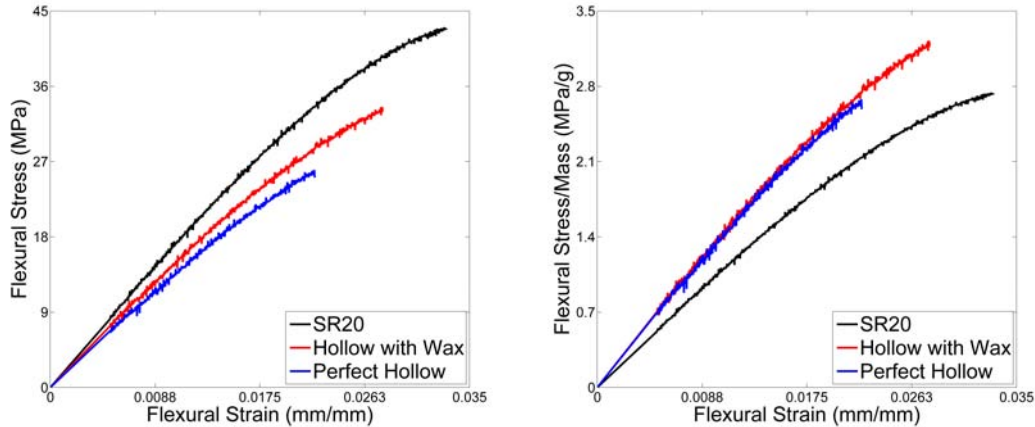


Figure 8.2: Flexural stress-strain curves for the hollow microtrusses left in the finisher for a day and a week compared to the baseline SR20 microtruss (left). The normalized version shows longer finisher time decreased ductility in the hollow structure (right).

parameters and polymer material properties. This time the polymer is the main material and is treated as the 'coating' with the core being hollow. The failure map for hollow polymer microtrusses is shown in Fig. 8.3 with the architecture designed here labelled as the black dot. Based on its position on the failure map, the model predicts the structure should either globally buckle inelastically in the top face sheet or reach its ultimate tensile strength and fracture on the bottom. Taking the non-dimensional load index that is predicted (0.00004) and adding the dimension back by multiplying by the non-dimensionalization parameter, a predicted peak load in bending of 114 N is extracted. Compared to the actual peak load in the three hollow samples ranging from 90 to 115 N, the prediction matches well.

Since the polymer fractured at the bottom and was filleted, it would have been expected to achieve better than the 114 N prediction as these secondary improvements were not included in the model. However, polymer finishing effects could decrease the strength of the polymer as could stress concentrators on the inside of the microtruss since the 3D CAD file did not fillet the interior hollow volume of the node. Regardless, the trends in failure mechanisms are still expected to follow this failure map and can provide a quick check on the ballpark estimation of failure load for complicated, hollow microtruss architectures.

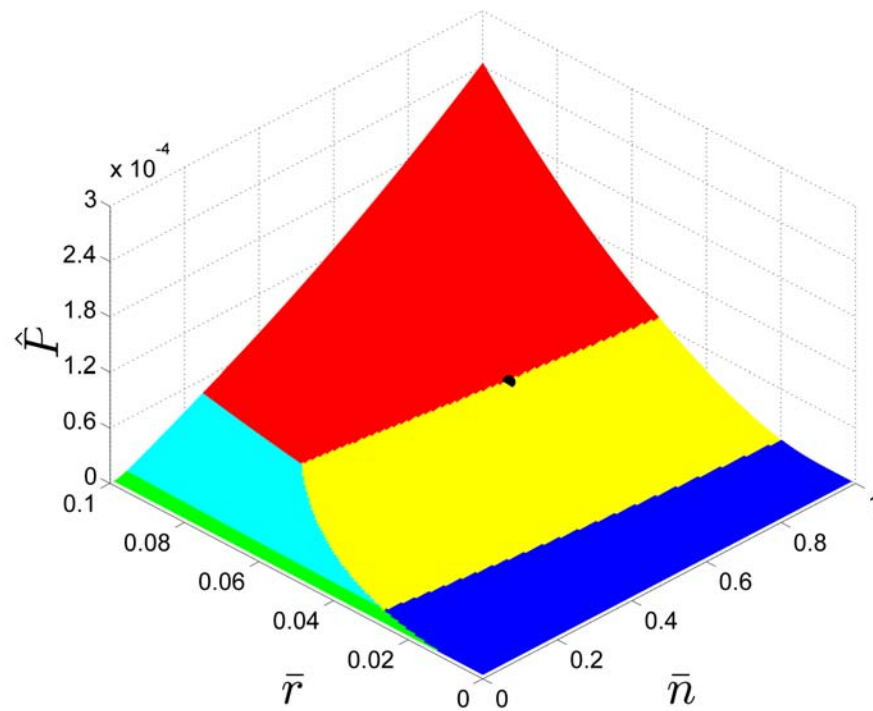


Figure 8.3: Failure mechanism map for the hollow polymer microtruss. Zones of failure are identical to those presented in previous chapters with the breakdown being elastic global buckling (blue), inelastic global buckling (yellow), ultimate tensile failure (red), elastic local shell buckling (green), and inelastic local shell buckling (cyan).

8.1.1 Combinations of structural improvements

Figure 5.19 in section 5.3.1 gathered all the information available from different structural improvements such as grading and filleting. With the addition of the ability to print hollow structures, it was checked to see what level of performance upgrade can be achieved through combinations of these different architectural modifications. Figure 8.4 shows two such structures that were attempted.

In the first, the benefits of both increased maximum mid-span deflection in filleted microtrusses and increased weight performance of graded microtrusses were put into one structure; the fillet radius was kept at 0.5 mm. The incorporation of filleting on the graded microtruss had the same effect it had on the introduction of fillets on the baseline SR20 microtruss - increased deflection before break. The fillets limit the impact of stress concentrators allowing the microtruss to reach larger deflections before a critical flaw leads to fracture on a tensile strut in the face sheet. However, because the curve's pre-filleting were already plateauing, the extra deflection led to minimal increases in flexural strength.

For the same graded microtruss with fillets, further reduction in mass by making the system hollow was attempted. The increase in normalized flexural strength was observed from the non-graded hollow microtruss to the graded one but not to the same degree as grading had on a solid microtruss. If the small decrease in strength from filleting is also taken into account, though, then grading had a larger impact than is strictly seen by comparison. Furthermore, the failure of a hollow microtruss well before a plateau is reached means the increased deflection filleting provides leads to a 30% increase in peak normalized flexural strength.

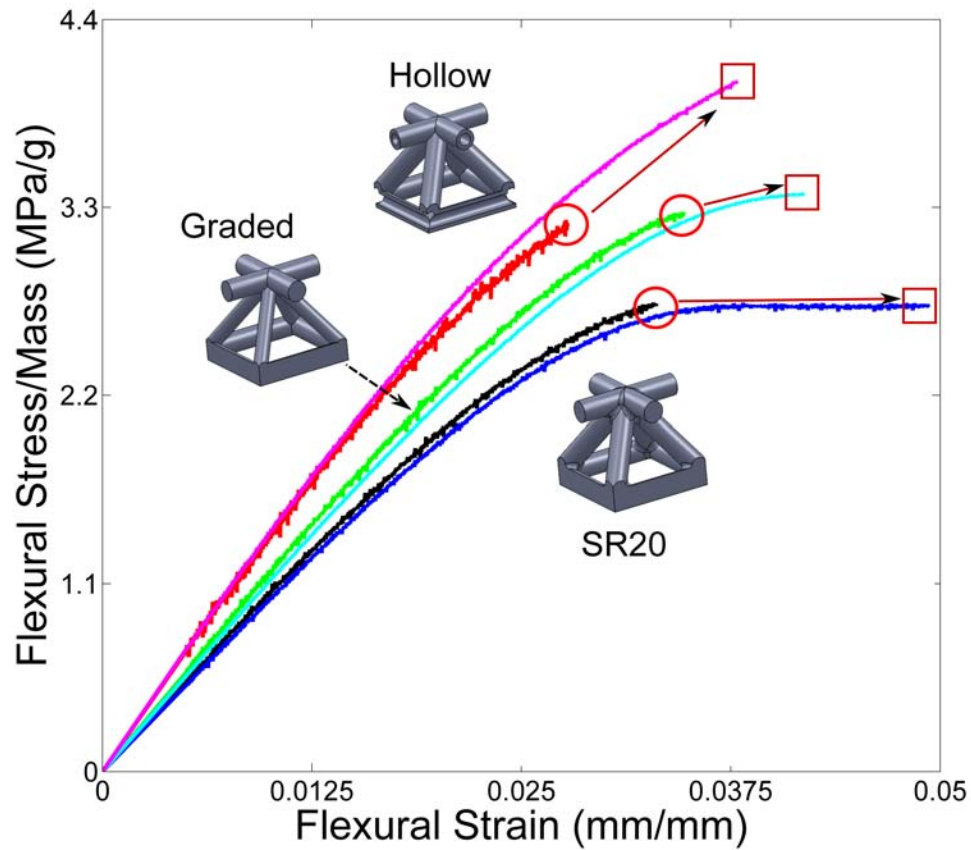


Figure 8.4: Normalized flexural stress-strain curves for cases of microtrusses with multiple improvements incorporated into the structure such as being graded and filleted or grading, filleting, and having a hollow interior. The baseline SR20 microtruss is shown along with the deflection increase possible with the addition of 0.5 mm fillets (identified as the shift from the circle to the square on the curve). The combination of grading the core and filleting is seen to have the same deflection increase as does filleting a hollow structure. Schematics show the repeat unit cell for each improvement before filleting.

8.2 Cumulative comparison of polymer and metal/polymer structures

The theme of comparing the efficiency of structures as each chapter has progressed served as a stage on which different processing techniques and materials could be fairly accessed and culminates in Fig. 8.5. The black points are structures made completely of the stereolithographic polymer and form a band of flexural strength values similar to how bubbles can be seen in the Ashby design maps (Fig. 2.1). This zone also includes the two combinations discussed in the previous section. At the extreme right side, the solid polymer block is placed, being a fully dense structure. The lack of a linear fit between these points is related to the deviation in material properties of the polymer. For example, the polymer blocks printed in different orientations all had the same density but differing peak flexural strengths. As the density is reduced towards zero, the flexural stress should also fall to zero.

For the two microtruss architectures metalized, their peak flexural strength and density are plotted along with lines of linear fit between the uncoated base structure and the most heavily electrodeposited composite. For the SR33 microtrusses, the data points for the seven tested architectures fall directly along the linear fit. This line does not need to extrapolate back to zero density as the addition of the second material introduces a second slope and terminates at the uncoated data point. The sole SR20 metal/polymer sample is also plotted along with its linear fit. Because the Ni and NiCo have similar densities and material properties, the matching linear trends are expected, even with the limited number of data points. Starting at any point in the polymer region, the addition of a Ni coating should make a similar linear trend towards higher flexural strength values.

Hypothetical data points are also placed on the figure for a hollow SR20 and SR33 microtruss with the same nominal coating thickness as the most thickly coated sample. The removal of the polymer core should shift all data points directly to the left at no expense of flexural strength, as was concluded for the metal/polymer rods. The magnitude of the shift

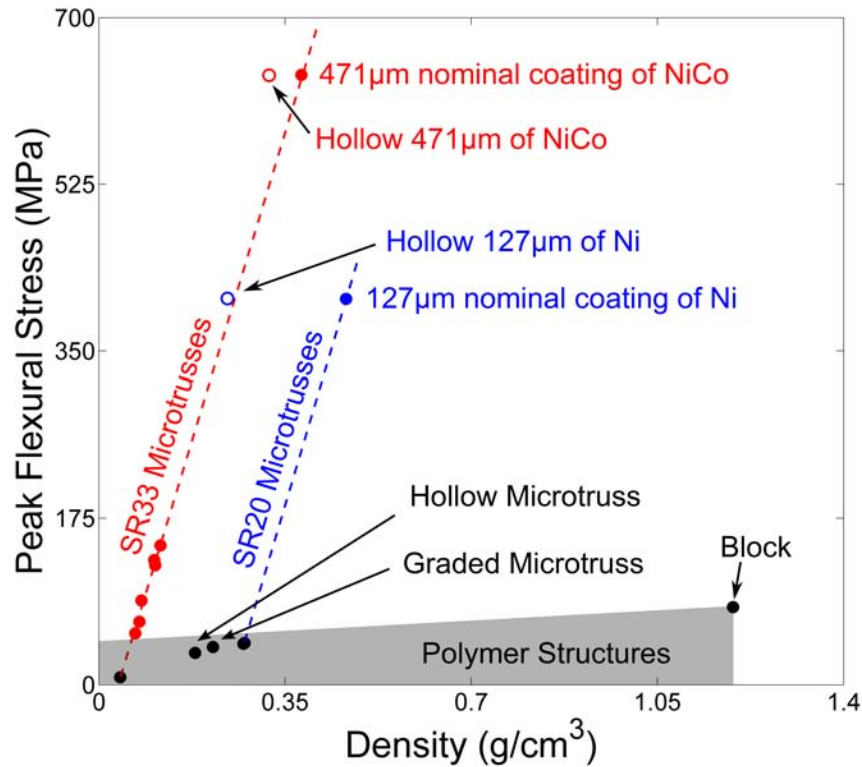


Figure 8.5: Peak flexural stress plotted for microtruss and block beams tested in three-point bending against their density calculated based on the bounding box surrounding the microtruss structure. Polymer structures lie in the band of low flexural strength at the bottom with the maximum density of the polymer block sample. Metal/polymer SR20 and SR33 microtrusses are included with their linear fits from the uncoated case up through the experimental data. Two hypothetical hollow structures show the differing benefit of core removal based on starting architecture.

when the polymer core is removed is identical to the density of the starting structure. The mechanical performance improvement in these metallic hollow microtrusses motivates a means to remove the polymer core, just as the theoretical predictions in chapter 6 did. The next section looks at a methodology to achieve this.

8.3 Hollow metallic microtrusses

While a technique has been developed that has had success plating onto the stereolithographic polymer, the ability to create a hollow microtruss made of metal requires the removal of the

polymer substrate inside the plated structure. Different approaches were attempted or examined for feasibility with two of those reported here. While a fully hollow metallic microtruss has not been fabricated with this methodology, the partial hollow structures here offer their own benefits that can make them attractive routes for high-efficiency structures.

8.3.1 Thermal properties of the wax and finished polymer

One methodology for extraction of the polymer core would be to place it in a hot environment such that the polymer either melted and flowed out or burned up and could be shook free. Based on the finishing step for the hollow microtrusses, the flowing out of a liquid from an internal cavity is very difficult and is not thorough enough to remove all the sacrificial mass. Processing techniques that require the removal of a template resemble casting, wherein the mold can be burned off to leave behind the desired architecture. This is popular for another class of cellular materials - foams - where the use of positive and negative molds in sequence can create a random cellular architecture [20].

To better understand the thermal properties of the stereolithographic polymer, differential scanning calorimetry (DSC) was done on small flakes of as-printed part (<7 g). The scans were set to increase the temperature at a rate of 25° C every minute starting at 0° C and maxing out at 450° C before returning to room temperature. On a DSC curve, peaks correspond to thermal changes that can identify physical transitions such as phase transitions, as demonstrated in Fig. 8.6.

At approximately 60° C, an endothermic transition is recorded (first dip) that matches the melting point of the wax support material. While the finishing technique resulted in no observable wax on the printed parts, a small amount remained either on the sample or within its porous structure. This could be very important for any future metal deposition steps as it could act as a barrier for good adhesion between the polymer and metal. After the wax has melted, the curve continued its descent before an exothermic process is detected at $\approx 250^\circ$ C. Because the printed polymer is a blend of ten or more precursors, this bump could be the crystallization

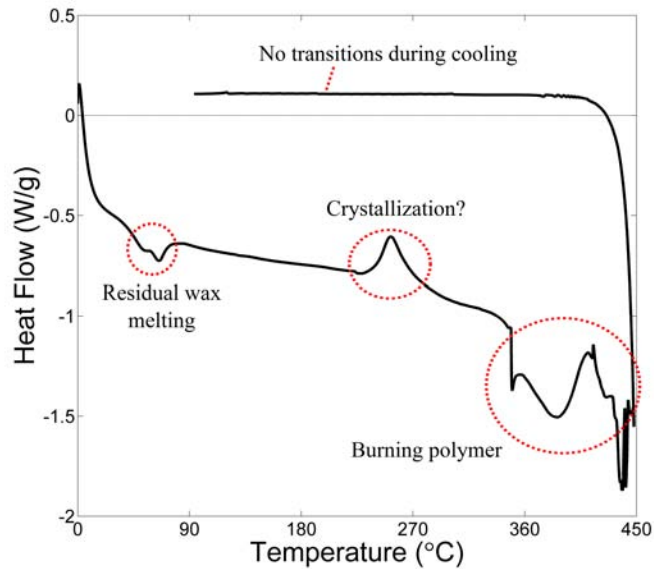


Figure 8.6: DSC curve for a Visijet Crystal printed polymer that had already been finished for two days at 65°C. Zones of wax melting, crystallization and burning are all identified on the heating portion but the cooling portion has no features implying the sample has been burnt to a crisp.

of one or more parts of the polymer, similar to curing in the sample.

From 350–450° C, a lot of endothermic transitions are ongoing and distinguishing individual peaks is near impossible. While not that useful on its own, when the reverse curve is shown as the sample is cooled back to room temperature, the lack of any peaks or valleys indicates that the polymer inside has undergone non-reversible transitions, meaning it has burned and shrivelled up inside the hermetic dish in the DSC chamber. In terms of an extraction methodology for the printed polymer, this seems to rule out temperature based techniques. The temperature this all occurs at is significantly above the maximum temperatures for nanocrystalline metallic coatings. This would lead to grain growth from nanocrystalline to polycrystalline grain sizes, and the loss of mechanical performance. Furthermore, the polymer would bubble and swell while burning opening the possibility of breaking through thin metallic coatings on the outside.

Overall, a lack of melting seen in the stereolithographic polymer and swelling of burnt polymer above the grain growth temperatures for nanocrystalline coatings rules out a temperature

based technique.

8.3.2 Polymer dissolution with strong acids and FDM microtrusses

In the experimentation for the smoothening of the polymer-wax interface roughness on finished parts, the use of sulfuric acid was highlighted because of its ability to dissolve the stereolithographic polymer material. While other solvents required constant removal of the dissolved surface or did not react quickly, sulfuric acid also has the benefit of being unresponsive to Ni coatings. Since the Watt's bath used to electroplate these coatings is mostly formed with sulfuric acid, it can be used to etch away polymer parts and leave the Ni exterior intact. Previous work in this research group has shown this ability with high molarity sulfuric acids at both elevated and room temperatures (Fig. 8.7).

The current limitation is how to introduce this acid throughout the interconnected network of struts in a polymer microtruss. One possibility is the removal of Ni from some sections of the hybrid microtruss to expose the underlying polymer and have the acid work its way through these access points (see Fig. 8.8). However, destruction of the coating in any spot introduces weak points in the architecture. Instead, the ability for this rapid prototyping technique to create an already hollow polymer microtruss points to a more elegant solution: flow the sulfuric acid through the porous interior. This technique would still have drawbacks of ensuring flow through all channels and would be limited by how small a pore acid could be pushed through without damaging the thin outer coating.

As the field of rapid prototyping continues to advance, new prototypers and apparatuses will be introduced that can go smaller, be faster, and work more reliably. An interesting alternative route to this approach relies on modification of the polymeric precursor. While modifying the chemistry of the stereolithographic resin has been performed, the presence of numerous compounds within the resin to control stability, structure, and allow for UV polymerization inherently make melting or dissolving the polymer more difficult. Instead, pure single material resins would be better tailored for extraction such as ABS. A typical material in the FDM mar-

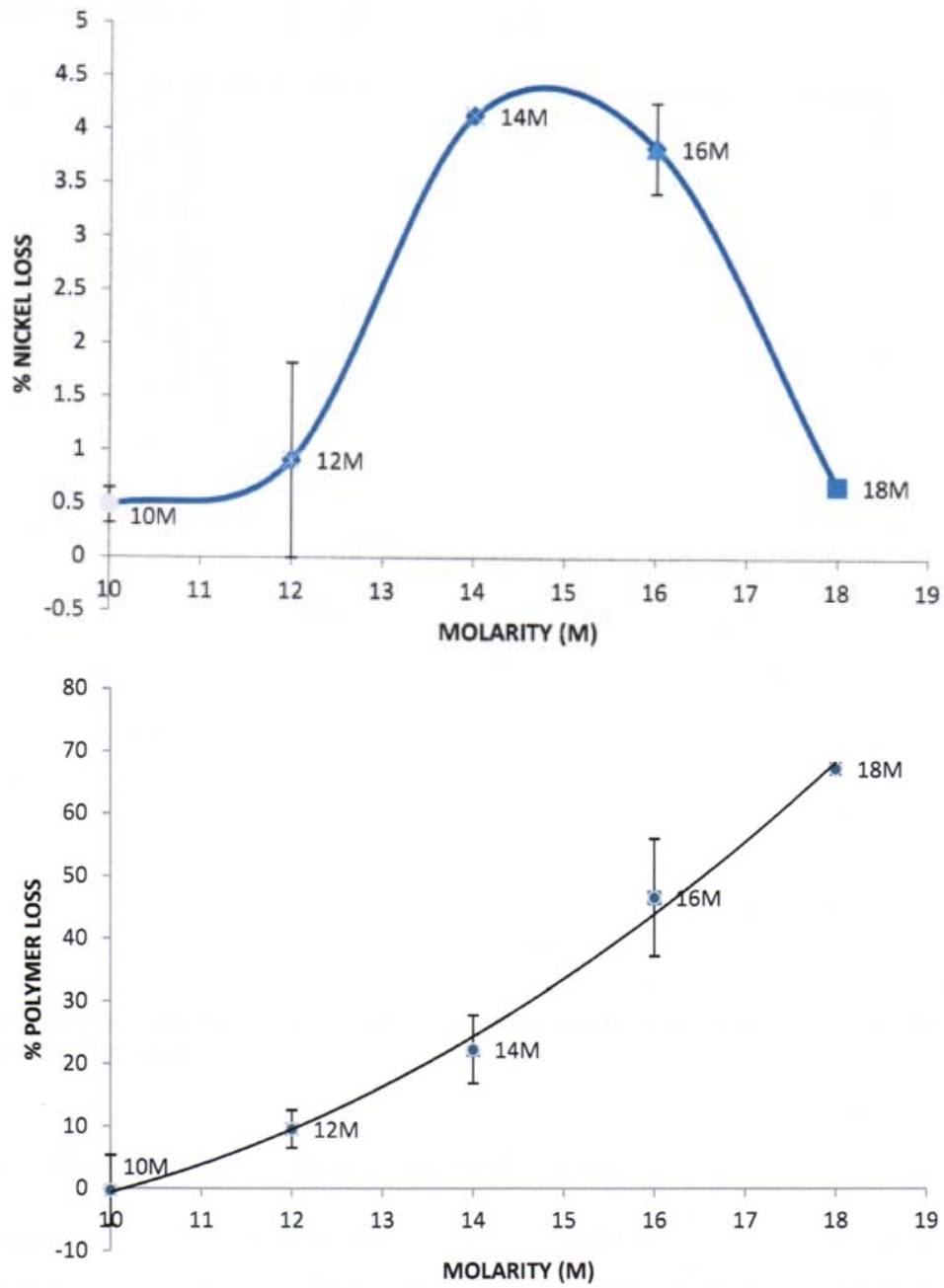


Figure 8.7: Percentage of Ni (top) and polymer (bottom) loss as a function of sulfuric acid molarity after being left for 23 hours in a sealed beaker, taken from Ref. [158]



Figure 8.8: Example of a fabrication route to making hollow metallic microtrusses for cores in sandwich panels, taken from Ref. [152].

ket, it has the benefits of being easy to metalize and electroplate while having well understood solvents to dissolve it away. The initial move away from FDM in this doctoral thesis was due to its inability to produce fine-featured architected but future improvements could bring it back into the fold. Its single material construction would then prove beneficial in the field of lightweight materials. As a proof of concept, a SR20 microtruss was printed using a Makerbot Replicator at the same scale as that in the comparative studies in previous chapters. It is important to note that the built-in software in this FDM prototyper takes any solid structure and builds a scaffold inside of it such that as little material is required in the final part. Typically, a honeycomb pattern is printed between the outer walls, as shown in Fig. 8.10.

Failure of the structure was governed by the strength of the adjoining layers. While in MJM parts, the polymer chains crosslink between layers to create a more robust material, a FDM process lays down freshly melted polymer filament onto a cold layer of previously layered material. Even with some pressure applied by the hot nozzle extruder, the layers do not have good adhesion to each other. Figure 8.9a highlights the first point of failure (circled) as the separation of the core struts from the nodes and upper face sheet. This continues in a series of drops in Fig. 8.9 as successive unit cells moving towards the lower supports fail in the same

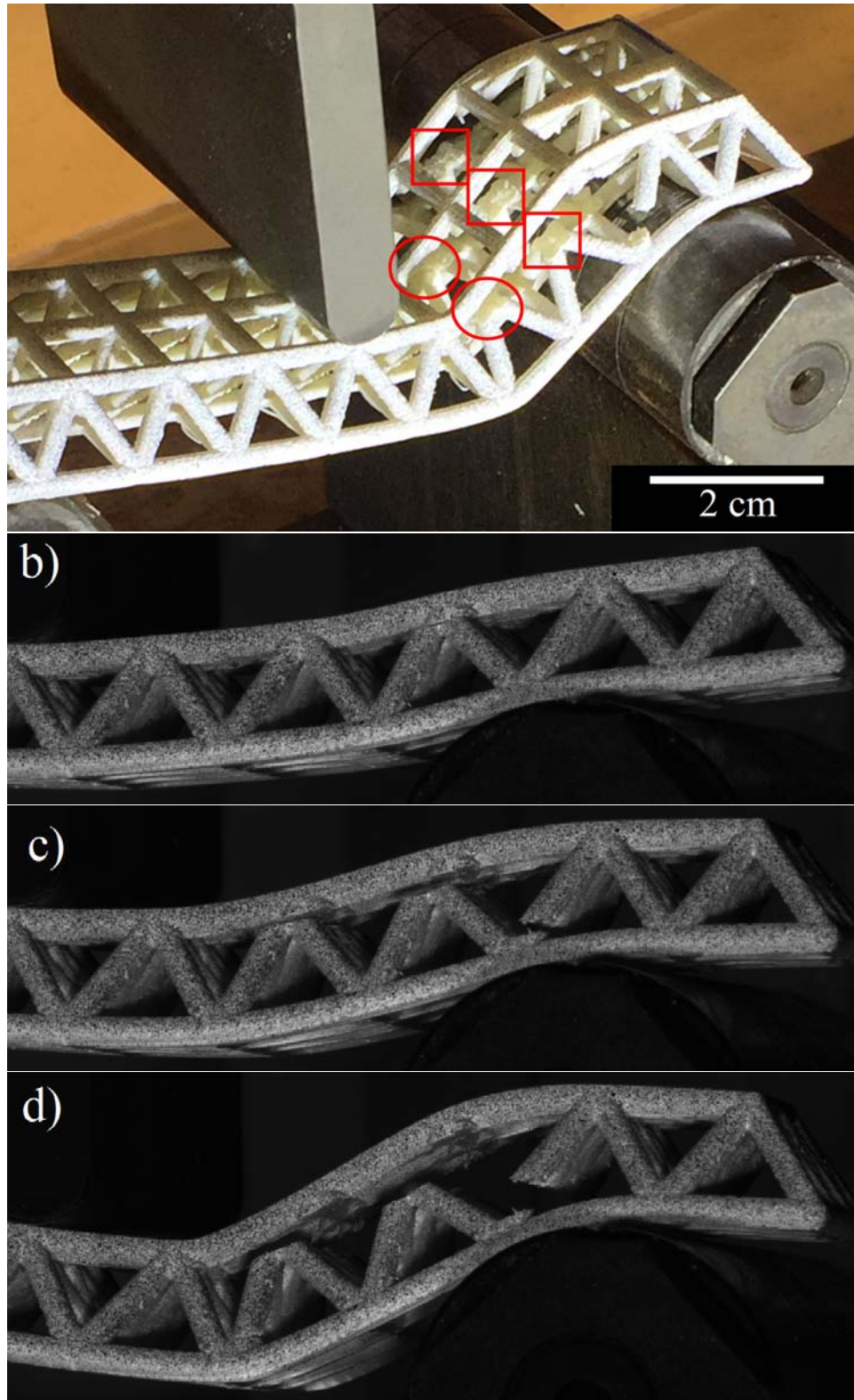


Figure 8.9: Snapshot taken of the FDM microtruss upon failure with the circled zones representing first failure by core shearing at the nodes and the squared zones being the next row hit by the same failure mechanism (a). DIC raw images of the FDM microtruss as it progressed from unfractured (b) to having two rows sheared within 1 second of each other (c). Much later, the planar failure surfaces are evident (d).

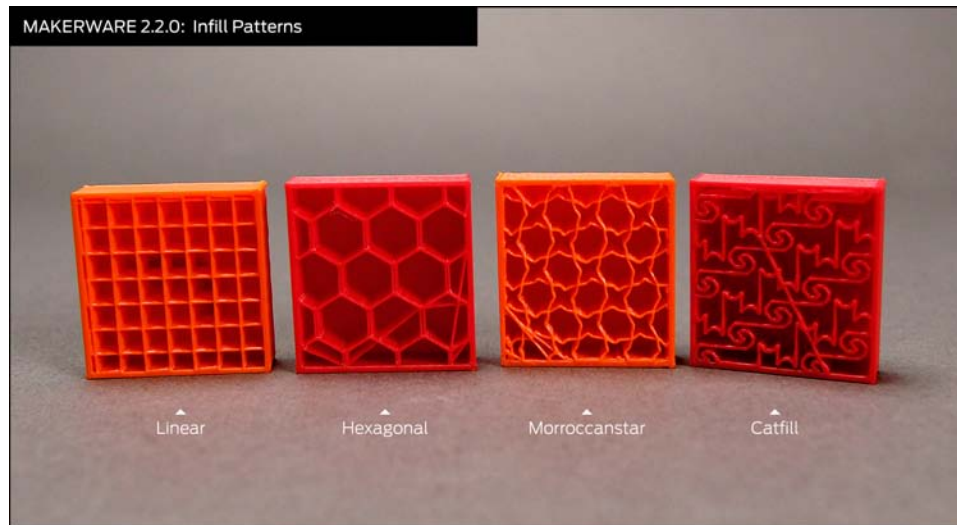


Figure 8.10: Various types of infill patterns that can be selected from the software used with the Makerbot Replicator FDM machine [159]. Further control is provided on the percentage of infill from 0 (hollow interior) to 100% (fully dense). The microtrusses printed with FDM here used a 75% infill with a hexagonal interior pattern.

manner (highlighted in the squared regions). The sequence is seen in higher quality from the DIC unprocessed images in Fig. 8.9b-c as the drops correspond to separation between the core and face in both unit cells within 1 second (time between snapshots). Much later into the test, the flat surface is seen on the underside of the face sheet (Fig. 8.9d).

Chapter 9

Conclusion

The work presented in this thesis is the culmination of a parallel approach between mathematical modelling and experimental fabrication of hybrid microtrusses. While techniques in recent years have created ultra-light metallic lattices and have shrunk the dimensions of these structures down to the nanometer regime, full geometric freedom has proven elusive. Most synthesis routes are tailored towards mass production or ease of manufacturing at the expense of architectural complexity. Instead, the fusion of rapid prototyping and electroplating offer a promising field straddling both the mechanics of optimal structures and the engineering of new nanomaterials. The main contributions of this work can be summarized as the ability to manufacture net-shape microtruss materials with nanocrystalline coatings as well as optimize their architectures using the developed analytical models. On the path to this realization, many more subtle minutiae explain how this process was completed. The take home messages that will apply to future work in both this work and other optimization and synthesis projects in the field of cellular materials are broken down into categories.

Analytical modelling centered on the derivation of failure mechanism equations active during bending of microtruss beams. Through the use of non-dimensionalization, failure mechanism maps were created for single material polymer systems, composite metal/polymer microtrusses, and hollow metallic structures. Within each of these maps, optimal trajectories were

located through the application of the Kuhn-Tucker condition. It was noted that while the use of stronger nano-coatings does increase performance, a true optimal hybrid will require the modification of architecture to utilize the high performance nanomaterial to its highest ability. Material selection and architecture are strongly intertwined in these structures.

In terms of characterization of the as-printed polymer, tensile dogbones laid flat had a larger UTS (45 MPa) and increased ductility (evidence of crazing during necking) compared to those vertically aligned (UTS of 37 MPa) who fractured before a peak strength was obtained. The pulling apart of the layers in the vertical direction led to this decrease in strength. This was also true for flexural bending tests where flat blocks outperformed vertical ones, again due to printing orientation. A flexural strength of 51 MPa and flexural modulus of 1700 MPa were reported. Finishing of the parts after printing resulted in shrinkage of up to 1% in each direction with overprinting vertical direction due to finite step sizes in the printer head's z-axis movement. Because of this, density values of 1.189 g/cm^3 were measured, higher than the 1.02 g/cm^3 quoted by the supplier. Work done to obtain reliable material properties of the as-printed polymer also resulted in the better understanding of the printing process and its impact on later hybridization steps. Polymer/wax interfaces were rougher due to diffusion between the liquid states before curing. This roughness could be removed with dissolution in sulfuric acid, a requirement to ensure even coverage during metallization and electrodeposition.

Rapid prototyping in the form of additive manufacturing was shown to be fully capable of making non-uniform microtruss materials with complexities like non-symmetric strut sizes, incorporation of filleting, and hollow interiors. Because the core was significantly less loaded in bending (as observed in DIC strain maps), weight reduction without compromise of load carrying capacity was possible with thinning of core struts. Filleting the nodal region also increased the ductility of the beams by limiting the impact of stress concentrations. Incorporating all these modifications into one structure resulted in the highest performance of those tested in the polymer state. Nanocrystalline SR33 microtrusses showed a 60x increase in peak flexural strength with only a 6x increase in density between the most heavily plated and the as-printed

samples.

Bringing it full circle, the models developed at the start of the thesis were successful in predicting the peak load carrying capacity of the various fabricated microtrusses with minor modifications. For polymer only structures, a size effect term was necessary when dealing with structures that failed by fracture in the sub-mm regime. Further reduction down to 5x the printer layer thickness or less was more difficult due to stochastic size effects and printer accuracy. For hybrid systems, the non-uniformity of the coating meant the model would output upper and lower bounds on predicted failure loads based on the thinnest and thickest struts in the microtruss. It was only in the thickest coatings that the model overpredicted the microtruss strength. Here, the recesses in the microtruss due to a lack of filleting resulted in incomplete coatings which short-circuited the predicted failure modes. Finally, the assumption that the metal reinforcement carries the majority of the load and the polymer core can be ignored in load carrying terms was proven through analysis of metal/polymer rods. The developed models were only able to predict the failure load when the force terms ignored the polymer core and assumed the structure was effectively a hollow metal tube. The importance here is that further optimization can more than halve the final density of an SR20 microtruss, for example, while maintaining the same load carrying capacity by removing the sacrificial polymer core using the sulphuric acid dissolution.

Bibliography

- [1] M. F. Ashby. The properties of foams and lattices. *Philosophical Transactions of the Royal Society A*, 364:15–30, 2006.
- [2] V. S. Deshpande, M. F. Ashby, and N. A. Fleck. Foam topology bending versus stretching dominated architectures. *Acta Materialia*, 49:1035–1040, 2001.
- [3] H. N. G. Wadley. Cellular metals manufacturing. *Advanced Engineering Materials*, 4:726–733, 2002.
- [4] U. Erb and A.M. El-Sherik. Pulsed direct current electrodeposition, 1994.
- [5] U. Erb, A. M. El-Sherik, C. K. S. Cheung, and M. J. Aus. Nanocrystalline metals, 1995.
- [6] M. A. Meyers, A. Mishra, and D. J. Benson. Mechanical properties of nanocrystalline materials. *Progress in Materials Science*, 51:427–556, 2006.
- [7] C. C. Koch. Structural nanocrystalline materials: an overview. *Journal of Materials Science*, 42:1403–1414, 2007.
- [8] K. S. Kumar, H. Van Swygenhoven, and S. Suresh. Mechanical behaviour of nanocrystalline metals and alloys. *Acta Materialia*, 51:5743–5774, 2003.
- [9] M. F. Ashby and Y. J. M. Brechet. Designing hybrid materials. *Acta Materialia*, 51:5801–5821, 2003.

- [10] M. F. Ashby. Hybrids to fill holes in material property space. *Philosophical Magazine*, 85:3235–3257, 2005.
- [11] M. F. Ashby. *Materials selection in mechanical design*. Elsevier: Butterworth-Heinemann, 3rd edition, 2005.
- [12] D. Zenkert. *An introduction to sandwich construction*. Sheffield, UK: Engineering Materials Advisory Service, 1995.
- [13] C. A. Steeves and N. A. Fleck. Material selection in sandwich beam construction. *Scripta Materialia*, 50:1335–1339, 2004.
- [14] C. A. Steeves and N. A. Fleck. Collapse mechanisms of sandwich beams with composite faces and a foam core, loaded in three-point bending. part ii: experimental investigation and numerical modelling. *International Journal of Mechanical Sciences*, 46:585–608, 2004.
- [15] W. C. Kim and C. K. H. Dharan. Facesheet debonding criteria for composite sandwich panels under in-plane compression. *Engineering Fracture Mechanics*, 42:643–652, 1992.
- [16] J. Hohe, V. Hardenacke, V. Fascio, Y. Girard, J. Baumeister, K. Stobener, J. Weise, D. Lehmhus, S. Pattofatto, H. Zeng, H. Zhao, V. Calbucci, F. Rustichelli, and F. Fiori. Numerical and experimental design of graded cellular sandwich cores for multi-functional aerospace applications. *Materials and Design*, 39:20–32, 2012.
- [17] L. J. Gibson and M. F. Ashby. The mechanics of three-dimensional cellular materials. *Proceedings of the Royal Society of London A*, 382:43–59, 1982.
- [18] Ultramet advanced material solutions: Reticulated vitreous carbon foam. http://www.ultramet.com/refractoryopencells_rvcf.html. Accessed: 2015-06-15.

- [19] Erg aerospace corporation: The basics of duocel foam. <http://www.ergaerospace.com/Descriptors.htm>. Accessed: 2015-06-15.
- [20] M. F. Ashby, A. G. Evans, N. A. Fleck, L. J. Gibson, J. W. Hutchinson, and H. N. G. Wadley. *Metal foams: A design guide*. Oxford, UK: Butterworth-Heinemann, 1999.
- [21] C. A. Steeves and N. A. Fleck. Collapse mechanisms of sandwich beams with composite faces and a foam core, loaded in three-point bending. part i: analytical models and minimum weight design. *International Journal of Mechanical Sciences*, 46:561–583, 2004.
- [22] R. B. Fuller. *Synergetic building construction*, 1961.
- [23] F. E. Griggs. Trajan's bridge: The world's first long-span wooden bridge. *Civil Engineering Practice*, 22:19–50, 2007.
- [24] C. Cichorius. The reliefs of trajan's column. plate number lxxii: Arrival of roman troops (scene xcvi); the emperor sacrifices by the danube (scene xcix); trajan receives foreign embassies (scene c), 1900.
- [25] J. C. Maxwell. On the calculation of the equilibrium and stiffness of frames. *Philosophical Magazine*, 27:294–299, 1864.
- [26] E. C. Zeeman. *Catastrophe Theory: Selected papers, 1972-1977*. London: Addison-Wesley, 1977.
- [27] V. S. Deshpande, N. A. Fleck, and M. F. Ashby. Effective properties of the octet-truss lattice material. *Journal of the Mechanics and Physics of Solids*, 49:1747–1769, 2001.
- [28] O. Sigmund. Topology optimization: a tool for the tailoring of structures and materials. *Philosophical Transactions of the Royal Society A*, 358:211–227, 2000.
- [29] H. N. G. Wadley. Multifunctional periodic cellular metals. *Philosophical Transactions of the Royal Society A*, 364:31–68, 2006.

- [30] L. J. Gibson and M. F. Ashby. *Cellular solids*. Cambridge: Cambridge University Press, 1988.
- [31] J. C. Wallach and L. J. Gibson. Mechanical behaviour of a three-dimensional truss material. *International Journal of Solids and Structures*, 38:7181–7196, 2001.
- [32] J. C. Wallach and L. J. Gibson. Defect sensitivity of a 3d truss material. *Scripta Materialia*, 45:639–644, 2001.
- [33] S. Chiras, D. R. Mumm, A. G. Evans, N. Wicks, J. W. Hutchinson, K. Dharmasena, H. N. G. Wadley, and S. Fichter. The structural performance of near-optimized truss core panels. *International Journal of Solids and Structures*, 39:4093–4115, 2002.
- [34] S. Ho, C. Ravindran, and G. D. Hibbard. Magnesium alloy micro-truss materials. *Scripta Materialia*, 62:21–24, 2010.
- [35] B. A. Bouwhuis, T. Ronis, J. L. McCrea, G. Palumbo, and G. D. Hibbard. Structural nanocrystalline ni coatings on periodic cellular steel. *Composites Science and Technology*, 69:385–390, 2009.
- [36] B. A. Bouwhuis, E. Bele, and G. D. Hibbard. Edge effects on compression testing periodic cellular metal sandwich cores. *Journal of Materials Science*, 43:3267–3273, 2008.
- [37] M. Suralvo, B. A. Bouwhuis, J. L. McCrea, G. Palumbo, and G. D. Hibbard. Hybrid nanocrystalline periodic cellular materials. *Scripta Materialia*, 58:247–250, 2008.
- [38] B. A. Bouwhuis and G. D. Hibbard. Failure mechanisms during periodic cellular metal fabrication by perforation stretching. *Metallurgical and Materials Transactions A*, 39:3027–3033, 2008.
- [39] B. Lee and K. Kang. Compressive strength of tube-woven kagome truss cores. *Scripta Materialia*, 60:391–394, 2009.

- [40] Y. Lee and K. Kang. A wire-woven cellular metal. part i: optimal design for applications as sandwich core. *Materials and Design*, 30:4434–4443, 2009.
- [41] B. Lee and K. Kang. A parametric study on compressive characteristics of wire-woven bulk kagome truss cores. *Composite Structures*, 92:445–453, 2010.
- [42] Y. Lee, B. Lee, I. Jeon, and K. Kang. Wire-woven bulk kagome truss cores. *Acta Materialia*, 55:6084–6094, 2007.
- [43] K. Kang. A wire-woven cellular metal of ultrahigh strength. *Acta Materialia*, 57:1865–1874, 2009.
- [44] L. M. Gordon, B. A. Bouwhuis, M. Suralvo, J. L. McCrea, G. Palumbo, and G. D. Hibbard. Micro-truss nanocrystalline ni hybrids. *Acta Materialia*, 57:932–939, 2009.
- [45] T. A. Schaedler, A. J. Jacobsen, A. Torrents, A. E. Sorenson, J. Lian, J. Greer, L. Valdevit, and W. B. Carter. Ultralight metallic microtrusses. *Science*, 334:962–965, 2011.
- [46] L. R. Meza, S. Ds, and J. R. Greer. Strong, lightweight, and recoverable three-dimensional ceramic nanolattices. *Science*, 345:1322–1326, 2014.
- [47] Q. Chen, S. C. Bae, and S. Granick. Directed self-assembly of a colloidal kagome lattice. *Nature*, 469:381–384, 2011.
- [48] A. G. Evans, J. W. Hutchinson, and M. F. Ashby. Cellular metals. *Current Opinion in Solid State and Materials Science*, 3:288–303, 1998.
- [49] A. G. Evans, J. W. Hutchinson, and M. F. Ashby. Multifunctionality of cellular metal systems. *Progress in Materials Science*, 43:171–221, 1999.
- [50] J. Priluck. Lattice block material, 1996.

- [51] Federal technology group: Advanced materials - lattice block structures. http://www.fedtechgroup.com/advanced_materials/lbs/lbs_index.html. Accessed: 2015-06-15.
- [52] M. L. Renaud, A. F. Giamei, M. S. Thompson, and J. Priluck. The effect of parent metal properties on the performance of lattice block material. In *Porous and cellular materials for structural applications*, pages 109–117, year =. Materials Research Society.
- [53] National Aeronautics and Space Administration. Lattice block and metallic foam materials. <https://technology.grc.nasa.gov/documents/auto/Lattice-Block-and-Metallic-Foam-Materials.pdf>. Accessed: 2015-06-15.
- [54] N. Wicks and J. W. Hutchinson. Optimal truss plates. *International Journal of Solids and Structures*, 38:5165–5183, 2001.
- [55] N. Wicks and J. W. Hutchinson. Performance of sandwich plates with truss cores. *Mechanics of Materials*, 36:739–751, 2001.
- [56] C. S. Daily, D. A. Lees, and D. D. McKitterick. Truss structure design, 2000.
- [57] J. Wang, A. G. Evans, K. Dharmasena, and H. N. G. Wadley. On the performance of truss panels with kagom cores. *International Journal of Solids and Structures*, 40:6981–6988, 2003.
- [58] N. A. Meisel, C. B. Williams, and A. Druschitz. Lightweight metal cellular structures via indirect 3d printing and casting. In *23rd Annual International Solid Freeform Fabrication Symposium*, 2012.
- [59] J. E. Campbell, M. Suralvo, G. D. Hibbard, and H. E. Naguib. Foamed core microtruss nanocrystalline ni cellular hybrids. *Journal of Composite Materials*, 46:63–70, 2011.
- [60] V. S. Deshpande and N. A. Fleck. Collapse of truss core sandwich beams in 3-point bending. *International Journal of Solids and Structures*, 38:6275–6305, 2001.

- [61] H. N. G. Wadley, N. A. Fleck, and A. G. Evans. Fabrication and structural performance of periodic cellular metal sandwich structures. *Composites Science and Technology*, 63:2331–2343, 2003.
- [62] D. J. Sypeck and H. N. G. Wadley. Cellular metal truss core sandwich structures. *Advanced Engineering Materials*, 4:759–764, 2002.
- [63] B. A. Bouwhuis and G. D. Hibbard. Compression testing of periodic cellular sandwich cores. *Metallurgical and Materials Transactions B*, 37:919–927, 2006.
- [64] B. A. Bouwhuis, E. Bele, and G. D. Hibbard. Plastic hinging collapse of periodic cellular truss cores. *Metallurgical and Materials Transactions A*, 39:2329–2339, 2008.
- [65] K. Abu Samk, B. Yu, and G. D. Hibbard. Architectural design in stretch-formed microtruss composites. *Composites: Part A*, 43:955–961, 2012.
- [66] B. Yu, K. A. Samk, and G. D. Hibbard. Optimizing the compressive strength of strain-hardenable stretch-formed microtruss architectures. *Metallurgical and Materials Transactions A*, 46:1985–1994, 2015.
- [67] G. W. Kooistra, V. S. Deshpande, and H. N. G. Wadley. Compressive behavior of age hardenable tetrahedral lattice truss structures made from aluminium. *Acta Materialia*, 52:4229–4237, 2004.
- [68] B. A. Bouwhuis, S. K. Tang, and G. D. Hibbard. Process-microstructure-property relationships in aa3003 expanded metal periodic cellular truss cores. *Composites: Part A*, 39:1556–1564, 2008.
- [69] D. J. Sypeck and H. N. G. Wadley. Multifunctional microtruss laminates: Textile synthesis and properties. *Journal of Materials Research*, 16:890–897, 2001.
- [70] M. Zupan, V. S. Deshpande, and N. A. Fleck. The out-of-plane compressive behaviour of woven-core sandwich plates. *European Journal of Mechanics A*, 23:411–421, 2004.

- [71] J. Lim and K. Kang. Mechanical behaviour of sandwich panels with tetrahedral and kagome truss cores fabricated from wires. *International Journal of Solids and Structures*, 43:5228–5246, 2006.
- [72] S. Hyun, A. M. Karlsson, S. Torquato, and A. G. Evans. Simulated properties of kagome and tetragonal truss core panels. *International Journal of Solids and Structures*, 40:6989–6998, 2003.
- [73] B. Lee, K. Lee, J. Byun, and K. Kang. The compressive response of new composite truss cores. *Composites: Part B*, 43:317–324, 2012.
- [74] V. Vadakke and L. A. Carlsson. Experimental investigation of compression failure of sandwich specimens with face/core debond. *Composites Part B: Engineering*, 35:583–590, 2004.
- [75] D. T. Pham and R. S. Gault. A comparison of rapid prototyping technologies. *International Journal of Machine Tools and Manufacture*, 38:1257–1287, 1998.
- [76] M. Mahesh, Y. S. Wong, J. Y. H. Fuh, and H. T. Loh. Benchmarking for comparative evaluation of rp systems and processes. *Rapid Prototyping Journal*, 10:123–135, 2004.
- [77] G. D. Kim and Y. T. Oh. A benchmark study on rapid prototyping processes and machines: quantitative comparisons of mechanical properties, accuracy, roughness, speed and material cost. *Proceedings of the Institution of Mechanical Engineers, Part B: Journal of Engineering Manufacture*, 222:201–215, 2008.
- [78] F. P. W. Melchels, J. Feijen, and D. W. Grijpma. A review of stereolithography and its applications in biomedical engineering. *Biomaterials*, 31:6121–6130, 2010.
- [79] C. W. Hull. Apparatus for production of three-dimensional objects by stereolithography, 1986.

- [80] R. A. Coleman. Polymerizable benzophenone uv absorber-condensation polymers, 1968.
- [81] H. Kodama. Automatic method for fabricating a three-dimensional plastic model with photo-hardening polymer. *Review of Scientific Instruments*, 52:1770–1773, 1981.
- [82] K. A. Schmidt, V. A. Doan, P. Xu, J. S. Stockwell, and S. K. Holden. Ultra-violet light curable hot melt composition, 2003.
- [83] M. T. Sherwood. Flash curing in selective deposition modeling, 2005.
- [84] D. L. Milius. Chemical energy conversion and power generation at the microelectromechanical systems (mems) scale. <http://www.princeton.edu/~cml/html/research/mems.html>, 2001. Princeton University, Ceramic Materials Laboratory, Accessed: 2015-06-15.
- [85] Jetted photopolymer. <http://www.custompartnet.com/wu/jetted-photopolymer>. Accessed: 2015-06-15.
- [86] S. S. Crump. Apparatus and method for creating three-dimensional objects, 1992.
- [87] S. H. Masood and W. Q. Song. Development of new metal/polymer materials for rapid tooling using fused deposition modelling. *Materials and Design*, 25:587–594, 2004.
- [88] Fused deposition modeling (fdm). <http://www.custompartnet.com/wu/fused-deposition-modeling>. Accessed: 2015-06-15.
- [89] Fused deposition modeling (fdm). <http://www.custompartnet.com/wu/fused-deposition-modeling>. Accessed: 2015-06-15.
- [90] D. W. Rosen. Computer-aided design for additive manufacturing of cellular structures. *Computer-Aided Design and Applications*, 4:585–594, 2007.

- [91] C. Chu, G. Graf, and D. W. Rosen. Design for additive manufacturing of cellular structures. *Computer-Aided Design and Applications*, 5:686–696, 2008.
- [92] R. J. Jackman, S. T. Brittain, A. Adams, M. G. Prentiss, and G. M. Whitesides. Design and fabrication of topologically complex, three-dimensional microstructures. *Science*, 280:2089–2091, 1998.
- [93] S. T. Brittain, Y. Sugimura, O. J. A. Schueller, A. G. Evans, and G. M. Whitesides. Fabrication and mechanical performance of a mesoscale space-filling truss system. *Journal of Microelectromechanical Systems*, 10:113–120, 2001.
- [94] B. A. Bouwhuis, J. L. McCrea, G. Palumbo, and G. D. Hibbard. Mechanical properties of hybrid nanocrystalline metal foams. *Acta Materialia*, 57:4046–4053, 2009.
- [95] A. T. Lausic, B. A. Bouwhuis, J. L. McCrea, G. Palumbo, and G. D. Hibbard. Mechanical anisotropy in electrodeposited nanocrystalline metal/metal composite foams. *Materials Science and Engineering A*, 552:157–163, 2012.
- [96] A. Jung, H. Natter, S. Diebels, E. Lach, and R. Hempelmann. Nanonickel coated aluminum foam for enhanced impact energy absorption. *Advanced Engineering Materials*, 13:23–28, 2011.
- [97] Y. Boonyongmaneerat, C. A. Schuh, and D. C. Dunand. Mechanical properties of reticulated aluminum foams with electrodeposited ni-w coatings. *Scripta Materialia*, 59:336–339, 2008.
- [98] E. Bele, B. A. Bouwhuis, and G. D. Hibbard. Work hardening as a strengthening mechanism in periodic cellular materials. *Materials Science and Engineering A*, 489:29–37, 2008.
- [99] E. Bele, B. A. Bouwhuis, and G. D. Hibbard. Microstructural design in work hardenable perforation stretch formed micro-truss cores. *Composites: Part A*, 40:1158–1166, 2009.

- [100] B. A. Bouwhuis and G. D. Hibbard. Relative significance of in-situ work-hardening in deformation-formed micro-truss materials. *Materials Science and Engineering A*, 527:565–573, 2010.
- [101] J. St-Pierre, N. A. Fleck, and V. S. Deshpande. The predicted compressive strength of a pyramidal lattice made from case hardened steel tubes. *International Journal of Solids and Structures*, 51:41–52, 2014.
- [102] E. Bele, B. A. Bouwhuis, C. Codd, and G. D. Hibbard. Structural ceramic coatings in composite microtruss cellular materials. *Acta Materialia*, 59:6145–6154, 2011.
- [103] B. A. Bouwhuis, B. Chebab, O. Bouaziz, D. Embury, H. Zurob, and G. D. Hibbard. Deformation twinning as a strengthening mechanism in microtruss cellular materials. *Scripta Materialia*, 63:609–612, 2010.
- [104] S. Markkula, S. Strock, D. Burns, and M. Zupan. Compressive behaviour of pyramidal, tetrahedral, and strut-reinforced tetrahedral abs and electroplated cellular solids. *Advanced Engineering Materials*, 11:1–2, 2009.
- [105] I. Chasiotis, C. Bateson, K. Timpano, A. S. McCarty, N. S. Barker, and J. R. Stanec. Strain rate effects on the mechanical behaviour of nanocrystalline au films. *Thin Solid Films*, 515:3183–3189, 2007.
- [106] Y. M. Wang, A. F. Jankowski, and A. V. Hamza. Strength and thermal stability of nanocrystalline gold alloys. *Scripta Materialia*, 57:301–304, 2007.
- [107] A. A. Karimpoor, U. Erb, K. T. Aust, and G. Palumbo. High strength nanocrystalline cobalt with high tensile ductility. *Scripta Materialia*, 49:651–656, 2003.
- [108] A. A. Karimpoor and U. Erb. Mechanical properties of nanocrystalline cobalt. *Physica Status Solidi A*, 203:1265–1270, 2006.

- [109] G. J. Fan, L. F. Fu, D. C. Qiao, H. Choo, P. W. Liaw, and N. D. Browning. Grain growth in a bulk nanocrystalline co alloy during tensile plastic deformation. *Scripta Materialia*, 54:2137–2141, 2006.
- [110] G. J. Fan, L. F. Fu, H. Choo, P. K. Liaw, and N. D. Browning. Uniaxial tensile plastic deformation and grain growth of bulk nanocrystalline alloys. *Acta Materialia*, 54:4781–4792, 2006.
- [111] I. Brooks, P. Lin, G. Palumbo, G. D. Hibbard, and U. Erb. Analysis of hardness-tensile strength relationships for electroformed nanocrystalline materials. *Materials Science and Engineering A*, 491:412–419, 2008.
- [112] Y. Nakamoto, M. Yuasa, Y. Chen, H. Kusuda, and M. Mabuchi. Mechanical properties of a nanocrystalline co-cu alloy with a high-density fine nanoscale lamellar structure. *Scripta Materialia*, 58:731–734, 2008.
- [113] L. Lu, Y. Shen, X. Chen, L. Qian, and K. Lu. Ultrahigh strength and high electrical conductivity in copper. *Science*, 304:422–426, 2004.
- [114] L. Lu, S. X. Li, and K. Lu. An abnormal strain rate effect on tensile behaviour in nanocrystalline copper. *Scripta Materialia*, 45:1163–1169, 2001.
- [115] L. Lu, L. B. Wang, B. Z. Ding, and K. Lu. High-tensile ductility in nanocrystalline copper. *Journal of Materials Research*, 15:270–273, 2000.
- [116] I. Brooks, G. Palumbo, G. D. Hibbard, Z. Wang, and U. Erb. On the intrinsic ductility of electrodeposited nanocrystalline metals. *Journal of Materials Science*, 46:7713–7724, 2011.
- [117] A. M. El-Sherik, U. Erb, G. Palumbo, and K. T. Aust. Deviations from hall-petch behaviour in as-prepared nanocrystalline nickel. *Scripta Metallurgica et Materialia*, 27:1185–1188, 1992.

- [118] A. M. El-Sherik and U. Erb. Synthesis of bulk nanocrystalline nickel by pulsed electrodeposition. *Journal of Materials Science*, 30:5743–5749, 1995.
- [119] H. Li, F. Ebrahimi, H. Choo, and P. K. Liaw. Grain size dependence of tensile behaviour in nanocrystalline ni-fe alloys. *Journal of Materials Science*, 41:7636–7642, 2006.
- [120] R. Schwaiger, B. Moser, M. Dao, N. Chollacoop, and S. Suresh. Some critical experiments on the strain-rate sensitivity of nanocrystalline nickel. *Acta Materialia*, 51:5159–5172, 2003.
- [121] K. S. Kumar, S. Suresh, M. F. Chisholm, J. A. Horton, and P. Wang. Deformation of electrodeposited nanocrystalline nickel. *Acta Materialia*, 51:387–405, 2003.
- [122] T. Ungar, A. Revesz, and A. Borbely. Dislocations and grain size in electrodeposited nanocrystalline ni determined by the modified williamson-hall and warren-verbach procedures. *Journal of Applied Crystallography*, 31:554–558, 1998.
- [123] A. Torrents, H. Yang, and F. A. Mohamed. Effect of annealing on hardness and the modulus of elasticity in bulk nanocrystalline nickel. *Metallurgical and Materials Transactions A*, 41:621–630, 2010.
- [124] J. D. Giallonardo, U. Erb, K. T. Aust, and G. Palumbo. The influence of grain size and texture on the young's modulus of nanocrystalline nickel and nickel-iron alloys. *Philosophical Magazine*, 36:4594–4605, 2011.
- [125] U. Klement, U. Erb, A. M. El-Sherik, and K. T. Aust. Thermal stability of nanocrystalline ni. *Materials Science and Engineering A*, 203:177–186, 1995.
- [126] M. Chauhan and F. A. Mohamed. Investigation of low temperature thermal stability in bulk nanocrystalline ni. *Materials Science and Engineering A*, 427:7–15, 2006.
- [127] H. Wei, G. D. Hibbard, G. Palumbo, and U. Erb. The effect of gauge volume on the

- tensile properties of nanocrystalline electrodeposits. *Scripta Materialia*, 57:996–999, 2007.
- [128] H. Li, K. Tao, H. Choo, and P. K. Liaw. Enhanced strength and ductility at a cryogenic temperature in a nanostructured ni-fe alloy. *Materials Science Forum*, 539-543:2828–2833, 2007.
- [129] A. Giga, Y. Kimoto, Y. Takigawa, and K. Higashi. Demonstration of an inverse hall-petch relationship in electrodeposited nanocrystalline ni-w alloys through tensile testing. *Scripta Materialia*, 55:143–146, 2006.
- [130] U. Erb, G. Palumbo, and J. L. McCrea. The processing of bulk nanocrystalline metals and alloys by electrodeposition. In S. H. Whang, editor, *Nanostructured Metals and Alloys*, chapter 5, pages 118–151. Woodhead Publishing, 2011.
- [131] C. C. Koch, I. A. Ovid'ko, S. Seal, and S. Veprek. *Structural nanocrystalline materials: fundamentals and applications*. Cambridge: Cambridge University Press, 2007.
- [132] C. E. Carlton and P. J. Ferreira. What is behind the inverse hallpetch effect in nanocrystalline materials? *Acta Materialia*, 55:3749–3756, 2007.
- [133] H. Gleiter. Nanostructured materials: basic concepts and microstructure. *Acta Materialia*, 48:1–29, 2000.
- [134] G. Palumbo, S. J. Thorpe, and K. T. Aust. On the contribution of triple junctions to the structure and properties of nanocrystalline materials. *Scripta metallurgica et materialia*, 24:1347–1350, 1990.
- [135] S. P. Timoshenko and J. M. Gere. *Theory of Elastic Stability*. Mineola, New York: Dover Publications, Inc., 2nd edition, 1961.
- [136] V. I. Weingarten, P. Seide, and J. P. Peterson. Buckling of thin-walled circular cylinders.

- Space Vehicle Design Criteria (Structures) monograph SP-8007, National Aeronautics and Space Administration, 1965.
- [137] H. W. Kuhn and A. W. Tucker. Nonlinear programming. In *Proceedings of the Second Berkeley Symposium on Mathematical Statistics and Probability*, pages 481–492, 1951.
- [138] F. R. Shanley. Inelastic column theory. *Journal of the Aeronautical Sciences*, 14:261–268, 1947.
- [139] E. Voce. A practical strain-hardening function. *Metallurgica*, 51:219–226, 1955.
- [140] 3d systems, inc. professional printers: Projet 3500 hd. <http://www.3dsystems.com/3d-printers/professional/projet-3500-hd>. Accessed: 2015-06-15.
- [141] ASTM D638-10. Standard test method for tensile properties of plastics. Technical report, American Society for Testing and Materials, West Conshohocken, PA, USA, 2010.
- [142] C. S. Henkee and E. J. Kramer. Crazing and shear deformation in cross-linked polystyrene. *Journal of Polymer Science: Polymer Physics Edition*, 22:721–737, 2003.
- [143] ASTM D790-10. Standard test methods for flexural properties of unreinforced and reinforced plastics and electrical insulating materials. Technical report, American Society for Testing and Materials, West Conshohocken, PA, USA, 2010.
- [144] A. T. Lausic, C. A. Steeves, and G. D. Hibbard. Failure mechanisms in rapid-prototyped polymer microtrusses. In *Canadian Conference on Nonlinear Solid Mechanics*, 2013.
- [145] S. Pellegrino and C. R. Calladine. Matrix analysis of statically and kinematically indeterminate frameworks. *International Journal of Solids and Structures*, 22:409–428, 1986.
- [146] S. Pellegrino. Structural computations with the singular value decomposition of the equilibrium matrix. *International Journal of Solids and Structures*, 30:3025–3035, 1993.

- [147] Z. P. Bazant. Size effect in blunt fracture: concrete, rock, metal. *Journal of Engineering Mechanics*, 110:518–535, 1984.
- [148] Z. P. Bazant. Size effect on structural strength: a review. *Archive of Applied Mechanics*, 69:703–725, 1999.
- [149] A. A. Griffith. The phenomena of rupture and flow in solids. *Philosophical Transactions of the Royal Society of London A*, 221:163–198, 1921.
- [150] Liu T., Deng Z. C., and Lu T. J. Design optimization of truss-cored sandwiches with homogenization. *International Journal of Solids and Structures*, 43:7891–7918, 2006.
- [151] Novamet specialty products corp. incofoam. <http://www.novametcorp.com/products/incofoam/>. Accessed: 2015-06-15.
- [152] A. G. Evans, M. Y. He, V. S. Deshpande, J. W. Hutchinson, A. J. Jacobsen, and W. B. Carter. Concepts for enhanced energy absorption using hollow micro-lattices. *International Journal of Impact Engineering*, 37:947–959, 2010.
- [153] B. Budiansky. On the minimum weights of compression structures. *International Journal of Solids and Structures*, 36:3677–3708, 1999.
- [154] S. M. Pingle, N. A. Fleck, V. S. Deshpande, and H. N. G. Wadley. Collapse mechanism maps for the hollow pyramidal core of a sandwich panel under transverse shear. *International Journal of Solids and Structures*, 48:3417–3430, 2011.
- [155] Integran technologies, inc. <http://www.integran.com/>. Accessed: 2015-06-15.
- [156] ASTM E8-09. Standard test methods for tension testing of metallic materials. Technical report, American Society for Testing and Materials, West Conshohocken, PA, USA, 2009.

[157] ASTM D695-10. Standard test method for compressive properties of rigid plastics. Technical report, American Society for Testing and Materials, West Conshohocken, PA, USA, 2010.

[158] P. Panjavarnam and M. M. Hussin. Fabrication of hollow tube nanocrystalline nickel microtruss. Bachelor of applied science thesis, University of Toronto, 2013.

[159] D. Pryadko. A tour around the world of 3d-printing technologies: extrusion deposition modelling. <http://aptgadget.com/a-tour-around-the-world-of-3d-printing-technologies-extrusion-deposition-mode>. 2015. Accessed: 2015-12-07.

Appendix A

Additional mechanical testing on rapid prototyped polymer parts

The contents of this appendix include elaborations on the time and finishing effects of the polymer compression coupons as well as polymer microtrusses. In particular, samples left out to air with equal time spent inside the finisher were seen to become more brittle up to one week after removal from the finisher. Tensile dogbones are also provided for samples made according to ASTM specifications. These samples were not included in the main portion of the document as finding the sweet spot between slipping and cracking the sample in the grips was random. This led to large spreads in material properties and inconsistent values. Finally, the NiCo tensile stress-strain curve used to make predictions on the fabricated metal/polymer microtrusses is provided with its Voce fit.

A.1 Time effect on polymer properties

An experimental design was needed to determine what were the optimal conditions. In order to obtain the best method for finishing complex parts, various finishing techniques were tested using polymer coupons modeled after ASTM D695 [157]. The samples were extracted from the rapid prototyper and placed inside the finisher at a constant 65° C, as recommended by

3D Systems, Inc. They were left inside the finisher to allow the wax to melt and drain off for up to 1 week (but at least 3 hours). For each of the finisher times, samples were extracted and tested in uniaxial compression. The time from extraction to testing varied from 5 minutes (running samples from the finisher to the universal testing machine) to 1 week of sitting at room temperature before testing in order to observe the required time before full hardening of the polymer.

Adjusting the finishing time of the samples revealed that the wax had been completely removed after 3 hours as long as kimwipes had been interchanged under the sample to collect the dripping wax. Without this step, some wax wets the polymer surface and does not drip off. Figure A.1 shows that if the setting time was the same then the amount of time that the samples spent in the finisher did not vary the compression test results. The critical parameter here is the time out of finisher, as seen in Figure A.2. From 4 to 45 minutes, the polymer column drastically increases in strength and stiffness as can be expected for a polymer cooling from 65° C to room temperature. After a full week, repeated samples all had the same general compression curve shape represented by the one dashed black line.

These tests were repeated on polymer microtrusses tested in bending and a similar behaviour was observed. When the samples were tested while still warm, the polymer had not been given enough time to solidify and was soft resulting in a decrease in stiffness and peak strength (Figure A.3). Additionally, the deflection at fracture was larger for the softer samples, as expected, but the failure mechanism was consistent among all tests - tensile fracture at the bottom edge at mid-span. Overall, the conditions for printing have been optimized to the extent of being able to create structures with good repeatability and reproducibility as long as the timing can be controlled and samples are not tested too quickly after extraction from the heated finisher.

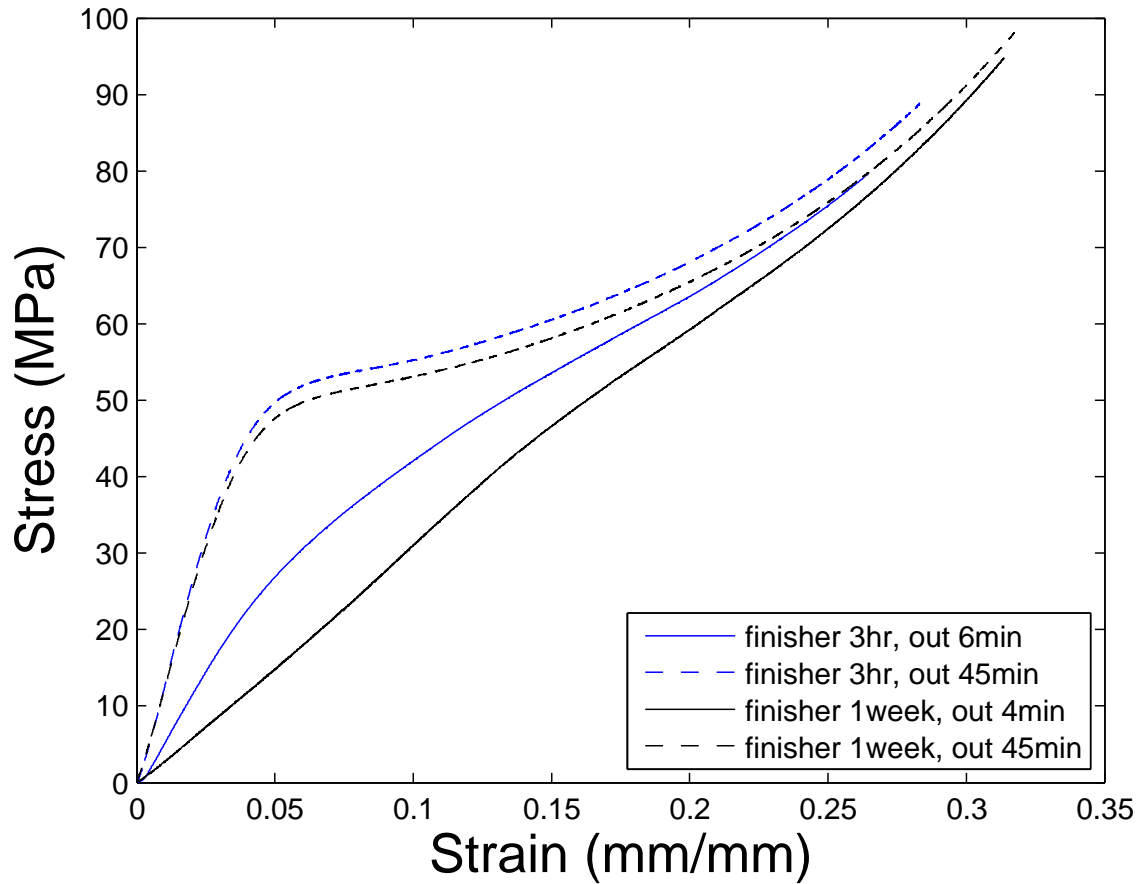


Figure A.1: Polymer ASTM D695 coupons tested after 3 hours and 1 week sitting inside a 65° C finisher. Each sample was also tested immediately after removal from oven (≈ 4 minutes) and 1 week later. Lower stiffness and yield strength are seen for samples not cooled adequately.

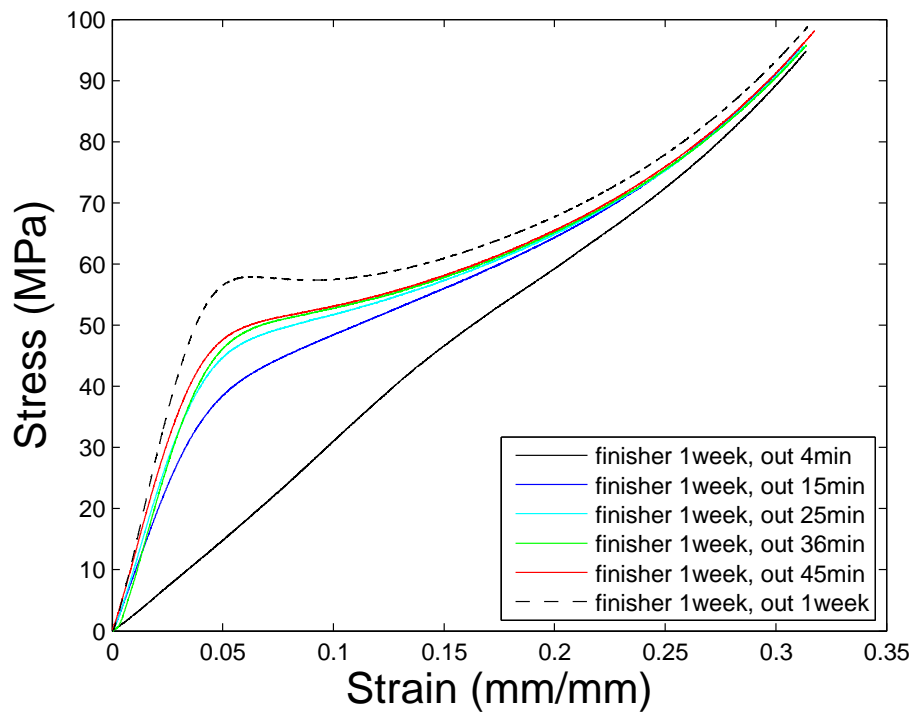


Figure A.2: Polymer ASTM D695 coupons tested after 1 week sitting inside a 65° C finisher. Samples were tested in varying time after removal ranging from 4 minutes to 1 week. A trend of increasing stiffness and yield strength is seen with increasing time as the polymer material sets and becomes more brittle.

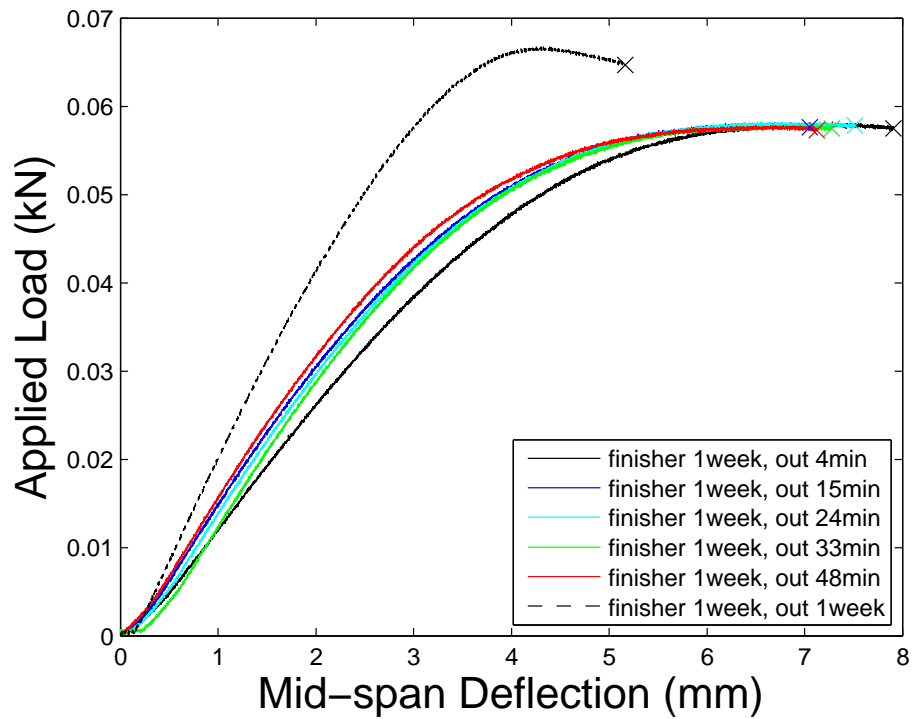


Figure A.3: Polymer square pyramidal microtrusses tested after 1 week sitting inside a 65° C finisher. Samples were tested in varying time after removal ranging from 4 minutes to 1 week. A trend of increasing stiffness and peak strength is seen with increasing time as the polymer material sets and becomes more brittle.

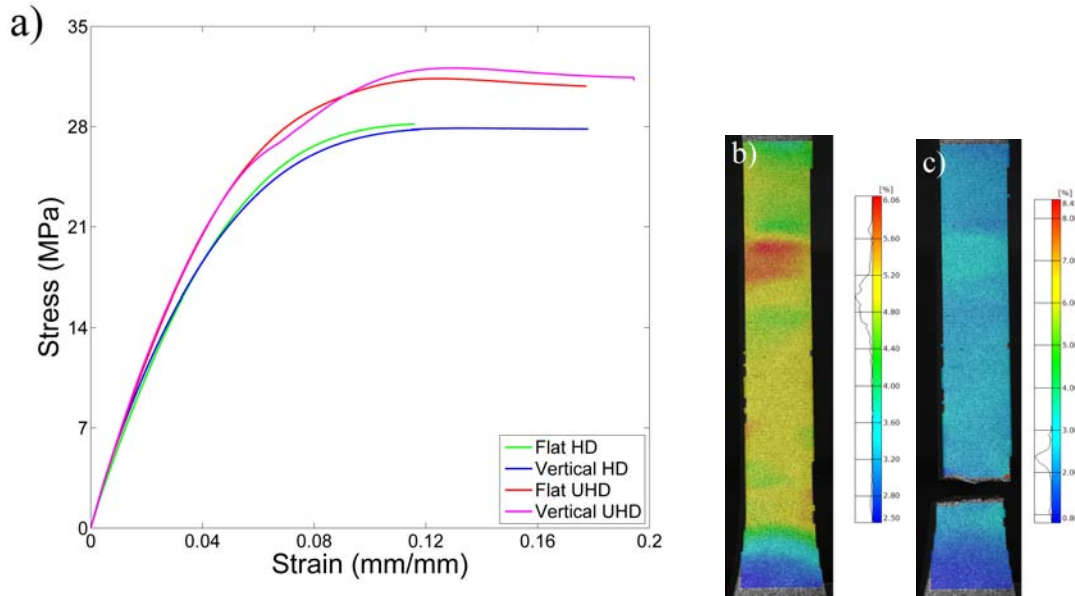


Figure A.4: Tensile stress-strain curves for the as-printed polymer dogbones fabricated in both the HD and UHD modes in flat and vertical directions (a). An increase in UTS with similar Young's modulus was observed for the UHD samples. DIC images of the UHD flat sample immediately before (b) and after (c) fracture at the shoulder.

A.2 Tensile tests on full-scale tensile coupons

Of the different types of sample sizes available in the standard, a preference to Type I is preferred and was initially selected. Coupons had a thickness of 7 mm, a width of 13 mm, a gauge length of 50 mm, and had a fillet radius of 76 mm. The as-standard samples were printed in both the HD and UHD modes of the ProJet 3500HD prototyper and finished accordingly.

Of the 30 samples that the study started with, ten tests were stopped before failure as it was observed that the grip areas of the dogbone were slipping out of the 50 kN load cell Shimadzu universal testing apparatus. Three samples were then tested with increased tightening of the grips at either end but all three then failed inside the grips as the teeth dug into the polymer creating crack initiation sites. Once a sweet spot of tightness and pressure on the dogbone was obtained, one sample from each set was tested. Figure A.4a shows the tensile stress-strain curves of the UHD and HD dogbones. While any distinguishing in UTS between vertical and flat samples is difficult to observe in a small sample set, the UHD dogbones are

considerably stronger owing to thinner layering. If a thinner layer is deposited, the UV curing penetrates deeper through the layer and into the previous ones resulting in more cross-linking and a stronger sample.

Upon closer examination, however, all five had failed at the extreme edge of the gauge - the spot where the fillet radius begins to curve outwards. At the second immediately before fracture, the DIC image in Fig. A.4b shows a large zone of increased strain near the middle of the gauge but also a smaller zone with similar strain at the shoulder. Because the printer does not have infinitely small resolution, a small step exists at this point and creates a stress concentration. Looking at the image taken one second later when fractured had occurred (Fig. A.4c), this smaller zone is where failure began. Note that the DIC was also able to pick up residual strain in the sample after failure - the larger zone has a now permanent 3 - 3.5% strain.

To correct for this, the next sample from each set was sanded on the thickness edge from top to bottom to attempt to remove any steps in the polymer. A fine grit paper was used for this. The testing was repeated and this time all four sample sets saw their UTS increase $\approx 15\%$ (fig A.5a). The DIC analysis immediately before fracture (fig A.5b) still showed a tendency for failure towards the ends of the gauge but within the failure zone, the maximum strain increased from 6% in the unsanded case to 10% in the sanded case. Even with this improvement, the UTS falls short of the 42.4 MPa quoted by the supplier [ref]. A larger subset of samples is required to more accurately probe this value. After fracture, the sample is also more uniformly stretched than in the unsanded case (fig A.5c). When collecting the remnants of the dogbone after testing, there are now three pieces instead of two as before - a top and bottom but also a small wedge. This wedge fits between the top and bottom implying a flaw on one side started a crack and it spread to the other side in two paths that went through the printed layers.

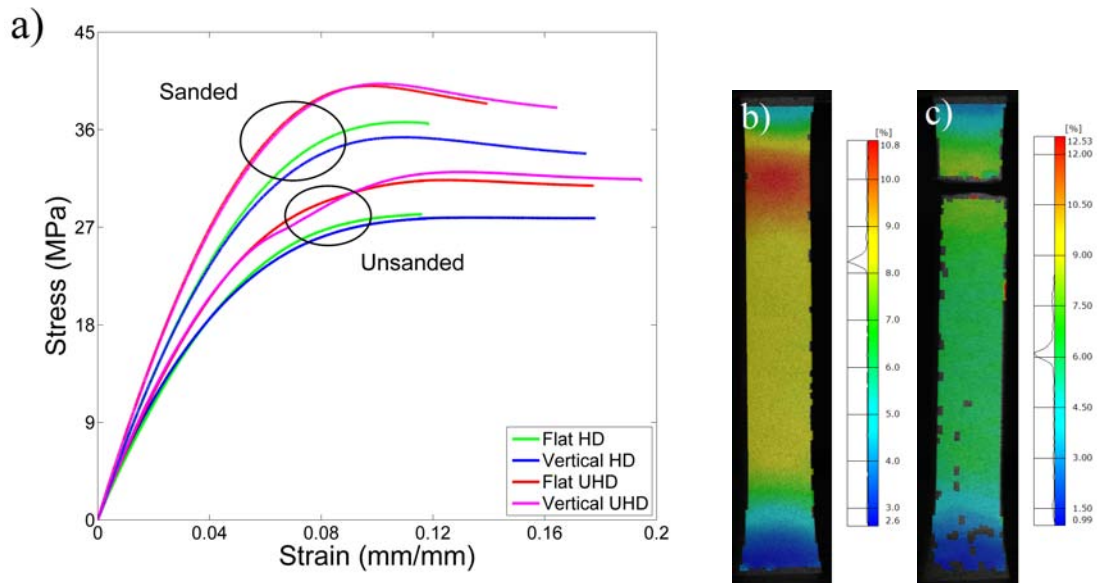


Figure A.5: Tensile stress-strain curves for the as-printed polymer dogbones fabricated in both the HD and UHD modes in flat and vertical directions (a). Samples have been sanded along the thickness direction in an attempt to remove the steps leading from gauge to shoulder that act as stress concentrations. An increase in UTS and Young's modulus was observed when comparing sanded to unsanded samples. DIC images of the UHD flat sample immediately before (b) and after (c) fracture at the shoulder. While sanding eliminated most of the steps, some remained and caused the same failure point, but at higher stress.

A.3 NiCo stress-strain curve and Voce fit

For the metal/polymer microtrusses fabricated in this thesis, the size of the finished polymer parts was on the order of 250 mm in length. Structures this large were plated by the industrial partner Integran Technologies, Inc. using their proprietary electrodeposition lines. When the various MEDXX-X samples being coated, a bath was selected that would deposit high performance NiCo alloys with grain sizes on the order of 20 nm. To predict the mechanical performance of this hybrid microtruss using the developed analytical models in this thesis, a tensile stress-strain curve for this material was obtained and fit to a Voce equation (equation 6.1).

Figure A.6 shows the true stress-strain curve as well as the overlaid Voce fit. After the UTS is reached, the tensile dogbone began to neck and the stress dropped off before fracture occurred in the middle of the gauge. Because of this decrease, the Voce fit was limited to up until the UTS (based on the true stress-strain response). Because values near the UTS immediately identify as beginning the tensile failure zone, this removal does not effect predicted behaviour. Based on a goodness-of-fit of $R^2=0.9997$, Voce fitting parameters were obtained with $A = 17$, $B = 1735$, and $C = 110$.

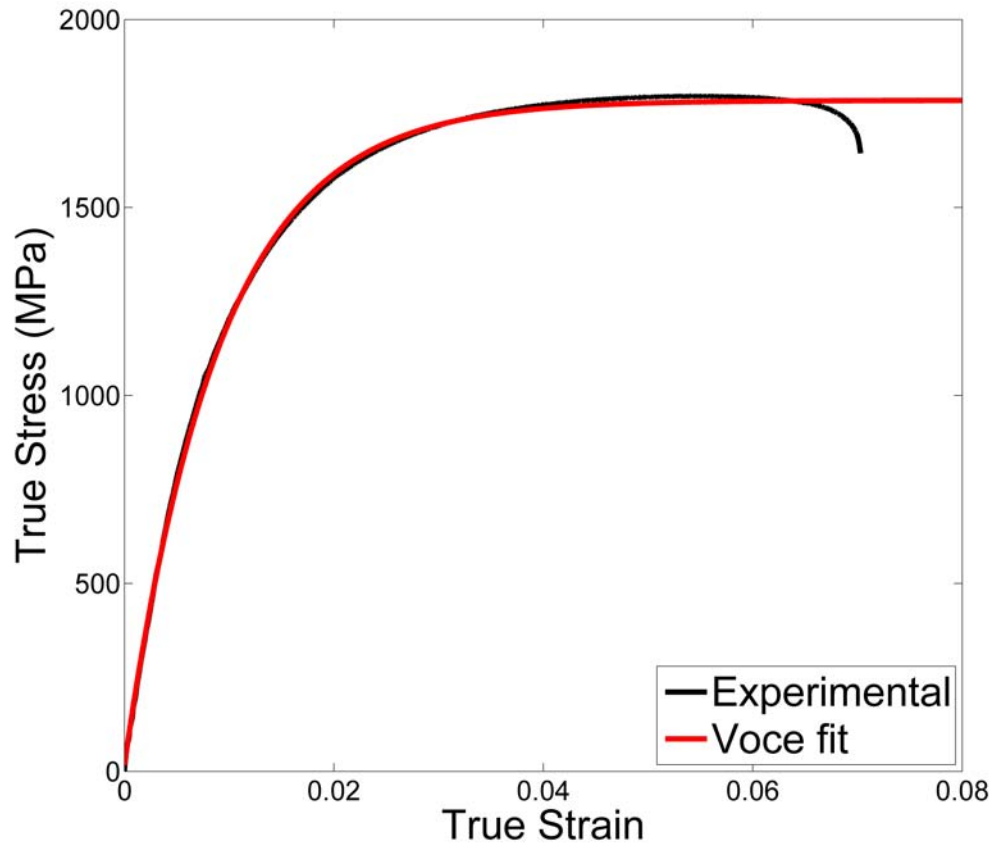


Figure A.6: Experimental tensile stress-strain curve of electrodeposited NiCo dogbone coupon with grain size of 20 nm. Overlain on top of the experimental data is the Voce fit performed using data points up to an including the UTS.

Appendix B

MATLAB code for the optimization of hybrid microtrusses in bending

While many versions of the core code were created for different scenarios, the one attached here is for a square pyramidal microtruss and the creation of the failure map for a NiCo reinforcement. The NiCo material parameters are input as Voce fitting parameters along with the material properties of Ni and the polymer to use for density. Modifications were created for cases of a hollow interior, for microtrusses made of a single material (but not hollow), and for different architectures (such as tetrahedral). These were all derivatives of this one and can be easily obtained by modifying the \hat{P} and \hat{M} equations accordingly. Additionally, for solid structures, the local shell buckling equations should be commented out.

```

clear
close all
tic

% choose the limits of rbar and ubar that you wish to go
rbar = linspace(0.0001, 0.25, 200);
nbar = linspace(0.0001, 5, 200);
ubar = 1/9; % choose and vary ubar for varying plots

% material properties
B = 1785; %from poly to 21nm: 225, 1003, 1189, 1435//NiCo=1785
C = 110; %from poly to 21nm: 1240, 219, 187, 120//NiCo=110
sigma_u = B*0.99; % ultimate tensile strength (MPa)
E = 195000; % Young's modulus (MPa) from poly to 21nm: 200, 199, 198,
162//NiCo=195
nu = 0.33; % Poisson's ratio
rho_polymer = 1190; % density of polymer (kg/m^3)
rho_nickel = 8912; % density of nickel
sigma_ref=222*0.99; %UTS for poly-Ni
kk=1;

% beginning of inelastic behaviour: E_T < inelas * E
inelas = 0.95;

% calculated quantities
rho_tilde = rho_polymer / rho_nickel; % filled truss
%rho_tilde = 0; % hollow truss

Phat_min = zeros(length(rbar),length(nbar));
Phat_b = zeros(length(rbar),length(nbar));
Phat_t = zeros(length(rbar),length(nbar));
Phat_r = zeros(length(rbar),length(nbar));
Phat_egb = zeros(length(rbar),length(nbar));
Phat_igb = zeros(length(rbar),length(nbar));
Phat_elsb = zeros(length(rbar),length(nbar));
Phat_ilsb = zeros(length(rbar),length(nbar));
Mhat = zeros(length(rbar),length(nbar));

for j=1:length(rbar)
    for k=1:length(nbar)
        Phat_b(j,k) = ( pi*rbar(j)^2*ubar^3*((1+nbar(k))^2-
1)*((49*rbar(j)^2*((1+nbar(k))^2+1))+24)/(sigma_ref*((3/sqrt(2))+(7*rbar(j)*(1+nbar(k))))));
        Phat_t(j,k) = ( pi*rbar(j)^2*ubar^3*((1+nbar(k))^2-
1)*((49*rbar(j)^2*((1+nbar(k))^2+1))+24)/(sigma_ref*((4/sqrt(2))+(7*rbar(j)*(1+nbar(k))))));
        sigma_r = sigma_u; % ultimate tensile failure (1)
        Phat_r(j,k) = Phat_b(j,k)*sigma_r;

        sigma_egb = (kk^2*pi^2*E*rbar(j)^2/4)*((1+nbar(k))^2+1); %
elastic global buckling (2)
        Phat_egb(j,k) = Phat_t(j,k)*sigma_egb;
    end
end

```

```

        sigma_igb = B*C*kk^2*pi^2/(C*kk^2*pi^2 +
(4/(rbar(j)^2*((1+nbar(k))^2+1))); % inelastic global buckling (3)
        Phat_igb(j,k) = Phat_t(j,k)*sigma_igb;
        if (C * (B - sigma_igb)) > (inelas * E)
            sigma_igb = 1e12; %set it to a large value so it isn't the
minimum
            Phat_igb(j,k) = Phat_t(j,k)*sigma_igb;
        end

        gammabar = 1 - 0.901 * (1 - exp((-1) / (16 * sqrt(nbar(k)))));
        sigma_elsb = gammabar * E * nbar(k) / (sqrt(3 * (1 - nu^2)));
% elastic local shell buckling (4)
        Phat_elsb(j,k) = Phat_t(j,k)*sigma_elsb;
        sigma_ilsb = gammabar * B * C / ((sqrt(3 * (1 -
nu^2))/nbar(k)) + gammabar * C); % inelastic local shell buckling (5)
        Phat_ilsb(j,k) = Phat_t(j,k)*sigma_ilsb;
        if (C * (B - sigma_ilsb)) > (inelas * E)
            sigma_ilsb = 1e12; %set it to a large value so it isn't
the minimum
            Phat_ilsb(j,k) = Phat_t(j,k)*sigma_ilsb;
        end

        Phat_min(j,k) = min(Phat_r(j,k), min(Phat_egb(j,k),
min(Phat_igb(j,k), min(Phat_elsb(j,k), Phat_ilsb(j,k)))));
        if Phat_min(j,k) == Phat_r(j,k)
            colour(j,k,1) = 1;%0.5;
            colour(j,k,2) = 0;%0.5;
            colour(j,k,3) = 0;%0.5;
        elseif Phat_min(j,k) == Phat_egb(j,k)
            colour(j,k,1) = 0;%0.8;
            colour(j,k,2) = 0;%0.8;
            colour(j,k,3) = 1;%0.8;
        elseif Phat_min(j,k) == Phat_igb(j,k)
            colour(j,k,1) = 1;%0.6;
            colour(j,k,2) = 1;%0.6;
            colour(j,k,3) = 0;%0.6;
        elseif Phat_min(j,k) == Phat_elsb(j,k)
            colour(j,k,1) = 0;%0.1;
            colour(j,k,2) = 1;%0.1;
            colour(j,k,3) = 1;%0.1;
        elseif Phat_min(j,k) == Phat_ilsb(j,k)
            colour(j,k,1) = 0;%0.2;
            colour(j,k,2) = 1;%0.2;
            colour(j,k,3) = 0;%0.2;
        end

        Mhat(j,k) = 8 * pi * ubar * rbar(j)^2 * (rho_tilde +
(2*nbar(k) + nbar(k)^2));
        end
end

hFig2=figure(2);

```

```

surf(nbar, rbar, Phat_min, colour, 'LineStyle', 'none')
hold on
colormap hsv
xlabel('$\bar{n}$', 'Interpreter', 'latex', 'FontSize', 30)
ylabel('$\bar{r}$', 'Interpreter', 'latex', 'FontSize', 30)
zlabel('$\hat{P}$', 'Interpreter', 'latex', 'FontSize', 30)
ylim([0 0.25])
K2=get(gca, 'XLim');
set(gca, 'XTick', linspace(K2(1), K2(2), 6))
L2=get(gca, 'YLim');
set(gca, 'YTick', linspace(L2(1), L2(2), 6))
M2=get(gca, 'ZLim');
set(gca, 'ZTick', linspace(M2(1), M2(2), 6))
set(gca, 'FontSize', 20)
set(hFig2, 'Position', [100, 100, 1049, 895]);
view([-45 45])
hold off

toc
tic
% -----
%First make the failure map with the boundaries to make checking for
%optimals easy
nbar_egbigb=0:0.01:max(nbar);
rbar_egbigb=sqrt((4*(B*C-E))./(E*C*kk^2*pi^2*((1+nbar_egbigb).^2+1)));
nbar_gblsb=0:0.01:max(nbar);
gamma_gblsb=1 - 0.901 * (1 - exp((-1) ./ (16 * sqrt(nbar_gblsb))));
rbar_gblsb=sqrt(4*gamma_gblsb.*nbar_gblsb./(kk^2*pi^2*sqrt(3*(1-
nu^2))*((1+nbar_gblsb).^2+1)));
%Now make the optimal equations that each have to be checked for a
given
%rbar to see if any nbar exists that makes it true
rbar_c = linspace(0.0001, max(rbar), 200);
nbar_c = linspace(0.0001, max(nbar), 500);
checkvector=ones(1,length(nbar_c));
check1=1;
check2=1;
check3=1;
check4=1;
% common terms that are useful for each equation with rest done in
loop
%RH = (rho_tilde*(2*nbar_c+nbar_c.^2)+1)./(rho_tilde*(1+nbar_c));
RH = (2*nbar_c+nbar_c.^2+rho_tilde)./(1+nbar_c);
GAM = 1 - 0.901 * (1 - exp((-1) ./ (16 * sqrt(nbar_c))));
GAM_P = 0.901*exp((-1) ./ (16 *
sqrt(nbar_c))).*(1./(32*sqrt(nbar_c.^3)));
BR_LSB = GAM*C + (sqrt(3*(1-nu^2))./nbar_c);
for i=1:length(rbar_c)
    BB = (4/sqrt(2)) + 7*rbar_c(i)*(1+nbar_c); %common to all four
types of equations but in book some are written as BL (IGB,ILSB)
    BR_IGB = C*kk^2*pi^2 + (4./(rbar_c(i)*((1+nbar_c).^2+1)));

```

```

T_EGB = 49*rbar_c(i)^6*((1+nbar_c).^6+(1+nbar_c).^4-(1+nbar_c).^2-
1) + (24*rbar_c(i)^4*((1+nbar_c).^4-1));
T_IGB = 49*rbar_c(i)^4*((1+nbar_c).^4-1) +
(24*rbar_c(i)^2*((1+nbar_c).^2-1));
T_ELSB = 49*rbar_c(i)^4.*GAM.*nbar_c.*((1+nbar_c).^4-1) +
(24*rbar_c(i)^2.*GAM.*nbar_c.*((1+nbar_c).^2-1));
T_ILSB = 49*rbar_c(i)^4.*GAM.*((1+nbar_c).^4-1) +
(24*rbar_c(i)^2.*GAM.*((1+nbar_c).^2-1));

RS_egb=RH.*(BB.*(49*rbar_c(i)^6*(6*(1+nbar_c).^5+4*(1+nbar_c).^3-
2*(1+nbar_c)) + (96*rbar_c(i)^4*((1+nbar_c).^3)))-
(7*rbar_c(i)*T_EGB))./...
(BB.*(294*rbar_c(i)^5*((1+nbar_c).^6+(1+nbar_c).^4-
(1+nbar_c).^2-1) + (96*rbar_c(i)^3*((1+nbar_c).^4-1)))-
(7*T_EGB.*(1+nbar_c))));
RS_igb=RH.*(BB.*BR_IGB.*(196*rbar_c(i)^4*((1+nbar_c).^3) +
(48*rbar_c(i)^2*((1+nbar_c)))) - (T_IGB.*(7*BR_IGB.*rbar_c(i)-
(8*BB.*(1+nbar_c)./(rbar_c(i)^2*((1+nbar_c).^2+1).^2)))))./...
(BB.*BR_IGB.*(196*rbar_c(i)^3*((1+nbar_c).^4-1) +
(48*rbar_c(i)*((1+nbar_c).^2-1))) - (T_IGB.*(7*BR_IGB.*(1+nbar_c)-
(8*BB./((rbar_c(i)^3*((1+nbar_c).^2+1))))));
T_P_ELSB=49*rbar_c(i)^4*(GAM_P.*nbar_c.*((1+nbar_c).^4-1) +
GAM.*((1+nbar_c).^4-1) + 4*GAM.*nbar_c.*((1+nbar_c).^3) + ...
24*rbar_c(i)^2*(GAM_P.*nbar_c.*((1+nbar_c).^2-1) +
GAM.*((1+nbar_c).^2-1) + 2*GAM.*nbar_c.*((1+nbar_c))));
RS_elsb=RH.*(T_P_ELSB.*BB - (7.*T_ELSB.*rbar_c(i)))./ ...
(BB.*(196*rbar_c(i)^3.*GAM.*nbar_c.*((1+nbar_c).^4-1) +
(48*GAM.*nbar_c.*rbar_c(i).*((1+nbar_c).^2-1)))-
(7*T_ELSB.*(1+nbar_c))));
RS_ilsb=RH.*(BB.*BR_LSB.*(GAM_P.*(49*rbar_c(i)^4*((1+nbar_c).^4-
1) + (24*rbar_c(i)^2*((1+nbar_c).^2-1))) +
GAM.*(196*rbar_c(i)^4*((1+nbar_c).^3) +
(48*rbar_c(i)^2*((1+nbar_c)))) - ...
(T_ILSB.*(7*rbar_c(i)*BB + BR_LSB.*(GAM_P*C - (sqrt(3*(1-
nu^2))./nbar_c.^2)))))./...
(BB.*BR_LSB.*(196*rbar_c(i)^3.*GAM.*((1+nbar_c).^4-1) +
(48*GAM.*rbar_c(i).*((1+nbar_c).^2-1)))-
(7*T_ILSB.*BR_LSB.*(1+nbar_c))));

```

```

[a_egb,b_egb]=intersections(nbar_c,checkvector,nbar_c,RS_egb/rbar_c(i)
);

```

```

if isempty(a_egb)==1
else
nbar_opt_egb(check1)=a_egb(1);
rbar_opt_egb(check1)=rbar_c(i);
check1=check1+1;
end

```

```

[a_igb,b_igb]=intersections(nbar_c,checkvector,nbar_c,RS_igb/rbar_c(i)
);

```

```

if isempty(a_igb)==1

```

```

else
    nbar_opt_igb(check2)=a_igb(1);
    rbar_opt_igb(check2)=rbar_c(i);
    check2=check2+1;
end

[a_elsb,b_elsb]=intersections(nbar_c,checkvector,nbar_c,RS_elsb/rbar_c
(i));
if isempty(a_elsb)==1
else
    nbar_opt_elsb(check3)=a_elsb(1);
    rbar_opt_elsb(check3)=rbar_c(i);
    check3=check3+1;
end

[a_ilsb,b_ilsb]=intersections(nbar_c,checkvector,nbar_c,RS_ilsb/rbar_c
(i));
if isempty(a_ilsb)==1
else
    nbar_opt_ilsb(check4)=a_ilsb(1);
    rbar_opt_ilsb(check4)=rbar_c(i);
    check4=check4+1;
end
end

[Pn Pr] = gradient(squeeze(Phat_min),nbar(2)-nbar(1), rbar(2)-
rbar(1));
[Mn Mr] = gradient(squeeze(Mhat),nbar(2)-nbar(1), rbar(2)-rbar(1));
Pg = Pn./Pr;
Mg = Mn./Mr;
A = Pg - Mg;
CCC = contours(nbar, rbar, A, [0 0]);
nL = CCC(1, 2:end);
rL = CCC(2, 2:end);
P_L = interp2(nbar, rbar, Mhat, nL, rL);

rexp=[0.033 0.033 0.033 0.033]; nexpp=[0.043 0.116 0.154 0.56];
hFig3=figure(3);
Phatzero=zeros(length(rbar),length(nbar));
surf(nbar, rbar, Phatzero, colour,'LineStyle','none'); %failure
regions
hold on
plot(nbar_opt_egb(find(rbar_opt_egb<0.01)),rbar_opt_egb(find(rbar_opt_
egb<0.01)),'k','LineWidth',3)
plot(nexpp,rexp,'ko','MarkerSize',10,'MarkerFaceColor','k')
line(nL(13:end-8), rL(13:end-8), P_L(13:end-8), 'Color', 'k',
'LineWidth', 3);
xlabel('$\bar{n}$ [mm/mm]','Interpreter','latex','FontSize',30)
ylabel('$\bar{r}$ [mm/mm]','Interpreter','latex','FontSize',30)
xlim([0 max(nbar)])
ylim([0 max(rbar)])
view([0 90])

```

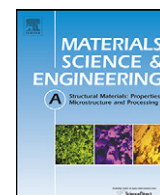
```
K3=get(gca,'XLim');  
set(gca,'XTick',linspace(K3(1),K3(2),6))  
L3=get(gca,'YLim');  
set(gca,'YTick',linspace(L3(1),L3(2),6))  
set(gca,'FontSize',20)  
set(hFig3,'Position',[100, 100, 1049, 895]);  
hold off
```

```
toc
```

Appendix C

Mechanical anisotropy in metal/metal foams

This appendix contains a study of the effects of coating anisotropy on metal foams, which was completed in parallel with the core contribution of this thesis. The through thickness of this metal foam was large enough that coating the interior cells was difficult due to shielding from outer cells. In the most heavily plated samples, a tenfold difference in coating thickness was seen between outer and inner struts. Additionally, struts were capable of shielding themselves in that the back side of a strut facing towards the interior of the foam was thinner than the front side facing the anodes in the bath. The addition of this work here serves as a reference for similar effects observed in metal/polymer microtrusses, although to a lesser degree.



Mechanical anisotropy in electrodeposited nanocrystalline metal/metal composite foams

A.T. Lausic^a, B.A. Bouwhuis^{a,b}, J.L. McCrea^b, G. Palumbo^b, G.D. Hibbard^{a,*}

^a Department of Materials Science and Engineering, University of Toronto, 184 College Street, Toronto, Ontario, Canada

^b Integran Technologies Inc., 1 Meridian Road, Toronto, Ontario, Canada

ARTICLE INFO

Article history:

Received 26 March 2012

Received in revised form 8 May 2012

Accepted 9 May 2012

Available online 17 May 2012

Keywords:

Cellular materials

Nanocrystalline materials

Nickel

Metal foam

Electroplating

ABSTRACT

Electrodeposition can be used to create new types of nanocrystalline metal/metal composites. In addition to increasing the strength and stiffness of conventional metal foams, electrodeposition also has the effect of introducing mechanical anisotropy to the cellular architecture. Because of electromagnetic shielding effects, outer ligaments receive more electrodeposited material than inner ligaments, creating a gradient in structural reinforcement. This study provides a first examination of the compressive strength and stiffness anisotropy introduced by nanocrystalline electrodeposition.

© 2012 Elsevier B.V. All rights reserved.

1. Introduction

New types of metal/metal nanocrystalline cellular hybrids can be created by reinforcing conventional metal foam or micro-truss materials using electrodeposition [1–8]. In effect, electrodeposition creates an interconnected network of conformal nanocrystalline tubes that control the mechanical properties of the hybrid cellular material. Even small coating thicknesses of nanocrystalline material greatly improve the weight-carrying capacity and energy absorbance compared to the starting foam structure [7,8]. In addition to the Hall–Petch Strengthening that can be achieved by grain size reduction to the nm-scale [e.g. see reviews in 9–11], this approach takes advantage of the fact that the ultra-high strength electrodeposited material is optimally positioned away from the neutral bending axis of the internal cellular struts or ligaments [3,4]. Overall, the effectiveness of the structural reinforcement (e.g. the strength increase, $\Delta\sigma$, divided by the accompanying density increase, $\Delta\rho$) depends on a complex interaction between the material properties of the nanocrystalline tubes, the cellular architecture of the starting pre-form and the adhesion between coating and substrate [5–7].

A critical aspect of the nanocrystalline structural reinforcement is the local thickness distribution of electrodeposited material over the starting foam or microtruss core. This thickness distribution

is a complex function of the cathode's cellular architecture, as well as the electrodeposition conditions such as electrolyte chemistry, electrolyte flow patterns, electrode geometry, and electrical parameters [e.g. 12–14]. Because of their more complex starting cellular architecture, metal/metal foam hybrids would typically be expected to be more significantly affected by thickness uniformity issues than metal/metal micro-truss materials. For example, in a recent study of nanocrystalline Ni (n-Ni) reinforced open cell aluminum foams, the average n-Ni tube thickness in the middle of the foam was ~40% of the nominal coating thickness calculated by assuming a uniform distribution of electrodeposited metal [5].

However, a gradient in the structural reinforcement may also present opportunities for tuning the mechanical properties of the cellular material. By having a larger fraction of the nanocrystalline reinforcement located near the outer surfaces of the composite foam, it may be possible to obtain enhanced weight-specific bending resistance compared to the limiting case of a uniformly coated foam core [5]. This study examines the mechanical anisotropy in the compressive stiffness and strength of a metal/metal composite foam in the presence of an electrodeposited n-Ni thickness gradient. It builds on a previous study of n-Ni/Al hybrid foams where the uniaxial compression loading axis was oriented parallel to the thickness gradient [5]. In that initial study, those cells in the middle of the foam having the least structural reinforcement failed first, limiting the achievable peak compressive strength increase [5]. The present study examines the anisotropy of the coating thickness in the hybrid foam and determines the impact on its compressive properties. Additionally, the loading axis is oriented

* Corresponding author. Tel.: +1 416 946 0437; fax: +1 416 978 4155.
E-mail address: glenn.hibbard@utoronto.ca (G.D. Hibbard).

perpendicular to the thickness gradient, such that it is not just one (weakest) region of the foam that controls the overall strength increase, but rather simultaneous failure through the full gradient of nanocrystalline structural reinforcement. Combined with the results from the previous study, an understanding of the compressive properties from every direction motivates their use in shock mitigation and impact absorption. Results from both loading orientations are used to map the mechanical anisotropy imparted to the cellular architecture by nanocrystalline electrodeposition.

2. Experimental

In order to provide a direct point of comparison, the same starting aluminum foam architecture and nanocrystalline Ni electrodeposition conditions that were used previously [5], were selected to create the n-Ni/Al foam hybrids of the present study. The starting precursor was Duocel AA6101 aluminum open-cell foam purchased from ERG Aerospace Corp. (Oakland, CA); the starting foam had a density of $\rho = 0.203 \pm 0.008 \text{ Mg m}^{-3}$, a nominal pore size of 1.27 mm pore size (20 pores per inch) and a specific surface area of $S = 1.19 \text{ mm}^2/\text{mm}^3$ [15]. The n-Ni structural reinforcement was deposited by pulse current electrodeposition using a modified Watt's bath, after [16,17], with the $76.2 \text{ mm} \times 76.2 \text{ mm} \times 12.7 \text{ mm}$ starting Al foam sheet placed between consumable Ni anodes. Hybrid foam densities of $0.486 \pm 0.027 \text{ Mg m}^{-3}$, $0.614 \pm 0.035 \text{ Mg m}^{-3}$, $0.690 \pm 0.024 \text{ Mg m}^{-3}$, $0.763 \pm 0.024 \text{ Mg m}^{-3}$ and $0.959 \pm 0.038 \text{ Mg m}^{-3}$ were obtained by controlling the electrodeposition time. The n-Ni distribution on the electrodeposited foams was characterized by optical microscopy and scanning electron microscopy (SEM) of polished cross-sections that had been cut by electrical discharge machining. The Ni nanostructure was characterized by X-ray diffraction using Co K α radiation ($\lambda = 1.79 \text{ nm}$) on aluminum coupons electroplated using the same deposition conditions as the n-Ni/Al hybrid foams. An average grain size of 16 nm was measured from diffraction peak broadening using the Scherrer relationship [e.g. 18], which is typical of n-Ni produced by pulse current electrodeposition, e.g. [19,20].

Electrical discharge machining was also used to cut $10.0 \text{ mm} \times 10.0 \text{ mm} \times 12.7 \text{ mm}$ coupons from the as-deposited n-Ni/Al foam sheets. The starting Al foam and n-Ni/Al hybrids were tested in uniaxial compression at a cross-head displacement rate of 1 mm/min. Four samples were tested for each thickness group. Recorded cross-head displacements, adjusted for machine compliance based on the measured load, were used to estimate the compressive strain. Vickers micro-hardness measurements on polished cross-sections of the $\rho = 0.959 \text{ Mg m}^{-3}$ sample (0.49 N load, 10 s dwell time) gave a value of $472 \pm 26 \text{ HV}$ which is typical of pulse-current electrodeposited nanocrystalline Ni [21]. Failure mechanisms of the electrodeposited hybrids were investigated by SEM characterization of samples pre-loaded to characteristic strain values.

3. Results and discussion

3.1. Characterization of the n-Ni thickness gradient

Fig. 1 presents backscattered electron SEM images of polished cross-sections through the 0.486 , 0.690 and 0.959 Mg m^{-3} n-Ni/Al foam hybrid sheets. All samples exhibited n-Ni thickness gradients in the through-thickness direction (axis 1, Fig. 1) of the starting Al foam sheet. As would have been expected based on the planar electrode geometry, there was no evidence of a thickness gradient in either of the in-plane sample directions (axes 2 and 3, Fig. 1). The electrodeposited gradients were quantified by making two

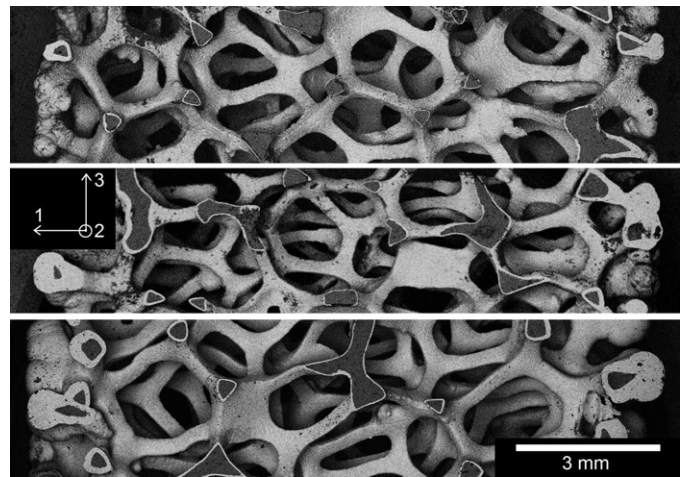


Fig. 1. Backscattered electron SEM micrographs showing the n-Ni thickness gradient (n-Ni sleeves are light, the Al foam core is dark) for the n-Ni/Al hybrids having densities of 0.486 Mg m^{-3} (a), 0.690 Mg m^{-3} (b) and 0.959 Mg m^{-3} (c).

n-Ni thickness measurements per ligament from SEM images, such as those seen in Fig. 1. Both measurements were made in the 1-direction, with one measurement oriented toward the outer surface of the foam sheet ($t_{\text{n-Ni}}^{\text{outer}}$) and one toward the inner (central) plane of the foam ($t_{\text{n-Ni}}^{\text{inner}}$); approximately 500 thickness measurements were made per sample type. Fig. 2 illustrates each of these parameters for the 0.486 , 0.690 and 0.959 Mg m^{-3} hybrids. For the $\rho = 0.486 \text{ Mg m}^{-3}$ hybrids, the outer sleeve thickness measurements ranged from ~ 15 to $380 \mu\text{m}$, while the inner sleeve thickness measurements ranged from ~ 13 to $90 \mu\text{m}$.

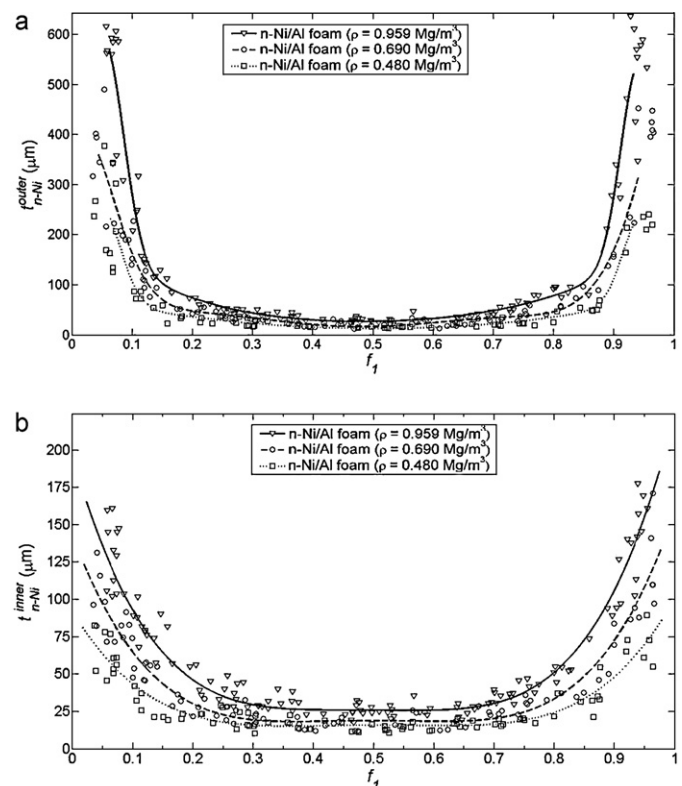


Fig. 2. Profile plots showing the outer (a) and inner (b) n-Ni sleeve thickness measurements made parallel to the thickness gradient and plotted as a function of the aluminum strut position through the foam height.

Table 1

Mechanical properties of the as-received AA6101 metal foams and electrodeposited n-Ni/Al foam hybrids summarizing the density (ρ), nominal n-Ni sleeve thickness (t_{n-Ni}^{nom}), compressive modulus (E_{33}), peak strength (σ_{33}^p), and valley strength (σ_{33}^v).

ρ (Mg m ⁻³)	t_{n-Ni}^{nom} (μ m)	E_{33} (MPa)	σ_{33}^p (MPa)	σ_{33}^v (MPa)
0.203 ± 0.008	0	104 ± 22	1.33 ± 0.07	1.14 ± 0.05
0.486 ± 0.027	24.2 ± 1.7	370 ± 14	5.24 ± 0.30	3.01 ± 0.59
0.614 ± 0.035	39.4 ± 3.8	407 ± 21	7.05 ± 0.28	3.67 ± 0.31
0.690 ± 0.024	46.2 ± 3.8	427 ± 70	8.46 ± 1.05	5.04 ± 0.47
0.763 ± 0.024	55.8 ± 4.4	475 ± 37	9.93 ± 0.68	5.26 ± 0.82
0.959 ± 0.038	71.9 ± 5.2	666 ± 75	13.96 ± 1.86	8.18 ± 1.72

The profile plots of Fig. 2 indicate that the n-Ni thickness gradient needs to be considered at two length scales. First, there was an overall thickness gradient in which each of the hybrid samples had a middle band that had received the least total n-Ni electrodeposition. In addition, there was also a gradient at the level of each individual ligament: reinforcement was thickest on the side oriented toward the nearest anode (t_{n-Ni}^{outer}) and thinnest on the side oriented toward the furthest anode (t_{n-Ni}^{inner}). These gradients can be considered in terms of a nominal reference coating thickness (t_{n-Ni}^{nom}) based on a calculated uniform distribution of electrodeposited mass (m_{Ni}) over the specific surface area (S) of the pre-form as:

$$t_{n-Ni}^{nom} = \frac{m_{n-Ni}}{SV\rho_{Ni}} \quad (1)$$

where ρ_{Ni} is the density of Ni, and V is the cuboid volume of the sample. Nominal n-Ni thicknesses ranged from $24.2 \pm 1.7 \mu\text{m}$ for the $\rho = 0.486 \text{ Mg m}^{-3}$ hybrid to $71.9 \pm 5.2 \mu\text{m}$ for the $\rho = 0.959 \text{ Mg m}^{-3}$ hybrid (Table 1).

Fig. 3 plots the ratio of average sleeve thickness to nominal coating thickness, $(t_{n-Ni}^{inner} + t_{n-Ni}^{outer}) / (2t_{n-Ni}^{nom})$, from those ligaments contained in the middle of the foam (from ~0.25 to 0.75 of the fractional foam height in Fig. 2). The distribution of n-Ni was most uniform during the initial stages of electrodeposition, with the plateau thickness being ~64% of the nominal value. As deposition continued, the plateau thickness dropped to ~42% of the nominal coating thickness in the $\rho = 0.959 \text{ Mg m}^{-3}$ hybrid, which can be understood in terms of the increased electromagnetic shielding provided by the thickening outer ligaments of the hybrid foam as electrodeposition progressed. Likewise, the orientational anisotropy was most pronounced at the outer surface of the foam. This can be seen in Fig. 4 where the ratio of inner to outer sleeve thickness ($t_{n-Ni}^{inner} / t_{n-Ni}^{outer}$) is plotted as a function of the ligament position for the $\rho = 0.959 \text{ Mg m}^{-3}$ hybrid. Within the middle half of the total foam height, the inner sleeve thickness measurements were

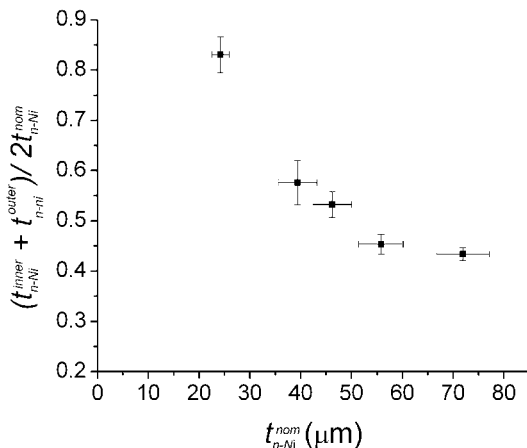


Fig. 3. Normalized minimum coating thickness plotted against the nominal coating thickness for the five n-Ni/Al hybrid foam densities.

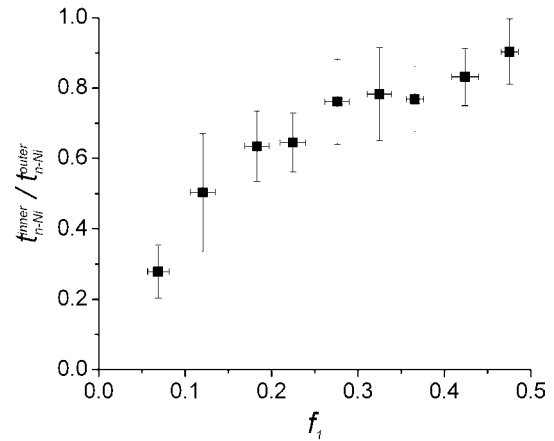


Fig. 4. Ratio of the inner coating thickness to the outer coating thickness plotted as a function of the fractional position in the through thickness (1-) direction.

~80–90% of the outer sleeve thicknesses. In contrast, the inner sleeve thickness measurements could be as low as ~25% of t_{n-Ni}^{outer} for the outermost cells of the starting Al foam; this inner sleeve thickness parameter is particularly important since it represents a direct measure of the minimum structural reinforcement on a given cellular ligament.

Fig. 5a presents typical uniaxial compression stress–strain curves for the n-Ni/Al hybrids when loaded perpendicular to the n-Ni thickness gradient (i.e. directions 2 and 3 in Fig. 1). As a point of comparison, the stress–strain curves for the previously studied case [5] of loading parallel to the thickness gradient (i.e. direction 1

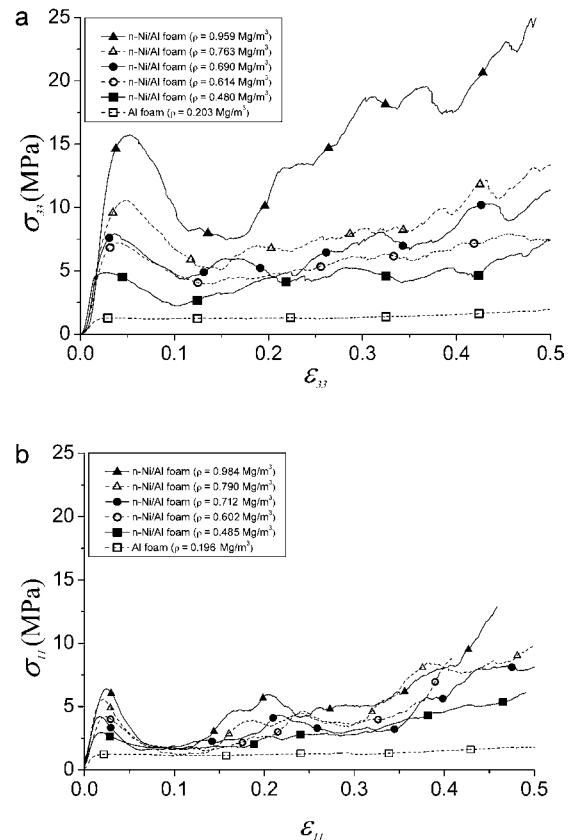


Fig. 5. Typical uniaxial compression stress–strain curves for the n-Ni/Al hybrids. Compression along the 3-direction from the present study is shown in (a), while previous data [5], corresponding to compression along the 1-direction, is shown in (b).

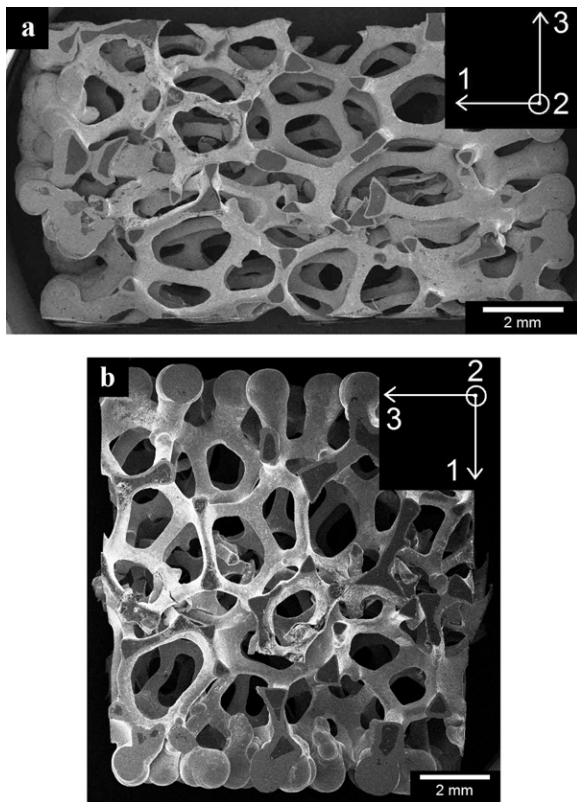


Fig. 6. SEM micrographs of partially crushed foam samples with a nominal coating thickness of $71.9 \pm 5.2 \mu\text{m}$ for a hybrid foam density of 0.959 Mg m^{-3} . Crushing was performed to compressive strains of $\epsilon = 0.30$ and 0.25 for compression (a) perpendicular (direction 3) and (b) parallel (direction 1) to the structural gradient, respectively.

in Fig. 1) are shown in Fig. 5b. In all cases, electrodeposition had the effect of increasing the initial compressive modulus and the peak compressive strength of the starting Al foam. Electrodeposition also had the effect of changing the overall form of the compression stress–strain curve. As would be expected, the starting Al foam collapsed at a nearly constant plateau stress [e.g. 22]. In contrast, the hybrid foams exhibited an initial peak stress that was followed by a decrease toward a minimum (or valley) strength before finally increasing again during densification. More significant, however, was the mechanical anisotropy introduced by electrodeposition. For example, nominal n-Ni thicknesses of $24\text{--}72 \mu\text{m}$ resulted in strength increases of $2.3\text{--}5.2 \text{ MPa}$ when loading occurred parallel to the thickness gradient; when the loading axis was perpendicular to the structural gradient, the strength increase was much higher at $4.0\text{--}10.5 \text{ MPa}$ over the same range of nominal coating thicknesses. Electrodeposition introduced similar orientation effects for the compressive modulus and valley strength (Table 1). However, for both loading orientations, the specific strength and stiffness of the n-Ni/Al hybrids was greater than that of the uncoated Al foam; the specific stiffness of the $\rho = 0.959 \text{ Mg m}^{-3}$ hybrids increased by 240% and 540% while the specific strength increased by 420% and 620% for the 11-direction (after Ref. [5]) and 33-direction (this study), respectively.

The failure mechanisms in the metal/metal composite foams were examined by SEM characterization of samples that had been pre-loaded to the valley strength just beyond the initial peak (i.e. compressive strains of $\epsilon \approx 0.2\text{--}0.3$). In both loading orientations, failure was initially confined to a narrow band of cells that extended across the sample cross-section (Fig. 6). This band of cells had almost completely collapsed by the time the valley stress was reached, while the rest of the foam height remained largely intact.

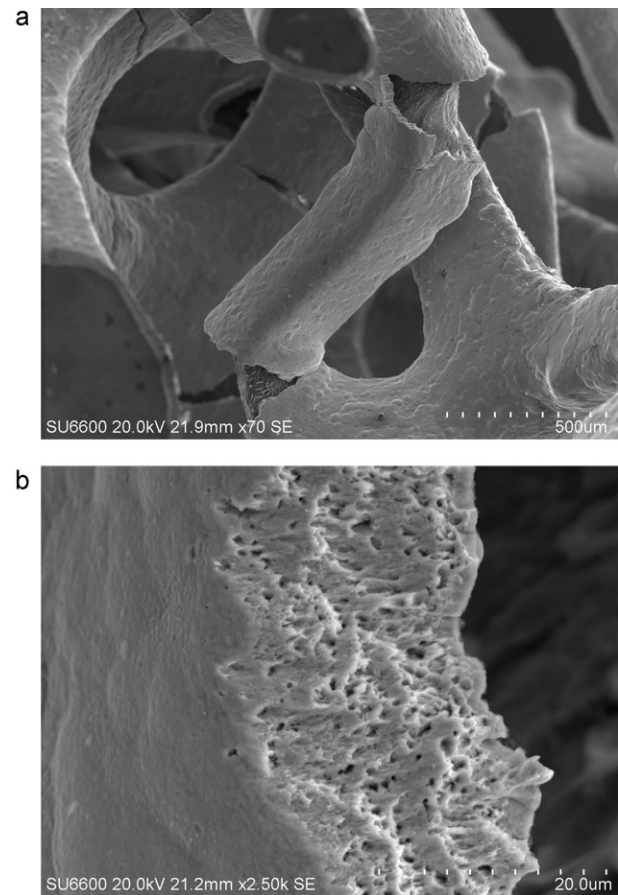


Fig. 7. Typical failed composite strut from the minimally reinforced middle of a $\rho = 0.486 \text{ Mg m}^{-3}$ sample pre-loaded to $\epsilon = 0.30$ (a) and μm -scale dimples can be seen in the fractured n-Ni sleeve (b).

In this sense, the hybrids failed in a similar way to what would have been expected for the starting Al foam, i.e. where collapse of the overall architecture was initiated by local cell collapse at a weak point (e.g. local architectural inhomogeneity) that progressively triggered a cascading collapse in adjacent cells until a full band of cells across the foam cross-section had failed [23]. Note that this failure mode occurred in all the n-Ni/Al hybrids tested despite the fact that failure was confined to just the weakest struts in one case (Fig. 6b) and extended across the full range of structural reinforcement in the other (Fig. 6a).

Figs. 7 and 8 present examples of typical failed struts from a $\rho = 0.959 \text{ Mg m}^{-3}$ hybrid loaded perpendicular to the gradient. Fig. 7a presents an example of a composite strut from the middle region of the foam where the average n-Ni sleeve thickness was on the order of $\sim 30 \mu\text{m}$. Extensive crack opening in the n-Ni sleeve has occurred on the tensile side of the rotating ligament, while the aluminum core itself remained largely intact. At higher magnifications (Fig. 7b), relatively deep microvoids, in the size range of $\sim 0.2 \mu\text{m}$ to $2 \mu\text{m}$, could be seen on the fracture surface of the nanocrystalline Ni sleeve. Sleeve fracture can also be seen on the tensile side of a rotating strut that was situated at the outer surfaces where the sleeve thicknesses were on the order of ~ 100 to $300 \mu\text{m}$ (Fig. 8a). However, in this case, localized deformation bands, identified by a series of nearly parallel micro-cracks and surface voids (Fig. 8b), could be seen within approximately $\sim 100 \mu\text{m}$ of the main n-Ni sleeve fracture surface. Morphologically similar micro-cracks have been reported previously during uniaxial tensile testing of electrodeposited nanocrystalline Ni and Ni-Fe alloys; propagation of the main tensile crack occurred via the formation and

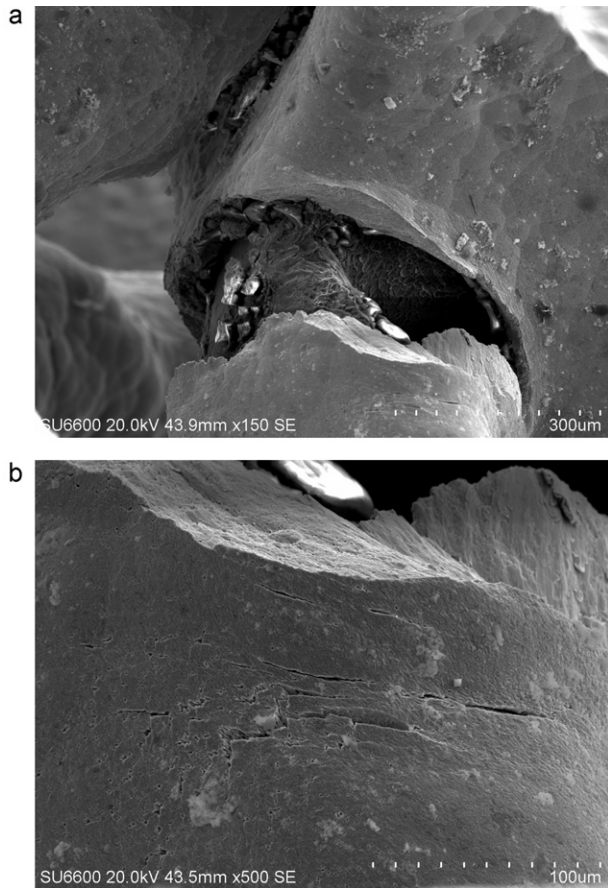


Fig. 8. Typical failed composite strut from the outer region of a $\rho = 0.486 \text{ Mg m}^{-3}$ sample pre-loaded to $\varepsilon = 0.30$ (a) and extensive micro-cracking can be seen adjacent to the main sleeve fracture (b).

subsequent joining of many smaller and stable micro-cracks [24]. While it is difficult to deconvolute the failure mechanisms across the composite ligaments having different spatial orientations, those struts near the outside of the foam will, on average, experience significantly greater rotational constraint than those in the middle of the foam because of their much larger n-Ni thickness. At a given initial compressive displacement, therefore, the maximum tensile stresses in the nanocrystalline sleeve induced by ligament rotation would be much higher for the composite struts having the thickest reinforcement. Beyond a certain compressive displacement, failure may tend to occur first in these struts and then progress inwards.

As a first approximation, the strength and modulus increase provided by nanocrystalline electrodeposition can be modeled using a composite cellular material approach based on the predicted behavior of a hollow tube nanocrystalline foam [5]. This method is based on an isostrain assumption in which each component of the cellular composite suffers the same strain during deformation. Since the reinforcing n-Ni phase does not displace any of the starting Al foam (as would be the case in a particle or fiber reinforced composite), the contributions from each component are additive and the increase in compressive modulus and strength can then be expressed as after [5]:

$$\Delta E = E_{n\text{-Ni}/\text{Al}} - E_{\text{Al}} \approx E_{n\text{-Ni}} \quad (2)$$

$$\Delta \sigma^p = \sigma_{n\text{-Ni}/\text{Al}}^p - \sigma_{\text{Al}}^p \approx \sigma_{n\text{-Ni}}^p \quad (3)$$

where the subscripts n-Ni/Al, Al, and n-Ni refer to the particular compressive property of the hybrid foam, starting aluminum foam, and hypothetical hollow tube nanocrystalline Ni foam, respectively.

However, the thickness gradient in the hybrid foam complicates the structural analysis since cells located near the outer surfaces of the hybrid foam will be both stiffer and stronger than those located in the minimally reinforced middle. A simple starting point to rationalize this structural reinforcement gradient is to use the inner thickness profiles of Fig. 2 to subdivide the sample into a piecewise set of zones having uniform mechanical properties. Note that in the following analysis, the contributions from the first and last 1/4 cell length of the thickness profile were excluded since these cut cells do not provide any significant structural support to the foam [23].

A predicted modulus for a hollow tube nanocrystalline Ni foam can be calculated using the relationship after [22]:

$$E_{n\text{-Ni}} = \alpha \frac{BE_{\text{Ni}}I_{n\text{-Ni}}}{2L^4} \quad (4)$$

where B is a parameter describing the end conditions of the ligament, E_{Ni} is the elastic modulus of nickel (207 GPa [25]), L is the ideal ligament length, and I is the second moment of area. A value of 192 was chosen for the constant B , after [22], for a ligament loaded at mid-span with both ends rigid. The moment of inertia for a hollow nanocrystalline Ni sleeve can be modeled as [22]:

$$I_{n\text{-Ni}} = \frac{\pi((d + t_{n\text{-Ni}})^4 - d^4)}{64} \quad (5)$$

where $t_{n\text{-Ni}}$ is the thickness of the nanocrystalline sleeve. Finally, models for the elastic modulus typically significantly over-predict the experimentally measured compressive modulus [e.g. 20]. In order to take this effect into account, a knockdown factor, α , for the starting aluminum foam architecture was introduced in Eq. (4). An estimate for the value of α can be taken by calculating a predicted value of the starting aluminum foam modulus and comparing it to the experimentally measured value. Using an average ligament diameter of $d \approx 0.2 \text{ mm}$ and ligament length of $L = 1.0 \text{ mm}$ (after [26]), the predicted value is 525 MPa. This is approximately five times larger than the experimentally measured value of $E_{\text{Al}} = 104 \text{ MPa}$ and corresponds to a knockdown factor of $\alpha = 0.20$.

When the composite foam is loaded in compression, the nanocrystalline Ni sleeves effectively act as individual springs – the thicker the coating, the stiffer the spring and the higher its spring constant. For compression in the 3-direction, the springs act in parallel and the total effective spring constant would be the weighted summation of all the individual spring constants. On the other hand, compression in the 1-direction is seen as springs acting in series where the total spring constant is the reciprocal of the reciprocal weighted sum of each individual spring constant. By treating each of these slices as a spring with spring constant $k = E_{n\text{-Ni}}$ the total modulus for the 1 and 3 compression directions is calculated using:

$$\frac{1}{E_{n\text{-Ni}}^{11}} = n \left(\sum_{i=1}^N \frac{1}{E_i^{11}} \right) \quad (6)$$

$$\frac{1}{E_{n\text{-Ni}}^{33}} = n \left(\sum_{i=1}^N E_i^{33} \right) \quad (7)$$

where n is the fractional length of each of each spring component and E_i is the predicted modulus at that step into the height of the foam. To obtain a single modulus prediction for each direction, the moment of inertia was calculated at each step along the thickness gradient (Fig. 2) with Eq. (4), each giving a different modulus value using Eq. (2). A weighted summation of these values was then calculated to obtain the total predicted modulus, $E_{n\text{-Ni}}$ using Eqs. (6) and (7). Overall, using a piecewise composite foam modulus approach was able to provide good agreement to the experimentally measured modulus increase for uniaxial compression across

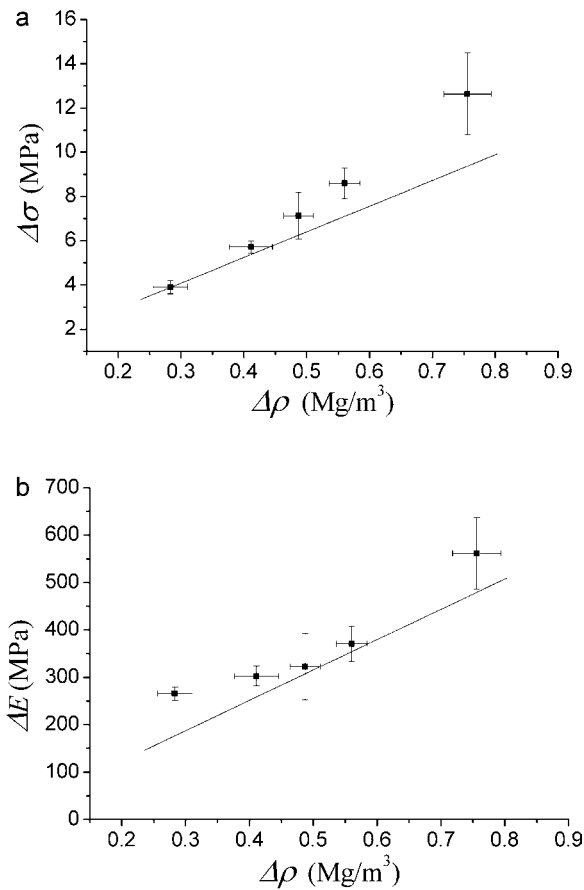


Fig. 9. Experimentally measured compressive modulus (a) and strength (b) increase for the n-Ni reinforced foams plotted as a function of the density increase. The straight line represents the predictions for modulus and strength increase based on Eqs. (7) and (10), respectively.

the thickness gradient, as seen in Fig. 9a. Note that subdividing the thickness gradient into more than ten pieces had little effect on the predicted value.

In a similar manner, the peak strength was calculated using the following relationship, after Refs. [22]:

$$\sigma_{n-Ni} = \frac{C\sigma_{YS,n-Ni}H_{n-Ni}}{L^3} \quad (8)$$

where C is a parameter describing the end condition, $\sigma_{YS,n-Ni}$ is the yield strength of the electrodeposited nanocrystalline Ni (900 MPa [27]), and H_{n-Ni} is the moment measuring the resistance to fully plastic bending. A value of 8 was chosen for the constant C , after [22], for a ligament loaded at mid-span with both ends rigid. In Bouwhuis et al. [5], the peak strength was simplified to only incorporate the minimal thickness, t_{mid} , at the center of the foam. The outer edges of the foam with increased coating thicknesses did not contribute to the overall strength of the foam in direction 1 direction compression. However, when compression is performed in direction 3, the thickly coated edges do indeed add to the total strength of the foam and are responsible for the larger $\Delta\sigma$ values. This strength increase for the 1 and 3 directions can be modeled as:

$$\sigma_{n-Ni}^{11} = \sigma^{11}|_{t_{mid}} \quad (9)$$

$$\sigma_{n-Ni}^{33} = n \left(\sum_{i=1}^N \sigma_i^{33} \right) \quad (10)$$

Applying the same methodology in calculating the modulus for both directions, the strength for each direction can also be

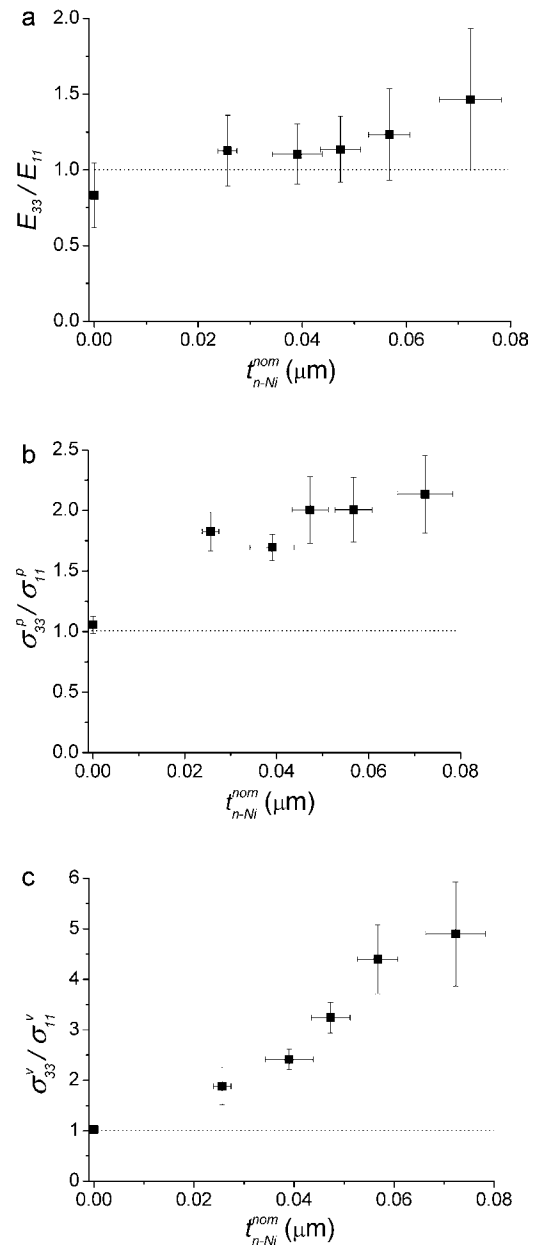


Fig. 10. The ratio of direction 3 to direction 1 compressive modulus (a), peak strength (b) and valley strength (c) plotted as a function of the nominal coating thickness and illustrating the mechanical anisotropy introduced during nanocrystalline electrodeposition.

determined. The comparisons between the experimental data and the predicted strength increase again match closely, as seen in Fig. 9b. For the stress, the model converges to a point slightly below the experimental one with all points lying within one standard deviation. Each slice of cells in the cross-section has a particular failure strength. In the 3-direction loading, the total strength is a combination of these individual strengths while loading in the 1-direction is controlled by that part of the foam in the middle that has seen the least reinforcement and is the weakest.

Finally, the significance of the mechanical anisotropy introduced during electrodeposition can be seen by plotting the ratio of mechanical properties measured parallel to and perpendicular to the n-Ni thickness gradient as a function of the nominal coating thickness (Fig. 10). Note that there was a subtle structural anisotropy in the starting Duocel foam itself, where the cells are typically elongated in one direction; the overall elongation factor

for a 1.27 mm pore size Duocel foam was found to be 1.24 (height-to-width ratio) through X-ray tomography analysis [23]. In the present study, the uncoated samples tested in each direction showed a small anisotropy effect with a compressive modulus of ~ 125 MPa and ~ 104 MPa, and a plateau stress of 1.26 MPa and 1.33 MPa when loaded in the 1 and 3 directions, respectively. But this anisotropy effect was vastly overwhelmed by the thickness gradient introduced during electrodeposition. The E_{33}/E_{11} ratio changed from 0.83 for the starting (uncoated) case to 1.46 for the thickest nominal coating thickness of $71.9 \mu\text{m}$, a change of 76% after nanocrystalline electrodeposition (Fig. 10a). A larger effect was seen for the peak compressive strength, which increased from $\sigma_{33}^p/\sigma_{11}^p = 1.06$ for the uncoated samples to $\sigma_{33}^p/\sigma_{11}^p = 2.13$ for the thickest coatings (an increase of 100%) (Fig. 10b). The largest effect, however, was seen for the valley strength, with $\sigma_{33}^v/\sigma_{11}^v$ reaching values of 4.90 compared to 1.02 for the uncoated case (a 380% change) (Fig. 10c). Overall, the electrodeposited thickness gradient has the effect of introducing increasingly significant mechanical anisotropy to the starting foam architecture. This gradient affects all aspects of the mechanical response: from initial elastic deformation through to the peak load carrying capacity through to the energy that can be absorbed during final collapse.

4. Conclusions

In addition to significantly increasing the strength and stiffness of conventional aluminum foams, electrodeposition also introduces a new type of mechanical anisotropy. For plate-like sheets of starting foam, the non-uniformity acts in the through-thickness direction and needs to be considered at two distinct length scales. The first acts over the full thickness of the starting foam sheet, while the second acts at the scale of the individual struts. Each type of structural gradient became increasingly pronounced such that there was an increasingly large difference between mechanical properties measured in the plane of the starting sheet and through the thickness of the starting sheet. For the largest nominal sleeve thickness of $72 \mu\text{m}$, the elastic modulus, peak compressive strength, and valley strength were $\sim 76\%$, 100% and 380% higher when loaded perpendicular to the thickness gradient than when loaded parallel to the thickness gradient. The particular form of the nanocrystalline sleeve thickness profile is therefore a critical design consideration in the development of hybrid nanocrystalline cellular materials.

Acknowledgment

Financial support from the Natural Sciences and Engineering Research Council of Canada (NSERC) is gratefully acknowledged.

References

- [1] M. Suralvo, B.A. Bouwhuis, J.L. McCrea, G. Palumbo, G.D. Hibbard, *Scr. Mater.* 58 (2008) 247–250.
- [2] J.E. Campbell, M. Suralvo, G.D. Hibbard, H.E. Naguib, *J. Compos. Mater.* 46 (2011) 63–70.
- [3] L.M. Gordon, B.A. Bouwhuis, M. Suralvo, J.L. McCrea, G. Palumbo, G.D. Hibbard, *Acta Mater.* 57 (2009) 932–939.
- [4] B.A. Bouwhuis, T. Ronis, J.L. McCrea, G. Palumbo, G.D. Hibbard, *Compos. Sci. Technol.* 69 (2009) 385–390.
- [5] B.A. Bouwhuis, J.L. McCrea, G. Palumbo, G.D. Hibbard, *Acta Mater.* 57 (2009) 4046–4053.
- [6] E. Bele, B.A. Bouwhuis, G.D. Hibbard, *Acta Mater.* 57 (2009) 5927–5935.
- [7] A. Jung, H. Natter, S. Diebels, E. Lach, R. Hempelmann, *Adv. Eng. Mater.* 13 (2011) 23–28.
- [8] Y. Boonyongmaneerat, C.A. Schuh, D.C. Dunand, *Scr. Mater.* 59 (2008) 336–339.
- [9] K.S. Kumar, H. Van Swygenhoven, S. Suresh, *Acta Mater.* 51 (2003) 5743–5774.
- [10] M.A. Meyers, A. Mishra, D.J. Benson, *Prog. Mater. Sci.* 51 (2006) 427–556.
- [11] C.C. Koch, *J. Mater. Sci.* 42 (2007) 1403–1414.
- [12] O.P. Koshcheev, V.I. Kichigin, R.M. Gabdrakhmanova, V.N. Antsiferov, *Russ. J. Appl. Chem.* 67 (1994) 1136 (Translated from *Zhurnal Prikladnoi Khimii* 67 (1994) 1287).
- [13] V.V. Kamelin, V.I. Kichigin, V.N. Antsiferov, O.P. Koshcheev, *Russ. J. Appl. Chem.* 69 (1996) 42 (Translated from *Zhurnal Prikladnoi Khimii* 69 (1996) 49).
- [14] A. Jung, H. Natter, R. Hempelmann, S. Diebels, M.R. Koblishka, U. Hartmann, E. Lach, *ECS Trans.* 25 (2010) 165–172.
- [15] ERG Aerospace website: www.ergaerospace.com.
- [16] U. Erb, A.M. El-Sherik, Nanocrystalline metals and processes of producing the same, US Patent 5,353,266, October 1994.
- [17] U. Erb, A.M. El-Sherik, C.K.S. Cheung, M.J. Aus, Nanocrystalline metals, US Patent 5,433,797, July 1995.
- [18] B.D. Cullity, *Elements of X-ray Diffraction*, second ed., Addison-Wesley, Don Mills, 1978.
- [19] A.M. El-Sherik, U. Erb, G. Palumbo, K.T. Aust, *Scr. Mater.* 27 (1992) 1185–1188.
- [20] A.M. El-Sherik, U. Erb, *J. Mater. Sci.* 30 (1995) 5743–5749.
- [21] I. Brooks, P. Lin, G. Palumbo, G.D. Hibbard, U. Erb, *Mater. Sci. Eng. A* 491 (2008) 412–419.
- [22] M.F. Ashby, A.G. Evans, N.A. Fleck, L.J. Gibson, J.W. Hutchinson, H.N.G. Wadley, *Metal Foams: A Design Guide*, Butterworth-Heinemann, Oxford, UK, 1999.
- [23] W.Y. Jang, S. Kyriakides, *Int. J. Sol. Struct.* 46 (2009) 617–634.
- [24] L. Hongqi, F. Ebrahimi, *Appl. Phys. Lett.* 84 (2004) 4307–4309.
- [25] J.R. Davis (Ed.), *ASM Specialty Handbook: Nickel, Cobalt, and Their Alloys*, ASM International, Materials Park, OH, 2000.
- [26] T.J. Lu, H.A. Stone, M.F. Ashby, *Acta Mater.* 46 (1998) 3619–3635.
- [27] Integran Technologies, Inc., unpublished research.

Appendix D

Electrodeposition and metalization recipe

The process by which a polymer substrate can be coated with a metallic layer requires many intermediate steps and hinges on the ability to make the polymer surface conductive. Without a conductive layer, polymer samples come out of the bath with zero deposited material. Through the assistance of fellow graduate student Adam Yaremko, the following process was developed that successfully created well-adhered metal/polymer composites.

After creating the CAD design of the microtruss architecture and feeding the .stl file into the rapid prototyper, the finished part was extracted and finished according to the technique presented in chapter 4. With the dry part that has had all the wax supports removed, the first step in preparing for metalization was the removal of residual wax that is hardened on the surface and smoothening the differing roughness across the part. To accomplish this, the part was submerged in a beaker of 98% sulfuric acid for upwards of 1 hour. To keep the part submerged, titanium meshes were used to hold down the sample. After smoothening, the surface is covered in a reddish hue byproduct that is rinsed off using a pressured blast of distilled water from a squeegee bottle. The parts are left to dry and then weighed and measured to determine amount of material removed.

The new surface of the 3D printed part is now actually a bit too smooth and a short etching step is performed. Samples are submerged for two minutes in potassium permanganate made

immediately before etching. Care is taken to swirl the sample inside the solution frequently. After removal, the sample is rinsed and left to dry.

Metalization begins by dipping the etched part in a solution of 3 g/L tin chloride mixed with 6 mL/L of hydrochloric acid. This step is run for five minutes at an elevated temperature of 40°C (using a standard hot plate) with frequent stirring. After rinsing the sample of residual liquids with distilled water, the part is placed in a beaker of 0.3 g/L palladium chloride mixed with 6 mL/L of hydrochloric acid. This process also goes for five minutes at the same elevated temperature of 40°C before rinsing with distilled water. Similarly, these solutions are made fresh at the start of each day.

To strengthen the metallic coating before electrodeposition, the part is placed in a Caswell electroless Nickel bath purchased from Caswell Canada. The solution is run at 85-90°C for 12 minutes to achieve an approximately 4 µm coating. The final step is pulsed electrodeposition to deposit the desired nickel coating in thicknesses not possible with electroless plating. For the metal/polymer rods fabricated during this doctoral thesis, a sulfamate nickel bath was used. The conditions of the bath were a temperature of 50°C bath with a pH of 4 using a 20% duty cycle and 75 mA/cm² current density. The constituents of this bath are 500 g/L nickel sulfamate, 32 g/L boric acid, and 0.2 g/L of sodium dodecyl sulfate.

To summarize, the main steps are:

1. place finished sample in 98% sulfuric acid for 1 hour at room temperature
2. use squeegee bottle to push off dissolved clumps of polymer that could still be stuck to the sample
3. etch the sample in a potassium permanganate solution for 2 minutes
4. sensitize polymer surface with tin chloride for 5 minutes at 40°C
5. activate surface with palladium chloride for 5 minutes at 40°C
6. apply thin (3-5 µm) coating of electroless Ni at 85-90°C (≈ 12 minutes)

7. perform electrodeposition in a sulfamate nickel bath at 50°C bath with a pH of 4 using a 20% duty cycle and 75 mA/cm² current density

Overall, the first three steps work to remove the uneven distribution of roughness across the printed part such that areas with or without polymer/wax interfaces are all smoothed equally. This uniform surface is then etched to create pores evenly across the sample which help adhesion during metalizing. Tin chloride is used to place a conductive monolayer of tin on the surface that the next palladium chloride wash can use to adhere a more stable palladium coating. With a metalized surface, a strike layer of Ni is deposited in an electroless bath before the final electrodeposited Ni coating is plated. Modifications can be performed in the final step to change which grain size of Ni is deposited by adding saccharin to the bath as well as the potential for alloying the Ni coating.